University of Southampton

University of Southampton Research Repository

Copyright © and Moral Rights for this thesis and, where applicable, any accompanying data are retained by the author and/or other copyright owners. A copy can be downloaded for personal non-commercial research or study, without prior permission or charge. This thesis and the accompanying data cannot be reproduced or quoted extensively from without first obtaining permission in writing from the copyright holder/s. The content of the thesis and accompanying research data (where applicable) must not be changed in any way or sold commercially in any format or medium without the formal permission of the copyright holder/s.

When referring to this thesis and any accompanying data, full bibliographic details must be given, e.g.

Thesis: Author (Year of Submission) "Full thesis title", University of Southampton, name of the University Faculty or School or Department, PhD Thesis, pagination.

Data: Author (Year) Title. URI [dataset]

UNIVERSITY OF SOUTHAMPTON

Faculty of Engineering and Physical Science

School of Engineering

Further Understanding of Dark Etching Region and White Etching Bands Development in Bearing Steels due to Rolling Contact Fatigue

by

Mostafa El Laithy

A thesis for the degree of

Doctor of Philosophy

March, 2022

University of Southampton

Abstract

Faculty of Engineering and Physical Science

School Of Engineering

Doctor of Philosophy

Further Understanding of Dark Etching Region and White Etching Bands Development in Bearing Steels due to Rolling Contact Fatigue

by Mostafa El Laithy

Rolling-element bearings undergo rolling contact fatigue (RCF) due to the cyclic loading they experience throughout operation, which leads eventually to failures due to surface or subsurface initiated cracking. During the life of rolling-element bearings, bearing steels experience a number of subsurface microstructural alterations such as dark etching regions (DER) and white etching bands (WEB) that could lead to damages bearing failures. WEB formation typically includes two stages, i.e. the early formation of low angle bands (LAB) followed by high angle bands (HAB). All of these microstructural alterations show inhomogeneity in phases and properties compared with the original bearing steel microstructure, which can influence the integrity of the bearings. Despite extensive research on DER and WEB spanning back to the 1940s, the formation mechanism of these features remains debated. It is unclear how these features initiate in bearings and what drives the carbon migration mechanism during their formation. However, the latest examination on RCF tested bearing samples in this study has shown a third component, i.e. elongated ferrite grains, within WEB, that was not considered in previous models. This raises some questions on how DER, LAB and HAB initiate and evolve during bearing operation and how these three features are linked as well as how they influence the final failure of bearings.

This study aims to elucidate the initiation and growth mechanisms of DER, LAB and HAB by investigating their microstructural characteristics at different stages. Bearings made from four steels including 100Cr6 martensite (two different grades of steel cleanliness), 100Cr6 bainite and a low carbon steel 50CrMo4 martensite RCF tested under contact pressures (2.9 GPa and 3.5 GPa) over a series of stress cycles, have been examined using light optical microscopy, scanning electron microscopy, electron backscatter diffraction, energy dispersive X-ray spectroscopy, transmission electron microscopy, atomic probe tomography and nanoindentation techniques. Initially, the growth pattern of each feature

was investigated optically to determine their evolution under the test conditions, based on which, a semi-empirical model has been developed to predict the initiation and growth of LAB and HAB. These features have all been examined at a variety of resolutions to provide evidence for the unified mechanism.

The results show that DER formation and development process in the low carbon steel 50CrMo4 is much prolonged compared to that in the high carbon 100Cr6 before LAB and HAB formation under similar conditions. Detailed inspection of the features at different stages has shown that DER initiates as groups of parallel, thin, heavily etched DER bands, with each group having a distinct directionality relative to the rolling direction. These bands are found to have led to martensite fragmentation and refinement of the parent microstructure, while the dark etching bands are also seen to break-down, leading to DER becoming 'brighter' at later stages. The grain refinement has been shown to contribute to high stress concentrations and recrystallization. Further development led to the formation of single equiaxed grain bands orientated at about 30° towards the contacting surface. As a form of recovery, elongated ferrite grains are found to form within the single equiaxed bands through grain rotation/coalescence mechanisms, confirmed by carbon measurements. The process is found to involve the release of carbon to nucleate lenticular carbides at the edges of the newly formed elongated ferrite grains. As more LAB form, the unstable geometries of the carbides break leading to the formation of HAB through recrystallization. Surface energy analysis has shown that the lenticular carbides structure in HAB is more stable than that in LAB. This has led to the uniform mechanisms for the global microstructural alterations of DER, LAB and HAB as a continuous cycle of energy build-up and release due to cyclic loading from small to large scales.

The analysis of failed bearing samples has shown that voids develop at the interface between lenticular carbides and ferrite band in WEB, which is a plane of weakness due to the difference in their hardness. Consequently this may initiate cracks at the interface, leading to bearing failure. WEB are also observed to have grown through non-metallic inclusions, which may have caused inclusion debonding from the steel matrix and crack initiation, leading to final bearing failures.

Table of Contents

Acknowledgements

I would like to express my gratitude to the University of Southampton and Schaeffler Technologies AG & Co. for giving me this opportunity to pursue my PhD degree. This study was made possible by Schaeffler and EPSRC who funded this project. This thesis is an accumulation of work that has been conducted over the past 4 years. It has been a long journey where I have grown both professionally and personally and am extremely grateful for the opportunities seized during these challenging times.

My first acknowledgement would go to my supervisors Ling and Terry who have been instrumental people throughout this project. I thank you both for the continuous support and guidance throughout my PhD journey and for always encouraging me and agreeing to meet me at short notice throughout the difficult and challenging times of this journey, especially over the past couple years. I am also grateful for the many opportunities given throughout my PhD study to attend and present my work through various international conferences. It has truly been a remarkable experience. I would also like to extend my thanks to the Peter Jost Foundation for providing me with the grant to travel to conferences around the world in pre-COVID times.

I would also like to extend my sincere gratitude to colleagues from Schaeffler for their interest in this project and conducting and providing test specimens for this project along with additional information and continuous support throughout this collaboration. Special thanks to Bernd and Wolfram for all the regular meetings throughout the past 4 years, our monthly discussions have always been a constant encouragement for me throughout this study. Your constant support willingness to help when possible has not gone unnoticed.

A very special thank you also goes to Dr Alexander Schwedt from RWTH Aachen University, Germany for our very interesting discussions about DER and WEB formation and for helping with conducting the EBSD analysis in this project in the times of COVID. I am grateful for your help during the time where travelling abroad to conduct tests myself was restricted. A thank you also to Dr. Richard Cook and Dr. Dichu Xu at the University of Southampton for their help and guidance in conducing the nanoindentation tests in this study. I would also like to thank Dr. Zabeada Aslam and Mr. John Harrington from Leeds University for their help in conducting FIB/TEM analysis and also Mr. Martin Mier from University of Oxford for conducting the FIB/APT test. Our many virtual meetings and your help in conducting these tests externally has assisted me in advancing through my PhD even with the travel restrictions. Funding for the APT test was provided by the Henry Royce Institute through the Royce Student Equipment Access Scheme.

A big thank you to all my colleagues (past and present) at Southampton who have made my time is Southampton truly enjoyable. I will not be able to go through all the names, but you know who you are. To all my friends here and back home, thank you for encouraging me and your support throughout this journey.

Last but not least, I would like to thank my family, especially my parents and my sister for your limitless support and encouragement throughout this journey right to the finish line. Thank you not just for your support throughout my PhD, but throughout my life. I would not be where I am today if it was not for you! Words could not express my gratitude for everything you have done for me.

Contribution of Work:

- RCF testing of ACBBs in this project has been conducted at Schaeffler while the sample preparation and metallographic procedure for the sample was conducted by myself.
- The test plan for EBSD analysis was carried out by myself while the operation of the EBSD was conducted by Dr. Alexander Schwedt at RWTH Aachen University. The interpretation of the results was conducted by myself.
- TEM and SAED procedure was carried out by Dr. Zabaeda Aslam at University of Leeds while the TEM lamella sample preparation was conducted using FIB by Mr. John Harrington at University of Leeds. Interpretation and indexing of the results was conducted by myself.
- Test plan for FIB/APT was carried out by myself while the procedure was conducted by Mr. Martin Mier at University of Oxford. Results have been analysed and interpreted by myself.
- Test plan and sample preparation for nanoindentation tests were conducted by myself while the nanoindentation procedure was conducted by Dr. Richard Cook and Dr. Dichu Xu at the University of Southampton.

Declaration of Authorship

I, Mostafa El Laithy, declare that this report entitled "Further Understanding of Dark Etching Region and White Etching Bands Development in bearing steels due to Rolling Contact Fatigue" and the work presented in it are my own and has been generated by me as the result of my own original research. I confirm that:

1. This work was done wholly or mainly while in candidature for a research degree at this University;
2. Where any part of this report has previously been submitted for a degree or any other qualification at this University or any other institution, this has been clearly stated;
3. Where I have consulted the published work of others, this is always clearly attributed;
4. Where I have quoted from the work of others, the source is always given. With the exception of such quotations, this thesis is entirely my own work;
5. I have acknowledged all main sources of help;
6. Where the thesis is based on work done by myself jointly with others, I have made clear exactly what was done by others and what I have contributed myself;
7. Parts of this work have been published as:
    - M. El Laithy, L. Wang, T. J. Harvey, and B. Vierneusel, "Semi-empirical model for predicting LAB and HAB formation in bearing steels," *International Journal of Fatigue*, p. 106230, 2021
    - M. El Laithy, L. Wang, T. J. Harvey, and B. Vierneusel, "Re-investigation of dark etching regions and white etching bands in SAE 52100 bearing steel due to rolling contact fatigue," *International Journal of Fatigue*, vol. 136, p. 105591, 2020
    - M. El Laithy, L. Wang, T. J. Harvey, B. Vierneusel, M. Correns, and T. Blass, "Further understanding of rolling contact fatigue in rolling element bearings-a review," *Tribology International*, vol. 140, p. 105849, 2019

Signed: .....

Date: .....

Definitions and Abbreviations

A_1	Offset value
A_2	LAB saturation level (%)
ACBB	Angular contact ball bearing
APT	Atomic probe tomography
BCC	Body centred cubic
BCT	Body centred tetragonal
BF	Bright field
BSE	Backscattered electrons
CI	Confidence index
DER	Dark etching region
$\frac{dSA}{dV}$	Surface area to volume ratio
dx	Time constant
EBSD	Electron backscatter diffraction
EDX	Energy-dispersive X-ray Spectroscopy
E_{LC}	Interfacial energy of carbide
FCC	Face centred cubic
FIB	Focused ion beam
γ	Specific interfacial energy between ferrite and carbide per unit area
GB	Grain boundary
HAB	High angle bands
$HAB\%$	Density of high angle bands
HAGB	High angle grain boundary
IPF	Inverse pole figure
IQ	Image quality
KAM	Kernel average misorientation
LAB	Low angle bands
$LAB\%$	Density of low angle bands
$LAB\%_{sat}$	Low angle band saturation level

LC	Lenticular carbide
LOM	Light optical microscopy
m	Linear slope at x=x_0
ND	Normal direction
OPS	Colloidal silica suspension
RCF	Rolling contact fatigue
RD	Rolling direction
SAED	Selected area electron diffraction
SE	Secondary electrons
SEM	Scanning electron microscopy
σ_{vM}	von Mises stress
τ_0	Orthogonal shear stress
τ_{45}	Unidirectional shear stress
TEM	Transmission electron microscopy
V_m	Molar volume of carbide
WD	Working distance
WEA	White etching area
WEB	White etching bands
WEC	White etching crack
x_0	Stress cycles to reach half the LAB saturation level

Chapter 1

Introduction

1.1 Background

Rolling element bearings are today widely used in multiple sectors such as automotive, marine, aerospace and industrial applications and are considered one of the most commonly used and vital components for transmitting loads and facilitating smooth rotation instead of sliding motion required in rotating machinery. The growing necessity of modern bearings has warranted an excellent understanding and knowledge of bearing operations such as bearing dynamics, elastohydrodynamic lubrication and rolling contact fatigue (RCF).

If a ball or rolling element bearing is properly mounted, loaded, lubricated and well isolated from foreign contamination, rolling contact fatigue is the ultimate mode of failure [4–6]. Failure due to RCF can be divided into two categories (ISO 15243):

1. Surface-originated pitting.
2. Subsurface-originated spalling.

Surface-originated pitting initiates as a consequence of surface stress risers, dents, scratches, surface contamination, surface roughness and textures [7]. However, under optimum surface conditions, sub-surface initiated fatigue becomes the main failure mode where cracks initiate in the subsurface at stress risers such as microstructural defects (dislocations, grain boundaries etc.), inclusions, residual stress build-up and secondary phases [7, 8] then propagate to the surface. A survey conducted by Harris et al. [9] has shown improper mounting, sealing and inadequate lubrication to contribute to 90% of bearing failures (Figure 1.1). Nonetheless, these can be avoided by optimising operating conditions whereas subsurface fatigue cannot be avoided when operating above the fatigue load limit due to the nature of bearing materials [6, 9] and hence is considered to be the ultimate failure mode in bearings. Modern manufacturing techniques such as steel purification, advanced sealing

and filtration methods are being developed to reduce harmful contacts (debris) towards the rolling contact zones to reduce wear and delay the occurrence of rolling contact fatigue [10] induced failure and thus prolong bearing life. Nonetheless, the study of the material response during RCF is vital to better understand conditions leading to RCF-induced failure and determine stages of material degradation in bearing steels which contribute to the manifestation of subsurface initiated failure.

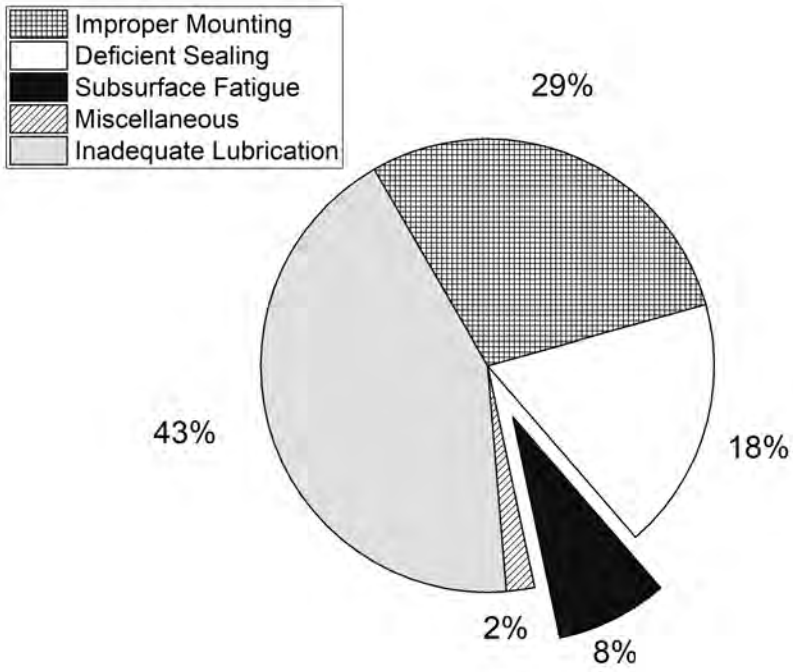

Figure 1.1: The occurrence of different failure modes in bearings. Adapted from [9].

1.2 Statement of the Problem

Steel bearings have been shown to experience subsurface microstructural alterations due to RCF which can manifest in many forms such as WECs, WEAs, DER, LAB and HAB which impact the durability of the bearing microstructure and mark the onset for final failure of the bearing. Significant research has been conducted to investigating the formation of these different microstructural alterations which is discussed in detail in Chapter 2. Over the past decade, localised microstructural alterations such as WECs and butterflies have been commonly investigated in literature while the majority of studies of global microstructural alterations in the subsurface such as DER, LAB and HAB are from pre-1990s. DER and WEB (LAB and HAB) develop in the subsurface of bearing steels under medium/high contact pressures and high rolling cycles. In 1947, Jones [11] was the first to notice that the stress induced during cyclic loading resulted in the formation of irreversible subsurface microstructural alterations within the bearing inner raceway. Several researchers have

reported similar alterations under different names such as troostite (tempered martensite) [11], low-temperature bainite [4, 8] and dark needles [12]. While DER and WEB have been analysed and reported for decades in the industry, there still lacks a universal understanding on the formation mechanism of each feature and how they are linked together. There have been various attempts of modelling the formation of both DER and LAB through carbon migration models but all models in the literature fail to address aspects from experimental studies such as the initiation, development and influence of the different constituents in the features such as equiaxed and elongated ferrite grains and carbides.

While WEB models have focused on investigating LAB, the modelling of HAB has typically been neglected due to their formation at later stages. Hence the development of a model incorporating both the initiation and development of LAB and HAB is needed to better predict the full material response during RCF. A full study analysing how they may influence the integrity of the material subsurface remains to be done. Bearings have become such an essential component for countless machinery today, that understanding the effects of bearing operation conditions on the microstructural alterations due to RCF such as DER, LAB and HAB is critical for improving materials and better predicting the bearing life.

1.3 Aim and Objectives

The aim of this study is to develop a further understanding of DER, LAB and HAB by investigating the initiation and growth pattern of DER, LAB and HAB and establishing a unified formation mechanism for all features based on experimental findings and model their development across the bearing life and their contribution to potential failure in steel bearings. The objectives of this project are highlighted below:

- To learn the cutting-edge research through a detailed and up to date comprehensive literature review on RCF and the associated microstructural alterations known as DER and WEB (LAB and HAB). The literature review is to provide an up-to-date review on current understanding of the microstructure features in DER, LAB and HAB, proposed formation mechanisms and theoretical models.
- To learn and develop skills using advanced microstructural characterization techniques such as Scanning Electron Microscopy, Electron Backscattered Diffraction, Transmission Electron Microscopy, Focused Ion Beam, Atomic Probe Tomography and nano-indentation hardness measurements and interpreting the resulting data.
- Investigate the subsurface of RCF-tested angular contact ball bearings to analyse the initiation and growth patterns on a global scale for DER, LAB and HAB in bearing

steels across different stress cycles, contact pressure, bearing alloys/ microstructures and steel cleanliness.

- Establish a working semi-empirical model to predict the formation and growth of both LAB and HAB in bearing steel under a range of contact pressures based on experimental findings.
- Perform a comprehensive microstructural analysis of the initiation of DER, LAB and HAB and their evolution throughout the bearing life and investigate the different stages of their development at micro, nano and atomic scale using various characterization techniques.
- Establish a unified formation mechanism to explain all experimental findings associated with DER, LAB and HAB including links between the transition of each feature and how these features may contribute to final failure of the bearing.

1.4 Thesis Outline

The outline of the thesis chapters is shown in Figure 1.2 while a brief overview of each chapter is shown below.

- **Chapter 2:** This includes a literature review on the fundamentals of rolling element bearings, RCF, and associated changes in the bearing steel subsurface. A detailed review is established on the development of the field of research regarding DER, LAB

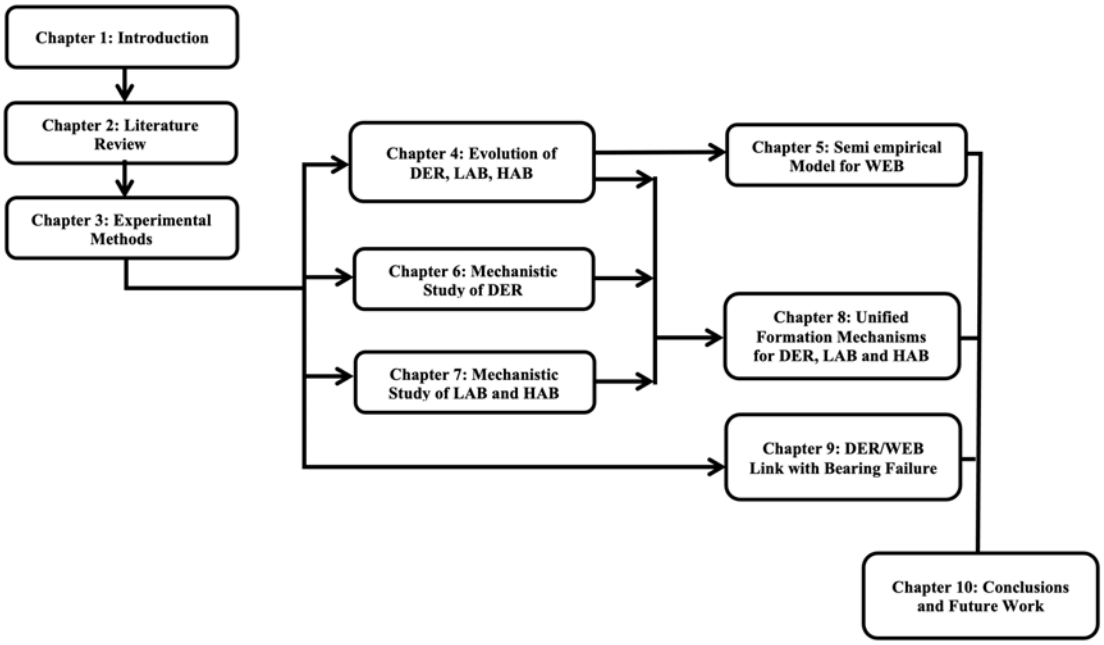

Figure 1.2: Outline of chapters in the thesis.

and HAB over the decades, findings to date and the uncertainties that still remain in understanding the formation mechanism and modelling of the features. A distinction between WEB and other white etching matters such as white etching cracks and butterflies is also highlighted which has caused confusion in literature. A summary of the literature review regarding DER, LAB and HAB is provided at the end followed by the research strategy employed in this study.

- **Chapter 3:** An overview of the experimental methods and analysis techniques employed in this study. This includes the test conditions for the RCF, the metallographic analysis procedure after and the different characterization techniques, methods and equipment used in this study.

- **Chapter 4:** The investigation of the development of DER, LAB and HAB on a global scale across the bearing subsurface is investigated optically in this chapter under different operating conditions and materials to record the associated growth patterns for each features. This includes the density growth of the features, their position in reference to shear and residual stresses, and comparison between the different features at various stages. Manual serial sectioning is also conducted to develop a 3D model of the LAB and HAB.

- **Chapter 5:** Findings from the growth patterns of LAB and HAB from Chapter 4 is utilised in this chapter to establish a semi-empirical model to predict the initiation and growth of LAB and HAB which is compared to published conditions from literature.

- **Chapter 6:** A mechanistic study is conducted mainly on 50CrMo4 bearing steel to investigate the initiation and growth of the DER microstructure from early to late stages and the corresponding properties of the microstructure using Scanning Electron Microscopy, Electron Backscattered Diffraction and nanoindentation to establish the formation mechanism of DER. This is later compared to the DER recorded in 100Cr6 bearing steel.

- **Chapter 7:** A mechanistic study of the LAB and HAB is conducted at various stages of their development using several characterization techniques to establish the formation mechanisms for each feature and how they are linked by investigating their constituents at micro, nano and atomic scale. Analysis of the carbides using imaging processing is also conducted to investigate the HAB initiation conditions. The majority of the samples in this study are 100Cr6 where a comparison to 50CrMo4 bearing steel is later carried out.

- **Chapter 8:** A unified formation mechanism for all three features is established based on findings from Chapter 4, 6 and 7 which links all three features as different stages of a continuous cycle of microstructural transformations in the subsurface of bearing steels.

- **Chapter 9:** The association of the microstructural alterations with potential failure through crack initiation and propagation is presented in this chapter by investigating both failed and non-failed (no raceway damage) bearing samples. The interaction between WEB and inclusions is also investigation as potential failure sites.

- **Chapter 10:** An overview of the project and thesis is presented followed by the main conclusions and findings from this study. Lastly, suggestions are made for future work.

Chapter 2

Literature Review

This chapter presents initially an overview on bearing fundamentals, steel manufacturing conditions and properties utilised in industry for rolling element bearings. An overview on rolling contact fatigue and the material behaviour of steel bearings under different stages and operating conditions of RCF is also provided followed by the formation of microstructural alterations in the bearing steel. This chapter reviews in detail the features and proposed formation mechanisms of DER and WEB currently in the literature and the influence of material properties on their development, which is the main focus on this study. A comparison is made between WEB and other white etching matters such as white etching cracks (WECs) and butterflies.

2.1 Bearing Fundamentals

There are various types of rolling element bearings commonly used in industry which depend on the shape of the rolling elements e.g. ball, cylindrical and spherical rollers as shown in Figure 2.1. Different bearing types are utilized in different applications based on the loading and lubrication requirements [10]. Common types of ball bearings are deep groove ball bearings (DGBBs) as shown in Figure 2.2 and angular contact ball bearings (ACBBs) as shown in Figure 2.3. Investigations in this study is focused on the ACBBs.

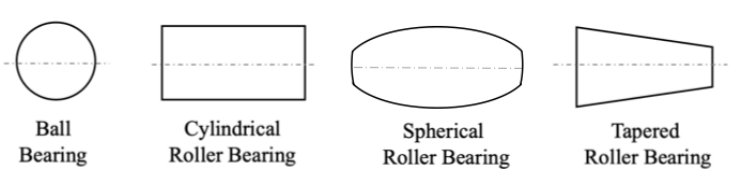

Figure 2.1: geometries of different rolling elements used in different types of rolling element bearings

Typically, a rolling bearing is composed of two rings (inner and outer rings), a number of rolling elements and a cage holding the balls or rollers in an angularly spaced relationship

[10]. The purpose of a bearing is to join rotating components in a machine. The simple cross section and geometry of a DGBB can be seen in Figure 2.2 with common terminologies used for sections of the inner ring. The rotating components can be connected to the inner and outer rings which rotate independently or one of the rings may remain stationary while the other rotates. In rolling element bearings, both rings are continuously kept in contact through the rolling elements where a force can be applied. The over-rolling direction is that in which the contact point between the ball and raceway moves, relative to the inner ring [13, 14]. Rolling bearings are applicable to diverse and precise machines ranging from extreme low-high temperature and vacuum environments of space applications in aircraft power transmission, wind turbine operations and automotive applications [10].

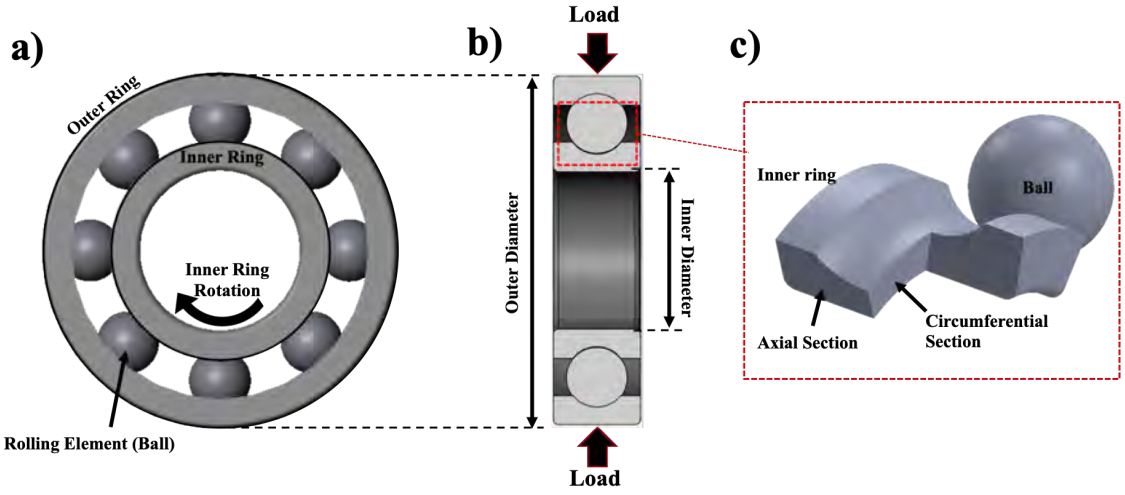

Figure 2.2: a) A DGBB diagram showing both inner and outer rings, and the balls keeping both rings in contact. b) Cross section showing the geometry of both rings and load applied to the bearing. c) Common terminology used for sections of the inner ring.

Deep groove ball bearings shown in Figure 2.2 have versatility [10], designed to operate with a radial load. Nonetheless, they are also capable of operating well under axial load as well as combined loads. The inner and outer raceway grooves usually have a radius of curvature between 51%-55% of the ball diameter for most commercial bearings. The inner ring is positioned to be concentric with the outer ring where the balls in between are separated uniformly through the cage.

ACBBs are designed to support a combined radial and axial load or heavy axial loads depending on the contact angle (see Figure 2.3b) [10]. Larger contact angle can support greater axial loads. They have a groove with the radius of curvature approximately 51-55% of the ball diameter while the contact angle shown in Figure 2.3b does not typically exceed 40°.

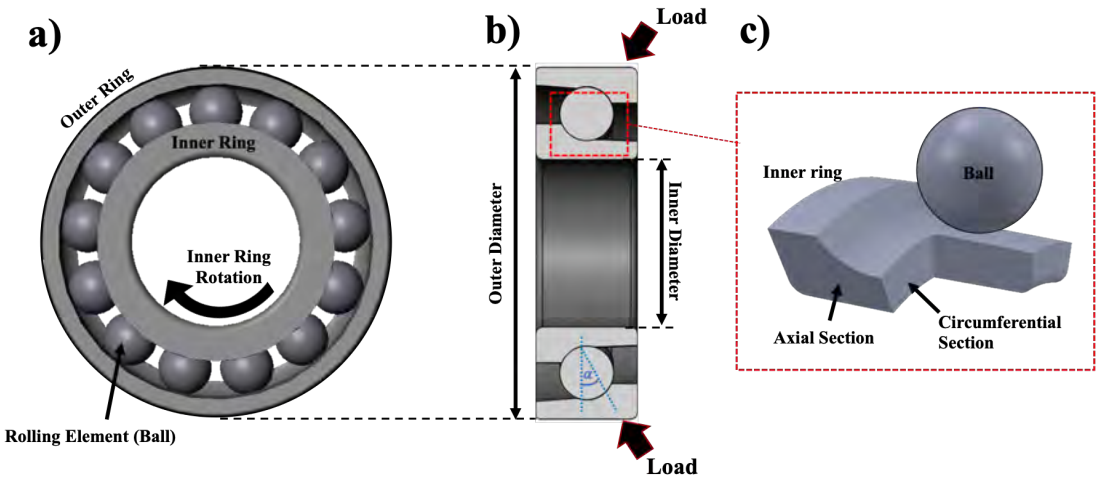

Figure 2.3: a) ACBB diagram showing both inner and outer rings, and the balls keeping both rings in contact. b) Cross section showing the geometry of both rings, typical load applied to the bearing depending on operating conditions and the designed contact angle α. c) Common terminology used for sections of the inner ring.

2.2 Bearing Steel

Rolling bearings are usually manufactured from steels that are hardened, at least on the surface [10]. SAE 52100 (100Cr6) is moderately rich in chromium and can easily be through hardened to 58-64 Rockwell C, equivalent to 660-800 Vickers Hardness which is appropriate for bearing components [10]. However, other alloys may be used depending on application, such as SAE 3310, 4150, 8620 and M50 [10]. Typical compositions are listed in Table 2.1. Low carbon steels (0.1-0.3wt%) have to be case-hardened bearings with the advantage of a relatively soft but tough core. High carbon steels such as SAE 52100 are used for through-hardened bearings [6]. Chromium, molybdenum and manganese are utilised to adhere the required hardenability. Molybdenum can enhance carbide thermal stability and toughness while manganese can prevent the segregation of sulphur [6, 15].

Table 2.1: Typical compositions of various steels (wt%) used in the bearing industry in accordance with ISO 683-17, EN 10083-3, EN 10250-3, EN 4957 and EN 10277-4 standards.

	C	Mn	P	S	Si	Ni	Cr	Mo
SAE 3310	0.08-0.13	0.45-0.60	≤0.025	≤0.026	0.20-0.35	3.25-3.75	1.40-1.75	-
SAE 4150	0.46-0.54	0.5-0.8	≤0.025	≤0.035	-	-	0.9-1.2	0.15-0.3
SAE 8620	0.17-0.23	0.65-0.85	≤0.025	≤0.035	≤0.4	0.40-0.70	0.35-0.70	0.15-0.25
SAE 52100	0.95-1.10	0.25-0.45	≤0.025	≤0.025	0.20-0.35	-	1.30-1.60	-
SAE M50	0.77-0.85	≤0.4	≤0.03	≤0.03	≤0.65	-	3.9-4.4	4.00-4.50

2.2.1 Heat Treatment

Martensitic or bainitic through-hardened microstructures are obtained by austenitisation at 850 °C for about 15 min [16], followed by quenching then tempering at 150 - 200 °C. Bainite is formed as the steel is quenched in a salt bath at temperatures ranging from 200 - 450 °C whereas martensite forms when quenched in an oil/water bath at around 60 °C [13]. Martensite is a highly strained body-centred tetragonal crystalline structure resulting from a diffusionless shear transformation of the austenite. It forms as a consequence of rapid cooling that minimises the duration for carbon atoms to diffuse out of the crystal structure to form cementite which therefore leaves the lattice with excess carbon [13].

Bainite and martensite are similar in many aspects. However, bainitic steels are more brittle than tempered martensite because the average cementite size is coarser in bainite. The cause of the coarser cementite in bainite is due to the mechanism of transformation. For both upper and lower bainite, growth is initially diffusionless. However for upper baininte (higher temperature, low hardness), the excess carbon is then rapidly partitioned into austenite from which it precipitates as coarse cementite during transformation. While for lower bainite, the partitioning of carbon is slower due to the relatively lower temperature leading to the ability to precipitate fine carbides within the ferrite (BCC structure). Nonetheless precipitation of cementite from the carbon-enriched austenite still occurs. For martensite, the carbon remains within the supersaturated plate until a tempered heat treatment can be given to precipitate fine carbides [17].

Quenching steel from the austenisation forms martensite with typically 3-15%vol of austenite retained [18] and 3-4%vol cementite which failed to dissolve during austenitisation. Cementite is distributed uniformly in the microstructure with an average size ranging from 0.4 µm - 0.6 µm [13]. The steel is later tempered to improve toughness, which consequently results in the decomposition of a portion of the retained austenite. Various transition carbides such as η-Fe_2C and χ-Fe_3C_2 may also precipitate [19, 20]. The strength of the steel then depends on the carbon in solid solution and the fine transition of iron carbides which are mainly ϵ-carbides ($Fe_{2.4}C$) [21]. The final microstructure consists of tempered martensite, retained austenite, ferrite and cementite (due to the decomposition of austenite), undissolved primary carbides and metastable ϵ-carbides (transitional) [16]. The prior austenite grain size is ASTM number 8 or greater and individual grain size should not exceed ASTM number 5 [22, 23] where the higher the ASTM number, the finer the grain size. Baughman [24] has reported that the RCF life of bearings may be enhanced with finer grain sizes in agreement with Zaretsky [25] and Ooki et al. [26].

Table 2.2: Transformations observed during tempering of martensite at different temperatures [27].

Tempering Stage	**Temperature Range**	**Transformation Phenomenons**
Stage 0	<100 °C	Carbon atoms segregate towards dislocations (it can represent up to 0.2 wt%C)
Stage 1	100-200 °C	Carbon leaves the oversaturated martensite and creates metastable ϵ-carbides
Stage 2	200-300 °C	Retained austenite which is considered a metastable phase, decomposes into a mixture of ferrite (α) and cementite (Fe_3C).
Stage 3	250-350 °C	Carbon exits the martensite structure to form cementite to the detriment of ϵ carbides
Stage 4	>350 °C	Carbides coarsen and spheroidize. The structure is subjected to recovery, and then recrystallization

Table 2.2 summarizes the different events experienced by martensite during tempering [27]. The changes during tempering can be summarized into two phenomena which consist of the precipitation of carbides from martensite and the transformation of retained austenite. As carbon is rejected from martensite, contraction occurs as the lattice size decreases [27]. However, an opposite effect also occurs where a slight expansion is observed arising from the carbide formation, but not enough to overcome the contraction as the there is an overall continuous contraction as carbon precipitates to cementite (Fe_3C) and ϵ-carbides. On the other hand, as the dense FCC structure of austenite decays to form ferrite and cementite, the volume is reported to increase [27].

2.2.2 Retained Austenite

Changes in retained austenite content can have a major impact on the dimensional stability of the bearing, consistent with the transformation density changes [23]. As a result, for aerospace applications, the retained austenite is limited to 2-5% while other applications may accept much higher contents. Austenite is considered a metastable phase at room temperatures because it exists outside its typical temperature range [28]. Large amounts of austenite (<15%) can typically be detected through optical microscopy while more accurate techniques such as X-ray diffraction methods are needed to measure lower amounts of retained austenite accurately [29]. The increase in volume from the transformation of austenite (typically 4-5%) induces internal stresses within the component, which cause dimensional instability and in extreme cases and can lead to crack formation [29]. The stresses are compressive in the region of decomposition. On the other hand, martensite decay into ferrite and cementite results in a decrease in specific volume which results in tensile internal stresses in the decay region [30].

Zaretsky [31] reported that the reliability of bearing operations to improve with a lower amount of retained austenite. Johnson et al. [32] examined the decomposition of retained austenite in the context of residual stress to find the latter to be proportional to the decomposition of the austenite. On the other hand, Muro et al. [12] proposed both phenomena to be independent. Even though high levels of retained austenite contribute to dimensional instability, the austenite can also improve rolling contact fatigue life. The ductility of retained austenite impedes crack growth by blunting the tips of newly formed cracks [33]. Compressive residual stresses generated by volume changes due to austenite decay may delay crack growth by clamping cracks [33]. The retained austenite can improve the impact strength of the material, making the steel more resistant to fracture when exposed to sudden loads. It is important to optimise the retained austenite level for a good balance between impact strength, improved fatigue life and dimensional instability. This, however, is dependant on the microstructure and bearing conditions such as the operating temperature, where high loads and temperatures intensify the rate of retained austenite transformation during operation. Nonetheless, Paladugu et al. [34] stated that retained austenite transforms slower in fine martensitic microstructures compared to those that are coarse as the plastic deformation inducing the retained austenite transformation is more pronounced in the latter case. Retained austenite can improve the steel life when the lubricant contains wear debris as it helps resist dents on the surfaces of the raceway [35]. The transformation of retained austenite to martensite absorbs energy, which may prevent temperature increases and hence enhance fatigue life [12].

2.2.3 Steel Cleanliness

Steel bearing reliability has significantly been enhanced since 1970's primarily due to the availability of cleaner steels given that impurities can impact the mechanical properties based on their size, type and distribution [36]. Cleaner steels that contain smaller and less non-metallic inclusions have longer fatigue life, which is inversely proportional to the square-root of inclusion size [37]. The fatigue of bearing steels is influenced by internal imperfections such as non-metallic inclusions, carbides and pores [38]. Alumina particles form during de-oxidation. Sulphides and large metallic primary carbides form on cooling during casting [36]. The oxygen concentration in the form of oxides has been proposed to correlate to RCF damage. Therefore, in modern steel bearings, the oxygen concentration is kept below 10 ppmw [13]. Historically, it is believed that oxides are the most harmful to RCF life of bearings [37, 39–42]. Nonetheless, awareness of the harmfulness of sulphides has been increasing over the past decades [43, 44]. This has lead to attempts to reduce more than just oxides in manufacturing down to 1-10 ppm [45]. A balanced approach to

reduce not only oxides but also sulphides can significantly enhance the performance [43]. Cost determines how clean the steel components should be [46]. Figure 2.4 demonstrates how the historical development of bearing steel cleanliness and consequences on bearing life.

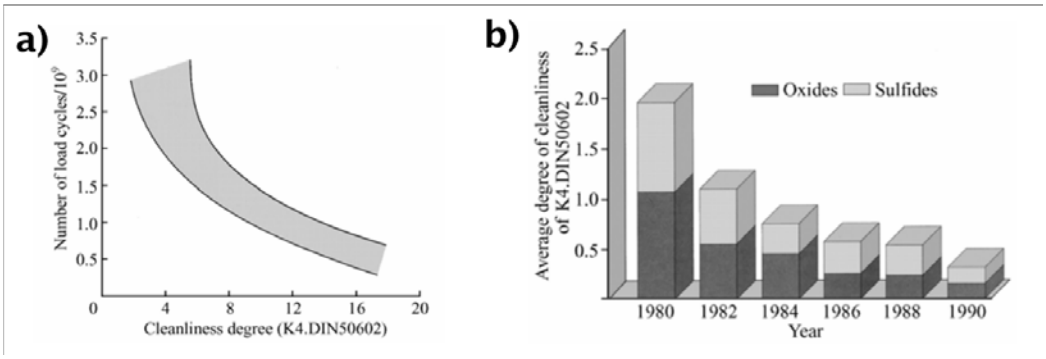

Figure 2.4: a) Impact of steel cleanliness on bearing life. b) Historical development of bearing steel cleanliness based on K4 index for oxides and sulphides [38].

Typical bearing fatigue damage occurs as spalling or flaking of the raceway as a consequence of smearing, plastic flow, bulk cracking or fatigue. Small spalls can grow if the bearing is not replaced because spall edges act as stress concentrators [47]. Surface-initiated failures are associated typically with low stress cycles, while subsurface-initiated failures typically arise from inclusions and are associated with high cycles [48]. Stress localisation between the inclusion and steel matrix interface can lead to fatigue failure due to differences in thermal expansion between the matrix and inclusion during heating/cooling. Differences between the elastic constants of inclusions and the matrix can similarly contribute [49]. However, Leslie [50] has suggested that for high cycle fatigue ($>10^5$) almost all cracks initiate from inclusions whereas for low cycle fatigue ($<10^5$), slip-band cracks dominate.

There is metallurgical evidence for fatigue initiating from inclusions in bearing raceways [36]. The critical size of inclusions may vary from 5-500 µm and decreases with increasing yield stress [51]. For high strength steel such as for bearings, the bearing life is reduced if inclusions greater than 13 µm are present within the microstructure [52]. The critical size of inclusions for fatigue initiation depends on many factors such as the applied load and depth from surface [45, 53]. Various reviews have suggested that the morphology, composition and distribution of inclusions is a more important factor affecting fatigue [13, 45, 54–56]. Inclusions with different shapes and compositions will exhibit various elastic and plastic properties while the coefficient of thermal expansion will determine the residual stresses around the inclusion [36].

In steel, the fatigue life is considered to be controlled by the crack propagation or nucleation which initiates early from a debonded interface [57]. These interfaces have been previously investigated and confirmed that the interface condition between the matrix and

the inclusion strongly influences the crack growth controlling RCF [36]. Enhancing the adherence of inclusions to the matrix and reducing porosity by hot isostatic pressing has been suggested to enhance the bearing life [58]. The strength and coherency of the interface are as vital as inclusion size for determining the crack nucleation [36], leading to the possibility of inclusion engineering through processing to achieve superior bonding with the matrix as shown in Figure 2.5 which gives a representation of the inclusion morphologies prior and after deformation [59].

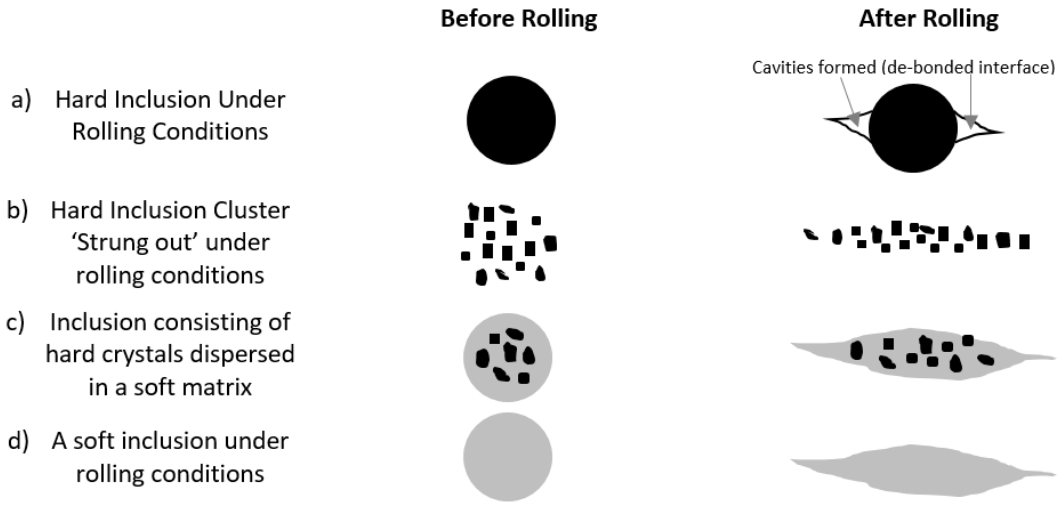

Figure 2.5: Schematic drawing showing the morphologies of different inclusions before and after deformation. Adapted from [59].

Steel cleanliness is described in terms of inclusions, with international standards followed in industry. The most widely used inclusion rating standard is ASTM E45 and DIN 50602, where a limit is set for the degree of purity. In the former, inclusions are classified into four categories A-D based on their morphology, Table 2.3. Each type is later classified into two subcategories based on the thickness or diameter of inclusions referred as 'thin' or 'heavy' series. Inclusions less than 2 µm in thickness are not rated. A severity level is later provided based on the number of inclusions and their length in a 0.5 mm^2 field of view which is calculated based on limits provided in the ASTM E45 standard. In the past, the ASTM E45 standard specified the magnification criteria where the inclusion rating must be determined with a compound microscope at 100x magnification (10x eyepiece and 10x objective lens). However, it now accommodates the growing trend in digital imaging, a minimum resolution of 1µm per pixel is now required when using a 10x objective lens [60]. The inclusions are divided into groups depending on how harmful they could be for the steel as shown in Table 2.3. Titanium inclusions, although existing in very small amounts, can be very harmful due to their sharp edges [36].

Table 2.3: Inclusions types found in bearing steels as rated by cleanliness standards ASTM and DIN 50602 [36, 38, 61, 62]

Type (ASTM E45)	**Type (DIN 50602)**	**Common Composition**	**Morphology**	**Hardness (HV)**	**Brittleness**	**Comment**
Type A	SS	Sulfide (MnS, CaS)	Elongated, plastically deformed (grey in optical image)	150-170	Very Low	The interface with the matrix is typically bonded sufficiently and relatively soft making it less harmful
Type B	OA	Oxides (Al_2O_3)	local accumulation of fragmented foreign particles with discontinuous elongation	about 2,200	Very High	Hard inclusions that are broken up to form long stringer and Interfaces may be de-bonded leading to stress points and crack initiation while the orientation relative to shear stress can accelerate crack propagation.
Type C	OS	mixed oxide systems (SiO_2)	elongated , plastically deformed (dark in optical image)	about 1,600	Low	Rarely found in bearing steels and typically not rated by manufacturers and researchers for bearings
Type D	OG	oxides (calcium aluminates)	globular individual with no preferred orientation typically less than 13 microns	900-2500	High	Harmful due to their size, residual stresses and poor interfacial bonding with the matrix, leading to cavities surrounding the inclusions caused by an inability of the matrix to plastically flow around the inclusion. They are not deformed during hot rolling
Type DS*	-	typically oxides, spinels, Ca modified MnS (Ca(O,S), (Ca,Mn)S)	oversized globular oxides typically greater than 13 microns	about 1,600	-	harmful due to their large size leading to greater voids due to de-bonding of the interface, residual stresses accumulation and cracks within the brittle inclusion.
Type T*	-	titanium carbonitrides (TiC, TiN)	elongated with sharp edges	2500-3000	Very High	Very harmful as the inclusion is relatively brittle where cracks can initiate in the inclusions and propagate to the matrix and sharp edges act as stress concentration points

* Not typically associated with ASTM E45 or DIN 50602 standard.

In the German standard DIN 50602 method K determines an index of percentage area of non-metallic inclusions in the microstructure referred to an area of 1000 mm^2 [62] while method M is used to determine the maximum size rating values for different inclusion types. Four main types of inclusions are analysed under the DIN 50602 standard, elongated sulphides (SS), elongated oxides (OS), dispersed oxides (OA) and globular oxides (OG). Oxide and sulphide inclusions can be distinguished through optical microscopy, oxide inclusions appear black in colour while sulphides appear dark grey. Under this standard, the degree of purity is provided through an index value or k value (K0, K1, K2, K3 and K4) referring to the percentage area of non-metallic inclusions in the microstructure referred to an area of 1000 mm^2 where K0 represents the smallest inclusions and K4 the largest. It should be noted that steel cleanliness measurements in this study is conducted in relation to the DIN 50602 method k.

Finite element modelling by Ebert et al. [38] demonstrates the impact of an inclusion at a depth of 0.24 z/b (z is the subsurface depth and b is half the contact width) below the center of contact on the equivalent stress distribution in the microstructure (see Figure 2.6a). Inclusions in the subsurface results in a major disturbance of the principal stresses and von Mises stress compared to the inclusion free model. The excess stress generated in this region would make the microstructure more susceptible to failure. The potential risk of a globular Al_2O_3 inclusion depending on the depth ratio z/b is demonstrated in Figure 2.6b. The increase in equivalent stress for three identical inclusions positioned at different depths is shown and it can be concluded the highest risk factor (largest increase in stress) of such an inclusion exists at a depth of 0.4 z/b which is interestingly similar to the depths of the microstructural alterations investigated in this project.

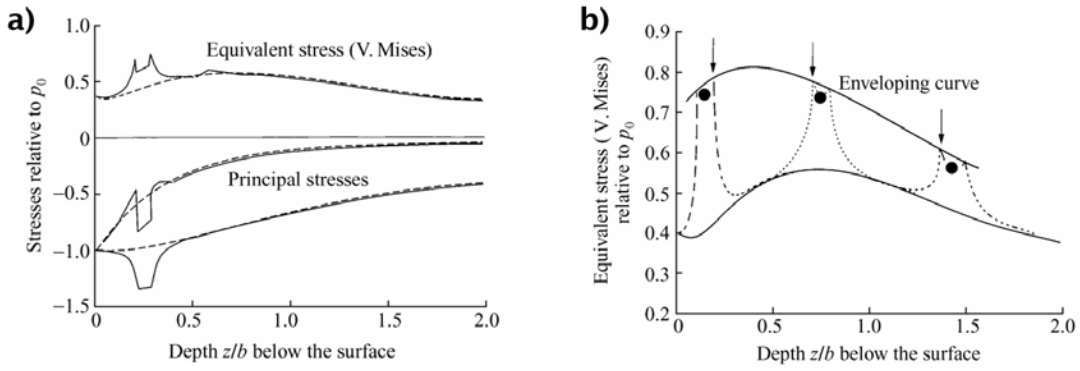

Figure 2.6: a) Principal stresses (y and z direction) and equivalent (von Mises) stress distribution in a undistributed (inclusion free) matrix (dashed) and matrix with an inclusion (solid) at depth z/b of 0.24. b) Risk potential of Al_2O_3 inclusion at different depths depending on corresponding increase in equivalent stress. Stress values are plotted relative to the contact pressure p_0. The increase in stress from inclusions at three different positions are also shown in dashed lines [38].

2.3 Rolling Contact Fatigue

Rolling contact fatigue originating from the material subsurface is considered the most common bearing failure if the bearing is mounted, aligned and lubricated appropriately, and not overloaded [7]. Assuming that rotating bearing life is limited to the probability of subsurface initiated spalling, there have been various rolling contact fatigue empirical and analytical models to estimate the performance of the rolling bearings [8]. RCF failure results in material degradation due to crack propagation arising from the alternating stress field within the material as defined by the Hertzian contact theory [13] where the pressure experienced is in the order of GPa [13]. Crack initiation leading to RCF failure can originate on the surface through stress raisers such as surface roughness and defects [7]. Nonetheless, under sufficient lubrication and surface finish, the performance of the bearing may be optimised but eventually will suffer from subsurface crack initiation and propagation to the surface leading to spalling on the bearing raceway [7]. Subsurface-initiated failure may originate from subsurface defects and discontinuities acting as stress points such as inclusions, carbides, slip bands or voids. The stages of developing spalling (Figure 2.7a) in this way are shown in Figure 2.7b and 2.7c respectively.

Steel cleanliness has been reported to reduce the probability of RCF failure significantly due to less inclusions in the subsurface which act as stress raisers and hence less possible crack initiation points [63]. Local damage such as butterfly cracks have been associated with the high stress accumulated at the vicinity of non-metallic inclusions [64] as discussed previously. Another important factor controlling the probability of fatigue spalls is the micro-plastic behaviour of the bearing steel under rolling which can be analysed through the Hertzian contact theory [8].

2.3.1 Hertzian contact theory

Rolling contact fatigue varies from classical fatigue. As the material is cyclically loaded, different regions in the material experience varying shear stresses during the load cycle [8]. RCF typically occurs within a small volume of the stressed material given that contact stresses are highly localised. This eventually leads to cracks as a consequence of the alternating contact stresses through over-rolling [65].

The resulting stress field due to two frictionless bodies statically pressed together into an elliptical contact whilst avoiding plasticity was initially examined by Hertz [66]. However, this analysis only involves frictionless elastic deformation which might not be fully representative of the operation of bearings since the raceway or rolling element surface tends

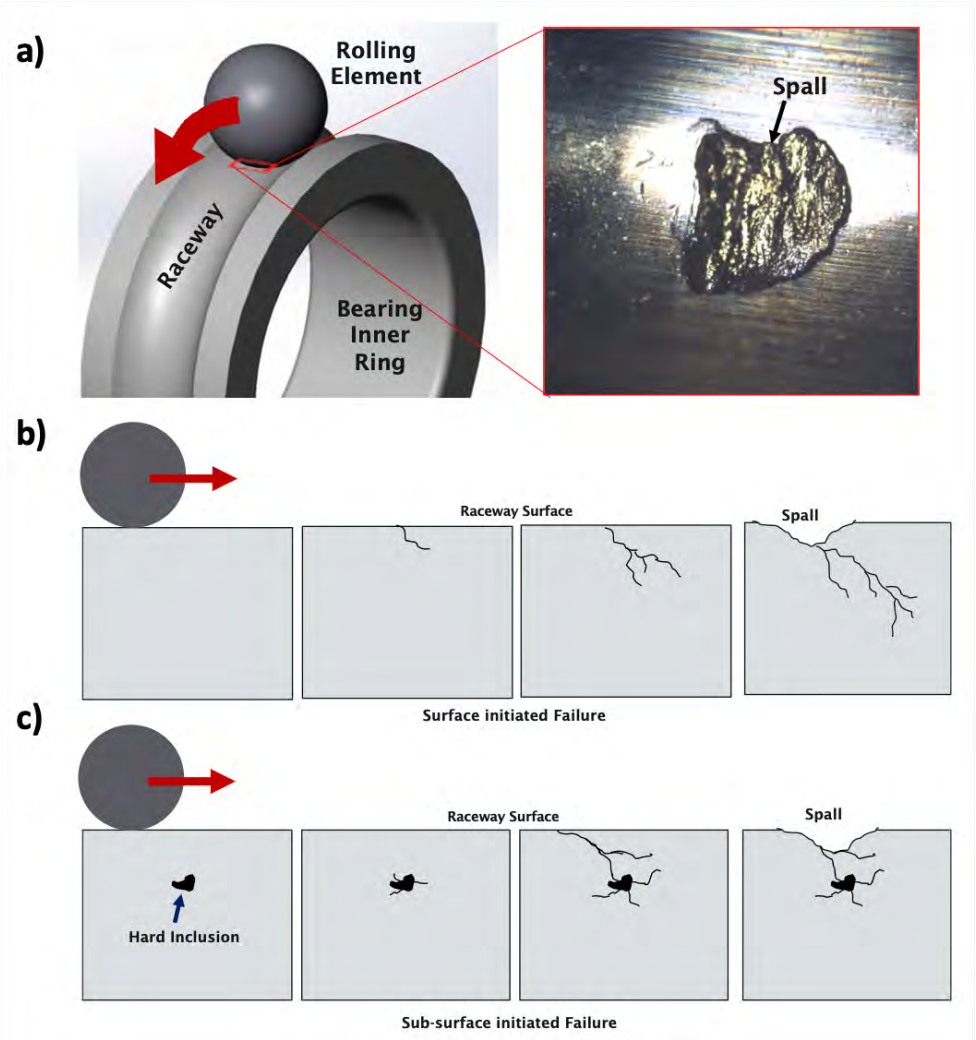

Figure 2.7: a) Spall formation at the contact area between the rolling element and raceway of the bearing inner ring. b) Formation mechanism of surface-initiated spalling origination from raceway surface c) example of formation mechanism of subsurface-initiated spalling originating from an inclusion.

to have a certain degree of roughness while the pressures experienced could be potentially large enough to cause a certain amount of plasticity [13]. Nonetheless, the contact area is relatively small compared to the two bodies and is dependant on the shape of the two bodies in contact. In ball bearings, the contact geometry is usually a point contact whereas in roller bearings it is a line contact but under an applied load, the point and line contacts become elliptical and rectangular respectively as shown in Figure 2.8 and 2.9.

The pressure normal to the contact area does not cause severe plastic deformation even under a contact pressures of 3 GPa given that the yield strength of 100Cr6 is about 2 GPa [36, 68]. The bearing steel material does not typically yield as the stress states below the indenter are highly triaxial (Figure 2.10a and b) and the shear stress at the surface is below 10% of the surface contact pressure P_0 [36] (Figure 2.10c). Consequently, the investigation of plastic deformation is commonly compared to the von Mises criterion which should be

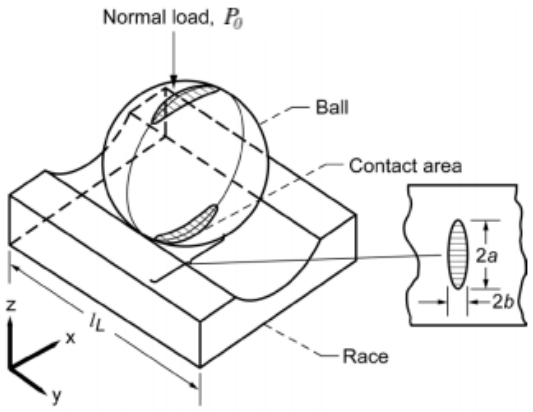

Figure 2.8: Ball on raceway model with elliptical contact area [67].

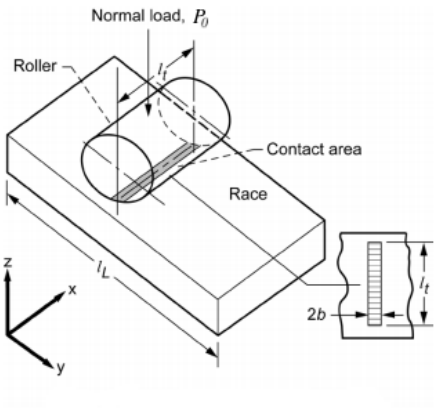

Figure 2.9: Cylindrical roller on raceway model with line contact [67].

below the material yield strength to prevent plastic deformation [69]. Half space models such as the Hertzian contact theory is sufficient to calculate the stress field below the contact surface given the contact surfaces are sufficiently separated by a lubricant film. This can be utilised to help explain subsurface microstructural changes that occur away from the contact surface and hence help develop a better understanding the material behaviour in bearings due to RCF.

The Hertzian model predicts the developed stresses initiated from elastic deformation of two curved smooth surfaces statically pressed together. However, actual contacts are rough and the stress field will be more complex than the Hertzian approach since peak pressures will be focused at raised asperities [70]. The stress state is represented by three normal stresses and six shear stress components. Given the symmetry of the tensor, this could be determined by the three normal stress components defined as σ_x, σ_y and σ_z and three shear stress components denoted as τ_{xy}, τ_{yz} and τ_{xz} [7, 8]. These regularly vary in magnitude during a stress cycle which consequently changes the direction of the maximum shear stress as well. The principal (maximum) shear stress (τ_{45}) shown in Figure 2.10c varies in magnitude and direction in relation to changes in the principal normal stress direction. The maximum shear stress τ_{45} is oriented at 45° to the principal stresses which are at an angle of 0 and 90° at the centre of the contact area, hence τ_{45} is orientated at 45° to the surface at the centre. However, the directionality of τ_{45} would vary away from the centre of the contact given principal stress orientation would vary under a fixed coordinate system. The orthogonal shear stress τ_0 acts parallel and normal to the surface at three planes of τ_{xy}, τ_{yz} and τ_{xz} and its maximum is located in the material subsurface. There is often a plane with the most significant τ_0 depending on the contact geometry. In Figure 2.10a, the significant τ_0 is orientated in the xz direction since the short half-width of the contact is

usually orientated in the rolling direction while the long half-width is perpendicular [71].

The maximum shear stress (τ_{45}) due to contact pressure P_0 occurs below the contact point (Figure 2.10c) at a depth of $0.76b$ for point contact with a value of $0.32P_0$ [72] and $\tau_{0,max}$ (Figure 2.11) occurs at a depth of $0.5b$ at a value of $0.25P_0$. For line contacts, τ_{45} and $\tau_{0,max}$ have values of $0.3P_0$ and $0.25P_0$ respectively at depths of $0.79b$ and $0.5b$ [23]. Figure 2.11 demonstrates how τ_0 in the xz plane varies with the movement of the rolling element where maximum τ_0 is experienced at a position of $\approx \pm\ 0.87\ x/b$ relative to the contact area centre while the maximum amplitude of τ_{45} occurs at the centre of the contact [16].

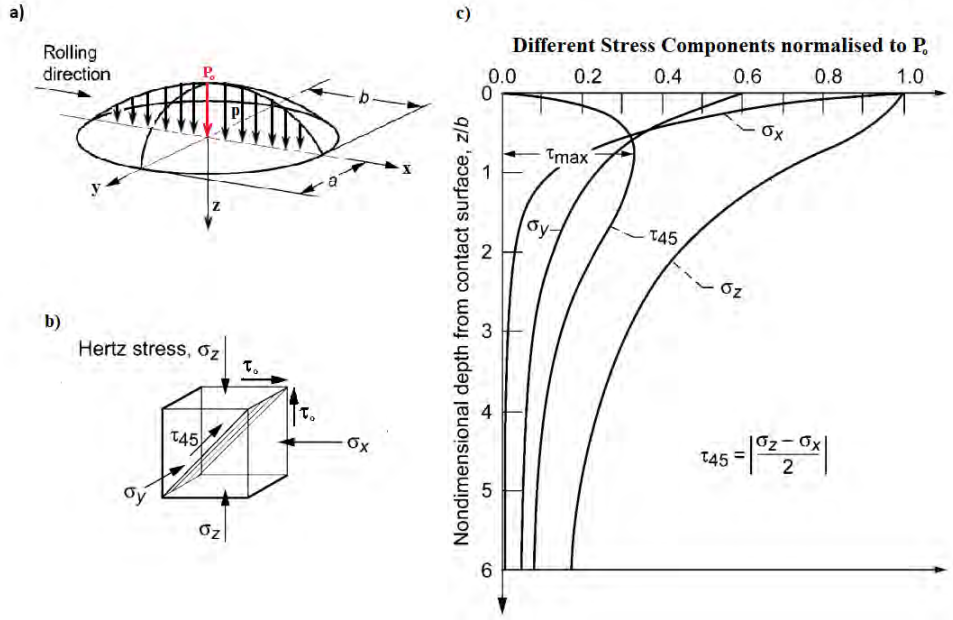

Figure 2.10: Parabolic distribution of contact pressure along elliptical contact with maximum contact pressure at the centre. b) Direction of principal stresses and shear stresses in the material subsurface. c) Variation of normalised principal stresses and maximum shear stress τ_{45} with normalised depth z/b in z direction at centre of contact. Adapted from [23].

There have been various hypotheses suggesting which stress component is the critical stress in rolling contact fatigue contributing to failure initiation and microstructural alterations. The fatigue life of rolling element bearings is heavily influenced by the contact geometry where fatigue tests have shown that for the same maximum Hertzian pressure, longer fatigue life is achieved when the contact width ratio $\frac{b}{a}$ increases [73–75]. In addition, Popinceanu et al. [76] observed that when $\frac{b}{a}$ increases, the orthogonal stress and von Mises stress decrease and therefore concluding τ_0 be the most influential of the stress components since the enhanced fatigue life corresponds with the reduced τ_0. However for microstructural alterations during RCF, there have been various debates on which stress component is most influential, some have suggested the microstructural alterations to occur at the depth of the maximum orthogonal shear stress while others have linked it to the maximum unidirectional shear stress τ_{45} and von Mises [12, 76–82]. This is discussed in detail later in the report.

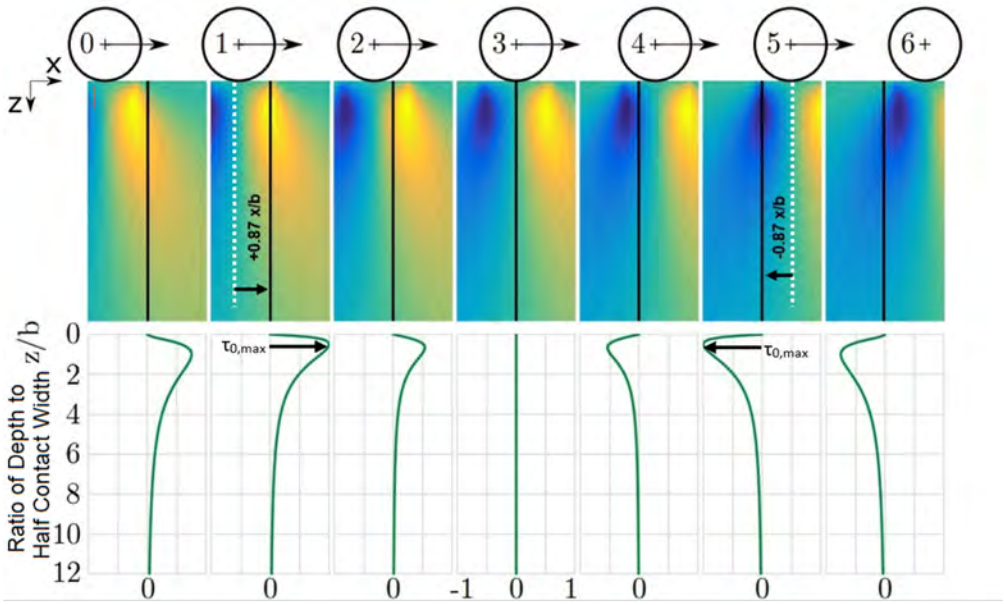

Figure 2.11: a) Variation in τ_{xz} with normalised depth at different positions within contact area between rolling element and raceway. The yellow and blue shades indicate positive and negative τ_{xz} respectively.

2.3.2 Stages of Rolling Contact Fatigue

The material degradation process induced by RCF can be divided into three stages referred to as (i) shakedown, (ii) steady-state elastic response and (iii) instability [8]. Voskamp [30] suggested a change in material response during each of these stages during RCF. The microstructural alterations observed at approximately 0.2 mm below the inner raceway of a deep groove ball bearing has been summarized by Voskamp [30] and can be seen in Figure 2.12 coupled with the approximate duration in running cycle in which these stages operate.

2.3.2.1 Shakedown

Shakedown is obtained when the bearing behaves elastically under further loading beyond the elastic limit [83]. When the elastic limit is exceeded in the initial cycle, a small degree of plastic deformation occurs which introduces residual stresses. This subsequently alters the material properties [30]. During shakedown, residual stress is built up while the material strength and micro-yield stress are both enhanced as an outcome of work hardening during the early bearing life [84, 85]. This is believed to be due to the partial transformation of retained austenite in the microstructure to martensite [36, 86] where the build-up of compressive residual stress is a consequence of the local shape variation which is constrained by the surrounding matrix [30].

Consequently, in the second stage, the load experienced by the material is subjected to

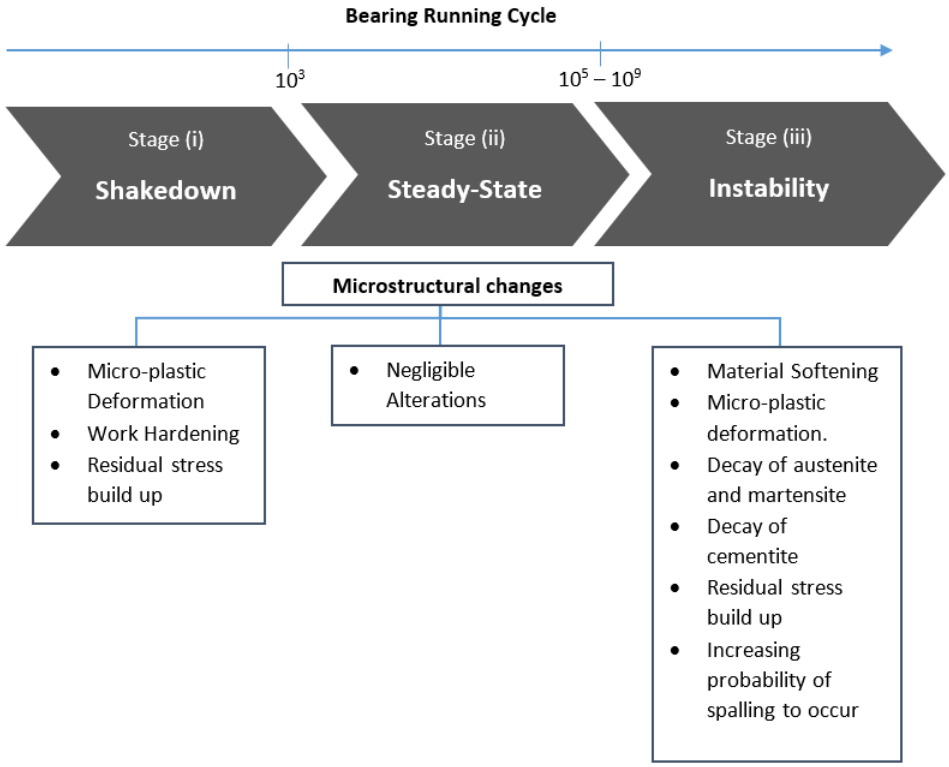

Figure 2.12: A representations of the material response at 0.2 mm below the inner raceway in the three different stages of bearing operation experiencing rolling contact fatigue [63].

both contact stresses and residual stresses introduced previously. Plastic micro-deformation befalls in previously unaffected regions in the first cycle resulting in work hardening and residual stress build-up as earlier. A certain number of running cycles is required ($\approx 10^3$ cycles [63]) for the whole subsurface volume of the material to be altered in the manner discussed. At this point, further plastic deformation is more difficult due to all the volume exposed to load is work hardened which marks the start of the steady-state stage [30, 66]. Experimental results from Arakere et al. [87] suggest the hardness of the subsurface volume of M50-Nil exposed to RCF gradually increases to reach a maximum saturation level between 13.5 x 10^6 - 240 x 10^6 stress cycles, indicating the start of the steady-state response.

Vegter et al. [88] reported the shakedown to occur before 10^4- 10^5 revolutions which corresponds to around 0.1-1% of the total bearing life. The shakedown limit for a given loading history is considered as the greatest stress that can be applied without inducing plastic deformation [13] which is within the yield criterion. However, micro-plastic deformation which depends on local stress raisers exists even when the applied stresses lie within the yield envelope [89]. The steady-state condition will only be reached if the stress induced from loading is below the shakedown limit. If greater than the shakedown limit, the material will continue to plastically deform in a macroscopic manner [30]. Typical shakedown limits can be seen in Table 2.4.

Table 2.4: Shakedown limits for 52100 steel depending on contact area compared to common operating pressures [90]

	Shakedown Pressure (MPa)	**Operating Pressure (MPa)**
Line Contact	2040	1400-1800
Point Contact	2400	2000-2800

Two approaches can be utilized to obtain the shakedown limit. A numerical model consisting of finite element mesh where the internal stresses and deformation of each element of the mesh due to an applied cyclic load can be determined [91]. After numerous cycles, once the residual stress and deformation no longer vary from one cycle to the other, this indicates elastic shakedown has occurred. For tribological problems, one component is modelled as a curved point or line contact and the other as a half space across which the first is traversed. Reproducing this method as the load increases in small increments can be used to determine the shakedown limit for the contact [92, 93]. Nonetheless, this analysis requires significant computational effort since it involves elastic-plastic finite element calculations and approaches steady state using an iterative technique. Given that this numerical method is non-analytic, it would be challenging to predict how variations in the material or the geometry would impact the shakedown. Indeed, there have been recent computational methods with enhanced efficiencies in approaching the steady state [94–98] but they remain non-analytic solutions.

Another approach utilizes shakedown theorems [99–101] of plasticity theory to obtain a lower and upper bound range for the shakedown limit. This provides a range of values where the limit lies within the accuracy of the method [91]. Given that this solution is analytic, the variables such as geometry become essential for the calculation, which is beneficial. This method approaches the steady state directly rather than through iterations and henceforth, require much less computational effort.

An overview of how the cyclic loading effects the material response at its early life is shown in Figure 2.13. If the load is beneath the material yield, this results in a perfectly elastic response of the material (see Figure 2.13a). Ideally, operating conditions would aim to keep the stress values within this limit but practically, commercial and industrial applications demand higher loadings. If the load exceeds the elastic limit, the material will experience shakedown. However, it is shown that there are two different types of shakedown which has been referred to by Williams [91] as elastic shakedown and plastic shakedown depending on the applied load as shown in Figure 2.13.

Under the condition where the load exceeds the elastic limit but under the elastic shakedown limit, plastic flow will be observed within the material in at least the initial

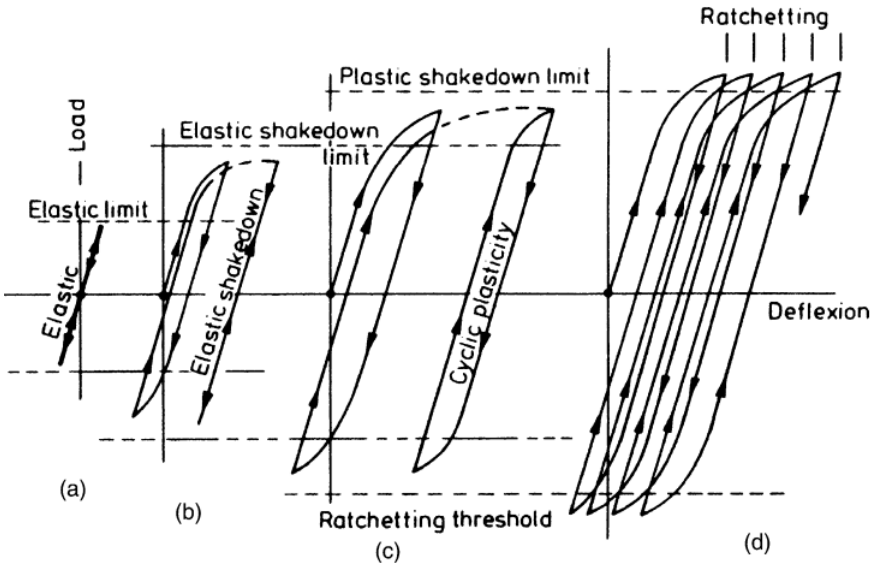

Figure 2.13: Various forms of structural response to cyclic loading showing a) perfectly elastic, b) elastic shakedown, c) plastic-shakedown and d) ratcheting [91].

application of the load [91]. Due to the generation of residual stress during operation, the steady cyclic state may remain completely elastic after the initial plastic flow as shown in Figure 2.13b. This regime is referred to as elastic shakedown. At loads beyond the elastic shakedown limit, each loading cycle would consequently lead to a combination of both elastic and plastic deformation. However, if the load remains below the plastic shakedown limit as shown in Figure 2.13c, the plastic deformation accumulation will disappear after a limited number of cycles [102]. Plastic shakedown is achieved when the response becomes one of cyclic plasticity where the steady-state strain cycle is closed (Figure 2.13c). Cyclic plasticity progresses when the load exceeds the plastic shakedown limit resulting in unidirectional strain accumulation and continuing plastic deformation [91, 103]. A contact with maximum pressure exceeding the plastic shakedown limit would cause incremental collapse or ratcheting (Figure 2.13d), making it liable to premature failure via wear or fracture due to the plastic deformation accompanying each load cycle. However, if the operating condition lies within the shakedown limit (elastic or plastic), a relatively prolonged bearing life would be expected.

2.3.2.2 Steady State Response and Instability

During the second stage, fatigue damage is unlikely since the cyclic response is elastic [86]. The microstructure can be assumed to be fairly similar to that developed in the shakedown stage. To improve the bearing life, maintaining the elastic response in this stage as much as possible is critical. This stage is heavily dependant on multiple parameters such as applied stress, operating temperature, number of cycles and material characteristics such as heat

treatments, alloy composition and inclusions, residual stress levels and hardening response during operation [86, 104]. Voskamp et al. [104] have also highlighted that the stability of finely dispersed carbides in tempered martensite can potentially extend the elastic response of the material significantly. Observations have suggested that the length of this stage can span up to 10^9 cycles without signs of further plastic micro-deformation [30]. The subsurface volume in this stage that is plastically deformed upon increasing revolutions is considered to be negligible up to a certain a certain point across the bearing life [84, 86].

Under the first stage of operation (shakedown), transformed retained austenite and residual stress development results in cyclic hardening, preventing further deformation and microstructural alterations for a number of cycles (steady-state response). However, the inevitable development of microstructural alterations in the subsurface such as phase transformations within the microstructure is associated with sudden bursts of energy dissipation at the moment of ball passage over the subsurface volume resulting in a localised temperature increase [30, 105]. A significant temperature rise in the subsurface is suggested to develop due to the internal deformation where the local temperature peaks is enforced at the moment of deformation (i.e moment of overrolling). The local temperature peaks can activate underpinning and potential slip systems causes cyclic softening [8]. This results in a decline in yield stress [30], causing the cyclic strain amplitude to increase which marks the start of the instability regime. During this stage microstructural deterioration accelerates which ultimately results in crack formation and spalling [90]. To extend the bearing life over a longer number of loading cycles, it is therefore vital to prolong the steady-state response of the material by delaying such microstructural alterations in the subsurface from initiating material softening and causing the material to enter the instability stage where the rate of material degradation is amplified [8, 63].

2.3.3 Residual Stresses

Residual stresses are produced when regions of the material are inhomogeneously deformed in a permanent manner [106]. Significant residual stresses may build up in components such as bearings as a result of various technological treatments and manufacturing processes. Therefore, when a bearing is exposed to external loading, the total stress state is composed of both the externally applied Hertzian stress and the residual stress within the microstructure. The occurrence of residual stresses in the subsurface during bearing operation can be linked to plastic yielding and phase transformations within the material [107]. Compressive residual stress appear during cyclic rolling contact below the contact surface and the depth distribution can vary with the experimental conditions [12, 80, 108, 109]. Figure

2.14 shows an example of residual stress distribution for various cycles. The residual stress measurements on the surface are typically compressive as shown in Figure 2.14 due to hard machining of the inner ring during manufacture. There have been conflicting reports regarding whether the residual stress distribution correlates with the orthogonal or maximum shear stress in tested bearings [12, 109, 110].

Residual stress varies along the material subsurface depth as discussed by Bush et al. [80]. At high applied stresses, it has been reported that peak residual stress within the subsurface occurs at a greater depth whereas lower applied stresses induce a residual stress which peaks much closer to the surface [80]. Muro et al. [12] experimentally demonstrated that residual stress build-up in the microstructure increased with greater Hertzian stresses and introduced a threshold Hertzian stress of 3.5 GPa, below which negligible residual stress is built up during bearing operation. Voskamp et al. [111] have shown residual stress build-up in the bearing subsurface tested at 3.2 GPa. There is an agreement that the residual stress magnitude in the microstructure increases with duration [12, 111]. The initial tensile stress in the bearing becomes compressive early in the bearing life and can increase in magnitude with cycles [12, 80]. It is suggested that the compressive residual stresses induced within the material below the raceway can enhance the fatigue life of bearings [31, 112]. Figure 2.14 shows the developed peak residual stress increases both with load and duration. However, at higher applied loads (3.5 GPa in Figure 2.14), a relaxation of residual stresses is observed after 10^8 revolutions, after which the peak value reduces [111].

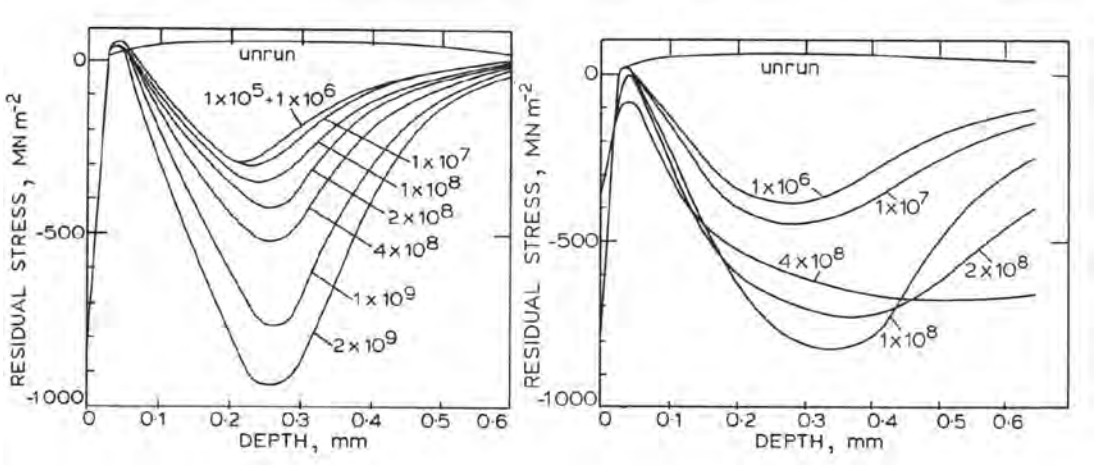

Figure 2.14: Typical residual stress pattern via XRD analysis in 6309 DGBBs inner races subsurface at different cycles where bearing speed was set at 6000 rpm and a maximum contact pressure of: Left) 3.2 GPa. Right) 3.5 GPa is applied [111].

2.3.4 Operating Conditions

In a lubricated rolling contact, when the contact pressure exceeds the shakedown limit, the cyclic stresses contribute towards continuing cyclic plastic deformation [103]. The loading conditions on steel bearings has a significant impact on the bearing life and the material response throughout operation. Experiments by Sadeghi et al. [113] suggested that for low load and high operating speed, the location of the maximum shear stress rises towards the surface. Tests by Voskamp [30] examined the amount of retained austenite at 0.2 mm below the inner raceway at different radial loads throughout the bearing operation. Figure 2.15 shows the decay pattern of austenite varies under each stage of RCF and the maximum contact stress. During shakedown there is a distinct decrease in retained austenite and the subsurface is exposed to plastic micro-deformation before around 10^3 cycles, essentially independent of the applied load [30]. However, at large loads, the decay of retained austenite accelerates. In the second stage (steady-state), the amount of retained austenite remains fairly constant but the length of this stage reduces significantly at greater applied loads. Given that the fatigue resistance of a bearing is dependant on pro-longing the steady-state response during operation, high loads reduce the bearing life and fatigue resistance [8]. During the third stage (instability), retained austenite decays rapidly with the number of cycles.

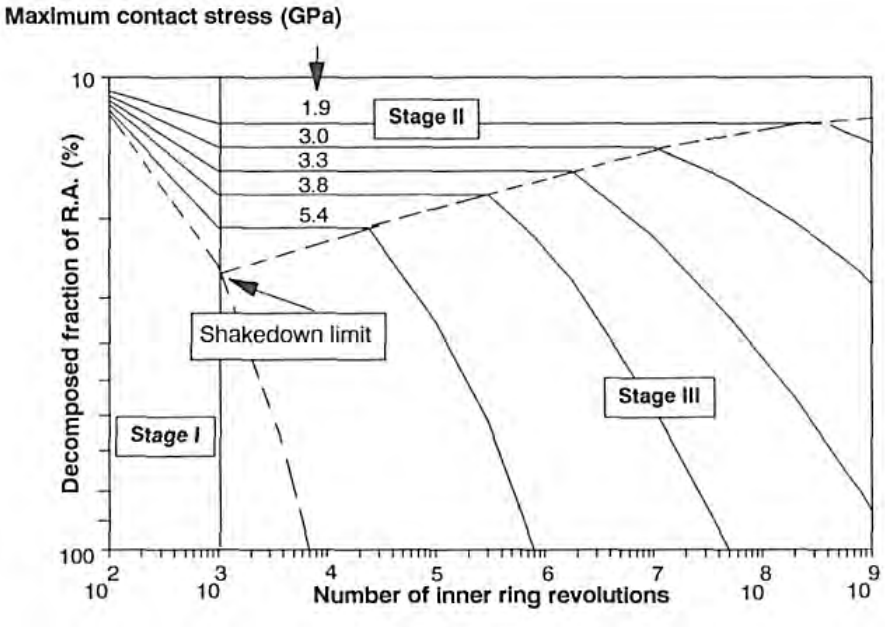

Figure 2.15: Model showing decomposition fraction of retained austenite (R.A) for different maximum contact stresses measured 0.2 mm below the inner ring raceway. Temperature was maintained at 53 °C and speed was fixed to 6000rpm [30].

In general, the applied stress should remain below the macroscopic yield limit to ensure an elastic response. However, for hardened bearing steel this is complicated due to the

small range of plastic deformation occurring between the yield limit and the failure of the material. The actual yield limit can change during loading due to work hardening or softening [30]. Stress-strain hysteresis is observed in cyclic stressing as the maximum stress is greater than the elastic limit which results in energy dissipation [30] which can be calculated by the enclosed area of the hysteresis loop in the stress-strain plot [114]. From the dissipated energy, 99% is in the form of thermal energy [115] while the remaining is absorbed as strain energy linked to microstructural alterations which consequently results in damage initiation. Cyclic stress above the elastic limit contributes to a variation in the internal energy and temperature increase [116]. The temperature increase during operation depends on the maximum stress and the cyclic frequency during operation as well as the environmental heat sink capacity [30]. Nonetheless, the value of temperature increase in the material subsurface during operating remains debated [4, 116, 117].

The operating temperature can also determine the length of the second stage and the evolution of the microstructural alterations in the third stage which can be seen in Figure 2.16. Reducing the temperature to 45 °C significantly enhances the duration of the steady-state elastic response (stage ii), where it becomes approximately 100 times larger compared to the bearing operated at 53 °C [30]. Nonetheless, increasing the temperature to 90 °C appears to reduce the duration of the second stage massively. This demonstrates the strong effect of operating temperature on the bearing life and probability of RCF. However, it is difficult to measure the temperature of the inner ring raceway during operation and therefore, only approximations can be made through measuring the temperature of the stationary outer ring or the inlet and outlet temperatures of the oil lubrication.

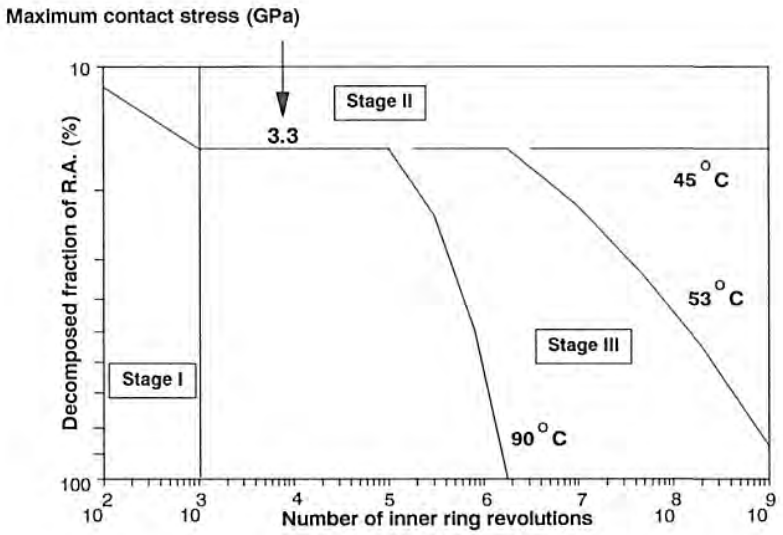

Figure 2.16: Decomposition fraction of retained austenite (R.A) for different operating temperature measured at 0.2 mm below the inner ring raceway. Maximum contact stress was maintained at 3.3 GPa and speed was fixed to 6000 rpm [30].

2.4 Dark Etching Region

Materials in rolling element bearings are subject to cyclic loading which consequently leads to irreversible subsurface microstructural alterations such as dark etching region (DER) and white etching bands (WEB). It is believed that the microstructural alterations in bearing steels occur at the steady-state response stage or even as early as the plastic shakedown stage of RCF where a steady state plastic flow is present [63, 118, 119]. DERs usually form under moderate to high contact stress in the area of maximum shear stress after a large number of rolling cycles ($>$ 5 million cycles) [4, 63, 80–82, 120–123]. The depth of the region varies from approximately 100- 650 µm beneath the contact surface. Nonetheless, it has been well established that their size and formation density increases with contact pressure and running time. The lower boundary of the DER expands quicker than the upper boundary close to the surface with running cycles, indicating that not only that DER thickness increases with running time, but also appears at the greater depth beneath the surface. It is generally accepted that the contact pressure magnitude, number of stress cycles and operating temperature all influence the formation of DER [14, 63, 79–82, 124–126].

The DER in the axial cross section shows a sickle shape (Figure 2.17), but details in the shape can vary (see Figure 2.17a and b) even though similar material and contact pressure is used. The reason for this observation remains unclear. Nonetheless, looking within the sickle DER structure, it is observed in Figure 2.17c that the DER consists various dark patches which are heavily etched compared to the parent microstructure. The DER in the circumferential cross section is seen to be parallel to the contact surface (Figure 2.18). However, given the sickle shape of the DER, it is essential to ensure the circumferential cut is made at the centre of the sickle shape to ensure a valid comparison across literature.

It is generally accepted that DER is a consequence of martensite decay under RCF due to stress-induced phase transformations [82, 123]. The altered microstructure consists of a ferritic phase with inhomogeneously distributed excess carbon corresponding to the parent martensite [118, 120, 128, 129]. DERs are believed to be a mixture of this phase coupled with residual martensite. The boundary between the deformed DER microstructure and the unaltered matrix is gradual [120]. The lower boundary of the DER is more gradual than the upper limit for reasons that are not clear. Throughout the depth of the region, the etching varies in intensity as shown in Figure 2.19b. In other words, the DER is not uniformly dark but consists of dark and lighter patches. The concentration of these patches can vary across the DER which leads to the inhomogeneous distribution of dark areas [6].

Figure 2.19a and Figure 2.19b shows the inhomogeneous distribution of dark patches intermixed with the bright areas and small white primary spheroidised carbides can be

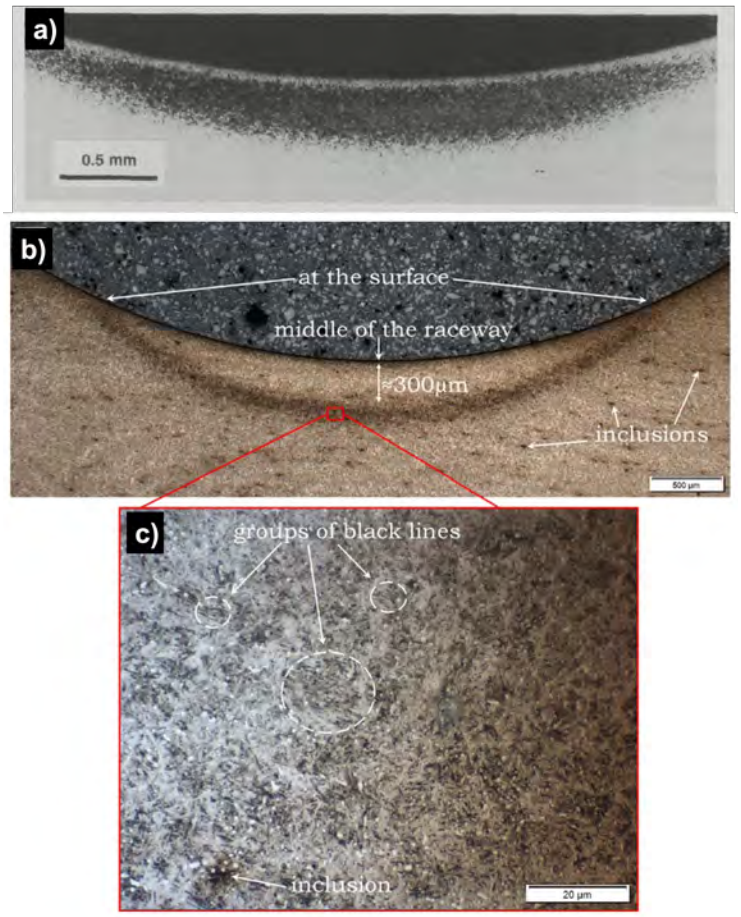

Figure 2.17: Optical images of DER bearing inner ring showing different sickle shapes from a) [82] and b) [127]. c) LOM image of DER area consisting of various dark patches.

seen. The primary spheroidised carbides appear smooth and flat protrusions in SE SEM but dark and spherical in BSE SEM. The DER observed in Figure 2.19a and Figure 2.19b is shown to consist of clusters of elongated dark features appearing as deep grooves in Figure 2.19c which appear as elongated grains (red arrows) in Figure 2.19d. Coupled with the elongated grains, small equiaxed grains are observed in both SEM images as a result of the stronger etchant attack at these sites (yellow circles) [120]. These grains have been reported to have a lower misorientation compared to the martensite matrix [120]. This coupled with the observation that equiaxed and elongated grains are attacked more by nital suggests the grains are ferritic.

There have been multiple debates on the formation mechanism of DER. However the main mechanism claimed in literature is a form of tempering of the martensite due to stress/strain [120, 121, 130]. The first theory developed by Jones et al. [11] reported DER appearing as troostite (mixture of cementite and ferrite) with a lower hardness compared to the parent matrix where the Hertzian stresses coupled with the internal friction of the material transfers the inflicted shear energy into heat. Bush et al. [80] reported that the DER develops in the region of the maximum orthogonal shear stress and resembles

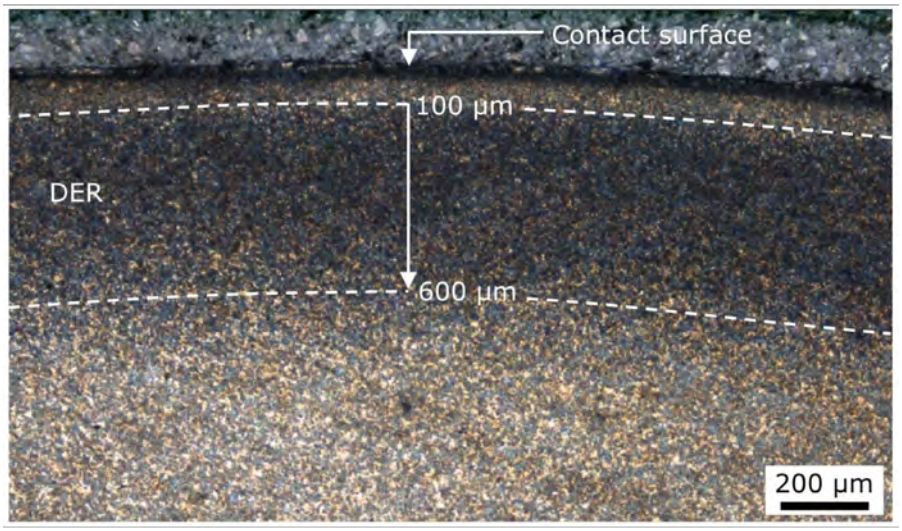

Figure 2.18: Optical image of DER from circumferential cross section [16].

tempered martensite. Their theory proposed that for DER (and WEB), the process begins when martensite crystallites within the vicinity of carbides yield, generating dislocation pile-ups at the carbide/matrix interface through a intrusion/extrusion mechanism. It is also highlighted that DER only develops when a threshold contact pressure of 2.5 GPa is exceeded where the nucleation rate of the DER increases with contact stress. The 2.5 GPa threshold value agrees with various experimental results and is believed to be due to the shakedown limit for 100Cr6 steel point contact which is around 2.4 GPa [6, 80, 118, 131, 132]. The sequence of microstructural alterations in bearing steel during operation is seen through changes in etching response of the microstructure which typically starts with DER. The name given is due to the dark appearance of this region when observed under LOM. The dark contrast observed is due to the scattered deformed and elongated patches with stronger etchant concentration [6]. However, the cause for such an etching response remains unclear.

Swahn et al. [82] reported the DER to consist of a ferrite phase with an inhomogeneous distribution of carbon and remains of the original marensite microstructure. The formation mechanism is believed to be linked to the redistribution of carbon from within the martensite lattice to dislocations which leads to an accumulation of plastic deformation. They were able to capture under TEM what they proposed as early (Figure 2.20a) and late (Figure 2.20b) stage DER where early stage image shows a mixture of transformed zones and residual martensite whereas the late stage shows patches where the parent martensite is completely transformed. Voskamp [63] later proposed a stress induced phase transformation theory where cyclic stresses in the subsurface contribute to local temperature rise which induces the diffusion of atomic carbon within the martensite matrix. As a consequence, dislocations that were previously pinned by carbon are no longer pinned, leading to the activation of potential slip systems through plastic deformation.

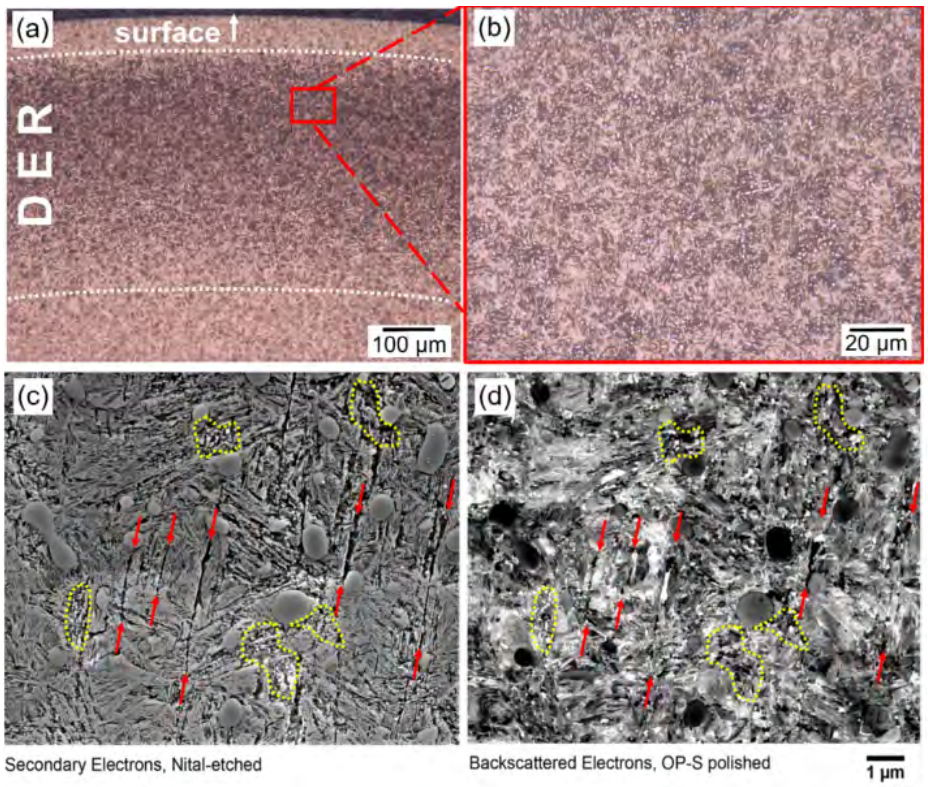

Figure 2.19: a),(b) Light optical micrographs of nital etched DERs. c) Same region observed with secondary electron SEM d) backscattered electron SEM (OP-S polished). Elongated and equiaxed grains are observed with red and yellow respectively [120].

The most recent mechanism for DER proposed in literature by Fu et al. [118] described the DER as patches of DER ferrite distributed in the parent matrix where the orthogonal stress component of the Hertzian contact pressure leads to a strain-induced carbon migration mechanism. This is proposed to be fundamentally guided by dislocation gliding (see Figure 2.21). In this theory, the build-up of strain due to cyclic stresses unpins the dislocations from carbon Cottrell atmospheres. The resulting dislocations glide due to strain and re-attract free carbon which leads to a carbon flux until the carbon atoms reach the vicinity of nano-sized tempered carbides. Hence their model is based on the thickening of tempered carbides through dislocation assisted carbon-migration. However, there remains a confusion towards which stress component correlates with the DER. Warhadpande et al. [4] suggest via optical microscopy tests that the depth of DERs closely corresponds to the depth of the maximum principal shear stress. While some authors have linked it to the maximum principal shear stress [4, 79, 128, 133, 134], others believe it is due to the orthogonal shear stress [80, 118, 135] or von Mises stress [76, 82, 136].

A prominent feature in the DER is the elongated structures observed in Figure 2.19c,d and 2.20a. These features although reported in different studies, have different names in literature such as ferrite microbands [137] , deformation bands [80], dark needles [125], persistant slip bands [126] and elongated ferrite grains [14, 120]. Hence it remains unclear

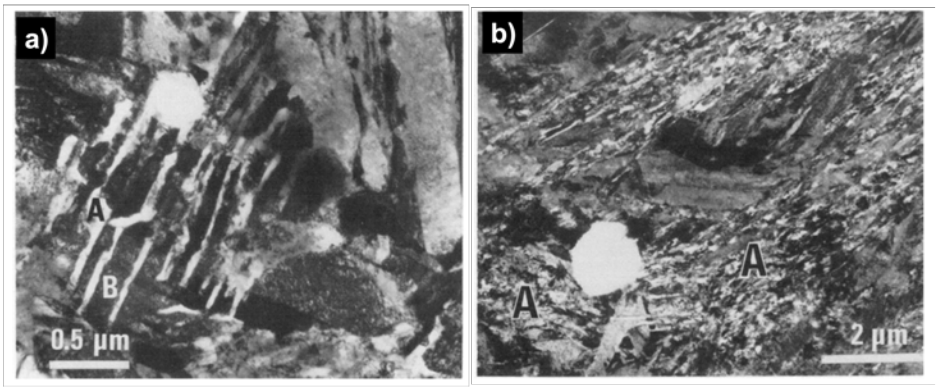

Figure 2.20: TEM image of a) early stage DER where A represents transformed zones separated by residual martensite shows as B. b) Late stage DER where the parent martensite has been fully transformed (at A) [82].

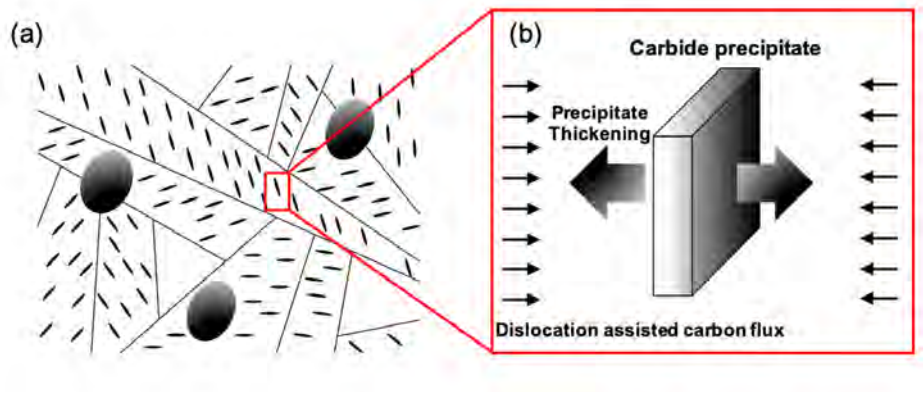

Figure 2.21: Schematic showing proposed DER formation mechanism through dislocation assisted carbon migration towards pre-existing carbide precipitates where a) shows the microstructure of tempered martensite and b) thickening of a carbide precipitate by dislocation assisted carbon-flux [118].

what these band structures actually are and their formation mechanism. Smelova et al. [120] proposed that the elongated and equiaxed grains in DERs are formed via dynamic recrystallization due to the low misorientation of the grains in the DER compared to the unaltered matrix and the existence of high angle grain boundaries between grains and gamma-fibre texture. However the sequence of the alteration process and which ferrite structure forms initially has not been established. No chemical element distribution is reported throughout the recrystallization process of the DER as primary spheroidised particles remain unaltered both crystallographically and chemically whereas the retained austenite is destroyed and transformed in the altered region to martensite [120]. It has been reported that slip marks in DERs are orthogonal to each other and at an angle of 45° from the material surface [5]. However, Sugino et al. [121] implied that the newly formed patches were directionally oriented towards undamaged martensite platelets even though other orientations have also been declared [82, 84]. Hence the inclination of these elongated structures in DER remains unclear and random [120].

Some have suggested that DERs have a slightly higher hardness compared to the unaltered microstructure due to the work hardening of the martensite or the transformation of retained austenite to martensite with reported increase of up to 100 HV [11, 12]. While others have suggested a slight reduction in hardness due to a lower carbon concentration in the region [6, 11, 80, 82, 120, 135]. From literature, a maximum reduction of 150 HV has been recorded in the DER region. Hardness reduction across the DER is shown in Figure 2.22. Hardness measurements in literature are found to generally lack in detail and have caused some confusion. Different hardness measurements observed could be due to competing mechanism of material softening (decay of martensite) and hardening (decay of austenite). EBSD data by Smelova et al. [120] suggests the distribution of primary spheroidised carbides remain homogeneously distributed and fairly similar to the unaltered region even though the retained austenite is considerably lower while a high chromium and carbon concentration exists in the primary spheroidised carbides [120]. Both carbon and chromium distributions in the DERs are similar to that of the typical unaltered 100Cr6 steel microstructure [120]. However, Fu et al. [118] have suggested a much lower carbon and chromium content in the ferrite patches in DER compared to the unaltered martensite matrix due to the carbon migration and the redistribution of Cr in the region of the Cr-enriched globular primary carbides. It is likely that such elemental redistribution occurs an nano-scale and hence difficult to detect with traditional mapping such as EDX.

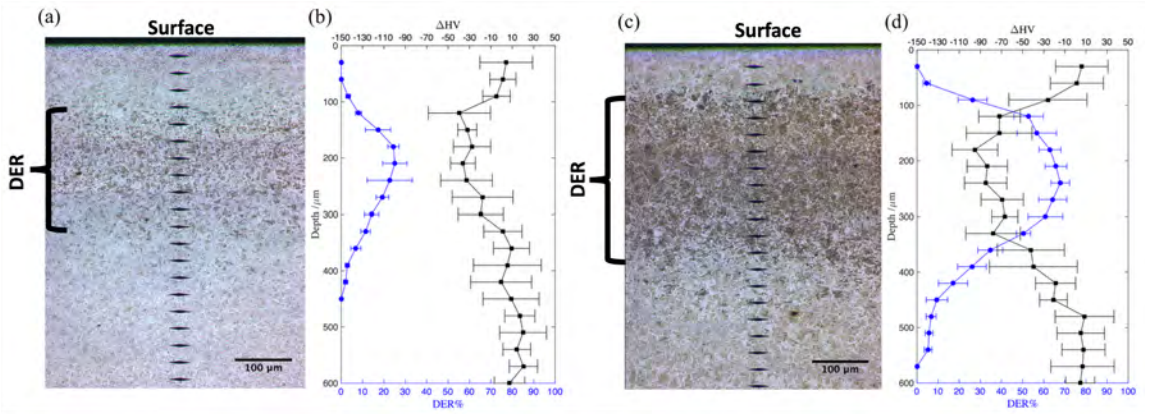

Figure 2.22: a,c) LOM images of DERs developed in the circumferential sections of bearing inner rings run after 10^7 and 10^8 cycles, respectively. (b) and (d) compares the relationship of DER% and change in HV from the original value prior to test with respect to depth measured from the samples shown in (a) and (c) [118].

While various models have been reported in literature, a formation mechanism based on the experimental observations such as the development of elongated DER features and equiaxed grains and their influence of the overall microstructure is not presented in literature to date.

2.5 White Etching Bands

White etching bands (WEB) typically form later on in the bearing tests under RCF within DERs [63, 82, 111, 118, 128, 131]. Although majority of literature report WEB as the next stage of microstructural alterations after DER, some studies have reported WEB without any DER surrounding it, suggesting they may be independent features where WEB could occur directly in a soft matrix tempered to 670 HV [135, 138, 139]. However, such studies have examined the microstructure under LOM rather than high resolution imaging, suggesting it may be possible that DER features exist, but not that developed. The link between DER and WEB in literature remains unclear as no study has established a link between both structures.

WEB are believed to be parallel three-dimensional thin plates parallel to the contact surface in the axial direction, perpendicular to the rolling direction and inclined to the contact surface in the circumferential cross-section as shown in Figure 2.23. They reveal no internal contrast under LOM and consequently etch white or light grey (hence their name) and demonstrate distinct directionality. Different types of WEB are typically reported as low angle bands (LAB) and high angle bands (HAB) which are shown in Figure 2.24b.

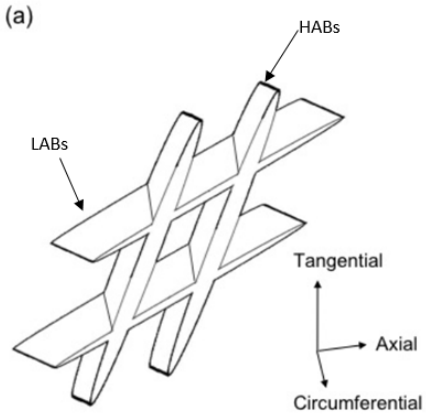

Figure 2.23: A schematic showing the overall morphology of white-etching bands believed in literature [6].

Similar to DERs, WEB are believed to develop within the position of the highest shear stress which would vary depending on loading conditions and contact geometry [8, 120, 140]. A comparison between DER, LAB and HAB is given in Table 2.5 based on a number literature sources. LAB are found to be inclined towards the surface in the rolling direction at angles ranging from 20-35° [13, 14, 63, 79, 82, 111, 123] and typically found to form prior to HAB which is typically inclined at 65-85°. Although LAB are typically reported with a thickness of 0.1 - 0.5 µm, they can reach 2 µm [63, 80, 139].

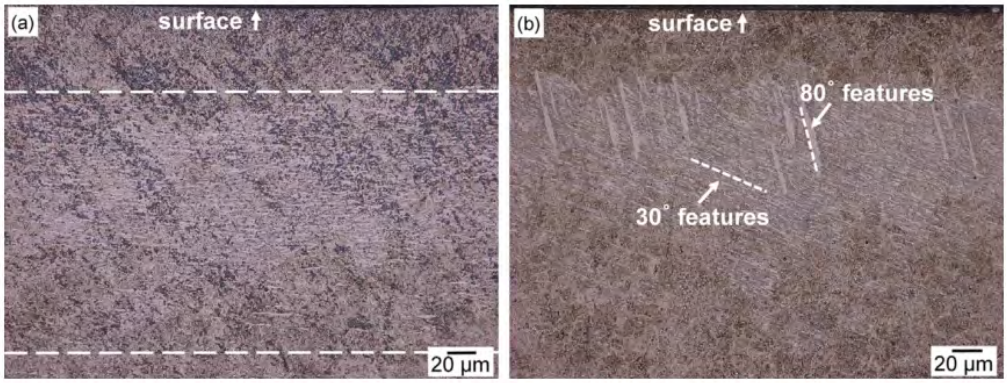

Figure 2.24: Light optical microscopy images of LAB (30° features) and HAB (80° features) in a) axial cross section b) circumferential cross section of bearing inner ring [120].

Table 2.5: Comparison of properties of DER, LAB and HAB [6, 13, 82, 120, 128, 141]

	Dark Etching Regions	***Low Angle Band (30°)***	***High Angle Band (80°)***
Dimensions	100-650 µm depth	5-30 µm length	≈100 µm length
Orientation*	Parallel to raceway	20-35°	65-85°
Band Thickness	-	0.1-0.5 µm	≈10 µm
Formation (cycles)	5-100 million	>100 million	>500 million
Carbon Content	Unaltered (1wt% for 100Cr6)	0.2wt%	0.06wt%
Structure	Ferrite + residual martensite	Ferrite with carbides at the edge	Purely Ferrite

* Circumferential cross section of inner ring.

2.5.1 Low Angle Bands

These bands have been reported to consist of different components: cell ferrite (equiaxed grains), carbide discs and needle-like structures which has been reported with different names by authors which has caused confusion (Figure 2.25). A recent study referred to this needle-like structure as elongated ferrite grains [120] as shown in Figure 2.25. LAB are considered to be pre-dominantly disc-shaped regions of cell ferrite free of primary carbides [79, 82, 123, 141] with a cellular size in the range of 100-200 nm [142]. Adjacent to the fine cellular structure exists carbide discs commonly known in literature as lenticular carbides [63, 79, 117, 142, 143] or carbon-rich areas [120]. This structure does not etch significantly like DER and WEB and it is narrower than WEB where the thickness can reach 1 µm and does not break during tempering [82, 143]. It has been reported that lenticular carbides are a result of plastic deformation of the primary spherical carbides [12]. However, Martin et al. [79] proved that the existence of lenticular carbides could not result from the deformation of pre-existing carbides by examining samples which were given a special double-austenitizing

heat treatment resulting in extremely fine primary carbides. Where the lenticular carbides formed, they were significantly larger than any pre-existing carbide. However, no alternative explanation was offered. Borgese [143] has suggested that lenticular carbides are formed as carbon diffuses over some microns within the bands as a consequence of the stress from the rolling contacts [82]. The diffused carbon precipitates in the form of lenticular carbides where the boundary between WEB and lenticular carbides is suggested to be a plane of weakness [12, 79] which may initiate damage during loading. Both WEB and lenticular carbide have been known to thicken with the number of cycles [117, 118]. Therefore the formation mechanism of WEB is believed to be a process of carbon redistribution due to RCF. However, there have been multiple theories for decades on the driving force for carbon migration which is discussed later. However, as shown in Figure 2.25c, multiple lenticular carbides develop within the band rather than only at the edge. An explanation for this observation in literature has not been established as majority of studies assume it only forms at the edge of the ferrite band.

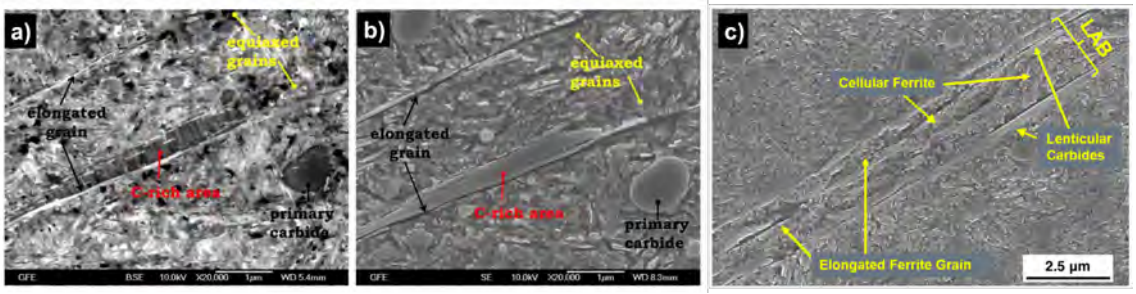

Figure 2.25: SEM image of LAB showing different the cellular/equiaxed ferrite, elongated ferrite and lenticular carbides/carbon-rich areas [120, 124].

The precise mechanism leading to the formation of the LAB has been a debate for decades. There are multiple theories which aim to provide an insight towards the formation mechanism of WEB listed below. The debate mainly consists of whether WEB formation is related to plastic deformation or carbon diffusion through temperature influence.

- Initial theories have suggested tempering to be the main cause of these alterations as a consequence of local temperature rise within the subsurface but no evidence has been shown [11, 79, 135]. However, given that threshold stresses have been found which must be surpassed for these alterations to occur suggests the mechanism is stress-induced [79, 83].

- It has been suggested that WEB formation is caused by an intrusion-extrusion mechanism. Where material is being carried from certain regions of the carbide particles into the neighbouring matrix and the shearing of spherical carbides is emphasized to explain the origin of lenticular carbides. Consequently creating an

intrusion in the carbide and an associated carbide extrusion in the matrix, resulting in WEB formation [80].

- Martin el al. [79] suggested white etching regions are located in areas corresponding to the maximum unidirectional shear stress and WEB formation is a direct result of plastic deformation of the material due to the cyclic, reversed plastic strain in selected volume elements. He also found that WEB did not form when the unidirectional shear stress <0.72 GPa which is similar to the elastic limit of 100Cr6 steel (0.62 GPa), suggesting plastic deformation plays a critical role in WEB formation. Martin et al [79] determined the position of the maximum unidirectional shear stress to closely correspond to the position of WEB in the subsurface, whereas the orthogonal shear stress peaked at a lower depth closer to the surface. The LAB are reported to be ferrite cells of low dislocation density surrounded by walls consisting of tangled dislocations. The dislocation density inside the cell was found to be less that that at the cell walls. It was further suggested that under increasing cycles, the dislocations would become more tangled until a gradual alignment along a certain favourable crystallographic plane is achieved, marking the formation of LAB. Suggestions of dynamic recrystallisation has been proposed [63, 120] in a preferred crystallographic direction.

- Becker [144] suggested a mechanism in which dislocations break away from their carbon atmosphere within the locally plasticized white region and consequently leaving behind a supersaturation of carbon in the ferrite which partitions towards adjacent regions to form lenticular carbides.

- Ochi et al. [145] mentioned the WEB to be due to strain localization where carbide dissolution was observed within the white areas. Given the hardness is reduced within the white etching bands, this indicates that carbon depletion by precipitating lenticular carbides to the boundaries of the ferrite bands. Swahn et al [82] reported the energy increase due to plastic deformation could act as the driving force for carbon flowing towards the surrounding matrix.

- Heckel et al. [117] suggested the flow of carbon to the surrounding matrix from the ferrite bands stems from stress gradient and carbon concentration where a model was created to determine the rate of thickness increase of lenticular carbides as a reference to WEB formation. Nonetheless, the results require a temperature rise of 200 °C to achieve the reported growth rate which has been challenged. Polonsky et al. [14] postulated a diffusion-based mechanism where carbon injection into the solid solution during dislocation annihilation promotes carbon leaving the ferrite bands. Carbon

diffused may become trapped at dislocations causing it to precipitate as layers of lenticular carbides [14, 135].

- Fu et al. [142] created a model to predict the thickening of lenticular carbides with bearing cycles to indicate WEB formation. The theory is based on stress-induced lenticular carbide formation during RCF. The growth of lenticular carbides during operation is achieved by consuming the carbon from adjacent ferrite bands which consequently forms WEB.

There is a general agreement that the rearrangement of dislocations in the ferrite bands, which could be linked to the redistribution of carbon, plays a significant role in LAB development. Given that ferrite arises due to plastic deformation, it may contain significant dislocation density. The strain field surrounding dislocations can attract carbon atoms [146] which consequently gives a strong interaction between the two. Bearing operation results in significant amounts of dislocation gliding, which can henceforth impact the carbon migration within the microstructure and explain the growth of both WEB and lenticular carbides with loading cycles. TEM analysis of the lenticular carbides (Figure 2.26) have proposed they consist of columns of crystallites that coalesce as they grow perpendicular to the LAB, an indication of carbon migration across the ferrite band to the edge.

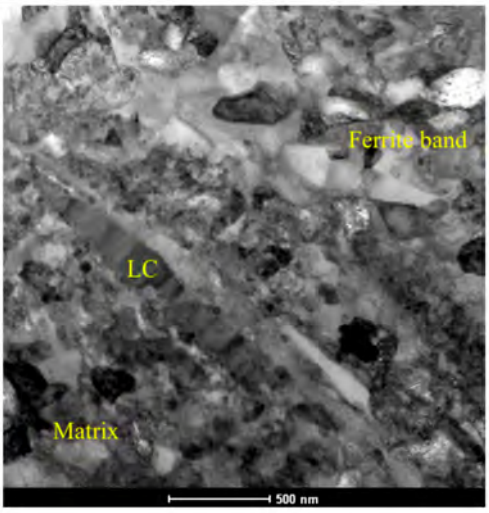

Figure 2.26: TEM image showing a lenticular carbide (LC) lying between the ferrite band and the matrix. [124].

The majority of studies on the formation of WEB were prior to the 1990s and although there are many attempted models for WEB development [14, 63, 83, 118, 142], no theory in literature has been found to successfully explain the transition of features from DER to LAB then HAB with increasing cycles while addressing the directionality of the features. All theories and models currently in literature have neglected to consider the different constituents of the LAB as highlighted recently [120]: cellular/equiaxed ferrite, elongated

ferrite (needle-like) and lenticular carbides into a proposed formation mechanism with studies typically neglecting the existence of the elongated/ needle-like grains. This has led to discrepancies when comparing theoretical models with experimental findings.

2.5.2 High Angle Bands

HAB are considered the final stage of the microstructural alterations, typically longer and thicker compared to LAB. HAB typically form beyond 500 million cycles (Table 2.5), with the cellular ferrite structure of the HAB forming closer to the surface and penetrating/consuming pre-existing LAB [79, 120] (see Figure 2.24b). However, Mitamura et al. [133] observed more HAB than LAB under high contact pressures of 4.6-5.5 GPa in the late stages of the bearing life, suggesting HAB may have formed prior to LAB. Nonetheless, this condition appears to be overload since the generated contact pressure of 5.5 GPa would result in significant plastic deformation based on the von Mises yield criterion. Therefore more experiments are needed to examine this observation. The 3-D structure of the LAB and HAB network has been reported in literature for decades as parallel discs as shown in Figure 2.23 which is generally well accepted based on the images of the bands in axial and circumferential cross sections of bearings (shown in Figure 2.24a and 2.24b). However, such a model does not demonstrate relative dimensional difference between LAB and HAB within a specific volume. Although a recent attempt was conducted to model the features, it does not clearly show the structure of each feature [147].

HAB investigations including experimental and theoretical modelling has been conducted less intensively compared to LAB with the majority of HAB analysis being conducted in literature pre-1990s. Similar to LAB, HAB has been shown to consist of cellular/equiaxed ferrite and elongated grains as shown in Figure 2.27. The higher misorientation in the elongated grains compared to the equiaxed suggest the elongated grains are slightly more deformed. However, the formation mechanism of each feature and their link remains unclear.

Unlike DERs, primary spheroidised carbides are completely broken down in WEB [120]. Figure 2.28 shows the altered microstructures consisting of 30° and 80° bands etched with nital under SE SEM (Figure 2.28a) in comparison to EDX maps (Figure 2.28b & c). Experiments carried out by Smelova et al. [120] suggests that chromium from the primary spheroidised carbides are homogenised within LAB and HAB (Figure 2.28b) while carbon is depleted homogeneously in 80° bands (Figure 2.28c). A similar carbon depleted region can be seen in LAB but are intermixed with the carbon-rich lenticular carbides. The chromium released from dissolved primary spheroidised carbides during RCF has been found to be compatible with the BCC lattice of growing ferrite and has been incorporated into newly

formed crystal structures [120], causing a chromium homogenisation in the altered regions independent of the orientation of the WEB as shown in Figure 2.28b. However, carbon released from primary spheroidised carbides is incompatible with the BCC lattice and consequently pushed out of the regions where the recrystallized ferrite grains grow. Carbon has been found to accumulate between globular regions of LAB and near the corners in which the LAB and HAB intersect, leading to carbon-rich areas believed to be carbide structures [120]. The driving force for recrystallization should be large if WEB are generated through intensely localised deformation and the resulting defects can consequently aid the process of diffusion [13]. Crystallographic determinations show a <111>axis parallel to the normal rolling direction for the equiaxed grains [120] which is similar the recrystallization texture observed in annealed cold-rolled ferritic steels [84]. The elongated grains in both WEB features also show a <111>{112} texture in a direction parallel to their long axis.

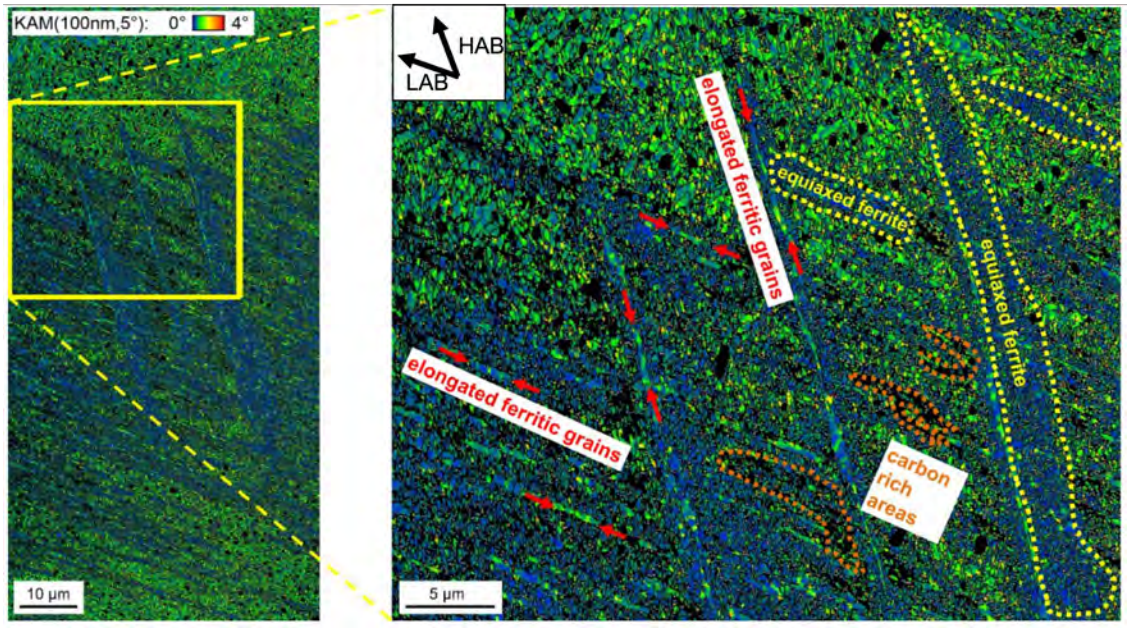

Figure 2.27: A KAM map of the area containing LAB and HAB, highlighting, equiaxed and elongated ferrite grains and carbon rich areas [127].

Residual carbides have been reported under TEM investigation as shown in Figure 2.29 which shows the cellular/equiaxed ferrite structure of the HAB. However, detailed inspection through dark field imaging and SAED pattern has shown small traces of cementite within the HAB. This suggests a breakdown developing within the band. Given the HAB is reported to be carbon depleted (lower than LAB ferrite), this suggests a carbon migration mechanism similar to the LAB is developing. However, a comparison between the migration within LAB and HAB has not been reported in literature.

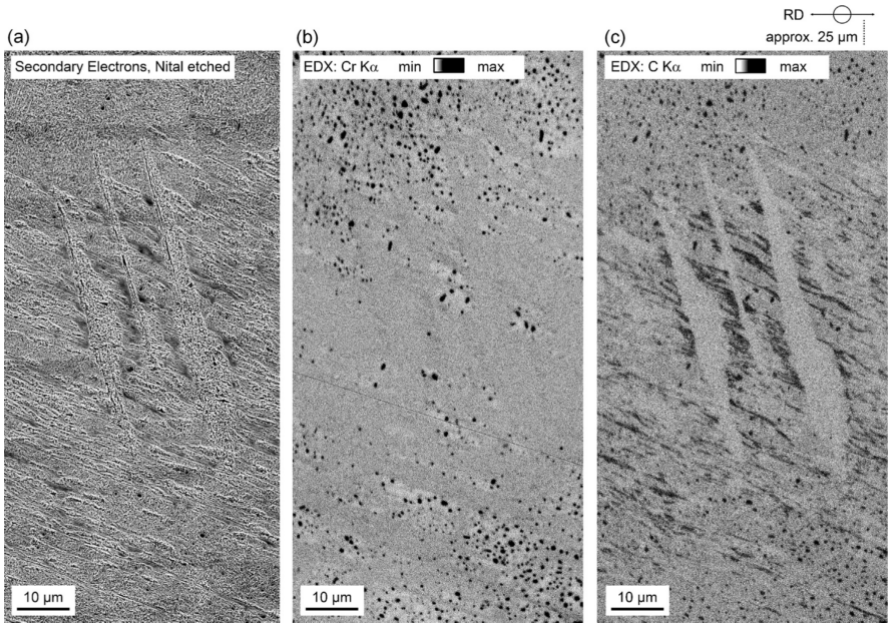

Figure 2.28: a) An image of LAB and HAB features using Scattered electron SEM (Nital etched). Energy-dispersive X-ray spectroscopy analysis of unetched area in a) conducted to show b) chromium map and c) carbon map [120].

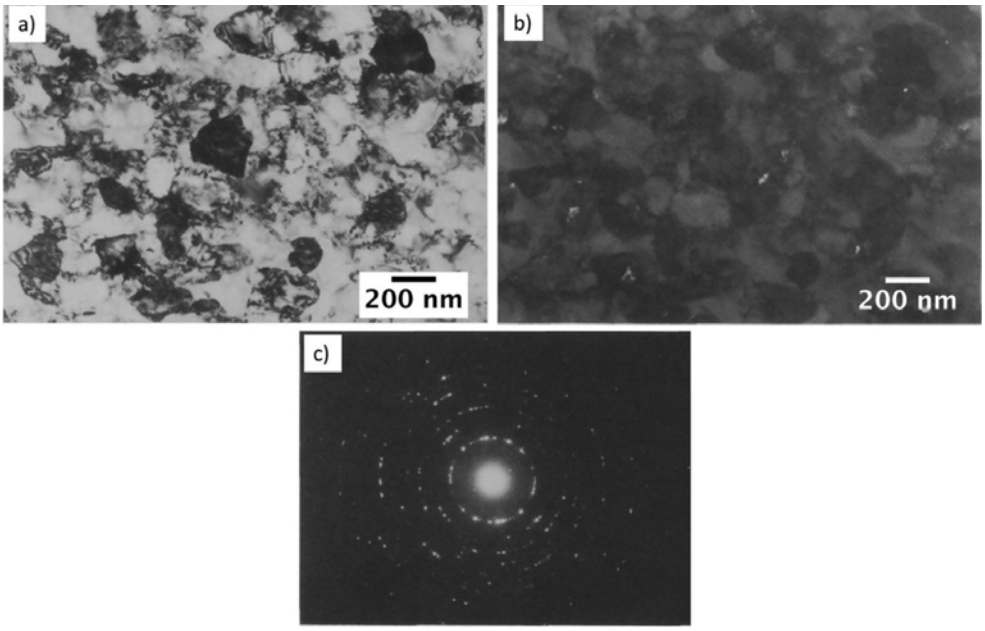

Figure 2.29: TEM of cellular/equiaxed ferrite and cementite in HAB. a) Bright field TEM image showing equiaxed ferrite grain size within the bands. b) Dark field TEM image taken using a cementite diffraction spot in (c) where undissolved cementite appear white while equiaxed ferrite is black [63].

2.5.3 Orientation of WEB

From current theories and debates regarding the formation mechanism, it could be concluded that carbon diffusion or redistribution has a vital role in the development of WEB during RCF. However, there yet remains a universally excepted explanation on the reason behind the distinctive orientations of 30°and 80°bands.

Among the first theories explaining the orientation of WEB was reported by Lyman [148] in 1970 where it was proposed that the WEB orientation was determined by the combination of shear stress acting along the WEB and the maximum normal strain 45°to the bands. However, this theory was only considered for the 30° bands. Zwirlein et al. [131] linked the orientation of 30° and 80° bands to plastic deformation where the orientation is determined by the state of stress at the location of the maximum von Mises stress. The proposed mechanism for 30° bands is that they grow perpendicular to the direction of the highest principal stress (relative tensile) while the 80° bands develop in the direction of the maximum shear stress. The calculation also includes surface friction and residual stresses for explaining the orientations. However, this theory has shown to be inconsistent with experimental observations when applied to bainitic steel bearings with residual stresses of 200-500 GPa [4]. The link between the orientation of WEB and surface friction proposed by Zwirlein et al. [131] has also been disputed by others [4, 14].

Johnson [140] proposed that the orientation of WEB is determined by the direction and location of the maximum shear stress. It was assumed that when 30° bands are formed, the compressive residual stresses are moderate where the ratio of the compressive residual stress to the applied Hertzian pressure is 0.06-0.08. However, this ratio increases to 0.2-0.25 later in the bearing life which leads to the formation of 80° bands. Nonetheless, Voskamp et al. [111] reported that enhanced amount of compressive residual stresses can develop early during the bearing life operation prior to 30° band formation, indicating potential deficiencies in Johnson's theory. Many of the theories currently suggested appear flawed and inconsistent. Polonsky et al. [14] provided three paradoxes listed below for the development of WEB and their orientation and demonstrated in Figure 2.30.

1. The 30° and 80° angles observed with WEB correspond to neither the direction of the maximum orthogonal shear stress (0 or 90° to the bearing raceway) nor the direction of the maximum unidirectional shear stress (45° to the principal stresses).

2. Contact stress is symmetrical about the centreline of contact in the absence of surface traction. Therefore, if one particular direction is favoured for the formation of WEB, another direction should exist for the growth of these bands via symmetry. Nonetheless, WEB are never observed in a symmetric direction unless the rolling contact direction is reversed.

3. WEB are not observed in conjugate directions. Multiple researchers have indicated that WEB growth is along the direction of unidirectional shear stress, principal stress or principal plastic strains. Nonetheless, each of these stress-strain quantities

mentioned are associated with a conjugate direction. Indeed this conjugate direction is never favoured for the growth of WEB throughout the microstructural alterations encountered by the steel [83]. The proposed direction which should be theoretically favourable for WEB is shown in Figure 2.30.

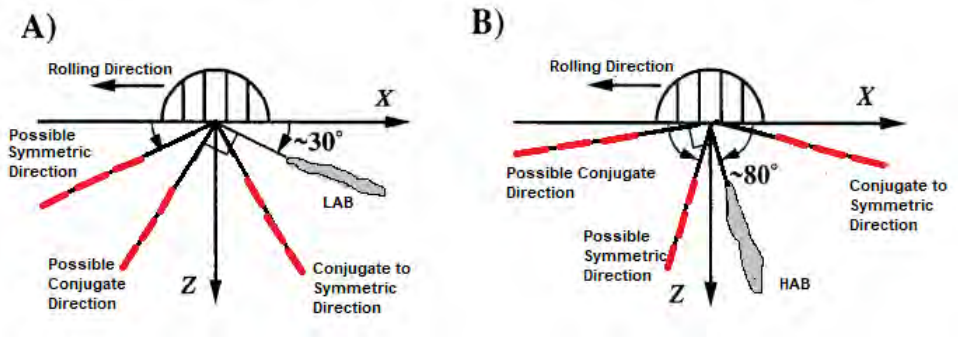

Figure 2.30: Possible orientation paradoxes for A) LAB and B) HAB. Adapted from [14].

Polonsky et al. [14] provided a hypothesis for the orientation of the LAB while answering the paradoxes listed above. Carbon diffusion was considered as the primary source for the formation of the WEB which is proportional to the residual pressure (effectively the pressure within the LAB region) which is given by equation 2.1:

$$p^r = \frac{2(1+\nu)}{3(1-\nu)} G\epsilon^p_{xx} \tag{2.1}$$

where G is the shear modulus of the material, ϵ^p_{xx} is the plastic strain in the direction perpendicular to the LAB and ν is poisson's ratio. It is concluded that when $p^r > 0$, carbon outflow is accelerated whereas the carbon outflow is retarded when $p^r < 0$. An analytical tool was developed to determine the magnitude of ϵ^p_{xx} at different positions in the subsurface and determined two critical stress quantities that alternate as the load transfers across the contact surface. These stresses were defined as the orthogonal shear stress τ_{xz} and the deviatoric stress S_{xx} defined as:

$$S_{xx} = \sigma_{xx} - \frac{1}{3}(\sigma_{xx} + \sigma_{yy} + \sigma_{zz}) \tag{2.2}$$

By analysing the evolution of these two stress components across the contact area under cyclic conditions, it was determined an extremum of τ_{xz} is achieved just prior the moment where the band exists the contact stress field which is the last of the four major extrema of S_{xx} and τ_{xz} [14]. It was proposed by Polonsky et al. [14] that under this condition, ϵ^p_{xx} would be positive which would result in $p^r > 0$ causing a carbon outflow from the LAB. Although this theory does address the paradoxes mentioned, it is rather complex and difficult to grasp. While it was also proposed that HAB results in the gradual dissolution of the lenticular

carbides (carbon rich areas) which form adjacent to the LAB. Where the HAB orientate in the direction which maximises the plastic deformation experienced by the lenticular carbides which is 45° of the lenticular carbides oriented parallel to the LAB at ≈ 30° which is similar to the reported orientation of the HAB (≈ 80°). However, an explanation for why or how such a breakdown occurs has not been provided. Although this theory complies with the first two paradoxes mentioned, it failed to satisfy the third paradox where no HAB are found to form at the conjugate direction which would correspond to an inclined angle of ≈ 15° opposite to the rolling direction which has never been reported in literature.

2.6 Models for DER/WEB Formation

While DER and WEB have indeed been investigated for decades, there is a lack of precise predictive models for these features which is attributed to the debates regarding the formation mechanism of the features and their drivers [4, 5, 8, 126].

One of the earliest models presented by Buchwald et al. [117] suggested that carbon flows from the ferrite band of LAB to the parent microstructure due to stress gradient and carbon concentration as the basis of their model for the determination of the rate of LCs thickness increase thus the WEB formation stage. The model proposed that WEB form due to dilational compressive strains caused by localized plastic deformation and the association of carbon with the increased dislocation density. It was suggested that the hydrostatic pressure under Hertzian contact is sufficient to dissolve precipitates in the matrix which later becomes LAB, resulting in a localized carbon concentration gradient. The carbon migration driven by the resulted carbon concentration gradient and stress gradient from the deformed region (white area) to the undeformed surrounding regions leads to the formation of LCs at the boundary that acts as a sink for the carbon solute. The LC growth rate is modelled by Buchwald et al. [117] to be equal to the sum of the concentration gradient flux and the pressure gradient flux (see Equation 2.3).

$$\frac{dX_L}{dt}(C_c - C_0) = D\frac{dc}{dx} + \frac{C_0 D}{RT}\frac{dv}{dx} \tag{2.3}$$

Where the LC growth rate is $\frac{dX_L}{dt}$, C_0 is the carbon concentration at the WEB boundary, C_c is the carbon concentration in the LC, D is the diffusion coefficient of carbon in ferrite, $\frac{dc}{dx}$ is the concentration gradient in the WEB at the moving boundary and $\frac{dv}{dx}$ is the potential gradient caused by pressure gradient at the moving boundary. In this model the carbon concentration gradient is assumed to be linear, i.e. the change between C_c and C_0 over the WEB thickness is linear, while the potential gradient is approximated as the elastic

strain energy accompanying the precipitation of a mole of carbide over the WEB thickness. The model by Buchwald et al. [117] requires a temperature increase of 200 K maintained between stress cycles in the subsurface, which is yet to be proven to be true in experimental findings. The diffusion rate in this model is too low to explain experimental observations.

Swahn et al. [82] created a simple plot to predict the formation of DER, LAB and HAB based on 80 RCF tests of bearings under the contact pressure between 3.2 and 3.7 GPa in 1970s. By determining the earliest stage of formation for each feature at the two pressures, a linear relation was applied to predict formation of DER, LAB and HAB under other pressures between the two tested pressures. However, it is difficult the determine whether the relationship is actually linear between the two points which causes some uncertainty in the feature prediction. As many subsequent works have shown, the model can only provide roughly guidance on the formation of these features even under the limited contact pressure range.

Polonsky et al. [14] proposed a model linking the WEB to recrystallisation due to a diffusion mechanism where carbon diffuses from the ferrite band and becomes trapped at dislocations or precipitates as layers of LCs. It was also suggested that primary carbides dissolve within the ferrite bands of LAB due to compressive strain arising from localized plastic deformation. While the model by Polonsky et al. [14] focused on the investigation of WEB orientations, it proposed that the driving force for carbon outflow is likely the stress induced release of carbon segregated at dislocations rather than the carbon solute concentration gradient in the WEB due to dissolving precipitates as proposed by Buchwald et al. [117]. Polosnky et al. [14] suggested that during operation, a quasi-equilibrium environment is achieved, where dislocations become unpinned under high subsurface stress and start multiplying rapidly that is compensated by dislocation annihilation, hence an overall constant dislocation density is roughly maintained. Dislocation annihilation in this case releases the carbon segregated at dislocations to become free carbon in ordinary solution. However, the relaxation time for the free carbon to re-segregate to the newly created dislocations is much longer than the average time between stress cycles, which is governed by the rotational speed and bearing geometry [14]. Hence the concentration of free carbon is increased in the band while the concentration of carbon segregated to dislocations reduces. While all carbon in martensite is assumed to be segregated in the form of dislocation atmospheres given the extremely high dislocation density and hence it is assumed the free carbon in the initial martensitic matrix is low. Therefore, the difference in free carbon concentration between the ferrite band and martensite acts as the driving force for carbon outflow to the edge of the band causing an overall reduction in the carbon content in the

band. Based on this hypothesis, Polonsky et al. [14] approximated the number of cycles (N) required to form a carbon free ferrite band of thickness (h) using Equation 2.4, where D is the diffusion coefficient of carbon in ferrite and n is the rotational speed.

$$N = \frac{h^2 n}{D} \tag{2.4}$$

This rather simple model has been shown to be insufficient when approximating the number of cycles since it does not take into consideration of the influence of contact pressure, which is known to heavily influence WEB formation. This model was shown to result in values of about a magnitude higher than the experimental data from Buchwald et al. [117]. However, a correction factor of 0.1 to 1 is proposed to account for the fact that, at moderate temperatures, the diffusion coefficient in a heavily dislocated material such as martensite can be considerably higher. Nonetheless, the approximation from this model is closer to the experimental data compared to the initial model by Buchwald et al. [117] which suggests this might be a more realistic formation mechanism.

A more recent study used a finite element (FE) elastic-plastic model coupled with a stress induced carbon diffusion-based model to predict the orientations of the LAB and HAB and to predict the initiation of LAB in the microstructure [149]. The model proposed by Polonsky et al. [14] did not sufficiently deal with the elastic-plastic Hertzian contact. Hence, this recent study developed their model based on the assumption that the dissipated plastic energy during elastic-plastic loading is the primary driver for carbon diffusion, depending on the time span for the diffusion process for each stress cycle, which is also dependent on both bearing speed and geometry. The model has shown to be able to predict LAB formation by predicting the number of cycles required for carbon diffusion across a certain LAB width. The model was based on Fick's first and second law to determine the concentration of a diffusing media under the presence of a pre-existing concentration gradient but the authors modified them to Equation 2.5 to include stress-assisted diffusion of free carbon.

$$\frac{\partial C}{\partial t} = D\nabla.\left(\nabla c + \frac{c\nabla V}{kT}\right) \tag{2.5}$$

where D is the diffusion coefficient of carbon in ferrite, k is the Boltzmann constant, T is temperature, c is the carbon concentration and V is the potential driving the diffusion process which is assumed to be the dissipated plastic energy and ∇ is the Laplace operator. The FE model showed that the orientation of the diffusional flux to be 25 - 40° in the subsurface depth of about 1 - 1.5b (b is the contact half width) and orientated at 75 - 80° at 0.5 - 1b deep. Indeed the orientations agree with the positioning of LAB and HAB in literature, however this suggests LAB and HAB each have a distinctive region in which they

form rather than LAB forming at the depth were HAB would form at a later stage, i.e. This model suggests both features form independently which does not agree with experimental observations.

Most recently, Fu et al. [118] modelled the formation of DER due to carbon migration through dislocation gliding from the martensite to nano-sized tempered carbides, which leads to carbide thickening and ferrite formation [118]. Based on similar hypothesis, they suggested that, under continuous cyclic loading, the remaining carbon atoms in the newly formed but heavily deformed saturated ferrite will migrate to the edge of the ferrite band due to carbon segregation at dislocations and dislocation gliding, which leads to the nucleation and growth of lenticular carbides (LCs), commonly associated with LAB [4, 117, 120, 150]. The thickening process of LCs was thus modelled as the development state of LAB [150] but no discussions on the formation of HAB were given. The model associates carbon migration with the gliding of dislocations due to plastic deformation in bearing materials under cyclic loading, and the accumulation of stress cycles during bearing operation is treated as a major role in their formation.

The carbide thickening process driven by dislocation gliding was calculated using the carbon flux equation due to dislocation gliding (Equation 2.6) and the Orowan equation [151] (Equation 2.7) for the plastic shear strain rate.

$$J_{dis} = \rho_m . \nu . n_c \tag{2.6}$$

$$\dot{\gamma} = b . \rho_m . \nu \tag{2.7}$$

Where J_{dis} is the dislocation assisted carbon flux, ρ_m is mobile dislocation density, ν is an average dislocation velocity, $\dot{\gamma}$ is the plastic shear strain rate, n_c is the number of carbon atoms captured by mobile dislocation of unit length per stress cycle which is estimated using the estimation by Cottrell and Bilby [146] and b is the magnitude of the Burgers vector. Combining Equations 2.6 and 2.7 , the carbon flux of the system was able to be determined through the measurement of plastic shear strain, avoiding the need of determining the mobile dislocation density and velocity, which is challenging to obtain especially for highly deformed structures such as in bearing steels. While determining the plastic shear strain in bearing steel due to RCF is difficult to obtain, recent studies have approximated such values through compressive cyclic tests. During such tests a decay pattern is observed by comparing the strain at different cycles, suggesting that at high stress cycles ($> 10^6$), the strain range reaches an asymptotic value for each contact pressure [6, 124]. Therefore by

developing a linear fitting, the plastic shear strain was approximated for the corresponding contact pressure [124]. However there is an uncertainty in this method as the true material response during RCF, given the material softening associated with DER and WEB may have an impact on the material's plastic shear strain, and thus may deviate from the asymptotic value proposed [6, 124]. If there was an increase in its plastic shear strain due to the formation of soft DER and WEB unaccounted for, the proposed model could over-estimate the formation of the WEB, i.e. predict the formation of WEB much later than they would actually form. The dislocation assisted carbide thickening model for LAB [124] makes use of an equilibrium between the carbon flux towards LC thickening and the dislocation assisted carbon flux shown in Equation 2.8 and the mass conservation of carbon in the system shown in Equation 2.9, highlighting the carbon content within the LAB (ferrite region and LC) is equal to the carbon content in the initial matrix over the same area.

$$J_{dis} = \frac{dl_{LC}}{dt} \left(C_{\nu\theta} - C_{\nu 0}\right) \tag{2.8}$$

$$\lambda C_{\nu 0} = l_{LC}.C_{\nu\theta} + \left(\lambda - l_{LC}\right).C_{\nu b} \tag{2.9}$$

Where $\frac{dl_{LC}}{dt}$ is the rate of thickness increase of the LC, λ is the thickness of a fully developed LAB, $C_{\nu\theta}$, $C_{\nu 0}$ and $C_{\nu b}$ are the carbon concentration per unit volume in LC, initial matrix and ferrite band respectively and l_{LC} is the thickness of LC. Combining Equations 2.6 - 2.9 makes it possible to observe the evolution of carbide thickening due to dislocation assisted carbon diffusion with cycles. According to this model, the estimated maximum thickness of a fully developed LAB was 9 µm [150] . According to Fu et al. [150], carbon flux due to dislocation gliding is many orders of magnitude larger than that due to the concentration gradient of free carbon, it was hence neglected. While this is acceptable, the actual carbon diffusion in the system is most likely to be stress-assisted due to the subsurface stresses acting on the material. Considering a potential gradient across the system that assists the diffusion of free carbon in addition to the carbon flux calculated according to Fick's first law will thus increase the overall flux, similar to that proposed previously [149, 150]. It is thus accepted that both mechanisms, i.e. carbon migration due to dislocation gliding and stress-assisted free carbon diffusion, are likely to contribute to the formation of WEB and the associated LCs. The model by Fu et al. [150] has been extended to model DER development under a similar mechanism where during strain-induced martensite decay, carbon in the martensitic phase migrates due to dislocation assisted migration in the matrix and reprecipitates at the pre-existed tempered carbides.

A thorough literature review has shown that, the existing LAB models in literature are

theoretical models based on LC thickening due to carbon diffusion while no model is available in literature to predict the formation of HAB. Although the theoretical LAB models are all based on carbon migration, conflicting modelling results are shown due to the uncertainty in LC thickness measurements used for validation. This is also caused by the simultaneous LAB formation and growth during bearing operation, leading to the large discrepancy in LC thickness quantification and challenges in accurately validating those models. Discrepancies in current models of DER and LAB is attributed to the fact that no universally accepted theory on the formation mechanism of these features and their transition from DER to LAB and HAB is available. There is a need to develop a unified formation mechanism for DER, LAB and HAB to link their influence on each other which has been commonly found experimentally in literature. Establishing such a unified formation mechanism would be valuable in aiding the development of predictive models that can predict the formation of all DER, LAB and HAB in bearings.

2.7 Other White Etching Matter

Other microstructural alterations in the material subsurface have been reported in literature. Other white etching matters commonly investigated in literature includes white etching cracks (WECs) and butterflies. Unlike WEB, white etching area (WEA) features such as WECs and butterflies can occur at a much earlier stage in the bearing life under lower contact pressures (1.3 - 1.5 GPa) [152]. Confusion in literature exists from differentiating WEB from the other white etching matters more commonly investigated in literature such as WECs and butterflies. WECs (see Figure 2.31a) are observed as long, parallel or branching micro-crack networks in bearing subsurface at various depths [16, 153]. In the circumferential cross section, the cracks appear more vertically orientated branching down to the core whereas the axial cross sections show cracks more parallel with the surface [88, 154–157]. WECs may propagate through grains as a form of transgranular cracking which suggests the grain boundaries have little influence on the crack propagation [158]. Another subsurface microstructural alteration in steels often mentioned in the context of WECs formation is butterflies. Butterflies (Figure 2.31b) form in steels due to cyclic shear stresses induced during RCF which becomes locally high at material imperfections such as non-metallic inclusions causing plastic deformation and initiating cracks and microstructural transformations (WEAs) locally.

Butterflies can form below contact surfaces of up to 1.5 mm and not necessarily in the region of the maximum shear stress [42, 121]. Size of butterflies can vary from 10 µm to 100 µm (wing tip to wing tip). At earlier stages butterflies have been reported to form

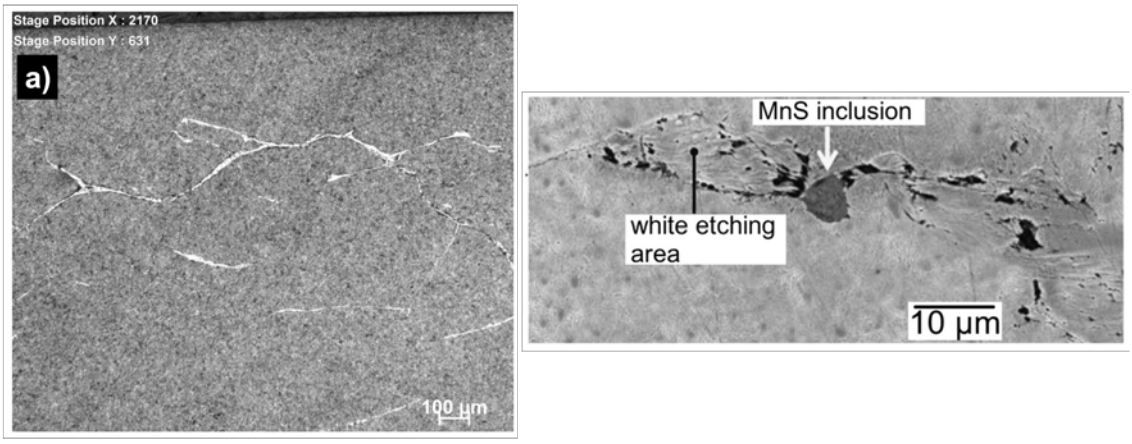

Figure 2.31: WEC found in a 100Cr6 spherical roller bearing in the circumferential cross section [159].

at shallower depths and increase in depth with further build-up of stress cycles, increasing temperature and increasing contact pressure [16, 160]. The cracks are typically inclined at 30 - 50° to the over-rolling direction [160–164], thus the unidirectional shear stress at 45° may play a significant role in their formation. The butterfly wing WEA is cited to consist of equiaxed nano-ferrite grains of size 10-100 nm in diameter [16, 79, 160–164], or lamella like grains of up to 300 nm equivalent diameter [160]. It has been reported that finer grains (10 - 50 nm) exist closer to the main crack while coarser grains (50-100 nm) exist closer to the butterfly boundary [16, 160]. WECs in contrast to WEB, is not limited to the maximum shear stress region [152]. WEA features such as WECs and butterflies are typically linked with an increase in hardness [165] whereas WEB have been reported to be softer than the surrounding microstructure [120, 138] which has caused some confusion in literature. Similar to butteflies, WECs show a WEA that has been identified by SAED patterns as nanocrystalline ferrite that is supersaturated with carbon with a grain size 10 - 50 nm [79, 127, 130, 137, 163] while APT investigations have shown that carbon is segregated at the grain boundaries rather than within the ferrite nano grains [166].

The formation mechanism of these features have been debated intensively in literature along with the influence of operating conditions on their formation. Theories have suggested the hydrogen intake (sourced from the lubricants) within the material subsurface may play a role in their formation [88, 156] while exposure to electrical currents or heat influence have also been reported to influence their formation [120, 152]. WECs is suggested to develop due to material defects leading to stress raisers such as inclusions, voids and large carbides [16, 121, 166, 167]. It also remains unclear whether micro-cracks or the WEA forms first or whether they develop simultaneously together. There are reports of cracks without WEA compared to cracks with WEA [16] which would suggest the cracks form initially where the rubbing of the crack surfaces may contribute to increased temperature due to

friction, recrystallization of nano-sized ferrite grains and carbon displacement all of which are considered potential drivers for the formation of the WEA [168]. WEB on the other hand have not been linked to such local stress raisers.

RCF-induced damage in the subsurface can appear in many forms as discussed. DER and WEB typically occur at high stresses (i.e above shakedown limit) which can be considered as a global damage or material degradation in the material as they develop continuously throughout the material under a certain depth (maximum shear stress), while other features such as WECs and butterflies develop from local material imperfections and stress points and hence can be described as more of a local damage. As shown in Figure 2.32, WECs and butterflies typically develop earlier in the bearing life (under certain conditions [169]) whereas DER and WEB develop at later stages. The focus of this thesis is to investigate DER and WEB rather than WECs and butterflies. A schematic of the different microstructural alterations in reference to the L_{10} life is shown in Figure 2.32.

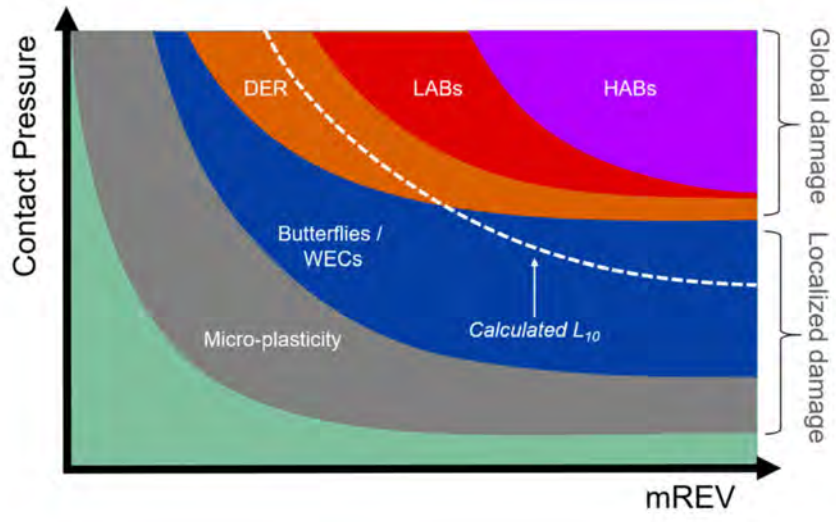

Figure 2.32: RCF induced microstructural alterations schematic showing the start of each mechanism in reference to contact pressure and millions of revolutions (mREV) [126].

2.8 Summary and Research Strategy

There has been intensive research towards understanding the microstructural alterations known as DER and WEB (consisting of LAB and HAB) that develop after prolonged RCF tests under high loading conditions (beyond shakedown limit) in bearing steels which impacts the durability of the material. The majority of studies have investigated these features in 100Cr6. Over the past decade, research towards WECs and butterflies has led to some confusion towards differentiating between the different white etching matters which has been highlighted in this review. On the other hand, even after intensive research,

there remains uncertainties over the formation mechanism of DER, LAB and HAB. While various models have been proposed in literature, there remain many questions unanswered when comparing theoretical models with experimental observations for all three features. A summary of each of the three features and current gaps in literature is highlighted below.

- DER is reported to develop within the maximum shear stress region (debated which stress component is responsible) and consists of regions of elongated/needle-like features and equiaxed ferrite grains. The nature of these features and their initiation and formation mechanism remains unclear. Models have assumed a carbon migration theory driving carbon migration from the newly formed ferrite grains towards tempered carbides but they fail to explain the formation of the different components within the DER shown in experiential studies. While experimental studies have shown the DER to consist of elongated bands and equiaxed ferrite grains, how they initiate and evolve during bearing operation remains unclear.

- LAB is typically found to develop within the DER at later stages, although some have reported LAB without DER, the direct link between DER and LAB has not been defined in literature. The LAB has been modelled to be due to dislocation assisted carbon migration where carbon migrates across the ferrite bands and nucleate as lenticular carbides at the edge. However, no model or theory has provided an explanation towards how the different components of the LAB including equiaxed ferrite grains, elongated ferrite grains and lenticular carbides are linked and how they initiate/grow during bearing operation.

- HAB has been the least investigated of the three RCF-induced microstructural alterations due to their formation at the latest stage after LAB where the majority of studies that looked into HAB from the 20th century. The latest study of WEB (including HAB) has shown that HAB consists of both equiaxed and elongated ferrite grains similar to LAB but at different orientation and dimensions. There is currently no proposed model or formation mechanism explaining the initiation and growth patterns of HAB and its constituents and their dependence on pre-existing LAB for their formation. In literature it is assumed HAB develops due to LAB given that the later form prior but no evidence has been shown to explain the origin of HAB. There is also no working model to predict the formation of HAB in literature.

- WEB have been linked with failure of the material due to the inhomogeneous features developing gradually within the subsurface. However, it is unclear how these features may influence the final failure in bearings through crack initiation or propagation.

To develop a further understanding of the RCF-induced microstructural alterations, this project has looked into addressing the gaps highlighted above by investigating the initiation and growth of DER, LAB and HAB from early to late stage through various characterization techniques at different scales. The project focused on investigating the formation mechanism of each feature based on experimental findings and establish a unified formation mechanism to highlight the link between DER, LAB and HAB and identify how these features may contribute to final failure.

At the beginning of this study, the evolution of all three features under different stress cycles, contact pressure, material and steel cleanliness were investigated to better understand the growth patterns of the features, stress influences and dimensions in both 2D and 3D. This is also used to investigate possible links and patterns between the development of all three features. The growth patterns from this study is later used to develop a semi-empirical model to predict the development of both LAB and HAB in different bearing steels and contact pressures which is compared to experimental conditions from literature to accurately predict the formation of the features.

High resolution analysis using different techniques highlighted in the next chapter is used to investigate the formation mechanism of DER, LAB and HAB by investigating the initiation and growth of the different constituents observed in each of the features i.e elongated grains, equiaxed grains and carbides and the carbon migration patterns. Findings from this section is then used to develop a unified formation mechanism for the first time that shows how the three different stages of microsturctural alterations due to RCF are linked and how the material develops globally during bearing operation. Finally the mechanical properties of the constituents of the features coupled with crack/void development in the material is used to investigate the role of the features towards final failure of bearing specimens where the interaction of the WEB with inclusions is also investigated to determine how the features may contribute to final failure. Details of the experimental procedure in this study is shown in the next chapter.

Chapter 3

Experimental Methods

3.1 Introduction

This chapter presents details of the experimental work conducted in this project including methods and techniques utilised to examine the microstrucutral alterations across various bearing test specimens. RCF tested bearings have been analysed through various techniques ranging from LOM, SEM, FIB/TEM, EBSD , FIB/APT and nanoindentation. The testing procedure can be seen in Figure 3.1 showing the stages of investigations of the samples. Bearing samples are initially RCF tested for set durations, later a series of metallographic preparation is conducted followed by various characterization techniques to reach the conclusions of this project highlighted in Figure 3.1 and presented in later chapters. All analysis in this study is aimed to develop a better understanding on the formation mechanism of microstructural alterations developing in bearing steel due to RCF, model their growth and understand their influence on the material performance and final failure. The following sections present detailed overview on each stage of the experimental method.

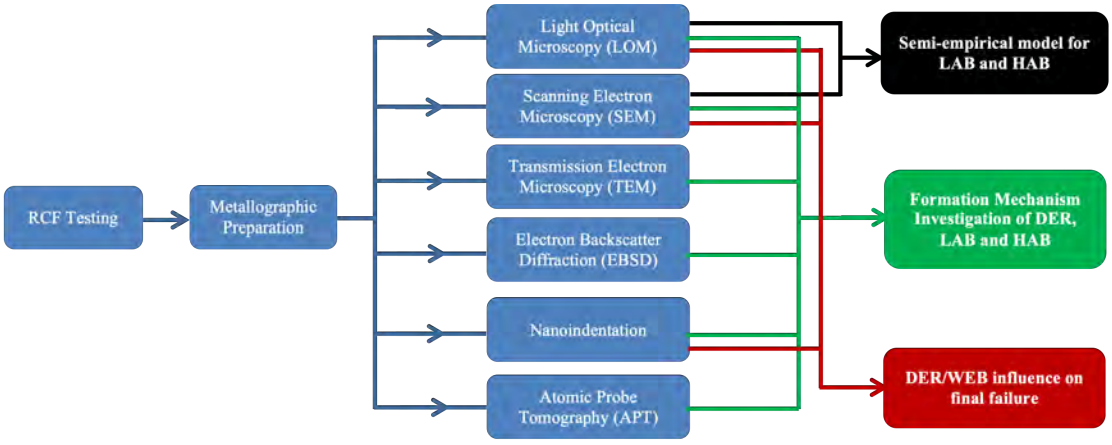

Figure 3.1: Flow chart describing the experimental stages in this project and the final outcome resulting from each analysis procedure.

3.2 RCF Test

Bearings investigated in this study are angular contact ball bearings (ACBBs) of 7205b type which have been RCF-tested on the L-17 test rig at Schaeffler Technologies AG & Co. KG. Images and schematics of the test rig can be seen in Figure 3.2. The L-17 is typically used to investigate the effect of material, heat treatment, surface properties (e.g roughness and coatings) and contaminated lubricants on fatigue life for ACBBs, taper roller bearings and spherical roller bearings under axial load. The test conditions on the L-17 in this study is summarized in Table 3.1. The lubricant used in this study is a standard gear oil which was used under EHL conditions.

Table 3.1: L-17 test conditions for samples in this study.

Speed of Inner Ring (RPM)	12,000
Lubricant	ISO VG 68
Outer ring Temperature	80 °C
Viscosity Ratio κ	2.67

Dimensions of the tested 7205b ACBBs in this study can be shown in Figure 3.3 which have been provided by Schaeffler for this project. All RCF tests have been run to pre-determined hours to cover early-late stages of RCF experienced by the bearing samples to study the microstrucutral alterations at different stages of development. All RCF tests have had an applied axial load of 11 kN and 21.3 kN which is equivalent to a contact pressure of 2.9 GPa and 3.5 GPa on the test bearings respectively. Test durations have varied from 19-1396 hours which is equivalent to 104-7668 million stress cycles.

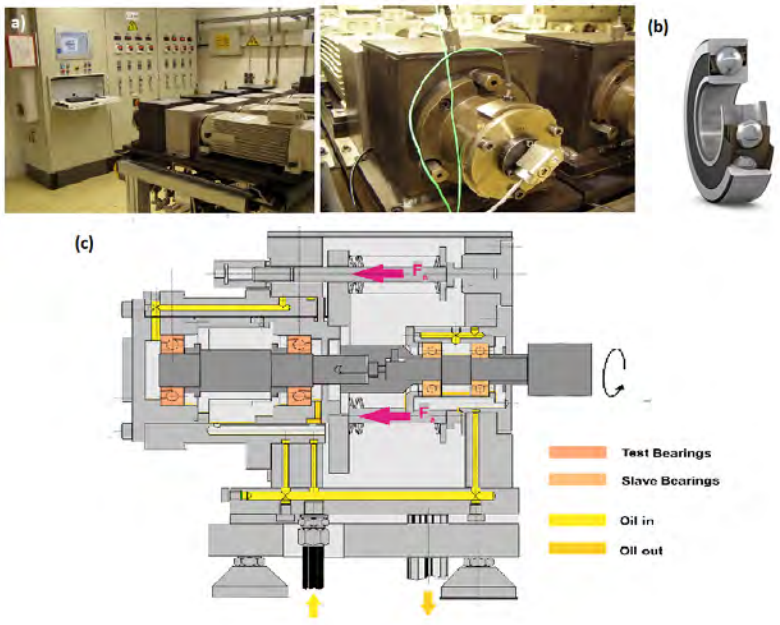

Figure 3.2: a) L-17 test rig at Schaeffler. b) Model of 7205 ACBB used for the L-17 fatigue test. c) Schematic of L17 test rig showing positions of test and slave bearings.

In total, 22 RCF-tested ACBBs (non-failed) have been been analysed in this project to examine the influence of different running time, contact pressure, steel cleanliness and material. Full details on the RCF tested bearing samples are shown in Table 3.2. The ACBBs in this project are made from two different alloys which are 100Cr6 (high carbon steel) and 50CrMo4 (low carbon steel) to examine their influence on the development of microstructural alterations. In 100Cr6 bearings, a comparison is also made between martensite and bainite microstructure along with a comparison between two different grades of steel cleanliness. The details of the materials and microstructure is shown in the following section. A flow chart is shown in Figure 3.4 to demonstrate the samples investigated.

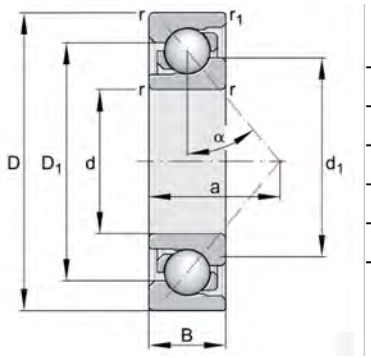

d	25mm
D	52 mm
B	15 mm
a	24 mm
D_1	42 mm
d_1	35.5 mm

Figure 3.3: Dimensions of ACBB 7205b type.

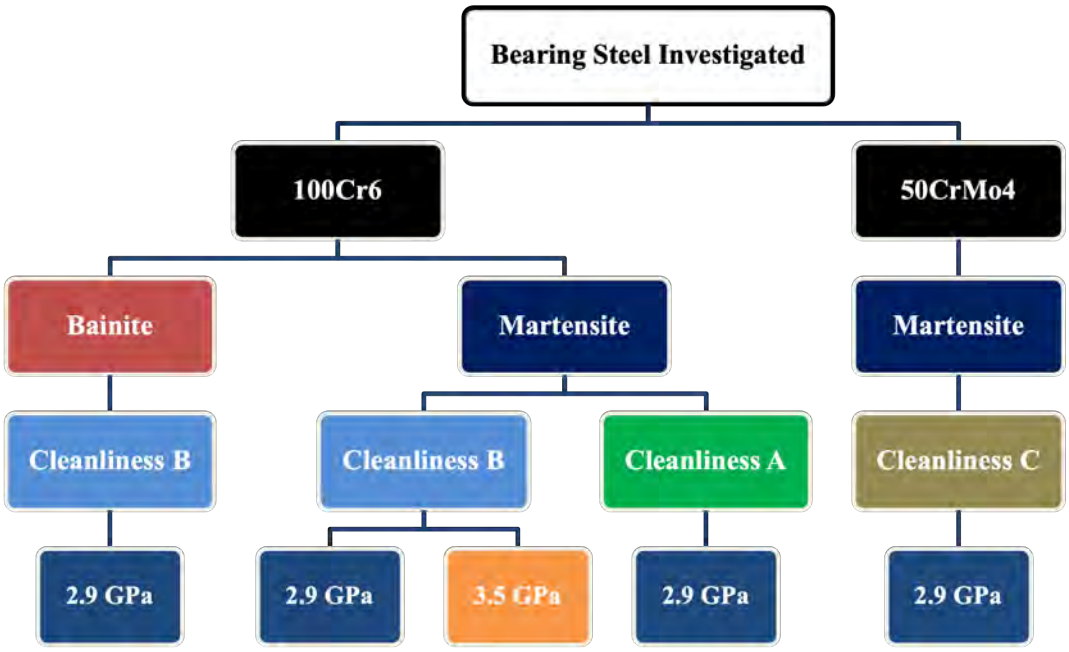

Figure 3.4: Flow chart showing the bearing steel alloys tested, microstructure, steel cleanliness and contact pressure utilised in each RCF test in this project.

Table 3.2: List of of RCF tested bearing samples in this project under various conditions.

Material	Steel Cleanliness	Contact Pressure (GPa)	Stress Cycle for Inner Ring (x10^6)	Running Time (Hrs)
100Cr6 Martensite	Cleanliness B	2.9	591	108
			1116	203
			1689	308
			2341	426
			3016	549
		3.5	151	29
			288	53
			447	82
			679	124
			885	162
	Cleanliness A	2.9	1337	244
			2961	539
			4141	754
100Cr6 Bainite	Cleanliness B	2.9	532	97
			897	163
			1448	264
50CrMo4 Martensite	Cleanliness C	2.9	104	19
			158	27
			846	154
			1626	296
			2038	371
			7668	1396

3.2.1 Material

Details of the bearing materials used in this project is discussed in this section. As discussed previously 100Cr6 and 50CrMo4 bearing steels have been used in this study with the elemental composition of both alloys shown in Table 3.3. The elemental data has been obtained using spark emission spectroscopy conducted at Schaeffler.

Table 3.3: Elemental composition of bearing steel alloys used in this study.

Material	Wt%															
	C	Si	Mn	P	S	Cr	Ni	Mo	Cu	V	Al	W	Pb	Sb	Ti	O
100Cr6	0.93	0.3	0.34	0.01	0.004	1.49	0.02	0.005	0.066	0.004	0.002	0.007	0.001	0.002	0.001	0.0012
50CrMo4	0.44	0.24	0.66	0.008	0.001	1.17	0.75	0.25	0.12	0.087	0.024	-	0.001	0.004	0.002	-

For the 100Cr6 martensitic bearing steel, standard heat treatment has been applied to the steel including austenitization at 850 ± 10 °C for 30 minutes, followed by quenching in oil to room temperature and tempered at 230 ± 10 °C for 2 hours. The bearing sample contain <5% retained austenite.

Analysis of the cleanliness of the bearing steels in this study is conducted with accordance of DIN 50602 where the K values are given for oxidic and sulphidic inclusions providing an index of percentage area of the non-metallic inclusions in the microstructure referred to an area of 1000 mm^2 [62]. With K0 representing the smallest inclusions and K4 the largest in this test. Two different steel grades are examined in the 100Cr6 alloy termed as 'cleanliness A' and 'cleanliness B' while one cleanliness grade is used for the 50CrMo4 steel alloy (cleanliness C). Details of the K values for all the samples can be seen Table 3.4, 3.5 and 3.6. It can be seen that cleanliness A has the least inclusions. The 50CrMo4 alloy generally has larger inclusions compared to the 100Cr6 alloy (K4 values) which are mainly oxides while the 100Cr6 alloy with cleanliness B mainly consists of sulphides.

Table 3.4: K values for 100Cr6 alloy with a cleanliness grade of: cleanliness B.

	K0	K4
Stretched Sulphides (SS)	37.6	0
All Oxides (O)	1.41	0
Total Kx (O+SS)	39.1	0

Table 3.5: K values for 100Cr6 alloy with a cleanliness grade of: cleanliness A.

	K0	K4
Stretched Sulphides	0	0
All Oxides	4.2	0
Total Kx	4.2	0

Table 3.6: K values for 50CrMo4 alloy (cleanliness C).

	K0	K4
Stretched Sulphides	1.9	0
All Oxides	15	0.2
Total Kx	16.9	0.2

3.3 Metallographic Preparation

This section discusses the metallographic procedure used in the investigation of DER and WEB development in the inner ring of the ACBBs. This is a destructive procedure as the bearings have been physically cut, and etched during the analysis. The steps of this procedure taken throughout the metallographic preparation is illustrated in the flow chart shown in Figure 3.5.

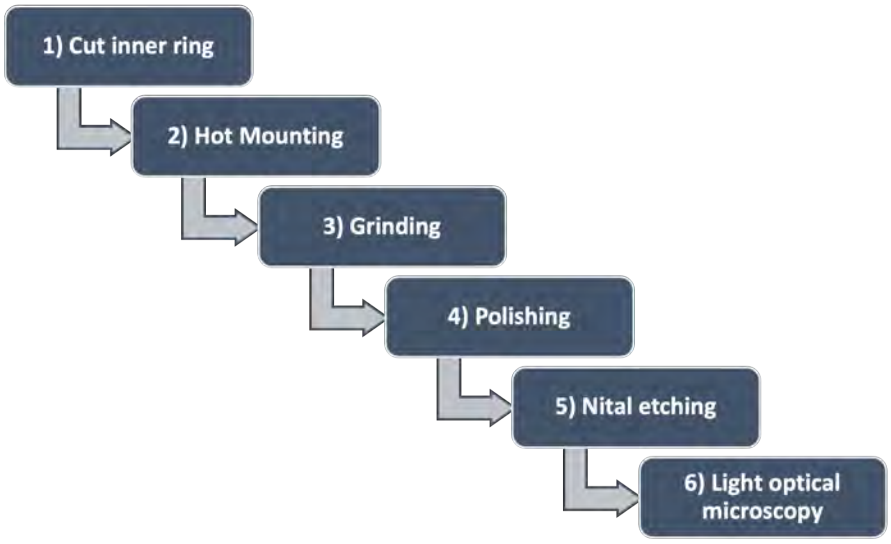

Figure 3.5: An overview of the different steps taken for metallographic preparation of bearing samples for DER/WEB examination.

The first step of preparation was to cut the inner ring of the bearings to prepare axial and circumferential cross section samples. It is essential for the cutting to be handled with care

to avoid damaging the sample. As a consequence of the short depth of field of LOM, sample surfaces cut must be flat to obtain sufficient focus in images. A Presi, Mecatome T210 precision saw with diamond disk is used for the cutting along with water used as a lubricant and coolant to avoid excess heat generation which might alter the steel microstructure. To reduce excessive heat accumulation, pulse cutting is used to avoid material damage. Samples from each bearing were cut in both axial and circumferential directions to inspect the features in both directions. For circumferential cuts, a sample holder has been designed on Solidworks (Figure 3.6) and 3D printed to hold each bearing sample while tilted to obtain a circumferential cut in the ideal location direction in the bearing raceway (parallel to contact angle) to ensure consistency when comparing cuts from different samples. The holder has a thickness of 3 mm and length of 4 cm with a gap of 2 mm between the plates to allow the 1 mm thick diamond disc to cut through the bearing accurately. It should be noted that all circumferential cuts in this study are taken at the middle of the contact area unless otherwise stated.

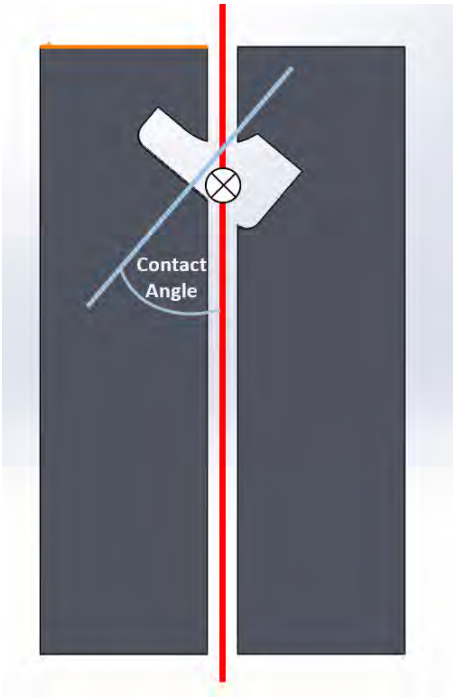

Figure 3.6: A illustration of the sample cutting holder that tilts the bearing section according to the contact angle. The red line represents the diamond cutting disc going into the page to cut the bearing inner ring circumferentially.

Once cut, the specimens are hot mounted with Bakelite to allow easier grinding, polishing and LOM analysis of the small samples. An automatic hot mounting press (ATM, OPAL 410) is used for this procedure where the mounting was conducted for a duration of 10 minutes (4 minutes heating and 6 minutes cooling) at a temperature of 180 °C and pressure of 234 bar. After mounting, the process of removing the damages and scratches generated from cutting starts with wet grinding with water and silicon carbide paper paper grid of 800,

1200 and 4000 grit in the specified order each for a duration of 2 - 3 min. The following step is polishing the samples successively with 6 µm diamond paste, 3 µm diamond suspensions, 1 µm diamond paste and finally 0.25 µm diamond suspensions with special cloths and lubricants to achieve acceptable surface finish for analysis. It should be noted that the samples are washed and dried following each grinding/polishing stage to maintain surface cleanliness and the surface is inspected between each grinding/polishing grade to ensure sufficient surface finish. For certain analysis techniques such as EBSD and nanoindentation, an extra polishing step using OPS (0.06 µm) is utilised as a final step to ensure the required surface finish quality is achieved.

Nital etching is performed to reveal the features of the steel microstructure such as DER and WEB. The samples are etched with 2% Nital solution for a few seconds until sufficient etching of the surface is achieved. Images of the samples are then obtained using the Olympus BX51 LOM while some samples are later chosen for further analysis.

3.4 Image Processing

Images captured in this project have been processed through the use of ImageJ/Fiji to quantify the formation density of LAB and HAB within the bearing microstructure which is presented in Chapter 4. The images captured through LOM are adjusted by maximising the contrast between LAB, HAB and the surrounding microstructure for optimal detection. One of the challenges is to differentiate co-existing LAB and HAB in one sample when the two features overlap. It has been found that using a polarised light, LAB and HAB can be effectively differentiated under LOM (see examples shown in Figure 3.7a and 3.7d), thus it has been used in this study to identify and quantify the two features that overlap separately. Raw optical images of LAB and HAB (Figure 3.7a and 3.7d) are uploaded to ImageJ and converted to 8-bit (black and white) shown in Figure 3.7b and 3.7e. An appropriate threshold is later applied to the grey scale images to isolate the LAB and HAB and quantify their density based on the area consumed by the features (Figure 3.7c and 3.7f).

Common term used in this study is $LAB\%$ and $HAB\%$ which is an indication of the percentage of the imaged area consumed by the black area (LAB and HAB) in processed images such as Figure 3.7c and 3.7f. For each bearing two cuts at random locations across the inner ring circumference were analysed and three measurements of the $LAB/HAB\%$ area in each cut were obtained. The average of the six measurements in total is used to represent the quantity of the two features in each bearing. This is discussed in more detail in Chapter 4 and Chapter 5.

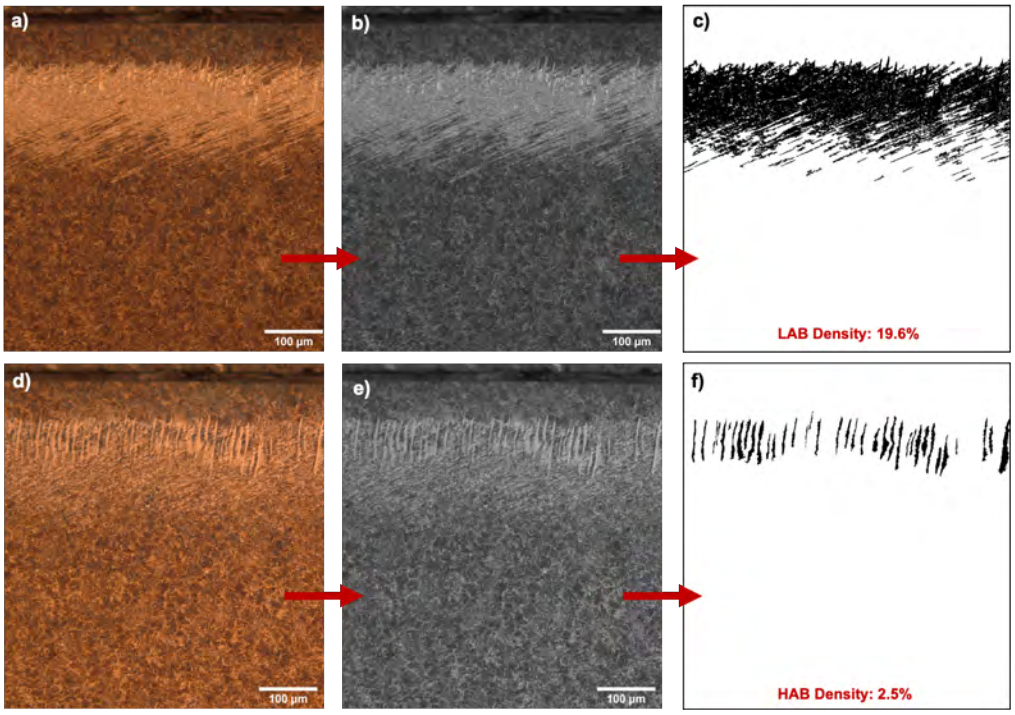

Figure 3.7: Optical images of etched bearing microstructure after polarizing light is applied to highlight a) LAB and d) HAB in the same area. Optical images are later transformed to gray scale using ImageJ b) and e). Images c) and f) are obtaining using ImageJ by applying thresholds to images b) and e) respectively to quantify the area covered by LAB and HAB.

3.5 Scanning Electron Microscopy

After LOM analysis, samples are investigated under SEM to obtain higher resolution images of the microstructural alterations. Majority of the SEM imaging in this project has been conducted using a JEOL JSM-6500F SEM to examine the microstructure in more detail with an accelerating voltage of 15 kV and an average working distance of 9 mm conducted in this study. Majority of the SEM imaging is SE SEM imaging conducted on an etched surface to highlight the individual components within DER, LAB and HAB. Another SEM (FEI Quanta 250 SEM) has been used under similar working distance (9 mm) and accelerating voltage (15 kV) depending on availability. Within the EBSD investigation, BSE SEM imaging has been conducted which is discussed in more detail in the following section. An energy dispersive x ray spectroscopy (EDX) has been conducted using Oxford Inca 300 for elemental analysis embedded in the SEM which is used for investigating inclusion compositions in Chapter 9.

3.6 Electron Backscatter Diffraction

EBSD investigation of all microstructural alterations in this study has been conducted using a JEOL JSM 7000F field emission SEM equipped with a EDAX Pegasus EBSD system. The

use of EBSD requires an polished smooth surface to minimise strain induced from polishing, hence OPS polishing is used as the final sample preparation procedure. BSE SEM imaging is conducted on the polished surface with a working distance of 5 mm and an accelerating voltage of 10 kV. BSE imaging typically reveals features due to variation in material composition and grain orientation. Lighter elements with a low atomic number result in a darker appearance while heavier elements appear brighter. The stronger composition contrast is achieved by using higher voltage, hence to reduce the influence of the composition on the overall contrast, comparatively low voltages of 10 kV is used for BSE imaging. In BSE imaging, variation in grain orientation with respect to the electron beam also leads to variation in brightness/contrast in the image.

After capturing BSE images, an EBSD analysis is conducted as a powerful tool to examine preferred crystal orientations, grain boundaries, lattice misorientation and phase identification. However, the EBSD is limited to materials with grain size larger than several tens of nanometres in diameter which could lead to some areas in EBSD maps as shown in Chapter 6 and Chapter 7 which appear as black due to limitation in the spacial resolution. For high quality EBSD results, surface finish of specimens has to be very smooth and deformation free to avoid influences of topography on the generated Kikuchi patterns. Hence the specimens are unetched and prepared using fine OPS polishing as the final stage of surface preparation to ensure sufficient surface finish for the analysis. Four different maps obtained from the EBSD analysis have been analysed in this project which are summarised below.

- **Inverse Pole Figure (IPF) Map:** IPF map is a crystal orientation map where a mixture of colours are assigned to different crystal planes to provide an overview of possible texture development in the analysed area. The maps are produced with respect to a pre-determined reference axis for example x (rolling direction), y (normal direction) and z (transverse direction). This study has focused on IPF maps with respect to the y direction (normal to the rolling direction in the bearing specimens) where an arrow of the axis is highlighted in each IPF map. IPF maps are best used to detect preferential grain growth orientation (texture development).

- **Kernel Average Misorientation (KAM) Map:** KAM analysis is used to determine the average degree of misorientation (orientation change) for every pixel within a kernel where a kernel is a set of pixels of a set size surrounding the scan pixel of interest. The average grain internal orientation change of the crystal lattice is determined for the kernel and assigned to the scan point of the centre of the kernel. For example in KAM maps, an abbreviation of (100 nm, 5°) depicts the average grain

orientation change of up to 5° of the crystal lattice over a distance on 100 nm. KAM maps are utilised to show a build-up or relaxation of internal strains and dislocation densities within the analysed material area. The rotations in crystals as a result of geometrically necessary dislocations or high internal strains (i.e. deformations) will be manifested by a high KAM value. For example, martensite phases have higher internal strains compared to ferrite, hence will show a higher KAM value in comparison.

- **Non martensite-martensite High Angle Grain Boundaries (HAGBs) map:** The use of non martensite-martensite HAGBs map is a useful tool to observe phase transformations and recrystallisation in the material. It presents grain boundaries with misorientation exceeding 15° that are not typical ones between martensite plates. In the HAGBs in this study, all pixels identified as HAGBs (misorientation exceeding 15°) are shown in blue. The use of the HAGB maps can detect boundaries not expected between martensite plates such as prior-austenite grain boundaries (PAGBs) or HAGBs which are formed by processes other than martensitic transformations such as newly formed grains.

- **Image Quality (IQ) Map:** The use of IQ maps can provide a visualization of the microstructure through measuring the intensity of kikuchi bands in the EBSD pattern of the analysed region. It is hence strongly influenced by local imperfections/defects of the crystal lattice within the interaction volume of the material. Defects such as local strain, grain boundaries, phases and dislocations can influence the intensity of the kikuchi bands [170]. IQ maps are therefore a useful tool to measure microstructural features such as grain boundaries, internal grain structures and dislocation densities. Defects captured such as grain boundaries, scratches, cracks or regions with high dislocation densities will appear as darker points due to poor pattern quality while areas with higher pattern quality (less defects) will appear brighter in IQ maps. For example, ferrite structures typically have a higher IQ contrast (brighter appearance) compared to martensite [170]. Products of recrystallization which are typically strain-free would also be expected to have a brighter appearance compared to deformed microstructures. [171].

Finally, after EBSD analysis, samples are slightly polishing to remove contamination and etched to capture SE SEM imaging for comparison. SE SEM imaging in this instance is conducted at an accelerating voltage of 15 kV and a working distance of 9 mm similar to the other SE SEM imaging from other equipment.

3.7 Transmission Electron Microscopy

To investigate the microstructural alterations under high resolution, FIB/TEM has been conducted which included the use of FIB for sample preparation followed by TEM analysis both of which were conducted at University of Leeds. The sample was prepared using a FEI Helios G4 CX DualBeam - High resolution monochromated, field emission gun, scanning electron microscope (FEGSEM) with precise Focused Ion Beam (FIB). The lamella thickness is reduced down to < 80 nm for TEM analysis. After transferring the bulk sample to the Dual Beam microscope, 500 nm of electron beam platinum (Pt) was deposited (at 5 kV, 6.4 nA for the electron source) to the surface of the target area. This was followed by a second, Ion Beam deposited, Pt layer (1 µm) using the FIB (at 30 kV, 80 pA for the liquid Ga ion source). A bulk lamella was initially cut (by the FIB at 30 kV, 47 nA), before a final cut-out was performed (at 30 kV, 79 nA). In-situ liftout was then performed using the Easylift needle. The lamellae was attached, using Ion Beam Pt (at 30 kV, 80 pA), to a copper FIB lift-out grid (Omniprobe, USA) mounted within the SEM chamber (in-situ) and then stored under vacuum before and during transport to and from the TEM. Thinning and polishing of the lamella to electron translucency was performed with a final polish/clean with a gentle ion beam (5 kV, 41 pA).

The TEM used was a FEI Titan Themis Cubed operated at 300 kV and fitted with a Monochromator. Bright-field TEM images are collected on a Gatan Oneview 16 Megapixel CMOS digital camera. It is fitted with the Super-X EDX system with windowless 4-detectors. The EDX maps obtained in the TEM sample were collected with a probe current of 200 pA and a dwell time of 20 µs. This has been used to obtain both bright field TEM images and SAED patterns of the microstructure.

3.8 Atomic Probe Tomography

APT has been used as a powerful tool for study the carbon distribution within the ferrite grains of the band at an atomic-scale. This allows for a detailed analysis of the elemental distribution within the band not possible under other techniques such as SEM, TEM and EDX. FIB/APT tests presented in this study has been conducted at University of Oxford.

APT is conducted on a needle-like specimen with a radius of around 50 nm. This needle specimen is prepared typically using FIB. When an atom bonded to the surface of the needle is exposed to a sufficiently high and properly directed electric field, its bonding becomes overcome by the electric field leading to the atom to be ionised. This as a result causes the ion to leave the material surface. This technique is known as field evaporation which is

considered a destructive technique. The evaporated ion is later accelerated by the electric field within a very short distance until a constant velocity is reached as the ion travels from the specimen tip to the ground potential. Once the ion is received by a position sensitive detector placed at the ground potential, the speed of the ion and mass-charge ratio is used to identify the ion element type and coordinates. This allows for the ability to construct a 3D elemental distribution model across the needle to allow for the atomic scale elemental analysis of the sample.

The lift out was conducted using a Zeiss NVision 40. Milling of two rectangular cuts is conducted around the sample of interest in a wedge shape to create the liftout bar. The bar is later welded onto a micromanipulator before being fully cut out where the liftout is conducted using the micromanipulator. Later a silicon coupon is used in the FIB chamber where 2 µm wide tips (posts) are etched onto it and act as support for one APT needle. The liftout bar is welded onto the posts and then cut so only a residual portion of the bar remains on the post while another portion remains on the micromanipulator. The remains on the micromanipulator is then welded to another post. This procedure is repeated until the entire liftout bar is consumed. In the next stage, the wedges on the posts are sharpened into tips with a diameter of approximately 50 nm. Once sharp, the tips are polished using an ion beam with an acceleration voltage of 2kV as opposed to 30 kV which was used for the prior steps. The use of a lower ion beam accelerating voltage at the end removes layers from the samples that are damaged by the 30 kV FIB beam.

The Atom probe used is a Cameca LEAP 5000 XR. This is a machine that uses a Reflectron for improved mass resolution. All samples were run in laser-assisted evaporation mode. The data was reconstructed and analysed in ApSuite 6.1, which is a software from Cameca Instruments / Ametek Inc. Experimental parameters included using a detection rate of 2%. The laser energy was set to 60 pJ at a temperature of 50 K and pulse frequency of 250 kHz.

3.9 Manual Serial Sectioning

Manual serial sectioning has been conducted on specified bearing samples to investigate the full structures WEB features. A serial section is performed in Chapter 4 to develop a 3D model the WEB network consisting of both LAB and HAB. This process involves taking LOM images of a defined area of WEB in the sample after being polished with 6 µm and 1 µm diamond suspensions to remove approximately 5 µm of the material at each step. The sample is etched with 2% Nital prior to imaging. The steps are repeated multiple times to capture various individual LAB and HAB within the data set. The surface removal rate has

been measured and controlled by putting micro-indents on the examined surface. Vickers indentation is used for the serial sectioning procedure where the depth of the indent is approximately $\frac{1}{7}$ of the diagonal width of the indent [172], therefore measuring the change of diagonal length of the indent was used to determine the surface removal. An overview of the serial sectioning technique can be seen in Figure 3.8. A similar serial sectioning technique is conducted in Chapter 7 and Chapter 9 but with a surface removal rate of 1 µm to examine individual constituents and voids associated with LAB using SEM imaging rather than LOM images.

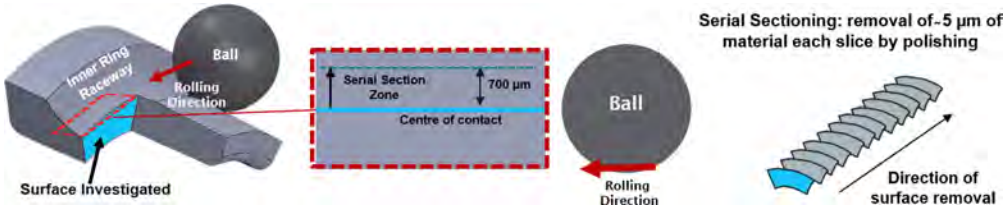

Figure 3.8: An illustration of the serial sectioning process on the circumferential cross section of the inner ring is shown.

The images obtained through serial sectioning are later aligned accordingly and stacked using Avizo 9.3 and volume rendered to create both an image stack of individual components within the LAB (Chapter 7), voids within LAB (Chapter 9) and a 3-D model of both LAB and HAB (Chapter 4).

3.10 X-ray Diffraction

X-ray diffraction has been used to measure the residual stress distribution across the subsurface of the bearing samples to compare with the development of microstructural alterations in the subsurface. This was conducted on non-cut bearing samples to avoid introducing potential stress relaxation within the microstructure that might influence the measured residual stress values. The measurements were performed by a D8 Discover diffractometer using a thin tube collimator (spot size of 1 mm). The analysis was conducted on the surface of the tangential cross section to measure the normal stress component (normal to rolling direction). Material removal was conducted in increments through electropolishing to measure the residual stress variation with subsurface depth up to a depth of approximately 400 µm.

3.11 Nano-indentation

Nano-indentation technique is conducted in this study to examine the hardness of the material which is determined by bringing together the material of interest to contact with a

known material (indenter). Different intenders can be utilised for hardness measurements. This study uses Berkovich indenter which is a three sided pyramid as shown in Figure 3.9.

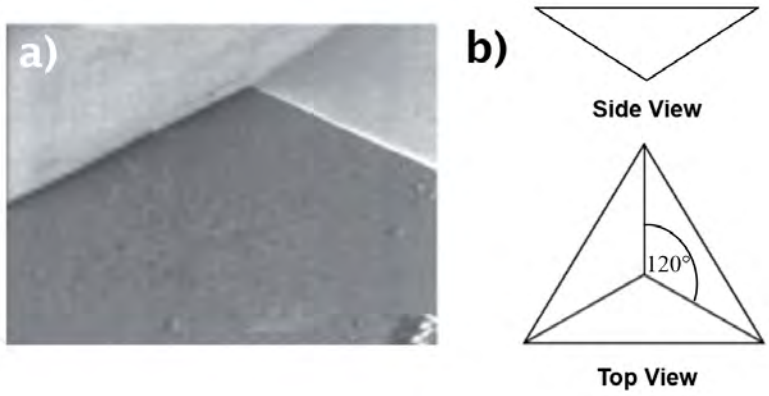

Figure 3.9: a) SEM image of Berkovich indenter b) diagram showing top and side plane view of the Berkovich indenter [173].

Nano indentation is conducted particularly to examine the hardness of the micro-features of WEB (Chapter 7) and the overall DER microstructure (Chapter 6). The tests have been conducted using a NanoTest Vantage (Micro Materials) nanoindentation system with Berkovich tip at University of Southampton. A matrix of nano-indentations have been carried out on a bearing inner ring sample with a developed WEB network to capture as many features as possible under the control mode where the maximum depth is defined as 50 nm. The test parameter included a fixed load/unloading rate of 0.075 mN/s. During the test, a 45 s dwell time at maximum load was used and thermal drift correction data was enabled with a collection time of 45 s. An extra polishing process has been conducted on the nano indented sample using OPS (0.06 µm) to minimise surface roughness prior to indentation. The diamond indenter has a possion's ratio of 0.07 and an elastic modulus of 1400 GPa. The hardness results are extracted from the load-displacement curves obtained from the test. Given the extremely small size of the indents, the indentations are carried out on an un-etched surface. SEM imaging is conducted after test without etching to locate the nano-indents which can be later removed by the etchant. The etching of the indented surface removed the indents given the maximum penetration depth of only 50 nm in the tests conducted in Chapter 7. After the indent matrix is capture through SEM, the sample is etched later to show the area of interested features in the sample by re-imaging the same area with a micro-indenter put on the surface as a reference. The two images are then overlaid to confirm the indent locations in relevance to the features of interest.

In Chapter 6, larger indentation size with a maximum penetration depth of 900 nm is conducted to examine the overall hardness variation in the subsurface microstructure across the DER rather than micro/nano scale components of the WEB in Chapter 7. The test

parameters in this test of the DER included a fixed load/unloading rate of 10 mN/s. The test included a 10 s dwell time at maximum load and thermal drift correction data was enabled with a collection time of 60 s.

Chapter 4

Evolution of DER, LAB and HAB

This chapter focuses on the analysis of DER, LAB and HAB under LOM to investigate the overall microstructure behaviour of the bearing subsurface during RCF and the growth patterns and dimensions of DER, LAB and HAB under the influence of two different contact pressures (2.9 GPa and 3.5 GPa), steel microstructure (martensite vs bainite), steel alloy (high carbon 100Cr6 and low carbon 50CrMo4), range of stress cycles and two different grades of steel cleanliness as highlighted in Figure 3.4. The investigation includes a study of the position at which DER, LAB and HAB develop for a range of stress cycles in reference to subsurface stress distributions. The density of both LAB and HAB are also examined to study the growth patterns associated with each feature. A serial sectioning of the WEB network has also been conducted in this chapter to highlight the full 3D structure of both LAB and HAB and capture the initiation points in the bearing subsurface.

4.1 Position of DER/WEB

In this section the position of these defects in the ACBB inner ring subsurface is measured in all the samples and compared to the subsurface stress distribution to investigate its growth pattern in reference to stress cycles, contact pressure, steel cleanliness and alloy composition. In order to investigate the position of the features, it is important to highlight their appearance in the axial and circumferential cross sections. Figure 4.1 shows the shape of both the DER and WEB in both sections. The DER in the axial cross section appears as a form of sickle shape, thickest at the centre and becoming thinner near the edges (Figure 4.1b). The LAB in the axial cross section appear as thin bands parallel to the surface while the HAB are shown as white blocks positioned within the LAB parallel to the surface (Figure 4.1b). In the circumferential cross section (Figure 4.1c), the DER is shown as a region parallel to the surface while the WEB demonstrate distinctive directions inclined to the surface in the rolling direction of $\sim 30°$(LAB) and $\sim 80°$(HAB).

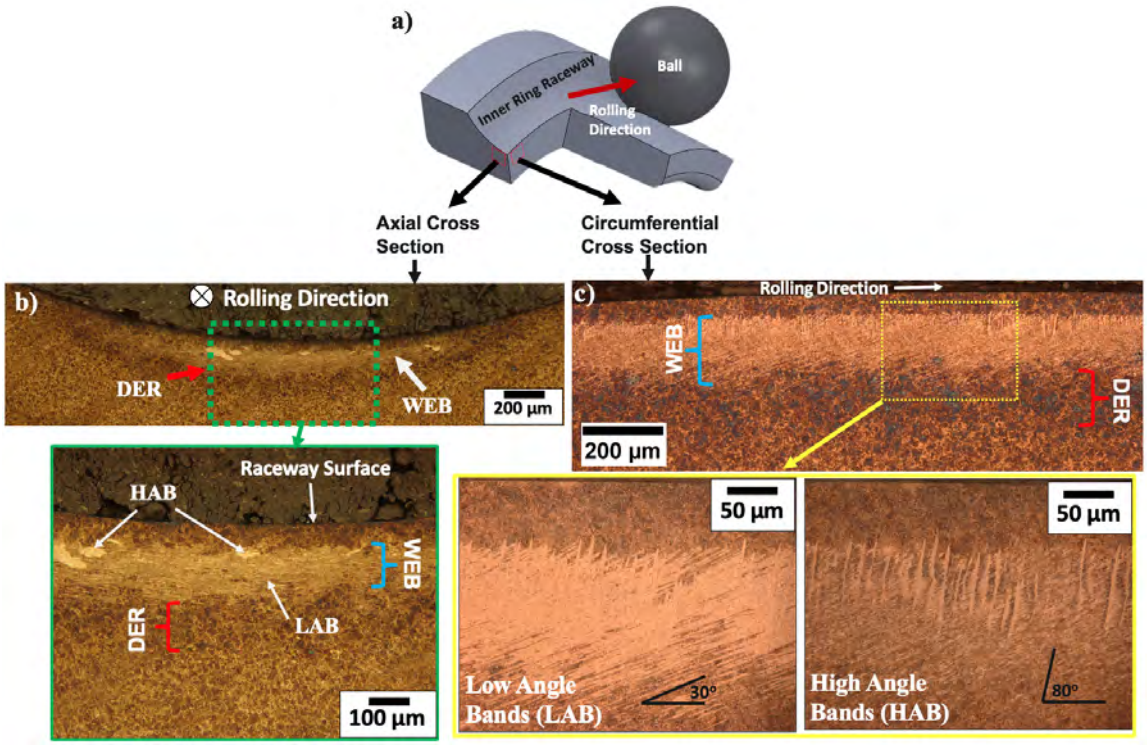

Figure 4.1: a) An illustration of the bearing showing cutting directions performed on bearing inner ring. b) Fully developed DER and WEB features observed in axial section. c) DER and WEB features in a circumferential section of an inner ring with images at a higher magnification showing LAB and HAB in the same area where filters have been applied highlight the particular feature. Images from 100Cr6 martensite samples run under 3016 million cycles (cleanliness B) and 4141 million cycles (cleanliness A).

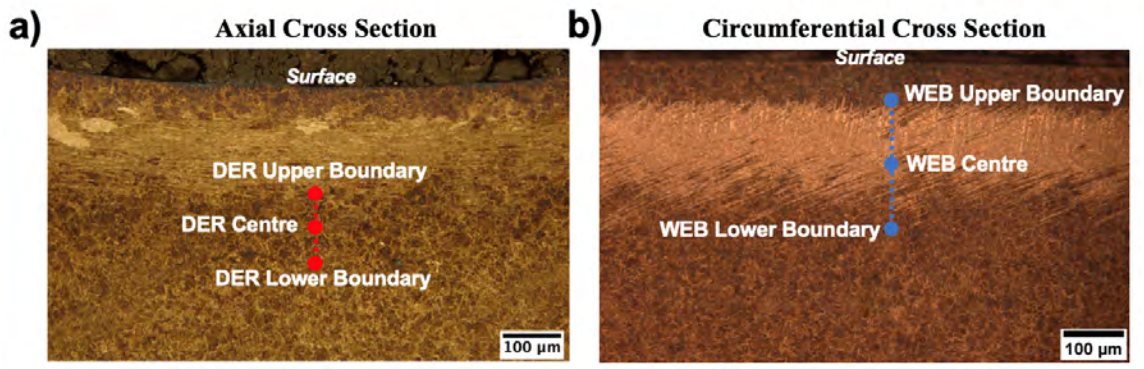

Figure 4.2: a) Defined depth of boundaries and centre of a) DER and b) WEB reported in this chapter.

Based on the observations shown in Figure 4.1 and Figure 4.2, the position of the DER was measured in the axial cross section at the centre where the thickness of the DER is greatest as shown in Figure 4.2a. The position of the WEB (consisting of both LAB and HAB) were measured in the circumferential cross section to capture their full dimensions since they are at an inclination to the surface (Figure 4.2b), hence more structural information of the WEB can be measured from the circumferential cross section. The depth measurements from the surface presented in this section (measured manually

using ImageJ) includes the upper and lower boundaries of the DER and WEB and the midpoint of both features from the surface as highlighted in Figure 4.2. For the depth measurements, the depth was measured across three different regions in two different cuts across the inner ring for each bearing sample giving a total of six measurements per bearing which have been averaged with standard deviation.

4.1.1 DER/WEB in 100Cr6 bearing

This section presents the DER and WEB growth pattern findings for 100Cr6 bearings under the conditions highlighted in Figure 3.4.

4.1.1.1 Influence of Contact Pressure on Martensitic Microstructure

The analysis of DER/WEB under of bearings (cleanliness B) run for a range of stress cycles at 2.9 GPa and 3.5 GPa here (Figure 4.3). To determine, the stress component driving the formation of these features, the subsurface depth of DER and WEB in Figure 4.3 is also compared to the subsurface stress depth distribution of the unidirectional shear stress τ_{45}, orthogonal shear stress τ_0 and von Mises stress σ_{vM} based on Hertzian theory. Although the subsurface stress distribution is assumed to remain constant with stress cycle build-up, it would vary under different contact pressures as demonstrated in Figure 4.3a and 4.3b.

It is observed in Figure 4.3 that the depth of DER and WEB features increase with both stress cycles and contact pressure. Increasing the contact pressure from 2.9 GPa to 3.5 GPa (Figure 4.3) has widened the spread (distance between the upper and lower boundaries) for both features while increasing the midpoint depth of both DER and WEB. The depths of the WEB is correlated with the σ_{vM} and τ_{45} stress distribution under both contact pressures while the DER is positioned deeper in the microstructure and an obvious stress correlation cannot be observed. An explanation of this observation is provided later in the chapter when investigating DER in 50CrMo4 bearings. After a build-up of about 1500 - 2000 million stress cycles, the depth of the WEB boundaries in the samples run under 2.9 GPa (Figure 4.3a) saturates (reaches a maximum). Samples run under 3.5 GPa (Figure 4.3b), which were recorded under lower stress cycles in comparison, shows the lower boundary of the WEB to increase (i.e move deeper in the microstructure from the surface) at a faster rate compared to the upper boundary. This coincides with the sharp/gradual reduction of stress (both σ_{vM} and τ_{45}) from the maximum stress point towards/away from the surface. This suggests the initiation of the WEB is likely to have been in the region of the maximum σ_{vM} or τ_{45}. Although the maximum stress point is not aligned with the center of the WEB, a σ_{vM} threshold in the order of 1300 MPa is proposed at which the boundaries of the WEB in

Figure 4.3a saturate when run for sufficient number of cycles (1500 - 2000 million cycles in this study for samples under 2.9 GPa).

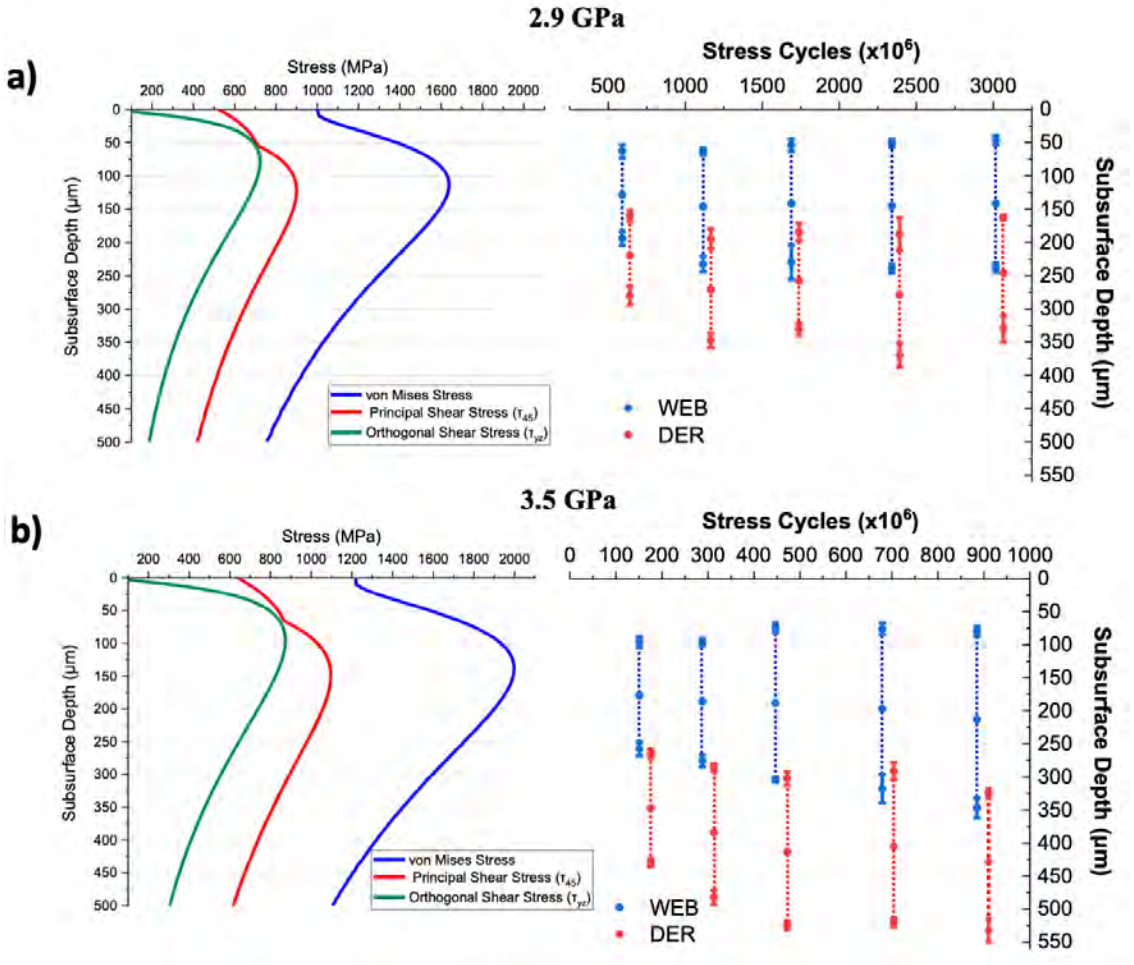

Figure 4.3: DER/WEB depth vs stress/load cycles for the 100Cr6 martensitic steel bearings (cleanliness B) showing the defined positions of the boundaries and centre of DER and WEB measured at (a) 2.9 GPa and (b) 3.5 GPa compared to the corresponding von Mises stress σ_{vM}, principal shear stress τ_{45} and orthogonal shear stress τ_0 distribution. It should be noted that the DER measurements are presented slightly shifted to the right for clarity.

The DER and WEB appear to be separated in Figure 4.3 where WEB are observed shallower than the DER which contradicts the common understanding in literature of a link between both features where WEB form within DER. It should also be noted that WEB in these samples show a distinctive boundary (both upper and lower) which made their observation clearer compared to the DER boundaries which was fading gradually into the parent microstructure leading to potential uncertainties in their true position. Indeed it could be argued that the dense LAB network has overlapped pre-existing DER, making it difficult to identify the true upper boundary of DER. Hence only a segment of the true DER deeper than the WEB is recorded in Figure 4.3. However, even at early stages of WEB, it was difficult to characterize the fully developed DER similar to observations in literature [138, 174]. Optical images of the sickle shape DER in the axial cross section can

be seen for the 100Cr6 martensitic samples run under 2.9 GPa (Figure 4.4) and 3.5 GPa (Figure 4.5) corresponding to the DER measurements shown in Figure 4.3a and Figure 4.3b respectively. Further investigation of the DER in the 50CrMo4 samples in this chapter and high resolution analysis of the formation mechanism of the DER and LAB in Chapter 6 and Chapter 7 later in the thesis has provided an explanation for this finding.

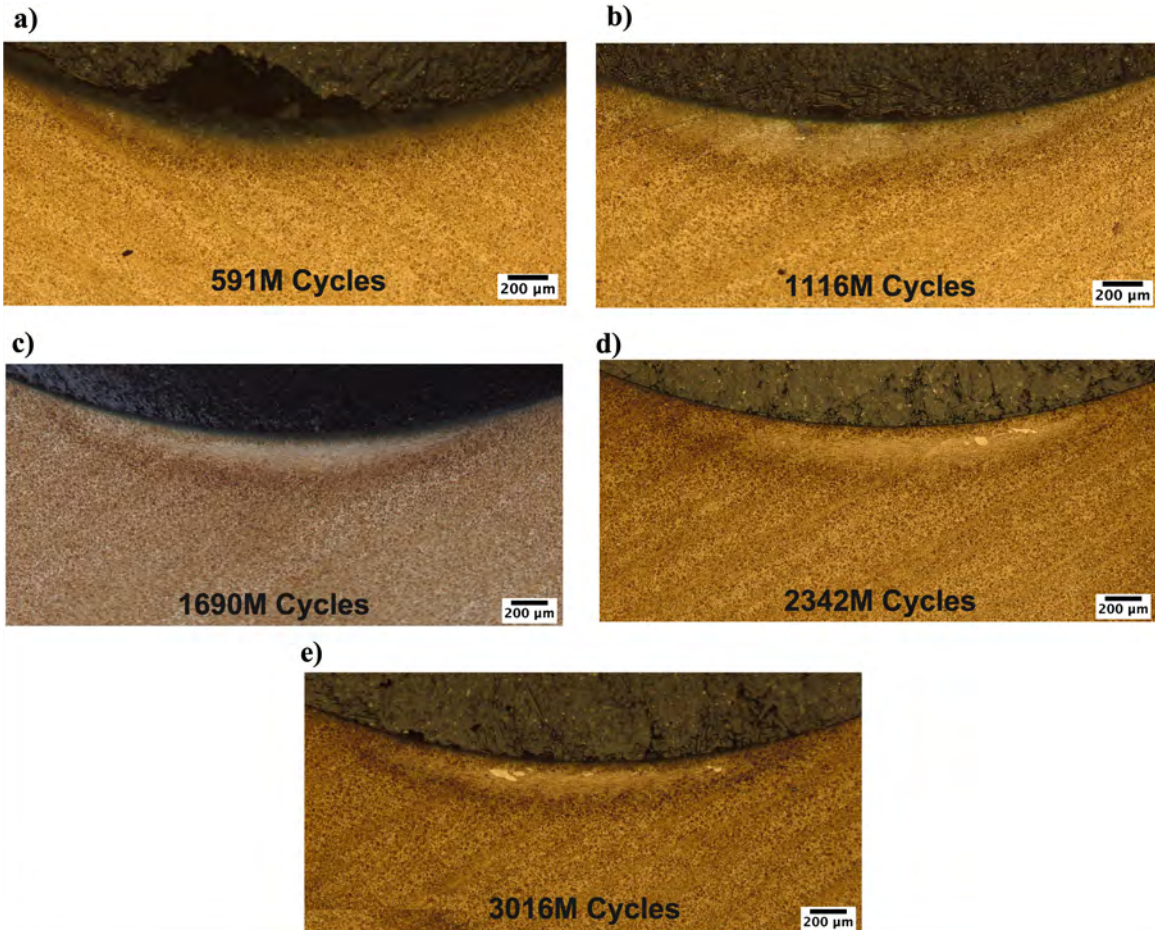

Figure 4.4: Axial cross section of 100Cr6 martensite samples (cleanliness B) showing the sickle shape DER in samples run under 2.9 GPa for a) 591 b) 1116 c) 1690 d) 2342 and e) 3016 million cycles.

In order to better distinguish the full DER structure, attempts of over etching the samples (Figure 4.5a) and adjustments of the LOM filters to enhance surface contrast have been made. Nonetheless, all the 100Cr6 samples in this study have shown the DER sickle shape structure presented in Figure 4.4 and Figure 4.5 where the detection of the DER under LOM was challenging. This has consequently led to uncertainties in confirming the actual boundaries of the DER features. Hence, the analysis of the feature density later in this chapter has focused on WEB (LAB and HAB) rather than DER since the former are more distinctive.

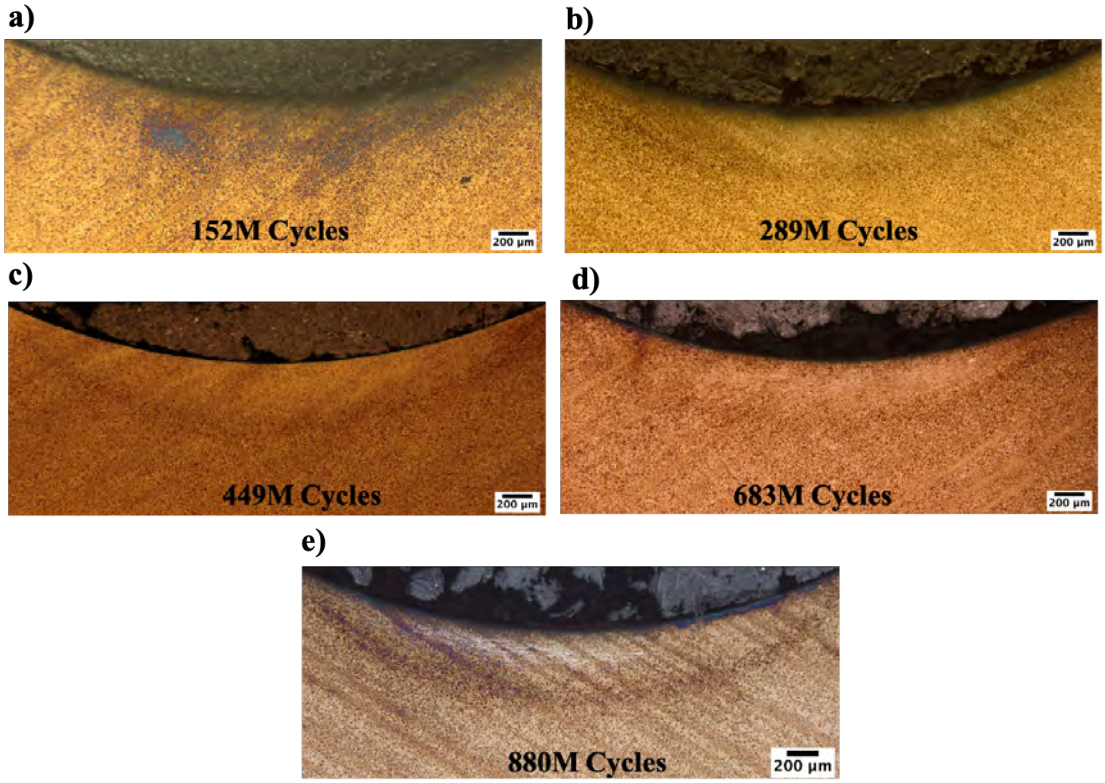

Figure 4.5: Axial cross section of 100Cr6 martensitic samples showing sickle shape DER in samples run under 3.5 GPa for a) 152 b) 289 c) 449 d) 683 and e) 890 million cycles.

4.1.1.2 Influence of Steel Cleanliness on DER/WEB

The depth of DER and WEB in the cleanliness A samples (Figure 4.6) has shown similar results to the lower cleanliness steel (cleanliness B) previously shown in Figure 4.3a and a similar influence of subsurface stress is observed. Optical images of the DER sickle shape

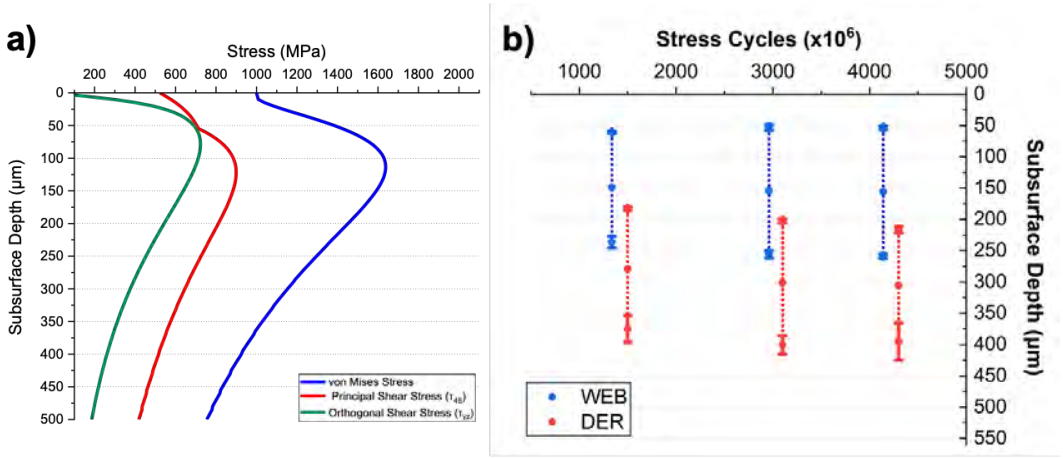

Figure 4.6: DER/WEB depth vs stress/load cycles for the 100Cr6 martensite (cleanliness A) steel bearings showing the defined positions of the boundaries and centre depth of DER and WEB measured under 2.9 GPa and corresponding von Mises stress σ_{vM}, principal shear stress τ_{45} and orthogonal shear stress τ_0 distribution. It should be noted that the DER measurements are presented slightly shifted to the right for clarity.

in the axial cross section of the higher cleanliness steel samples is shown in Figure 4.7. This is similar to previous observations in Figure 4.4 where the DER boundaries are not as pronounced as WEB (presented later in this chapter).

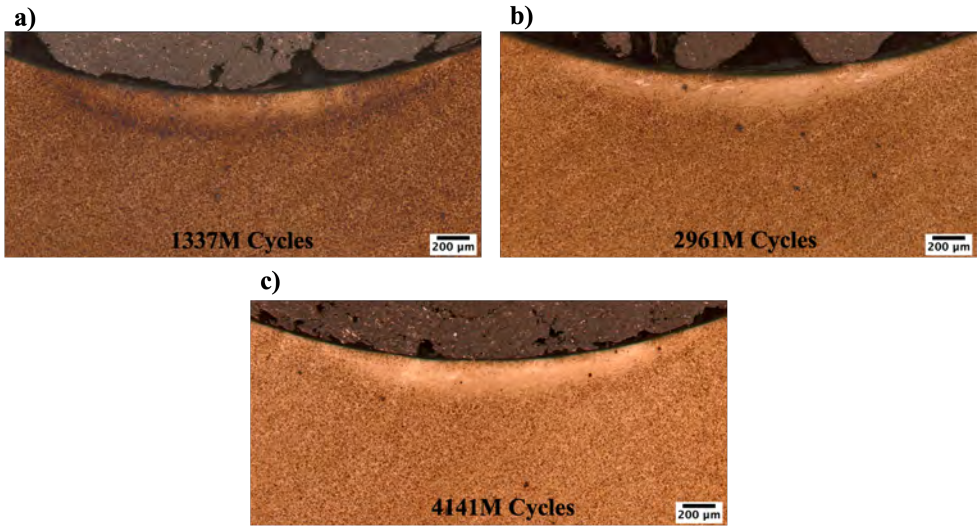

Figure 4.7: Suburface stress distribution defined depth of boundaries and centre of DER and WEB axial cross section of cleanliness A 100Cr6 martensite samples showing the sickle shape DER in samples run under 2.9 GPa for a) 1337 b) 2961 and c) 4141 million cycles.

4.1.1.3 DER/WEB in Bainite vs Martensite Microstructure

The development of DER and WEB in the bainitic microstructure is shown in Figure 4.8 where a similar development of the microstructural alterations to that of the martensitic microstructure is shown (compared to Figure 4.4). However, it is observed in Figure 4.9 that the DER develops shallower and not as spread as in the martensite samples shown in Figure 4.3a. Similar to optical images of the DER shown earlier (Figures 4.4 and Figure 4.7), the DER in Figure 4.9 is not very prominent.

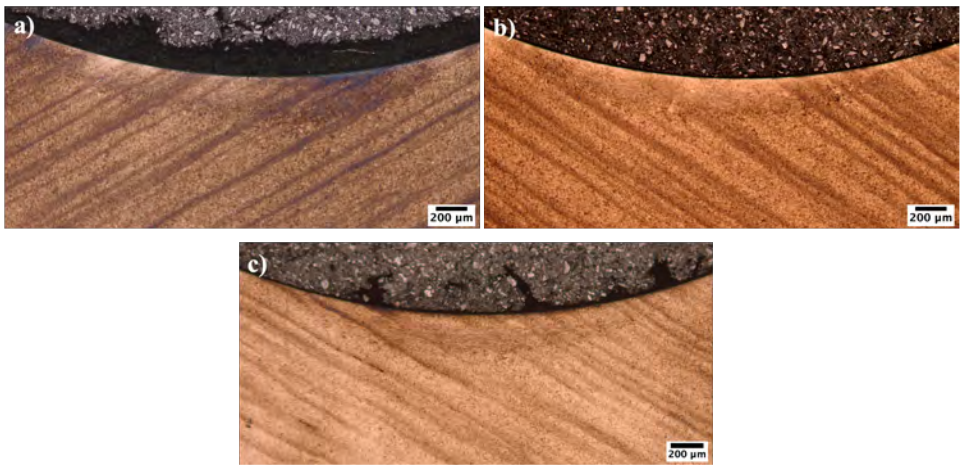

Figure 4.8: Optical images of the axial cross section of 100Cr6 bainite sample showing the sickle shape DER in samples run under 2.9 GPa for a) 532 b) 897 c) 1448 million cycles.

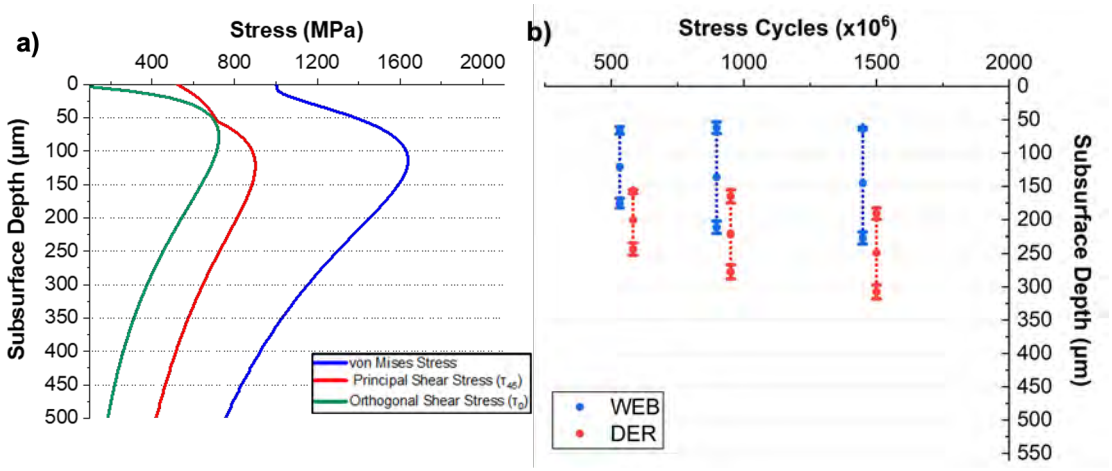

Figure 4.9: a) DER/WEB depth vs stress/load cycles for the 100Cr6 bainite (cleanliness B) steel bearings showing the defined positions of the boundaries and centre depth of DER and WEB measured under 2.9 GPa and corresponding von Mises stress σ_{vM}, principal shear stress τ_{45} and orthogonal shear stress τ_0. Distribution It should be noted that the DER measurements are presented slightly shifted to the right for clarity.

Diagonal streaks have been observed in the steel samples in this study in both martensitic (Figure 4.4) and bainitic microstructures (Figure 4.8). These streaks are typically found as a result of the manufacturing stage where segregation of alloy elements in the steel such as chromium in 100Cr6 steel occurs. A close-up of this region is shown in Figure 4.10 which is a consequence of the chromium segregation throughout the microstructure. However, it should be noted that the formation of DER and WEB have not been shown to be influenced by such segregations.

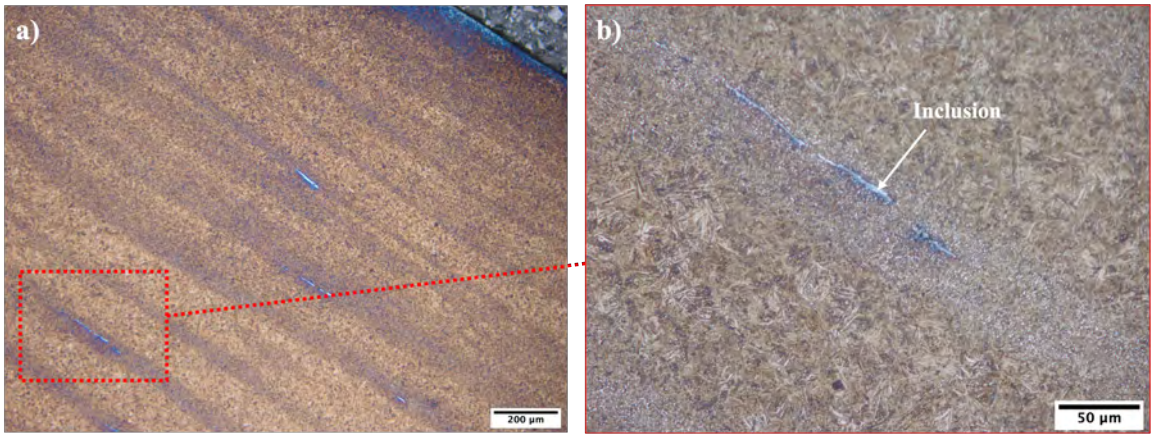

Figure 4.10: a) Bainite microstructure (away from contact area) in axial cross section in sample run under 2.9 GPa for 1448 million cycles showing diagonal lines across the etched material. b) Close-up of microstructure showing the diagonal streaks as segregation of chromium from manufacturing and elongated inclusion within.

4.1.2 DER/WEB in 50CrMo4 bearing

The DER in the 50CrMo4 samples is more defined with distinctive boundaries (see Figure 4.11) compared to the 100Cr6 samples samples at comparable stress cycles (Figure 4.4, Figure 4.7 and Figure 4.9). However the WEB is shown to be less pronounced in the 50CrMo4 samples, suggesting they are at an earlier stage of formation.

The DER in 50CrMo4 bearings from earliest stage in this study (Figure 4.11a), is shown at the center of the contact area and grows across the contact region (Figure 4.11b-d) as number of stress cycles increases. However, at the latest stages in this study (Figure 4.11e and 4.11f) i.e highest stress cycles, a more sickle shape similar to the 100Cr6 samples presented earlier in Figure 4.4 is observed where the area shallower to the contact surface becomes brighter. This suggests a similar progression stage is happening but is delayed in the 50CrMo4 samples i.e occurs over much later stress cycles in 50CrMo4 bearings (observed after 2038 million cycles) compared to 100Cr6 (observed at earliest sample after 591 million cycles). Nonetheless, the DER at the early stages of the 50CrMo4 samples in this study (Figure 4.11a-d) is shown to coincide with the τ_0 stress distribution (Figure 4.12). However, due to the 'brightening' of the shallower portion of the DER at later stages as discussed previously, the remaining DER patches at late stages (Figure 4.11e and f) does not correlate with the stress distributions in Figure 4.12. This is similar to the position of DER recorded in the 100Cr6 samples in Figure 4.3, Figure 4.6 and Figure 4.9 where no comparison could be made between the DER position and the subsurface stress distributions.

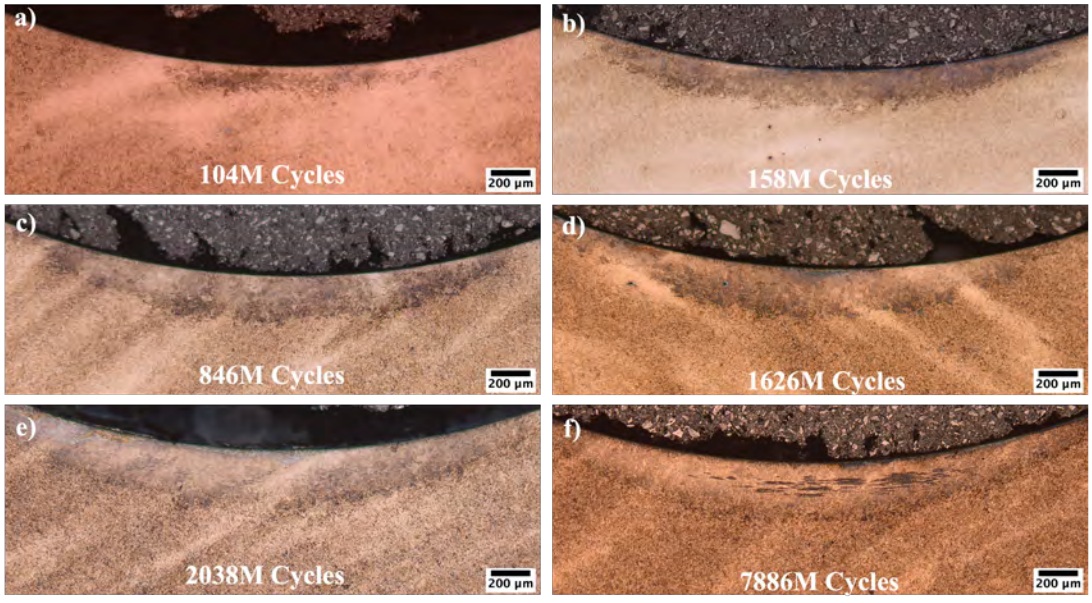

Figure 4.11: Optical images of the axial cross section of 50CrMo4 bearings showing the DER in samples run under 2.9 GPa for a) 104 b) 158 c) 846 d) 1626 e) 2038 and f) 7668 million cycles.

The WEB in the 50CrMo4 specimens are less dense/pronounced compared to the 100Cr6 specimens under comparable stress cycles (see Figure 4.4c and Figure 4.11d). It should be noted that the WEB in Figure 4.11f appears dark due to the set direction of polarised light utilized when capturing the image to enhance the contrast of the DER sickle shape with the surrounding microstructure. However, a similar orientation of polarised light in the 100Cr6 samples did not yield clearer images of the DER. It is observed in Figure 4.12 that the position of the WEB is similar to the position of the features in the 100Cr6 bearings (Figure 4.3a, 4.6 and 4.9) i.e coincides with the σ_{vM} and τ_{45} stress distribution.

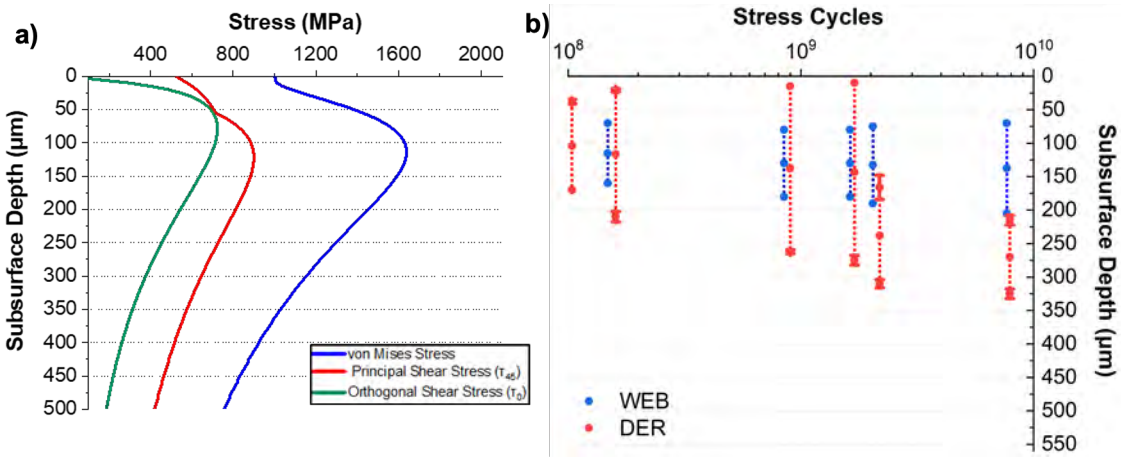

Figure 4.12: DER/WEB depth vs stress/load cycles for the 50CrMo4 steel bearings showing the defined positions of the boundaries and centre depth of DER and WEB measured under 2.9 GPa and corresponding von Mises stress σ_{vM}, principal shear stress τ_{45} and orthogonal shear stress τ_0 distribution.

4.2 Density Comparison of LAB/HAB

Figure 4.13 and Figure 4.14 shows the LOM images of the LAB and HAB respectively for 100Cr6 martensite samples (cleanliness B) run under 2.9 GPa where the area consumed by both LAB and HAB increases with cycles. Comparison between martensitic and bainitic 100Cr6 samples and different steel cleanliness showed near identical behaviour (for equivalent cycles) indicating that the difference in microstructure between these two materials has no effect on the evolution of WEB. Hence, a comparison is not shown here. Reader is referred to Appendix B to see the optical images of WEB in the other materials.

A significantly lower density of WEB is observed in the 50CrMo4 samples (see Figure 4.15) in contrast to the 100Cr6 samples (see Figure 4.13) under comparable stress cycles. Similar to Figure 4.11 which showed the features in the axial cross section, the circumferential cross section of the same 50CrMo4 samples shows the DER growing across the subsurface at earlier cycles (Figure 4.15a-d) but eventually becomes brighter (etch-

resistant) as the LAB develops in the maximum shear stress region i.e brightening of DER coincides with the position of the LAB. This transformation is further investigated in Chapter 6. It should be noted that in the 50CrMo4 samples, no HAB have been observed which is likely due to the delayed development stage of the WEB. To allow imaging the LAB in the 'bright' DER, the orientation of the polarised light was altered (compared to 100Cr6 samples) which produced a dark appearance of the LAB (Figure 4.15) to distinguish the bands clearly from the surrounding microstructure.

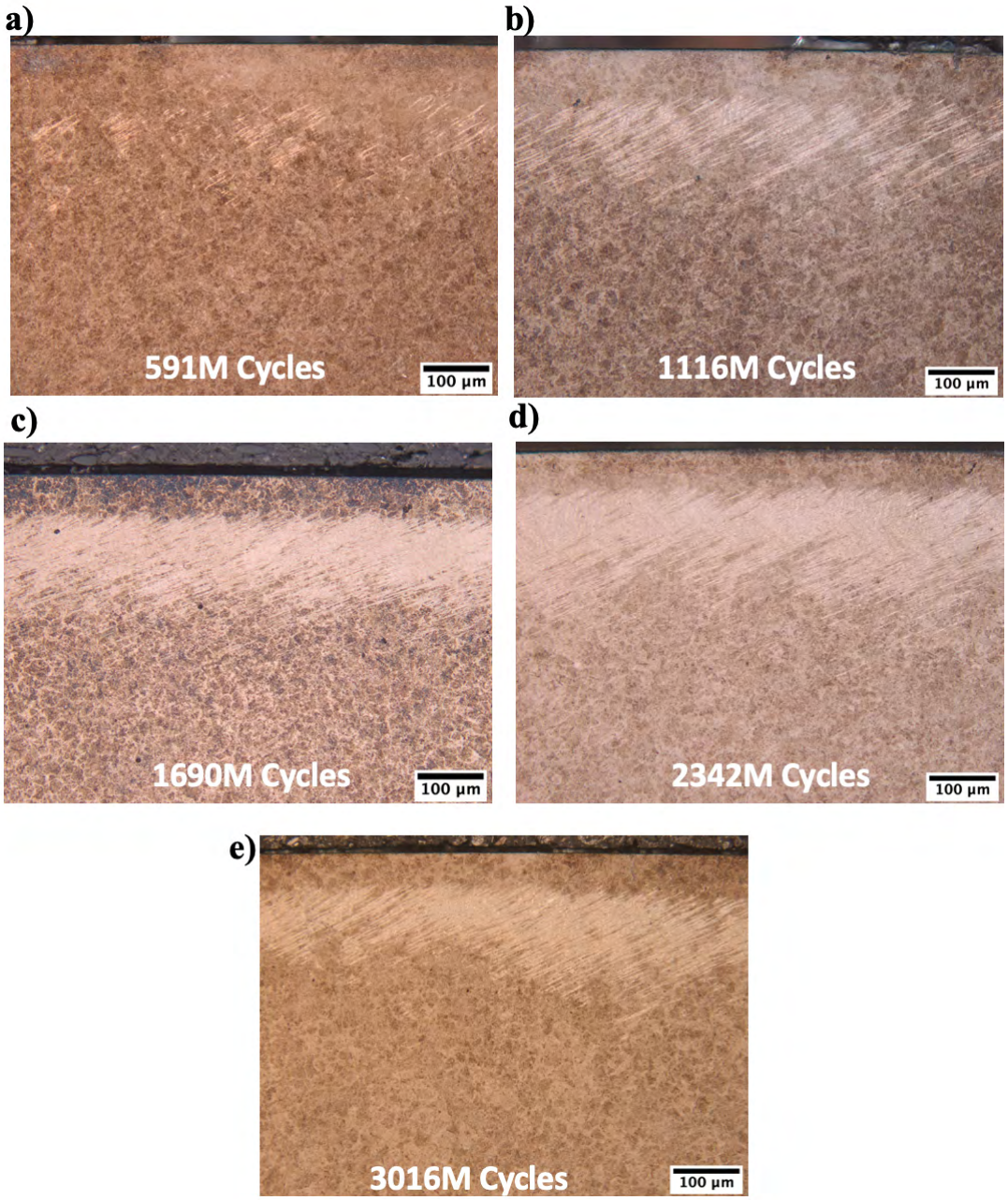

Figure 4.13: LOM images of LAB in circumferential cross section of 100Cr6 martensite samples (cleanliness B) run under 2.9 GPa for a) 591 b) 1116 c) 1690 d) 2342 and e) 3016 million stress cycles.

Circumferential cross sections of 100Cr6 martensite samples (cleanliness B) at 3.5 GPa

contact pressure is shown in Figure 4.16 which depicts LAB to be positioned deeper compared to the same sample batch run under 2.9 GPa as previously shown in Figure 4.3. However, it is also shown that the LAB are less dense compared to the samples shown in Figure 4.13 due to relatively lower number of stress cycles experienced.

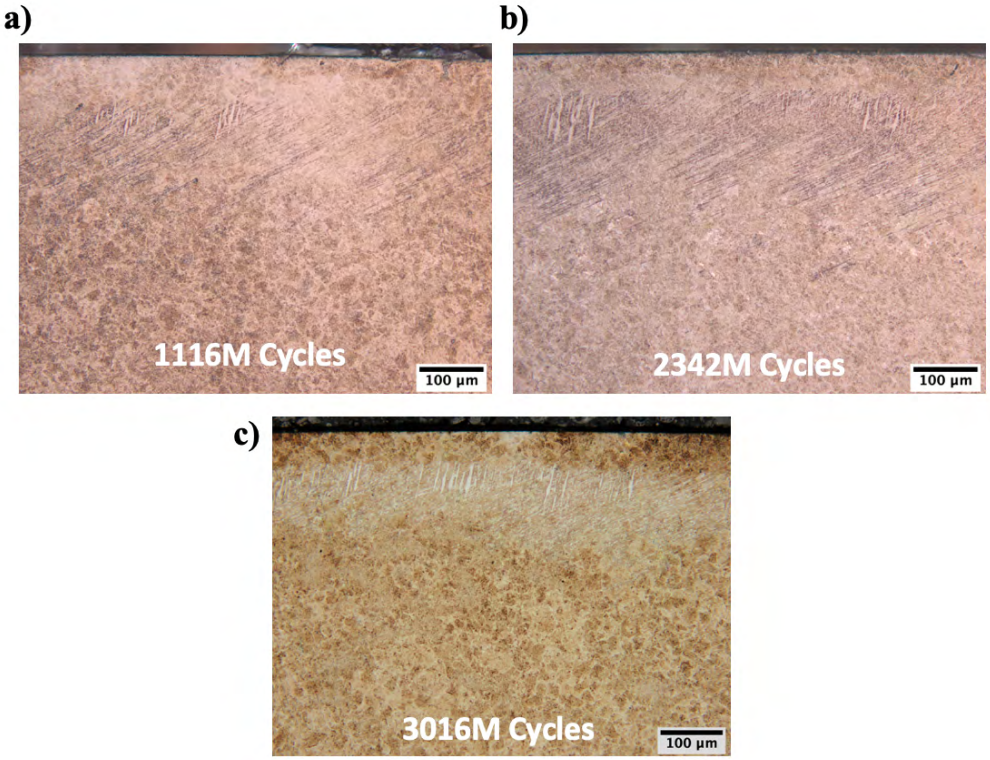

Figure 4.14: LOM images of HAB in circumferential cross section of 100Cr6 martensite samples (cleanliness B) run under 2.9 GPa for a)1116 b)2342 c) 3016 million stress cycles.

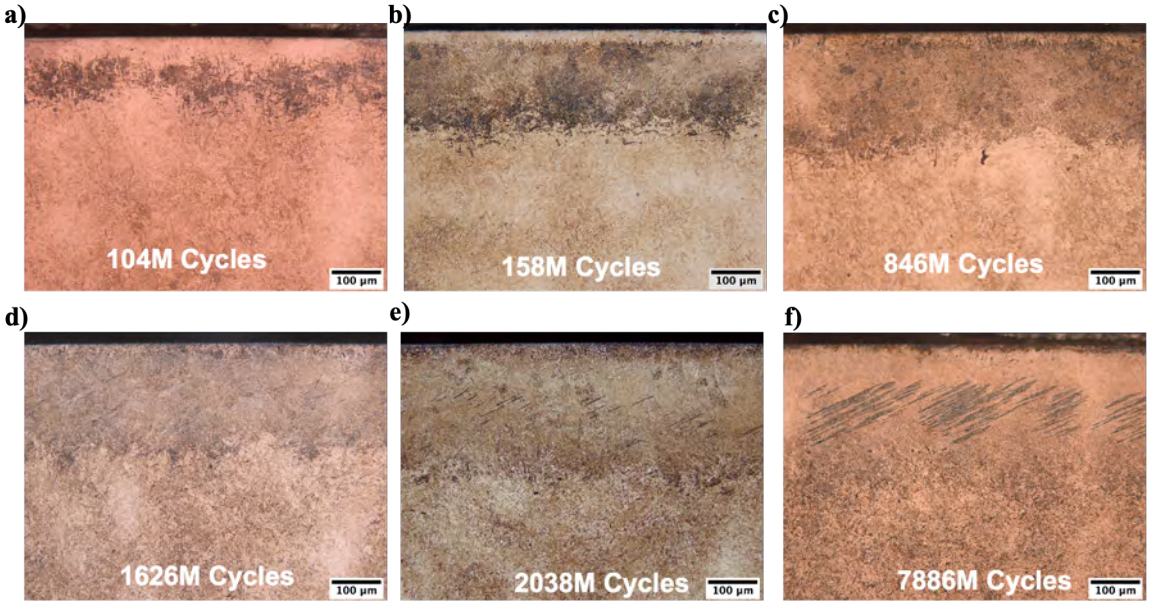

Figure 4.15: LOM images of DER and LAB in circumferential cross section of 50CrMo4 martensite samples run under 2.9 GPa for a) 104 b) 158 c) 846 d) 1626 e) 2038 and f) 7668 million stress cycles.

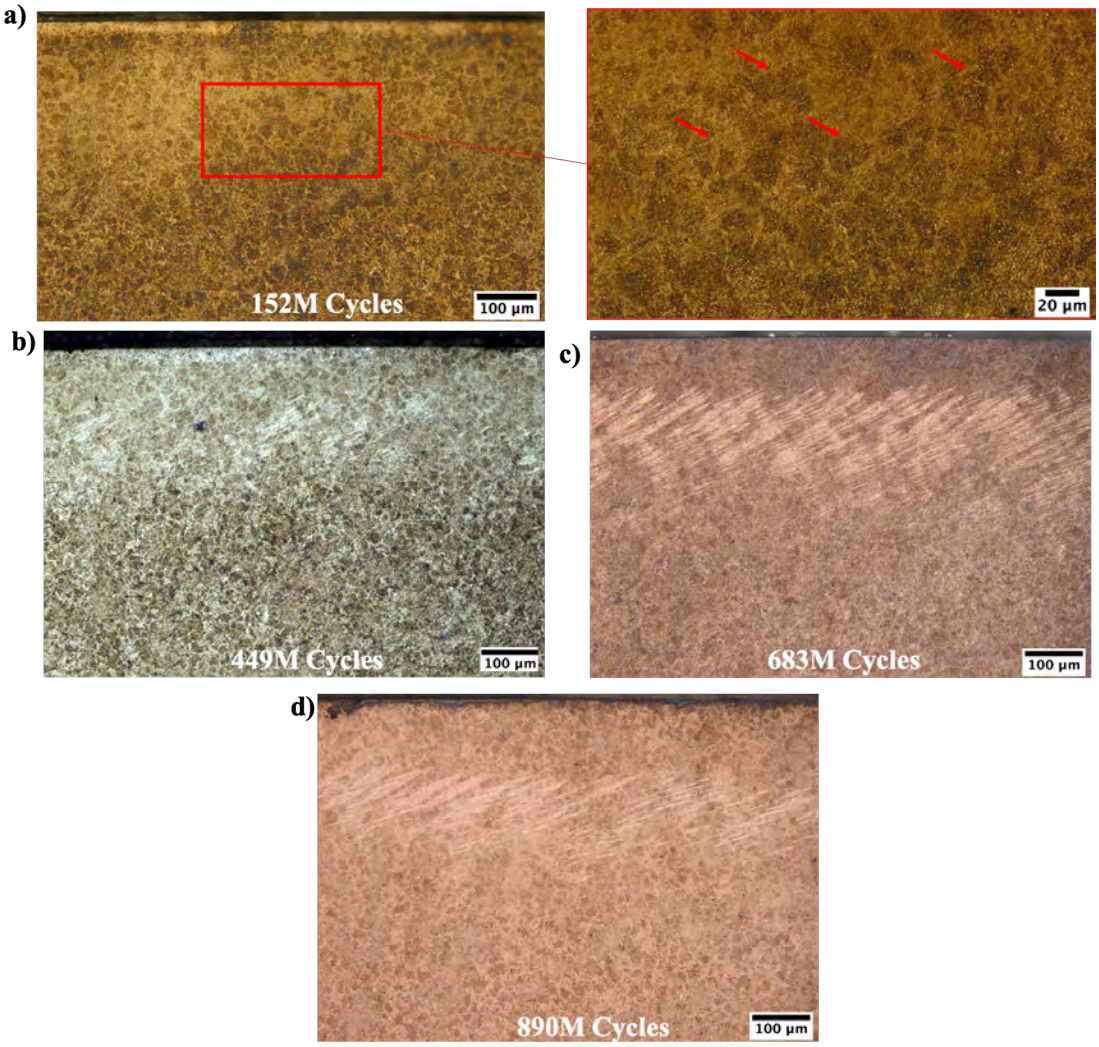

Figure 4.16: LOM images of LAB in circumferential cross section of 100Cr6 martensite samples (cleanliness B) run under 2.9 GPa for a) 152 b) 449 c) 683 d) 890 million stress cycles.

In the following section, the density of LAB and HAB in all samples are quantified to provide a systematic comparison of the growth patterns in reference to stress cycles variation.

4.2.1 LAB/HAB Density vs Cycles

Both LAB and HAB have been quantified by applying appropriate thresholds (in ImageJ) of polarized LOM images to quantify their densities as discussed in Section 3.4. The density of LAB and HAB ($LAB\%$ and $HAB\%$) is defined as the percentage of the image area (667 µm x 860 µm) covered by LAB and HAB features as shown in Figure 3.7. Hence a $LAB\%$ of 15 would indicate 15% of the imaged area is covered by LAB. The results from of the quantification of the WEB density ($LAB\%$ and $HAB\%$) for all samples can be seen in Figure 4.17. Different trends can be seen for the density variation of LAB and HAB with stress cycles. For the 100Cr6 martensite samples under 2.9 GPa, LAB show a trend which

is a steady growth from early stage until just below 2 x 10^9 stress cycles where a level of saturation has been reached (equivalent to $LAB\%$ of 15 as shown in Figure 4.17). This saturation level corresponds to the point where the boundary of the LAB in Figure 4.3a becomes level irrespective of increasing stress cycles i.e. when they are fully developed. This saturation level is further explored in Chapter 5 to develop a semi-empirical model for the WEB.

For HAB, it can be seen that a negligible level of HAB is maintained until just under 2 x 10^9 stress cycles when a rapid increase in $HAB\%$ can be seen in Figure 4.17. This coincides with the point where LAB achieve their saturation, after which HAB start to grow significantly. This suggests the formation of HAB is provoked by the high density of the LAB formed within the region. The correlation between the dense closely-packed LAB and HAB development is explored further in Chapter 7. A link between LAB density and HAB development would elucidate why samples with low $LAB\%$ show no or negligible $HAB\%$ and hence, given the slow growth rate of LAB in the low carbon 50CrMo4 bearings ($LAB\%$ in Figure 4.17 depicting less regions covered by LAB), no HAB have been observed in all 50CrMo4 samples even when tested for 7886 million cycles. While 100Cr6 samples under same contact pressure have reached a much higher $LAB\%$ under comparatively lower stress cycles and therefore, show developed stages of HAB as evidenced by the $HAB\%$ in Figure 4.17.

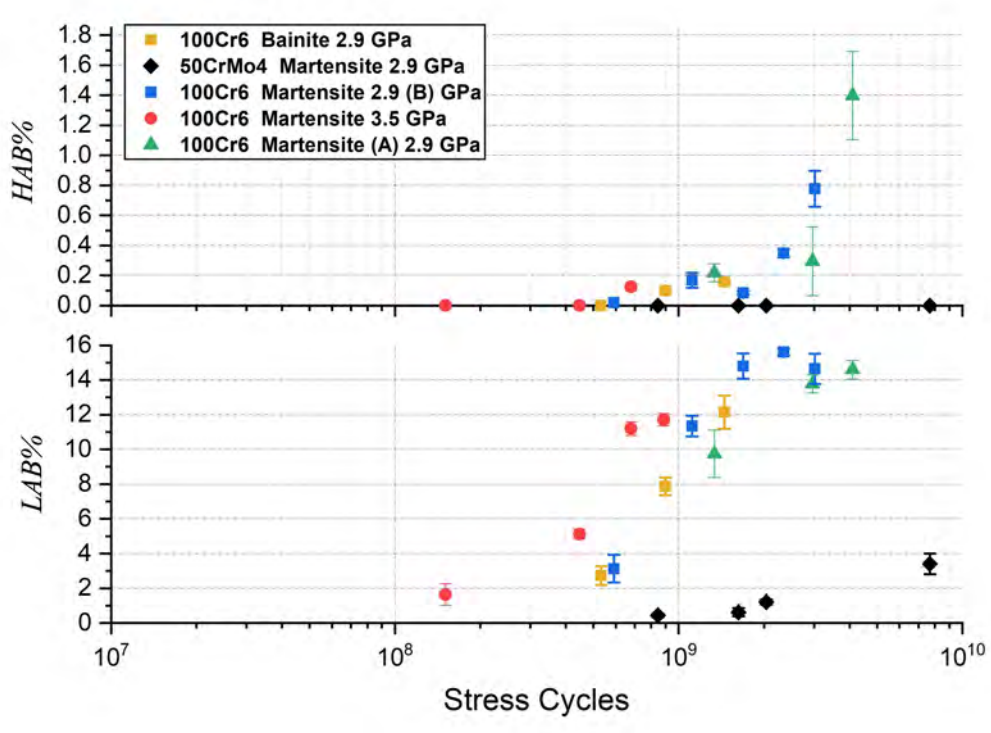

Figure 4.17: $LAB\%$ and $HAB\%$ recorded for each sample in this study vs stress cycles.

Comparing both cleanliness grades of 100Cr6 martensite under 2.9 GPa (cleanliness A vs B) has shown a similar trend. The data of the specimens with cleanliness A are within the experimental error compared to cleanliness B samples and hence consistent with the trend established in terms of both LAB and HAB development discussed previously. Comparing the influence of martensite vs bainite microstructure, it is also evident that the WEB develop similarly in both microstructures as well. However, the development of the LAB is shown to initiate earlier in the bearing life under higher contact pressure (2.9 GPa vs 3.5 GPa).

4.2.2 LAB Density vs Depth

In this section the density of the LAB is analysed across the subsurface depth of each sample to determine if subsurface stress levels are a clear factor in their formation, as some indications have shown in Section 4.1. Figure 4.17 shows a correlation between the pre-existing LAB density and the formation of HAB. Figure 4.18 shows the upper boundary of the LAB (where HAB form) contains denser/closely packed regions of LAB compared to the lower boundary which would support the hypothesis linking dense LAB to HAB formation.

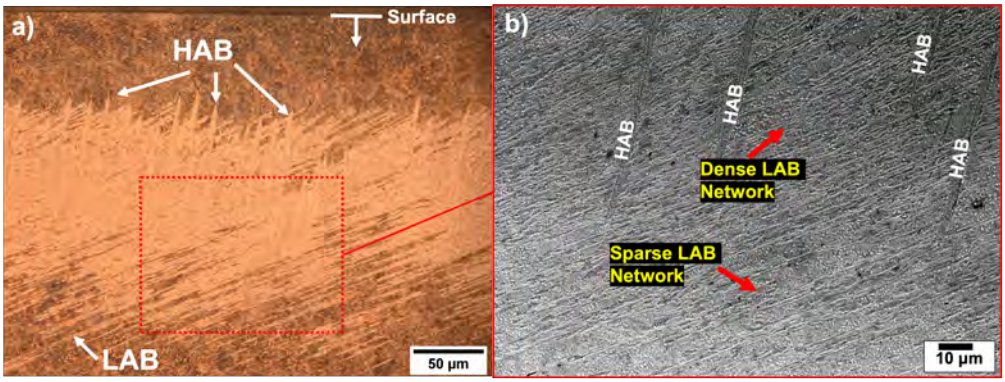

Figure 4.18: a) LOM image and b) SE SEM image of LAB/HAB network in sample 100Cr6 martensite sample (cleanliness A) run under 2.9 GPa for 4141 million cycles showing the variation of LAB density vs depth from surface compared to the position of the HAB.

During the early stages of HAB (see Figure 4.19a), the features appear as conglomerates whereas they become more uniformly distributed at later stages (Figure 4.19b). Prior to the saturation of LAB discussed previously, which occurs between 1500 - 2000 million cycles for the 100Cr6 samples under 2.9 GPa, the distribution of the LAB is not uniform as local regions appear denser than others as demonstrated by the red circles in Figure 4.19a which correlates with the early positions of HAB. At later stages i.e beyond the LAB saturation level, LAB become more dense and evenly distributed towards the upper boundary of the WEB as shown in Figure 4.19b. Hence, the HAB are also shown to be more evenly distributed as well. This supports the correlation between HAB development and the dense pre-existing LAB.

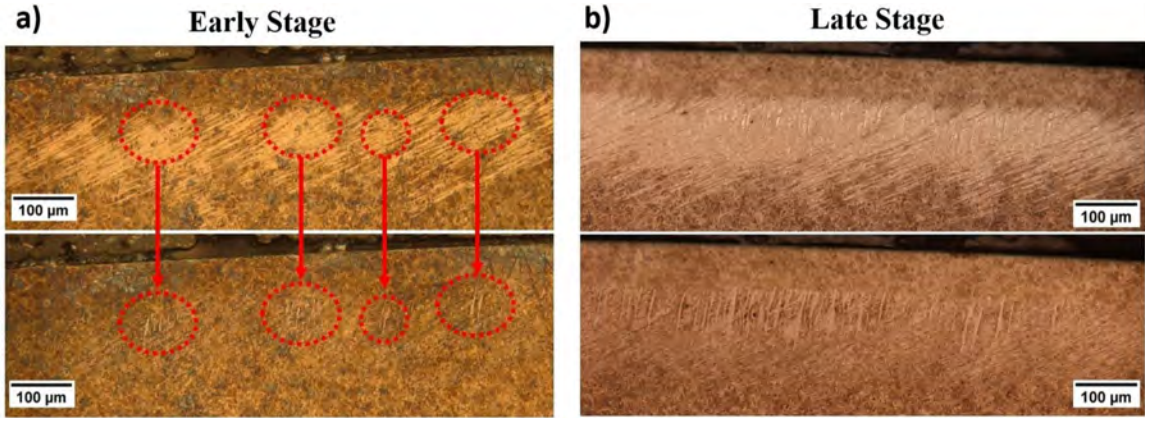

Figure 4.19: Optical image of LAB (top) and HAB (bottom) from 100Cr6 samples run under 2.9 GPa for (a) 1116 million cycles (cleanliness B) and (b) 4141 million cycles (cleanliness A). The dense LAB regions highlighted in red in a) correlates with the early development of HAB.

Further investigation is conducted by analysing the variation in %LAB density with respect to the microstructure depth from the raceway surface across different stages of the bearing life. This is achieved by marking slices with a depth of 10 µm across the processed LAB threshold image (see illustration in Figure 4.20).

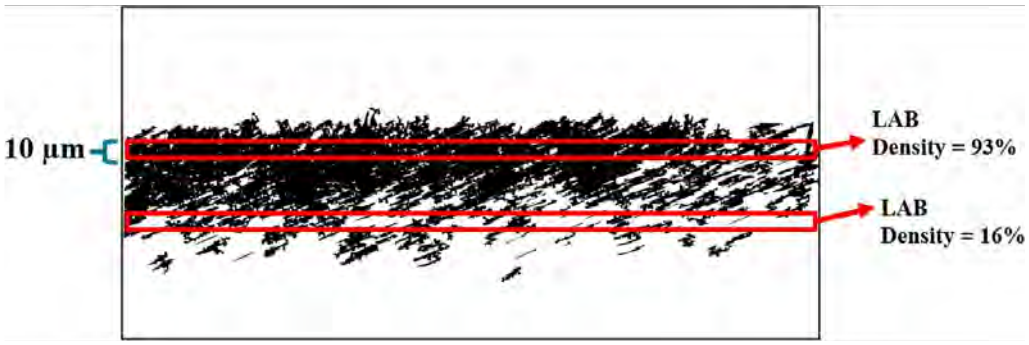

Figure 4.20: Illustration of the method used to determine the LAB density variation with depth. Drawing of slice is not drawn to scale for clarity.

The LAB density distribution across the depth from the bearing surface is shown in Figure 4.21 for four tests under 2.9 GPa. While Figure 4.3a shows the WEB position to coincide with the σ_{vM} and τ_{45} stress distribution, it should be noted the centre of the WEB does not coincide with the maximum shear stress point. The LAB density distribution vs depth presented in Figure 4.20 coincides well with the distribution of the distribution of the von Mises and principal shear stress. The earliest stages (Figure 4.21b-c) shows a sharp peak of %LAB coinciding with the position of the maximum stress which becomes broader at later stages due to the emergence of HAB in that region. Nonetheless, the position of the maximum LAB density coincides with depth of the maximum σ_{vM} and τ_{45} point (at 120 µm and 115 µm respectively) across the bearing life rather than τ_0 (maximum at depth of 80 µm). This indicates the initiation point of the LAB is likely to be the maximum stressed

point. Comparing the density of the LAB with the position of HAB in Figure 4.21c, 4.21d and 4.21e shows an obvious correlation where the HAB is positioned in the region of the highest LAB density similar to observations in Figure 4.18.

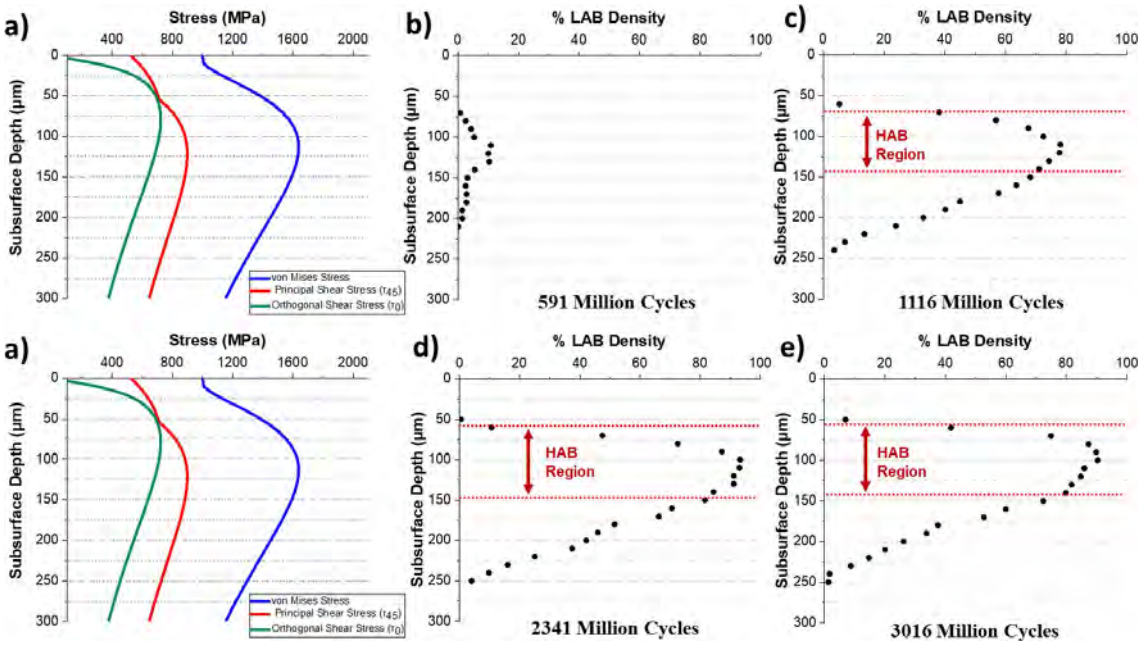

Figure 4.21: a) Subsurface stress distribution of von Mises stress (σ_{vM}) principal shear stress (τ_{45}) and orthogonal shear stress (τ_0) under a contact pressure of 2.9 GPa. LAB density distribution across the depth is shown from 100Cr6 martensitic (cleanliness B) samples run under 2.9 GPa for (b) 591 c) 1116 (d) 2341 (e) 3016 million cycles. Red lines in c-e represent the upper and lower boundary of HAB found in the corresponding sample.

4.3 Influence of Residual Stress

Investigation of the residual stress in the material subsurface of the samples was conducted to learn if and how the residual stress influences the evolution of microstructural changes. Figure 4.22 shows the residual stress distribution in reference to depth from the raceway surface for both virgin and RCF-tested 100Cr6 martensite (cleanliness B) samples under 2.9 GPa and 3.5 GPa. The virgin sample shows a relatively uniform distribution of tensile residual stress that remains fairly unchanged when RCF-tested under 2.9 GPa for up to 1262 million cycles (see Figure 4.22a). In contrast, a build-up of compressive residual stress is measured when samples are tested under 3.5 GPa as shown in Figure 4.22b.

Comparing the residual stress distribution in samples run under 2.9 GPa in Figure 4.22a with the development of the WEB and their position from Figure 4.3a and Figure 4.21, it is obvious that while the WEB develop and grow within the microstructure with increasing stress cycles, the residual stress remains unchanged which suggests it does not contribute to their development unlike the principal shear stress and von Mises stress which

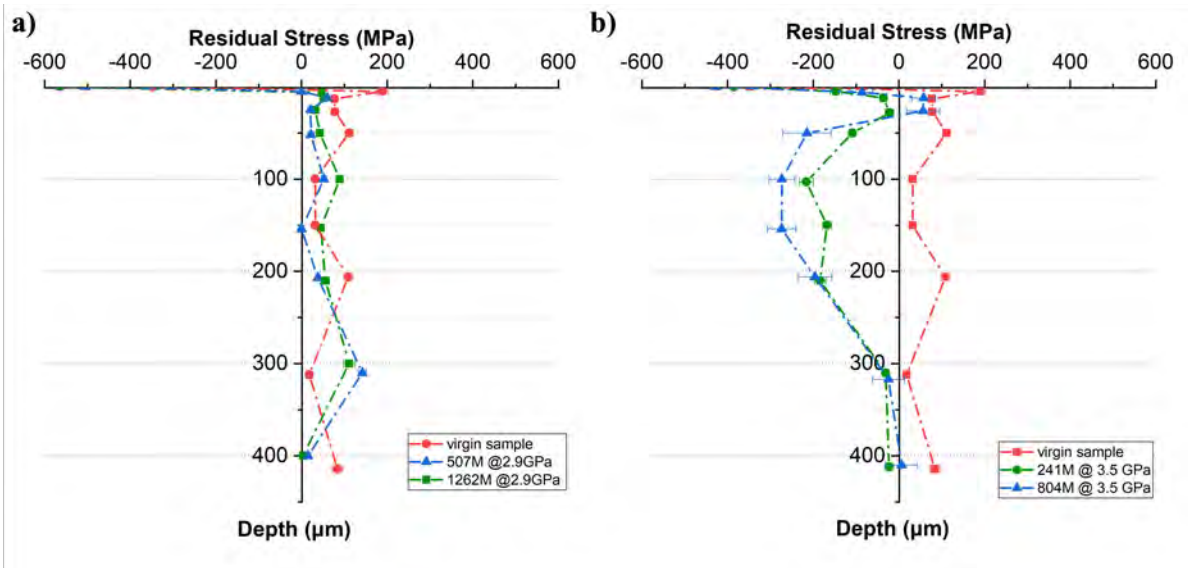

Figure 4.22: Residual stress distribution against subsurface depth from the surface for 100Cr6 martensitic microstructure (cleanliness B). Measurements include virgin sample (untested) and RCF-tested samples run at a range of stress cycles under a contact pressure of a) 2.9 GPa and b) 3.5 GPa.

shows a better correlation with the feature position from early stages. The compressive residual stress build-up in samples tested under 3.5 GPa increases with stress cycles (Figure 4.22b). However, a direct correlation between the residual stress distribution could not be established. The depth of the maximum compressive residual stress in the RCF-tested samples in Figure 4.22b coincides with the maximum τ_0 distribution (see Figure 4.3b) while the WEB as discussed previously coincides with σ_{vM} and τ_{45}. Nonetheless, given that WEB develop at a faster rate at higher contact pressure (see Figure 4.17), the compressive residual stress build-up at higher contact pressures may influence their growth rate but given that WEB also develop in RCF-tested samples under 2.9 GPa, which show no residual stress build-up, residual stress is not a driver for their formation.

4.4 Serial Sectioning of WEB

Manual serial sectioning is performed on WEB to investigate the full structure of the features and construct a 3D model of the WEB network which consists of both LAB and HAB. Details of the serial sectioning technique is described in Section 3.9.

The serial sectioning conducted in this section was performed on the 100Cr6 martensite sample (cleanliness A) run under 2.9 GPa for 4141 million cycles as the 100Cr6 sample tested with highest stress cycles in this study. Images of the 3D WEB model constructed can be seen in Figure 4.23 where an orthogonal slice is performed in the xy plane (Figure 4.23b) and yz plane (Figure 4.23c) based on the directions indicated in Figure 4.23a. The thickness,

length and span of the bands are measured across the x, y and z directions respectively. It is shown in Figure 4.23b that the WEB structure consists of closely packed LAB with a few scattered HAB. Observing the WEB network in the yz plane (Figure 4.23c), the LAB appear as thin parallel lines similar to the axial images shown in Section 4.1 while the HAB appear as dense blocks similar to that shown in Figure 4.2b which confirms these large blocks in the axial cross section are indeed HAB.

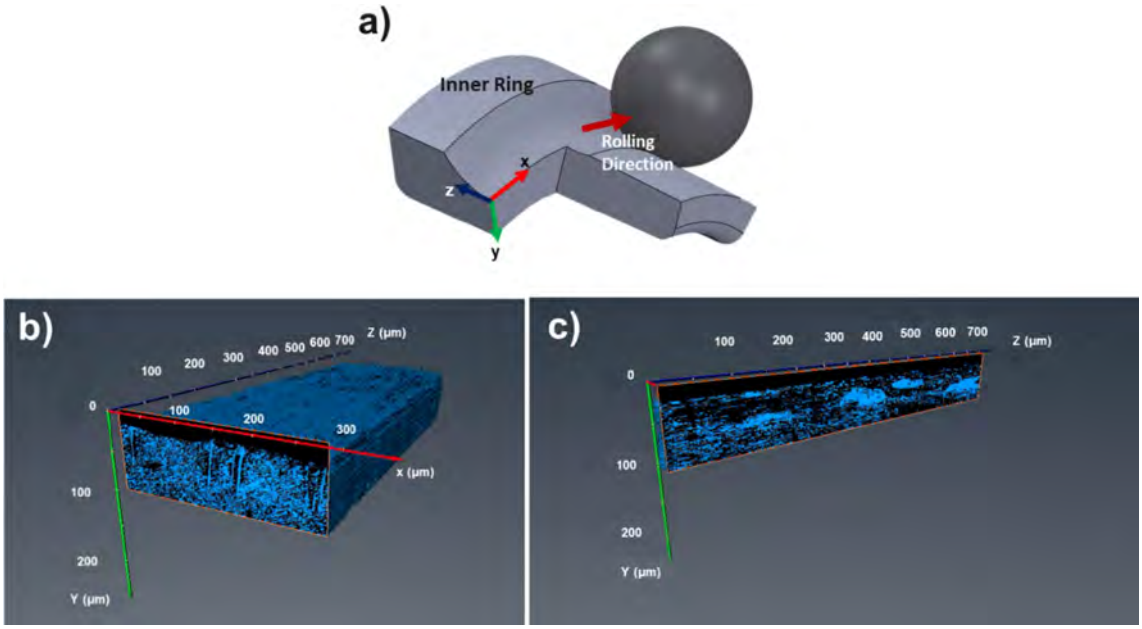

Figure 4.23: a) Defined planes of the 3D model relative to the bearing geometry were xy plane corresponds to circumferential cross section and yz plane corresponds to axial cross section. b) A WEB 3D model with an orthogonal cut in the xy plane. c) A WEB 3D model with orthogonal cut in yz plane. See video 1 for serial orthogonal cuts of WEB 3D model in yz plane.

Segmentation of the 3D model is shown in Figure 4.24 to highlight individual HAB within the WEB network. The span of the HAB measured as shown in Figure 4.24b ranges from 25 µm to over 575 µm. Although the HAB with the largest span recorded (red band in Figure 4.24) is not fully exposed, it is still greater than a third of the contact width a (1.65 mm in z direction from Figure 4.23a). Throughout the HAB span, it appears to vary in both thickness and length rather than being of uniform size. This suggests local variations in the microstructure such as LAB density may have an influence of the growth of HAB. This is explored further in Chapter 7 through SEM analysis. Statistical data on the dimensions of HAB and LAB recorded from the 3D WEB model is shown in Table 4.1.

The 3D model of the HAB is been modified in Figure 4.25 to show the position of inclusions within the WEB network modelled to determine if they influence the formation of these features. Various inclusions have been found in the WEB volume, with some being at the edge and within the HAB (WEB interactions with inclusions is explored further under

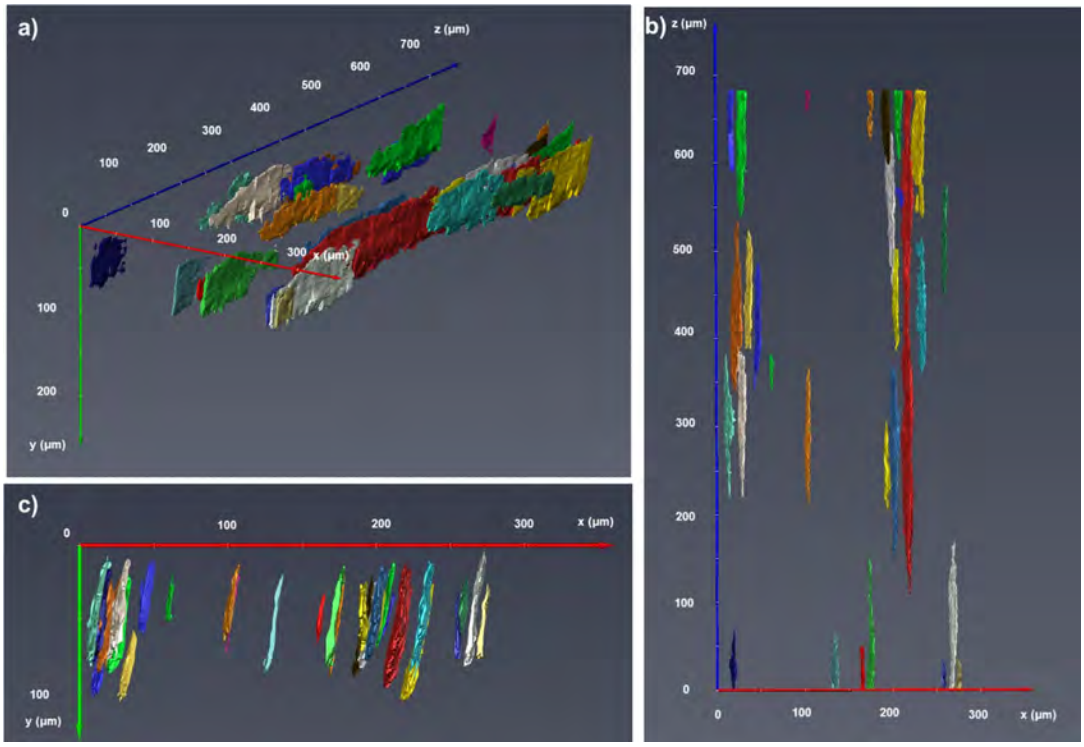

Figure 4.24: a) 3D model of multiple HAB within the WEB network in Fig. 4.23. b) View of the 3D HAB model in the xz plane. c) View of the 3D HAB model in the xy plane. See video 2 for 360° rotation of the 3D model.

Table 4.1: 3D dimensions of HAB and LAB obtained from serial sectioning results.

	HAB			LAB		
	Min	**Average**	**Max**	**Min**	**Average**	**Max**
Length (µm)	13	60	90	12	52	118
Thickness (µm)	2	5.6	10	0.1	1.6	4.8
Span (µm)	25	160	575*	9	44	105

*Full HAB span was not reached, hence actual value is greater than the presented value.

SEM in Chapter 9). Given that the majority of the HAB in Figure 4.25 appear to form independent of any surrounding inclusions, this suggests their influence on HAB and LAB is minimal where the existence of inclusions near or within WEB could be based on statistical probabilities.

Observations during serial sectioning of the HAB have shown three different characteristics / shapes when looking at the edges of the HAB where they start to appear until they become fully formed (see Figure 4.26). One characteristic highlighted in Figure 4.26a is the HAB growing in thickness and length (in both directions from the surface) until a maximum size is reached. In Figure 4.26b, the HAB is shown to grow in length initially followed by thickness. An interesting observation in Figure 4.26c shows the HAB initially consisting of separate small white etching matter from individual LAB (orange arrow in 4.26c2-4) which eventually join together to form a single HAB (red arrow 4.26c4-6) that

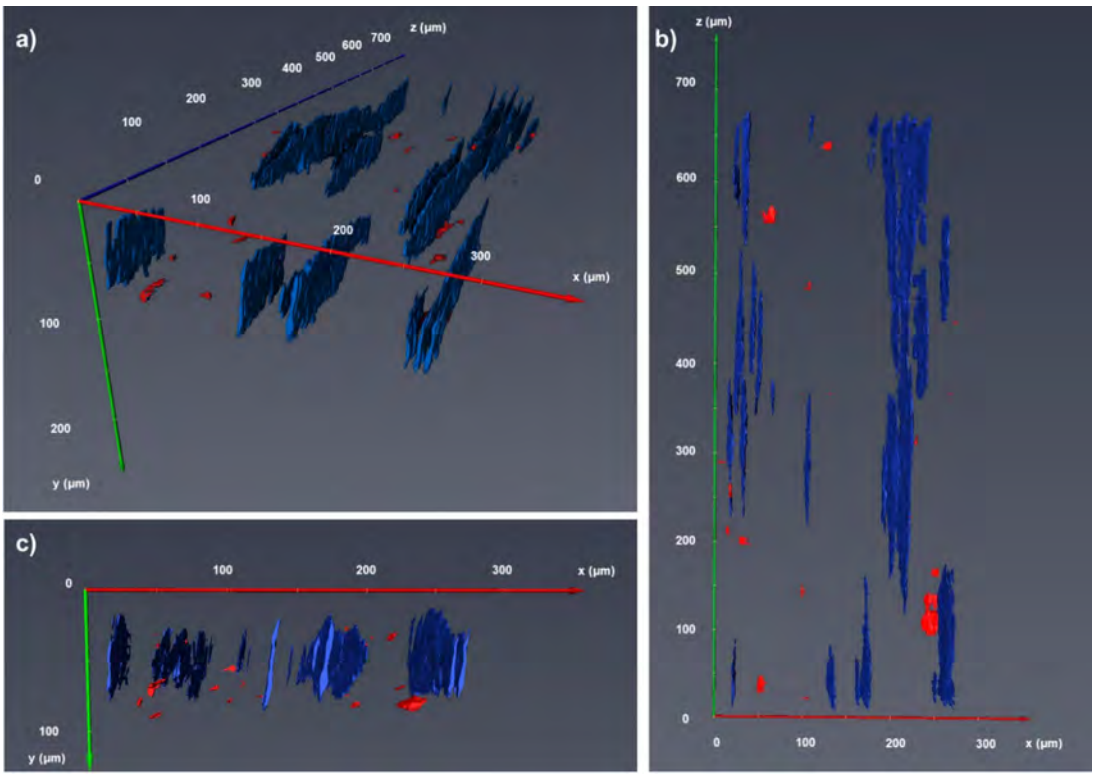

Figure 4.25: a) 3D model of HAB from Fig. 4.24 compared to inclusion positions. b) View of the 3D HAB/inclusion model in the xz plane. c) View of the 3D HAB/ inclusion model in the xy plane. See video 3 for 360° rotation of the 3D model.

later grows in length and thickness similar to other HAB. This provides strong evidence that HAB originate from pre-existing LAB where white etching matters from individual LAB join together forming a single HAB. This agrees with previous findings in this chapter showing a correlation between LAB density and HAB development. Hence the correlation between HAB development and dense pre-existing LAB is investigated further under higher resolution in Chapter 7 to confirm this correlation.

4.5 Discussion

Multiple studies have analysed the formation of WECs and WEAs in different materials such as 100Cr6 [153, 156, 175, 176], M50 [177], 100CrMo7 [178] and 17CrNiMo6 [179]. Different treatments have also been examined such as martenitic through hardened steel [121, 161, 163], case hardened [180–182] and bainite [42, 183]. However, DER and WEB studies in literature in contrast has focused on martensitic 100Cr6. Hence this chapter has investigated the influence of different alloys (high carbon 100Cr6 and low carbon 50CrMo4 steel), microstructures (bainite vs martensite) and steel cleanliness on the development of DER and WEB. The influence of contact pressure (2.9 GPa vs 3.5 GPa) is also investigated.

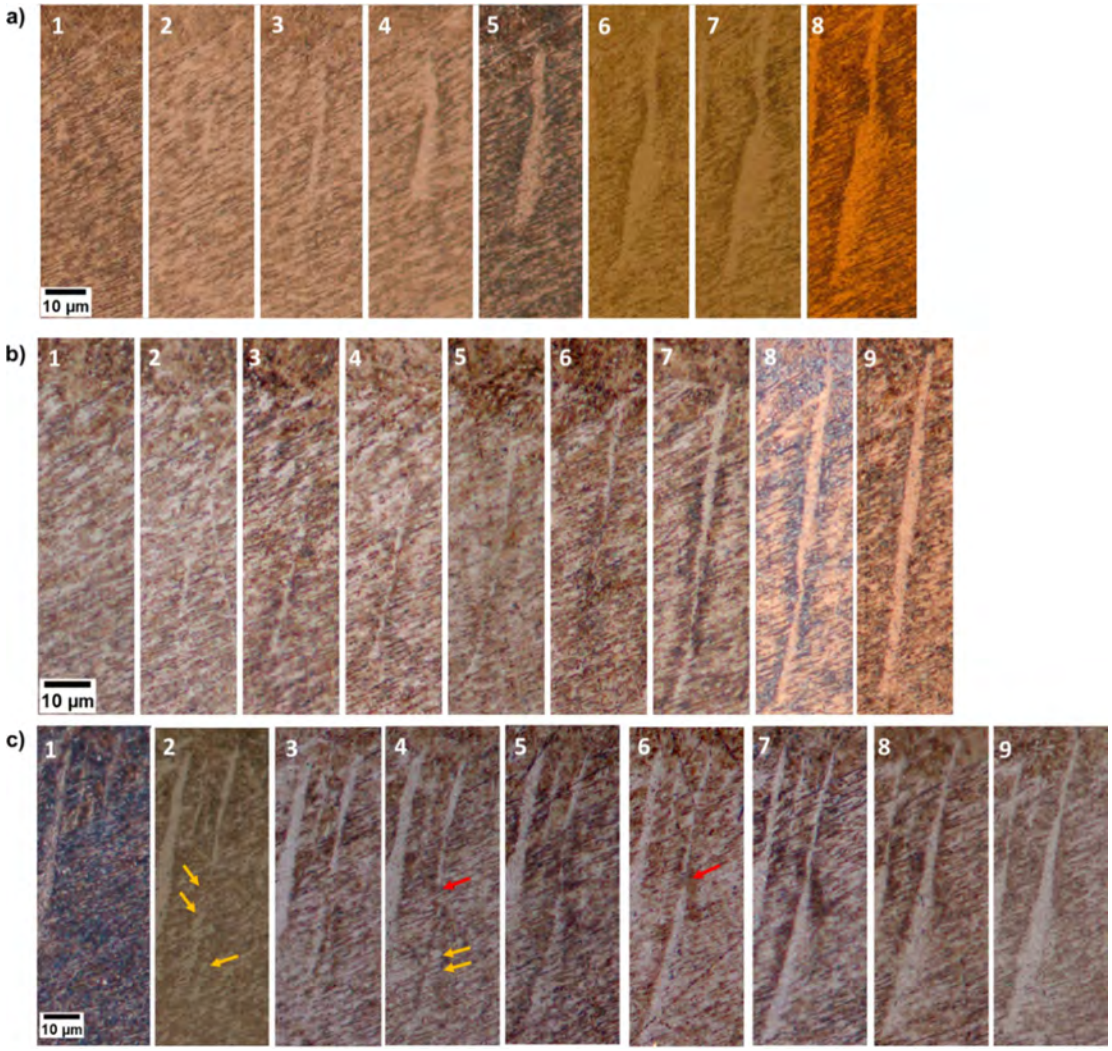

Figure 4.26: Growth of HAB from span edge to full development obtained from serial sectioning in xy plane showing (a) HAB growing in thickness and length simultaneously (b) HAB growing in length initially followed by thickness (c) HAB forming from individual white etching matter from LAB which joins to form a single HAB. Numbers indicate number of slice with each being 10 µm apart. Red arrows shows gaps between HAB prior to merging together while orange arrows show individual segment of white etched areas from LAB prior to becoming full HAB.

4.5.1 100Cr6 microstructural comparison (martensitic versus bainitic)

DER and WEB have been observed at similar subsurface depths under similar stress cycles under both microstructures while the progression (growth rate) of LAB and HAB has also shown similarities when investigating the $LAB\%$ and $HAB\%$ increase vs stress cycles in Figure 4.17 and hence no clear distinctions have been highlighted. Optical images of both martnsite and bainite samples showed no disparity in terms of microstructural transformations (Figure 4.8 and Figure 4.4). While it has been stated WEB may develop in both martensitic and bainitic microstructures [4], there is a lack of experimental evidence in literature to confirm this. Findings in this study confirm not only that both DER and WEB develop in a similar manner in both microstructures, it is also shown the region (depth under

similar contact pressure) in which both DER and WEB form and the growth rate of WEB (LAB and HAB) are similar under identical conditions. In both 100Cr6 microstructures in this study, the WEB are clearly evident from the microstructure while the DER in both microstructures was more challenging to distinguish.

4.5.2 Effect of material cleanliness

The influence of steel cleanliness has been investigated to confirm possible correlations between the formation of DER/WEB and non-metallic inclusions. It has been shown in the 3D model developed via serial sectioning (Figure 4.23-4.25) that the majority of LAB and HAB develop outside the vicinity of inclusions. The growth patterns of $LAB\%$ and $HAB\%$ in the 100Cr6 martensite microstructure of both cleanliness levels show similar patterns and grow rates (see Figure 4.17). Hence it is evident that inclusions play no role in the formation of DER/WEB. Comparing the position of the WEB and inclusions in the serial sectioned volume suggests the interaction between both features is likely to be based more on statistical positioning of the inclusions rather than having an influence on the formation process of the bands. It should be noted that there is currently no study in literature investigating possible interactions between WEB and inclusions. Nonetheless, current findings suggest the conditions leading to the formation of WEB is unlikely to be local stress points such as with butterflies and inclusions [64, 157] but rather more global stress-induced conditions in the subsurface which initiates LAB and HAB (this is explored in Chapter 7). A study on the interaction of inclusions with LAB/HAB is examined in greater detail in Chapter 9 where rather than influencing the formation of WEB, interactions between inclusions and LAB/HAB is shown to contribute to bearing failure through void development.

4.5.3 Effect of contact pressure

While it has been difficult to highlight the position of DERs with accuracy in 100Cr6 samples, LAB which have a preferred orientation ranging from 20 to 35°, was more detectable. LAB show a growth pattern coinciding with σ_{vM} and τ_{45} rather than τ_0 (see Figure 4.3 and Figure 4.21) from the earliest stage. Investigating the WEB (specifically LAB) in all the different materials in this study under different contact pressures and a range of stress cycles has led to the same conclusion. Given the similarity of both maximum stress point for both stress curves based on Hertzian theory (120 µm and 115 µm for σ_{vM} and τ_{45} respectively), it is difficult to confirm which component is responsible or whether it is a combined influence. It is clear from Figure 4.3 and Figure 4.21 that the orthogonal shear stress does not coincide with the WEB which opposes previous findings and proposals [14, 30, 80]. This difference in findings could be explained to be due to

looking at circumferential cross sections deviated from the contact centre, which given the sickle shape of the features in the axial cross section (Figure 4.4), could heavily influence the recorded depth position of the features. Another explanation could be that studies have not accurately differentiated between DER and WEB. As shown later in Chapter 6 and Chapter 7, there are some similarities between both features which could have made it challenging to differentiate between them under SEM. However, there have been other studies that have suggested WEB coincide with τ_{45} [79, 134, 138] while others have suggested σ_{vM} to coincide with the WEB [76].

Based on the position of LAB, it is difficult to confirm with confidence which stress component (σ_{vM} or τ_{45}) is the driver for LAB formation or whether it is a combined influence. Nonetheless, the WEB boundaries measured in Figure 4.3a at late stages (WEB boundaries have saturated) coincides with a σ_{vM} threshold in the order of 1300 MPa, hence σ_{vM} is proposed to best coincide with the WEB rather than τ_{45} which establishes that LAB formation is stress-induced [150]. The threshold observed in this study is comparable to other thresholds proposed in literature corresponding to a principal shear stress in the order of 0.72 GPa [79]. A τ_0 threshold of 0.56 GPa for DER formation has been proposed by Fu et al. [118] in 100Cr6, however DER distribution in 100Cr6 and 50CrMo4 (more pronounced) of this study contradicts this even though DER is observed to coincide with τ_0 in this study as well (Figure 4.12 prior to its brightening). The data presented in Figure 4.3b shows the boundary limit lower than the proposed threshold due to the relatively lower stress cycles. The saturation level of WEB is reached in Figure 4.3a between 1500 and 2000 million cycles and hence the samples shown in Figure 4.3b have not reached that level (test duration too short). Given WEB are believed to be a manifestation of plastic deformation, it has been hypothesised by Fu et al. that the broadening on the WEB formation range should saturate when the principal shear stress equals the yield shear strength of approximately 0.74 GPa for 100Cr6 steel bearing [138]. This hypothesis is similar to the experimental results of this study (Figure 4.3a) but a better fit with σ_{vM} is established in this study. The correlation of WEB with σ_{vM} is utilised in Chapter 5 to establish a semi-empirical model for predicting both LAB and HAB.

There have been multiple reports linking the development of these microstrucutral alterations to the subsurface residual stress. [30, 63, 80, 107, 111]. Findings reported in Figure 4.22a shows no residual stress build-up in the subsurface with increasing stress cycles under 2.9 GPa even though WEB have been well established within the microstructure. This suggests that the residual stress is not a driver for WEB formation. On the other hand, samples RCF-tested at 3.5 GPa (Figure 4.22b) show a build-up of compressive residual

stress with increasing cycles where the maximum stress point coincides with the maximum τ_0 rather than σ_{vM} or τ_{45}. Even though the residual stress is not a proposed driver for WEB formation, the compressive residual stresses in the region were WEB exists may yet influence their evolution given the growth rate of WEB at 3.5 GPa is faster than samples tested under 2.9 GPa (Figure 4.17). Further investigation in the future is needed to confirm this. Residual stress build-up in the subsurface is heavily influenced by the contact pressure. It has been proposed by Muro et al. [125] that residual stress build-up increases with greater Herztian contact pressure and stress cycles due to the gradual phase transformations i.e. retained austenite decomposition in the subsurface but introduced a contact pressure threshold of 3.5 GPa below which negligible residual stress build-up occurs which agrees with the findings from Figure 4.22. Voskamp et al. [111] on the other hand presented a build-up of compressive residual stress in 100Cr6 bearings operating under 3.2 GPa and 3.5 GPa which increases with stress cycles. Hence it is likely that a true threshold lies between 2.9 GPa and 3.2 GPa where residual stress build-up in the microstructural becomes significant. Nonetheless, given the dense WEB network observed in samples run under 2.9 GPa for various stress cycles, this suggests residual stresses have a minimal role in their formation which opposes some of the proposed formation mechanism models in literature which consider residual stresses as a contributor to the formation of the features [14, 140].

4.5.4 Material composition comparison (100Cr6 vs 50CrMo4)

It is interesting to compare the development of both DER and WEB in 50CrMo4 and 100Cr6 as shown in Figure 4.15, 4.11 and Figure 4.13, 4.4 which shows different patterns for both features. LAB development is significantly slower in the low carbon 50CrMo4 samples compared to the high carbon 100Cr6 (see in 4.17). The contrast in LAB density is best compared by observing Figure 4.13c and Figure 4.15d which were run under similar stress cycles. Previous studies have linked the LAB formation to carbon migration [14, 117, 134, 149, 150] and hence this would explain why the growth rate is greater in the 100Cr6 compared to the 50CrMo4 samples. The formation mechanism of LAB and HAB is investigated and compared in both alloys in Chapter 7 to understand the conditions leading to their initiation.

The DER in 50CrMo4 samples have well defined boundaries in contrast to the 100Cr6 samples in this study. Comparing the position of the DER from the earliest stage (Figure 4.12), it can be seen that the DER coincides with τ_0 similar to previous findings [82, 118]. The LAB however remain aligned with σ_{vM} and τ_{45} as previously discussed. It is interesting that each microstructural alteration (DER and WEB) are influenced by different stress

components and hence different formation mechanisms for each feature should be expected. This is further explored in Chapter 6 and Chapter 7.

Early stages of the DER in the 50CrMo4 samples (Figure 4.11a-d and Figure 4.15a-d) appears as dark heavily etched patches aligned with the τ_0 distribution (Figure 4.12). With the build-up of stress cycles, the DER grows in span across both upper and lower boundaries (see Figure 4.12 and Figure 4.15a-d). However, beyond the test duration of 2038 million cycles in this study, for the first time, a brightening mechanism is reported where the microstructure becomes brighter within the DER in the region coinciding with where the LAB first appears (Figure 4.11e,f and Figure 4.15e,f). A recent DER study in literature did show optical images of RCF-tested balls where a bright region can be seen within the DER but this was not highlighted or investigated further [174]. While it may be possible that previous studies have neglected this and assumed the DER is still 'expanding', this appears to be a part of the mirostructural transformation process of the DER and hence is investigated in detail in Chapter 6 to determine the conditions leading this variation in etching response. Given the DER brightening in the 50CrMo4 occurs at a similar stage where the LAB become pronounced (Figure 4.15e-f), this could explain the challenges in capturing the DER in the 100Cr6 samples under optical images which show LAB developing earlier i.e the dark appearance of the DER is prolonged in the 50CrMo4 sample compared to the 100Cr6 samples. This brightening towards the upper boundary of the DER (Figure 4.15e-f) at late stages (high stress cycles) while the lower boundary remains dark would explain the sickle shapes observed in the 100Cr6 samples in the axial cross section (Figure 4.4, 4.5, 4.7 and 4.8) which is similar to the latest stage of the 50CrMo4 sample (Figure 4.11f). Nonetheless, this indicates a correlation between the brightening of the DER and initiation of LAB. Findings in Chapter 6 and 7 have shown the brightening in the DER corresponding to a grain refinement mechanism where stress points developed within lead to the initiation of LAB.

4.5.5 LAB/HAB interaction and serial sectioning

The majority of WEB investigations in the literature is focused on LAB rather than HAB given the former develops earlier than the latter. Significant evidence in this study suggests the initiation of HAB stems from pre-existing LAB which is best shown in Figure 4.19 and later confirmed in Chapter 7. HAB initially appears in the material as conglomerates typically centred around the most dense LAB locations (Figure 4.19a) which is later reported to be correlated to the instability of the carbide structures of the dense closely-packed LAB (see Section 7.6 for more details). As the LAB saturates after sufficient stress cycles, HAB

become more evenly distributed resulting in a more uniform scatter of HAB across the subsurface (see in Figure 4.19b). When comparing the density vs depth of the LAB to the location of the HAB (see Figure 4.21), it is obvious the HAB are positioned near the upper boundary of the LAB where the LAB are most dense which confirms that HAB originates from dense LAB.

The growth of the HAB in relation to the LAB (see in Figure 4.17) shows a rapid escalation in HAB growth once the LAB saturation level is achieved. Looking at the structures of individual HAB (see Figure 4.24 and Figure 4.26), they are not as perfectly parallel plates as previously proposed [6, 63, 82], instead they vary in thickness and orientation across its length as shown in Figure 4.26. This suggests they are heavily influenced by local microstructural variations such as LAB density i.e proximity of individual bands. It is shown in Figure 4.26c under serial sectioning that individual white etching matter corresponding to individual LAB (Figure 4.26c2-4) grow at $\sim 80^{\circ}$ and join together leading to a single HAB shown in Figure 4.26c9. It can also be observed from Figure 4.26a5 that in some cases, HAB do not have a sharp smooth boundary (right edge of HAB), instead it appears the white etching matter of the HAB to be inclined towards LAB at the HAB boundary which affirms the relation between the two features. As mentioned in Figure 4.19a, the LAB density initially is not uniform as some local regions are denser than others. Given the HAB stems from such dense local areas, it is reasonable to assume the initial HAB growing would vary in thickness and orientations as it grows from dense LAB local areas to relatively less dense areas. While HAB that initiate later in the bearing life will grow under a more uniform LAB structure (Figure 4.19b) and hence may not fluctuate in dimensions and orientations as much. The HAB shown in Figure 4.26a had the largest span of all HAB observed through serial sectioning (red HAB in Figure 4.24) which suggests it may have initiated from the early stages to support this theory. Further examination of early stage and late stage HAB through scanning electron microscopy is conducted in upcoming chapters to further investigate the correlations found in this chapter and determine the conditions leading to the formation of both LAB and HAB.

Conducting the serial sectioning of the WEB network provides a full overview on the 3D structure of fully developed HAB compared to the LAB and inclusions within the same volume. While majority of literature report HAB to be generally longer [4, 5, 63, 79, 82, 120] the serial sectioning of fully developed HAB compared to multiple LAB has suggests that the average length of both bands to be similar, although the HAB is thicker on average and have a significantly larger span (see Table 4.1) which can exceed a third of the contact width. Based on the 3D dimensions of the LAB and HAB obtained from serial sectioning,

a simplified model of the WEB network is shown in Figure 4.27 to give a realistic overview on the WEB network, a schematic of the DER is also drawn based on the appearance of DER in both axial and circumferential cross sections.

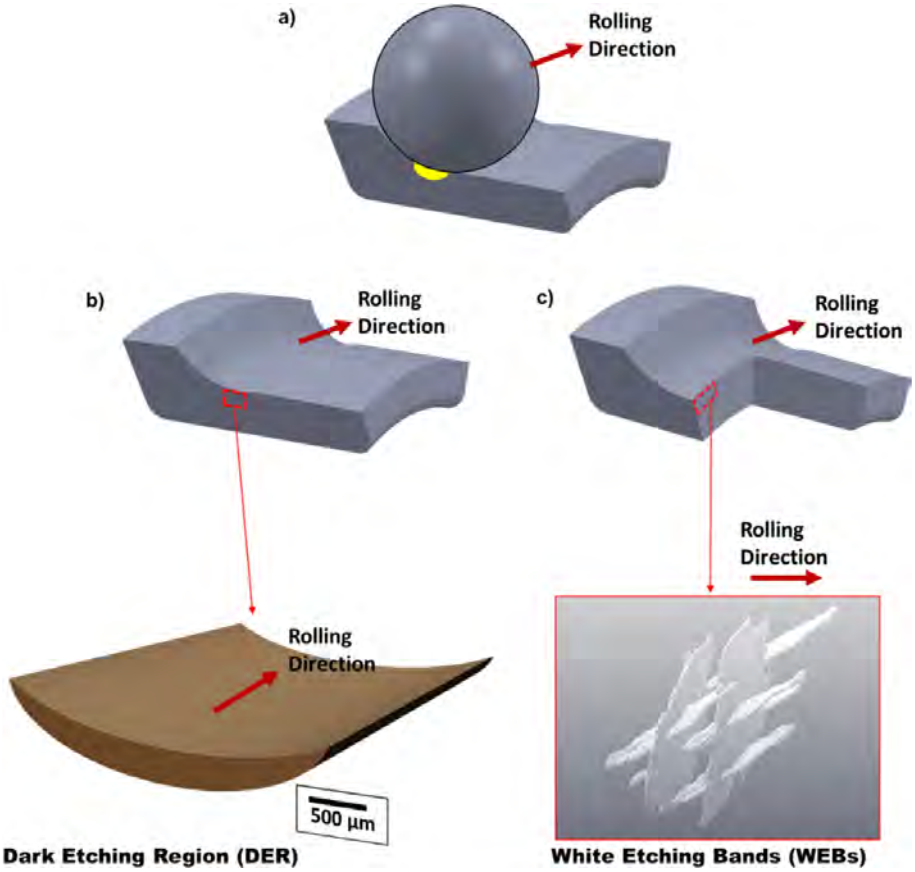

Figure 4.27: a) Position of ball and bearing inner ring and resulting stressed region (yellow) due to the contact ellipse. The 3D structure of b) DER and c) WEB (LAB and HAB) based on dimensions in Table 4.1 relative to their position in the bearing inner ring within the stressed region.

4.6 Conclusion

This chapter presents experimental characterization of the progression of DER, LAB and HAB throughout the bearing life under the influence of contact pressure, material, steel cleanliness and the influence of stresses on their formation. Based on the results presented in this chapter, the following conclusions are drawn:

- The position of WEB correlates well with the distribution of the principal shear stress and von Mises stress in all samples investigated, initiating in the maximum stress point and grows across the subsurface until the boundaries of the WEB saturates between 1500-2000 million stress cycles at depth position equivalent to a σ_{vM} threshold of 1300 MPa. No correlation is found between τ_0 and the WEB depth distribution.

- No correlation has been found between residual stress build-up in bearings during operation and the formation of DER/WEB.
- Increasing the contact pressure increases the region in which DER and WEB develop due to the corresponding subsurface stress distribution. It is also shown that WEB develop earlier in the bearing life under higher contact pressure.
- No variation in the growth pattern of DER and WEB is found when comparing bainitic and martensitic 100Cr6 microstructures while varying the steel cleanliness grade of martensitic 100Cr6 samples also showed no variation. Hence it is concluded inclusions have no role in the formation of the features.
- DER in 100Cr6 samples appear as a sickle shape in the axial cross section with only the lower edge of the DER visible while the full DER (upper and lower boundaries) is more pronounced in 50CrMo4 samples under similar cycles and is found to coincide with τ_0.
- As number of stress cycles increases, DER in 50CrMo4 initiates as dark patches that become more dense across the subsurface and covers a larger region in the subsurface (spread of upper and lower boundaries). However, with further increase in stress cycles, the DER becomes brighter in the region where LAB initiate. Brightening of the upper section of the DER results in a sickle DER shape in late stages of the 50CrMo4 samples where only the lower boundary region is visible, similar to observations in 100Cr6 samples. Hence the DER development stage is pro-longed in the 50CrMo4 samples compared to 100Cr6.
- LAB in 50CrMo4 samples develop at a significantly slower rate compared to 100Cr6 samples under similar stress cycles. No HAB have also been observed in 50CrMo4 samples due to the slower growth rate of the WEB.
- HAB growth rate is shown to increase rapidly once the saturation level of LAB is achieved. Serial sectioning has shown white etching matter develop from multiple individual LAB in the HAB orientation and later joins together to form a single HAB across pre-existing LAB. Evidence presented in this chapter confirms the initiation and growth of HAB is governed by the density of pre-existing LAB.
- 3D modelling of the WEB has shown the LAB to be thin parallel plates while the HAB in the axial cross section appear as irregular white blocks due to their thicker dimensions and orientation. Fully developed LAB show a similar length to HAB but a lower thickness and span in comparison.

Chapter 5

Semi-Empirical Model for WEB

This chapter introduces a semi-empirical model for predicting the formation of LAB and HAB under different contact pressures for 100Cr6 and 50CrMo4 bearing steel microstructures. Measurements of the $LAB\%$ and $HAB\%$ from Chapter 4 are utilised to develop the model in this chapter.

5.1 Quantification of LAB and HAB

100Cr6 (both martensite and bainite) and 50CrMo4 samples have been incorporated in the model in this chapter as input data to develop the semi empirical model. The quantification of both LAB and HAB was conducted by processing optical images using ImageJ to compare the area of the features in reference to a fixed area (see Figure 3.7). In this study, the fixed reference area captured by the LOM (667 µm x 860 µm) is used. The terms $LAB\%$ and $HAB\%$ which have been previously introduced in Figure 4.17 are defined as how much of the reference area is covered by LAB and HAB (see Equation 5.1 for $LAB\%$). An example is shown in Figure 5.1 where the measured area in Figure 5.1b consumed by LAB is 89,764 µm^2 and the total area is 586,960 µm^2 (667 x 880). This yields a $LAB\%$ value of 15.

$$LAB\% = \frac{LAB\ Area\ (black\ area)}{667\ \times\ 880} \times 100 \tag{5.1}$$

5.1.1 Saturation level

Based on findings from Chapter 4, the percentage of LAB formed in the bearing subsurface varies with contact pressure and stress cycles but always forms within a band of depths in the bearing inner ring subsurface within an upper and lower boundary coinciding with a 1300 MPa von Mises threshold as shown in Figure 5.2. The position of the upper and lower boundaries of the WEB are defined as y_1 and y_2 respectively and vary with the contact

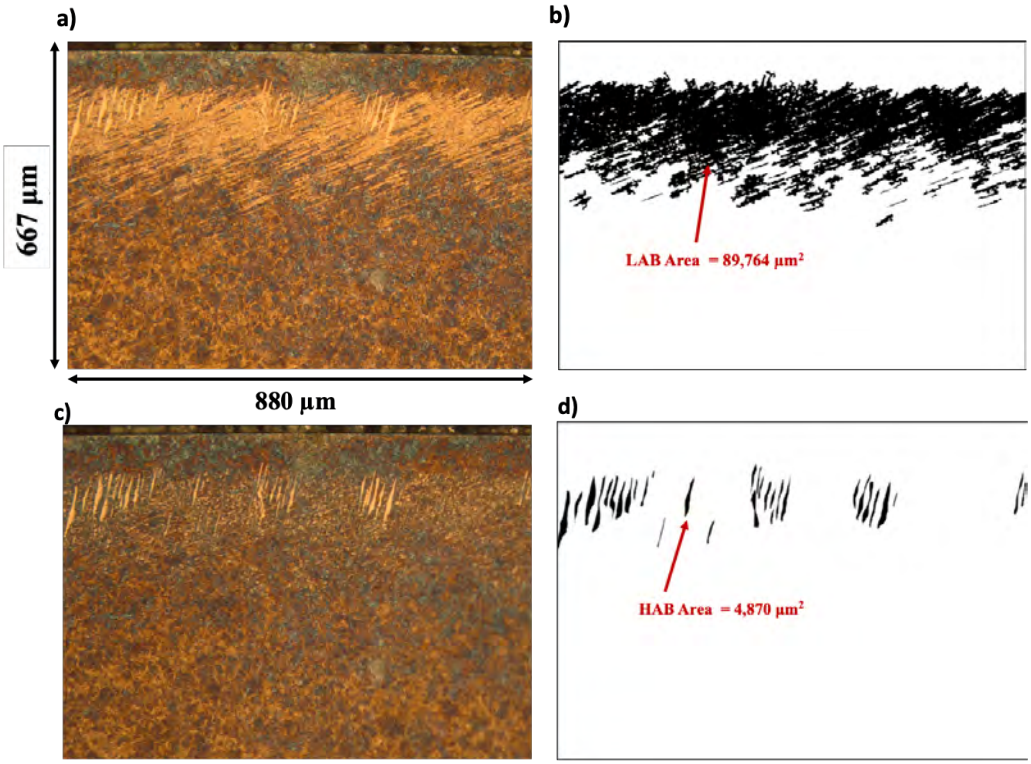

Figure 5.1: Optical image of a) LAB and b) HAB showing an area covered by LOM and image processed using ImageJ to measure the b) LAB area and d) HAB area. which is used to determine $LAB\%$ and $HAB\%$ Features from 100Cr6 martensite sample at 3016 million cycles under 2.9 GPa

pressure. This can be calculated by the corresponding von Mises distribution. The $LAB\%$ is found to reach a saturation level after sufficient number of cycles, this appears to be around 15 for the 100Cr6 under 2.9 GPa and is achieved after approximately 1700 million cycles (as shown in Figure 4.17). This percentage is thus referred to as the LAB saturation level, $LAB\%_{sat}$ and is employed in Equation 5.2.

Although a similar $LAB\%$ growth trend is observed in samples tested under 3.5 GPa, a LAB saturation is not reached due to the relatively low number of stress cycles experienced (See Figure 4.17). Nonetheless, the $LAB\%_{sat}$ can be calculated for samples tested under 3.5 GPa based on the threshold zone depth boundaries in which the WEB form. As shown in Figure 5.2c, the threshold zone (highlighted in red) is determined based on the von Mises stress.

When comparing the area of LAB in the sample relative to the threshold zone (880 x (y_2 - y_1)) rather than to the full optical image area (880 x 667), the maximum area of LAB achieved during the saturation level mentioned earlier is found to be equivalent to 48% of this threshold zone (Equation 5.3). Under different contact pressures, due to the variation in von Mises stress the material is subject to, the maximum area of the LAB varies however the percentage in the threshold zone is considered to remain the same as that under 2.9

GPa (48%) . Hence utilising Equation 5.2 and Equation 5.3 , the $LAB\%_{sat}$ is estimated to be 28 for the samples tested under 3.5 GPa as the corresponding (y_2 - y_1) is 390 µm.

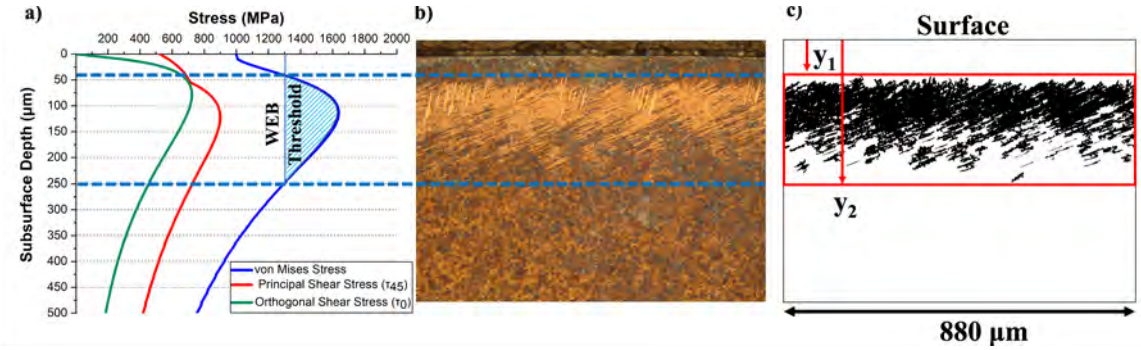

Figure 5.2: a) Subsurface stress distribution of ACBB samples under 2.9 GPa. b) Boundaries of WEB in 100Cr6 martensite (cleanliness B) run for 3016 million cycles under 2.9 GPa which is considered at the saturation stage. c) Threshold zone highlighted in red which the WEB form within.

$$LAB\%_{sat} = \frac{Maximum\ LAB\ Area}{667\ \times\ 880} \times 100 \tag{5.2}$$

$$Maximum\ LAB\ Area = 0.48 \times (y_2 - y_1) \times 880 \tag{5.3}$$

The quantification of the $LAB\%$ under different stress cycles (experimentally) and determining the $LAB\%_{sat}$ through Equation 5.2 and Equation 5.3 under each contact pressure, the LAB evolution from the initiation point to the saturation point can be modelled as shown in the following section.

5.2 Modelling WEB formation

Based on the experimental data points obtained for the 100Cr6 samples, a curve fitting is applied to derive the relationship between LAB density ($LAB\%$) and stress cycles under 2.9 GPa and 3.5GPa. According to previous models [6, 150], carbon atom migration and diffusion follows a sigmoidal pattern, and this was found to agree with the experimental data well as shown in Figure 5.3 using the standard Boltzmann curve fitting equation shown in Equation 5.4. The sigmoidal pattern derived from the experimental results is a typical relationship for diffusion processes. In Equation 5.4, x is the number of stress cycles, A_2 is the LAB saturation level ($LAB\%_{sat}$), x_0 is the number of cycles required to reach half of the LAB saturation level and A_1 is an offset value to start the curve from 0, i.e. no LAB at the start of the RCF test. The value of dx is a time constant dependent on the linear slope m of the curve at x=x_0 as shown in Equation 5.5.

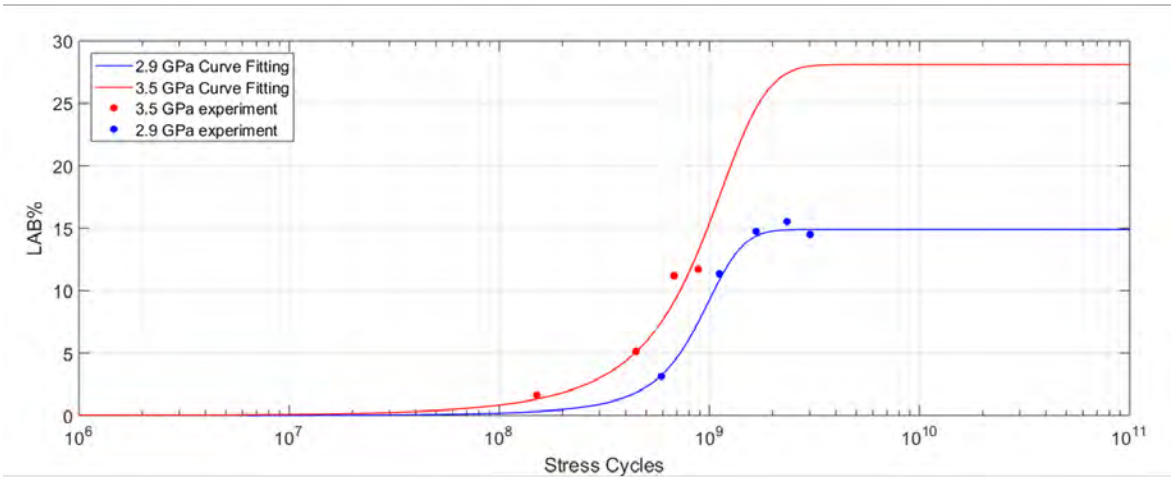

Figure 5.3: LAB density ($LAB\%$) evolution curve fitting as a sigmoidal pattern with stress cycles for 2.9 GPa and 3.5 GPa for 100Cr6 martensitic samples.

$$LAB\% = \frac{A_1 - A_2}{1 + e^{(\frac{x - x_0}{dx})}} + A_2 \tag{5.4}$$

$$dx = \frac{A_2 - A_1}{4m} \tag{5.5}$$

The curve fitting data for the 2.9 GPa and 3.5 GPa samples have been obtained using Origin 2018b and the constants for the 100Cr6 martensitic samples as well as those for intermediate contact pressures are given in Table 5.1 where the intermediate values have been calculated through regression analysis. Firstly, $LAB\%_{sat}$ (A_2) is calculated using Equation 5.2 and 5.3 for each contact pressure. Using the curves obtained from the samples under 2.9 GPa and 3.5 GPa and their corresponding constants, x_0 and dx are then determined directly through regression analysis as a function of contact pressure (Appendix C). Finally, the offset value A_1 is determined by applying the initial condition $LAB\%$=0 when x=0 to Equation 5.4.

Table 5.1: Calculated constants for the determination of the LAB density curve fitting under contact pressures between 2.9 GPa and 3.5 GPa based on logarithmic regression for 100Cr6 bearing steel samples.

Contact Pressure (GPa)	x_0	dx	A_2	A_1
2.9	8.71E+08	2.40E+08	15	-0.41
3	8.67E+08	2.61E+08	18	-0.65
3.1	8.63E+08	2.83E+08	20	-0.95
3.2	8.59E+08	3.08E+08	22	-1.35
3.3	8.55E+08	3.35E+08	24	-1.87
3.4	8.51E+08	3.64E+08	26	-2.50
3.5	8.47E+08	3.95E+08	28	-3.28

While there are various regression methods available providing a variety of curve

fittings for the pressures between 2.9 GPa and 3.5 GPa, based on a recent study that has demonstrated how the LAB initiation point varies with contact pressure [150], where a logarithmic curve fitting was established, the same approach (detailed in Appendix C) is taken to determine the value of x_0 and dx for pressures other than 2.9 GPa and 3.5 GPa. A plot of the obtained curve fittings including intermediate pressures between 2.9 GPa and 3.5 GPa is shown in Figure 5.4. Similar to Fu et al. [150], an arbitrary value of $LAB\%$=1 is selected as the LAB 'initiation' point (see Figure 5.4), where the density of the LAB becomes significant enough to be observed under LOM. Although this has shown to be much earlier than that predicted based on the experimental observations in this study (discussed in detail in the following section), it provides a prediction compatible to other theoretical models [150].

Significant evidence accumulated suggests HAB form from pre-existing dense and closely-packed LAB (Findings from Chapter 4). According to experimental findings, the earliest HAB formed is in 100Cr6 bainite sample run under 2.9 GPa for 897 million cycles , which corresponds to a $LAB\%$ of 8% (Figure 4.17). No sample with a lower $LAB\%$ has shown to have developed HAB in this study (including all materials), hence it is modelled to predict HAB initiation based on the curve fittings in Figure 5.4, where the number of cycles required to initiate HAB is when the curve reaches $LAB\%$=8%. According to the data points obtained in Figure 4.17, the highest $LAB\%$ (=5%) without HAB is the 100Cr6 martensitic sample tested for 447 million cycles under 3.5 GPa. Therefore, it is likely that the actual HAB initiation point lies between $LAB\%$ of 5-8%. Since 8% LAB is a confirmed result, it is used to predict the initiation of HAB as shown in Figure 5.4. Given the data range in this study lies between 2.9-3.5 GPa, the curves calculated have been limited to pressures within this range but may be extrapolated beyond this which is discussed later.

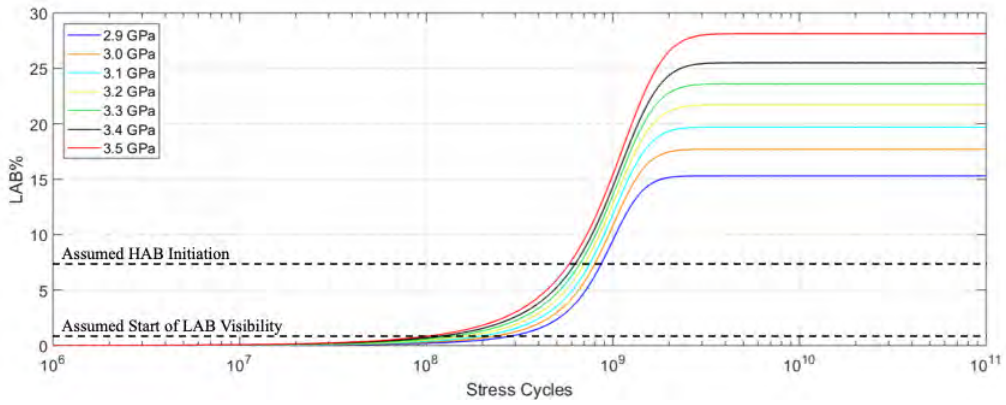

Figure 5.4: $LAB\%$ variation with stress cycles under contact pressure between 2.9 GPa and 3.5 GPa (100Cr6) using the evolution modelling showing the initiation of LAB visibility in the subsurface when $LAB\%$=1 and HAB initiation when $LAB\%$=8.

Based on the experimental data points for 50CrMo4 samples under 2.9 GPa shown in Figure 4.17, the same approach is implemented to model this material's LAB evolution, considering $LAB\%_{sat}$ to be the same as 100Cr6 samples (for same contact pressure). As shown in Figure 5.5, a different prediction from that of the 100Cr6 is obtained, i.e. due to the significantly lower growth rate of LAB in this material, both initiation and saturation of the LAB is predicted to occur after much more number of stress cycles for the lower carbon steel. As discussed earlier, due to the similar behaviour of bainite and martesnite samples in terms of LAB development (Figure 4.17), the WEB evolution in the 100Cr6 bainite would have the same curve fitting as the martensite samples (see Figure 5.6 for comparison). Optical images of 100Cr6 martesnite and bainite samples under similar stress cycles in Figure 5.6b-e show how comparable the growth rate of LAB are for both microstructures.

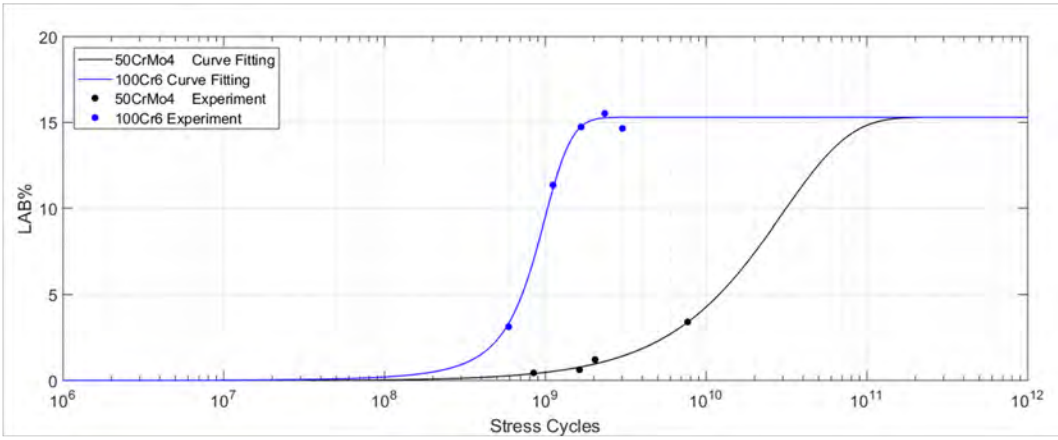

Figure 5.5: LAB density evolution curve fitting as a sigmoidal pattern with stress cycles under 2.9 GPa for 100Cr6 and 50CrMo4 bearing samples.

To summarise, the semi-empirical model proposed in this chapter is based on the following assumptions:

- The depth boundaries of saturated WEB are defined by the depths of the corresponding 1300 MPa von Mises threshold.
- At saturation, $LAB\%$ reaches 48% of the area defined by the 1300 MPa threshold.
- HAB formation is dependent on pre-existing LAB and HAB initiation is assumed when $LAB\%$ reaches 8%.

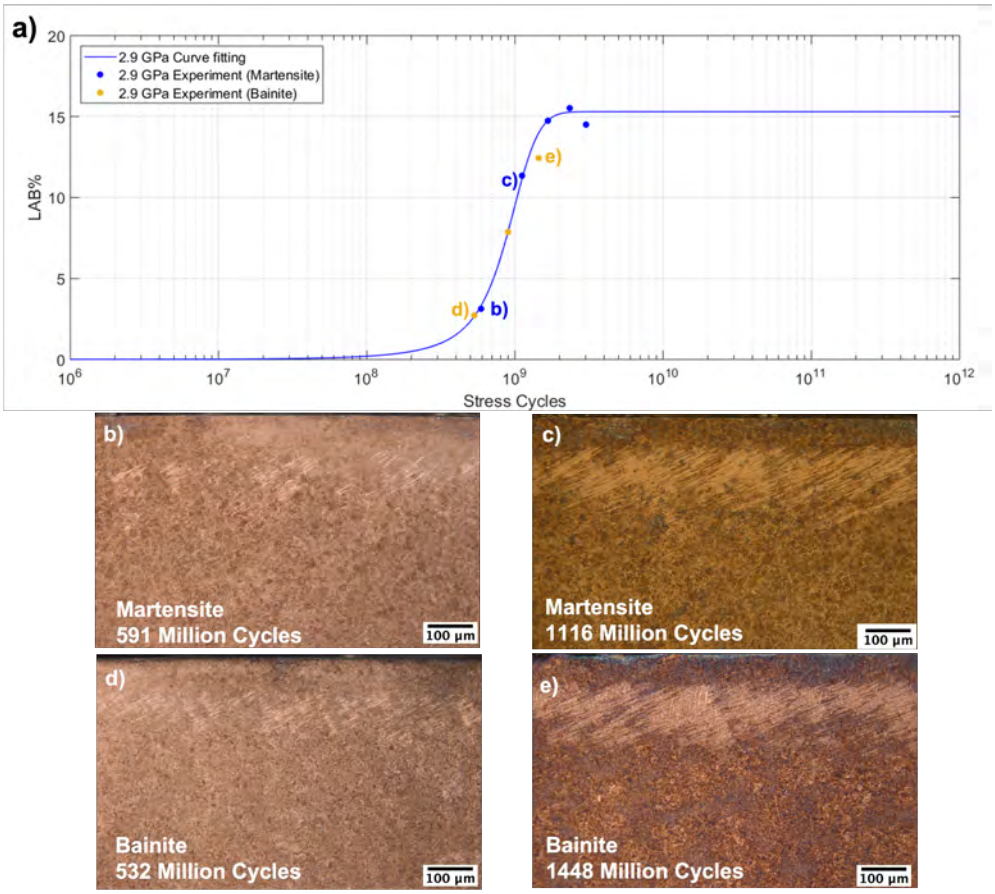

Figure 5.6: A curve fitting and experimental data for 100Cr6 martensitic samples at 2.9 GPa compared to experimental data for 100Cr6 bainite samples under 2.9 GPa. b,c,d,e) Optical images of LAB from martesnite and bainite 100Cr6 samples recorded in a).

5.3 Discussion

WEB have been reported to consist of ferrite grains (equiaxed and elongated grains) and lenticular carbides that form adjacent to the bands [120]. However, the 'white' constituents in WEB have remained undefined in literature. The comparison between LOM and SEM images of LAB and HAB in the 100Cr6 martensite sample (etched surfaces) tested for 679 million cycles under 3.5 GPa is shown in Figure 5.7. It can be seen that the white area is associated mainly with the equiaxed ferrite grains (red arrows) in the WEB while the lenticular carbides (yellow arrow) and adjacent elongated grains appear dark in the LOM images. However, the appearance of the white or dark color of the LCs may be different when the direction of the polarised light is adjusted under the optical microscope.

Nital is expected to attack the relatively soft equiaxed ferrite structure and ferrite-cementite grain boundaries [4, 149] which has caused confusion toward why the reflectivity of the equiaxed ferrite gives a white appearance whereas ferrite grains in DER give a darker appearance under a similar etching process. Grain size may play a critical role in increasing etching resistance of the WEB ferrite but it remains unclear in literature. The etching

response of the different constituents is discussed further in Chapter 6 and Chapter 7. Based on the findings from this work, the modelling has been based on the white area in LAB and HAB that is attributed to the ferrite grains formed in the steel microstructure as opposed to other models [6, 14, 117, 150] based on the thickening of LC adjacent to individual LAB due to carbon diffusion.

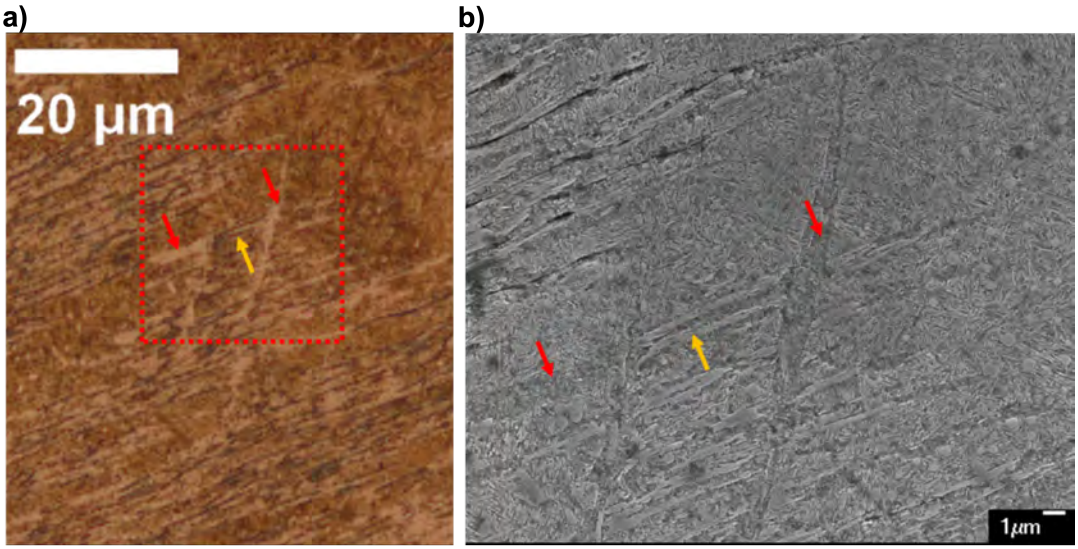

Figure 5.7: a) An optical image of an etched 100Cr6 martensite sample tested under 3.5 GPa over 679 million cycles, showing white bands (both LAB and HAB) formed in the sample. b) The corresponding SEM image showing the area highlighted in red square of the optical image to show the LC (yellow arrow) and equiaxed ferrite (red arrow) in both images.

The most recent model for microstructural alterations by Fu et al. [150] is based on thickening of nano-sized tempered carbides for DER and on thickening of LCs for LAB where the evolution of the LC thickness over stress cycles follows a sigmoidal pattern similar to that of the LAB ferrite area growth in this study. Different from the modelling of carbide thickening of individual bands in most literature, a semi-empirical model based on the overall white etched areas growth in WEB is proposed from this study. Nonetheless, the growth of white etched areas in the LAB may be proportional to the dislocation-assisted carbon migration causing the carbide thickening, leading to the similar prediction patterns from both approaches.

The semi-empirical model from this study is presented in Figure 5.8 compared to that established from the LC thickening model proposed by Fu et al. [150] using operating conditions of this study under 2.9 GPa. The semi empirical model in this study shows that LAB form much earlier than that predicted by Fu's model. This finding can be expected since the semi-empirical model prediction is based on the measurement of the white etched areas of the WEB i.e the equiaxed ferrite formation while Fu's model focuses on the formation of LCs. It is expected the equiaxed ferrite region (white area) to form prior

to LCs. The carbon migration in the material (resulting from either dislocation gliding or diffusion of free carbon) contributes to the nucleation and thickening of LCs. This carbon migration is a consequence of the inability of the ferrite grains (associated with the LAB) to dissolve the excess carbon from the parent matrix (carbon solubility in ferrite is 0.02wt%). Therefore, it is plausible to assume prior to the formation of LCs, there exists a LAB which is purely ferrite supersaturated with carbon. This excess carbon later migrates to form LCs. This is confirmed later in Chapter 7 by analysing the different development stages of LAB under a range of characterization techniques. This is also supported by the comparison between the LC thickening model [150] and the semi-empirical model of this study with the latter predicting earlier LAB formation than the former. The sigmoidal pattern established in this study and by Fu et al. [150] suggests the WEB formation mechanism is driven by a diffusion process. Nonetheless, the variation in the curve distribution between the two studies leads to uncertainties in the proposed driver for WEB formation in literature.

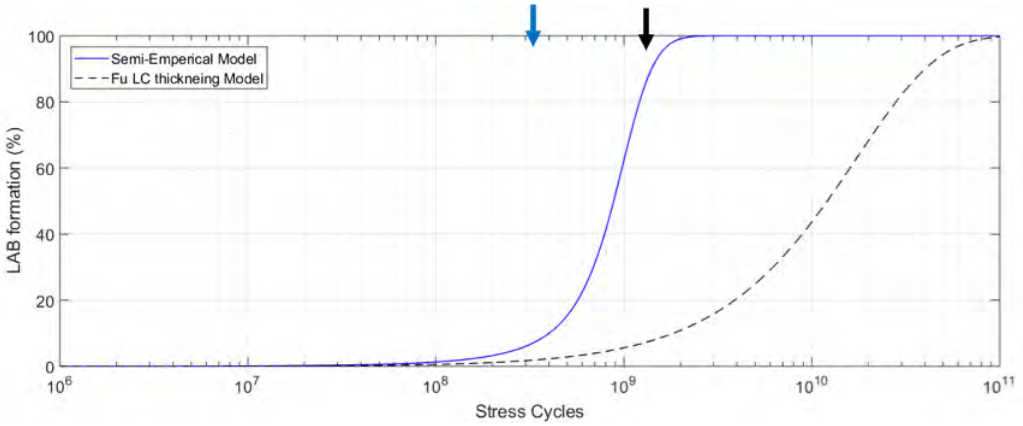

Figure 5.8: A comparison of the LAB prediction models between the semi-empirical model from this study and the model by Fu et al. based on LC thickening [150] under 2.9 GPa (normalized to 0 – 100% LAB). Blue and black arrow shows the LAB initiation point based on the semi-empirical modal in this study and the LC thickening model respectively.

Given the nature of a sigmoidal curve, i.e. no definitive point for approaching 0% LAB, Fu et al. [150] took an arbitrary value of 1% of the number of cycles for the curve to fully saturate as the LAB initiation point i.e. at 1.2 x 10^9 stress cycles (see black arrow in Figure 5.8). This predicted initiation point is much later than that predicted by the semi-empirical model (3.15 x 10^8) which has been demonstrated by experimental observations. Two samples in this study, tested for 5.91 x 10^8 and 1.116 x 10^9 stress cycles (prior to the initiation point proposed in [150]) have developed LAB as shown in Figure 4.17.

A similar comparison is made for the higher contact pressure under 3.5 GPa (Figure 5.9). Although the two curves are closer, the model by Fu et al. still predicts LAB initiation later than the semi-empirical model from this study, i.e. 1.2 x 10^8 cycles vs. 2.6 x 10^8 cycles, due to similar reasons as discussed previously. However under high contact pressure, the migration

of carbon driven by dislocations would be more rapid thus the two curves become closer. A comparison of the LAB initiation predictions under a range of contact pressures made by the semi-empirical model and Fu's model is presented in Figure 5.10. Fu's hypothesis arbitrarily assumes the initiation point as 1% of the stress cycles required to reach LAB saturation. The semi-empirical model differs as it predicts the point when the $LAB\%$ is 1% (i.e. certain LAB area is achieved) is the LAB initiation and this is calculated from the sigmoidal fitting, this has been taken as this is practically where LAB can be distinguished from the surrounding microstructure under LOM. Although still not definitive, it has been demonstrated by experimental observations. The actual initiation point might be even earlier considering the initiation of LAB is caused by nano to micro-size cellular ferrite grain formation. The sigmoidal relationship obtained from the experimental data in this study supports a diffusion mechanism leading to WEB formation. Under this process, there is no definitive point when the features initiate therefore it is only when the features become sufficiently developed that it can be seen (assumed when $LAB\%$ is 1%).

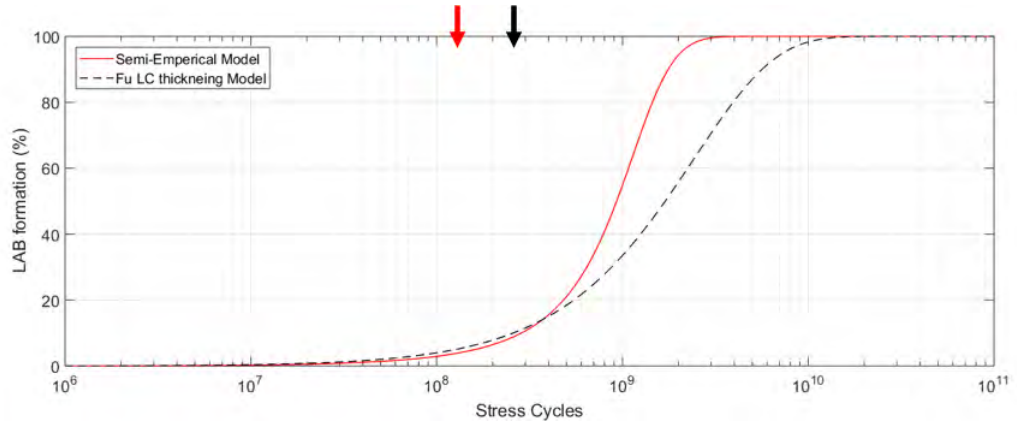

Figure 5.9: A comparison of the LAB prediction models between the semi-empirical model from this study and the model by Fu et al based on LC thickening [150] under 3.5 GPa (normalized to 0 – 100% LAB). red and black arrow shows the LAB initiation point based on the semi-empirical modal in this study and the LC thickening model respectively.

It has been previously proposed in literature that a contact pressure of 2.5 GPa (approximate shakedown limit of 100Cr6 [90]) is the threshold pressure for the formation of microstructural alterations (DER and WEB). This suggests the initiation curve shown in Figure 5.10 would approach asymptotically at a contact pressure of 2.5 GPa. This is not observed in the LAB prediction curve from the semi-empirical model due to the regression analysis limitation of the data range between 2.9 -3.5 GPa being extrapolated to 2.5-4 GPa. However, there is limited experimental studies available in literature examining WEB at low contact pressures to further investigate.

Although no prediction models have been established in literature, it is generally agreed that HAB form after LAB [47, 79, 82, 111, 127, 139, 147]. The experimental results in

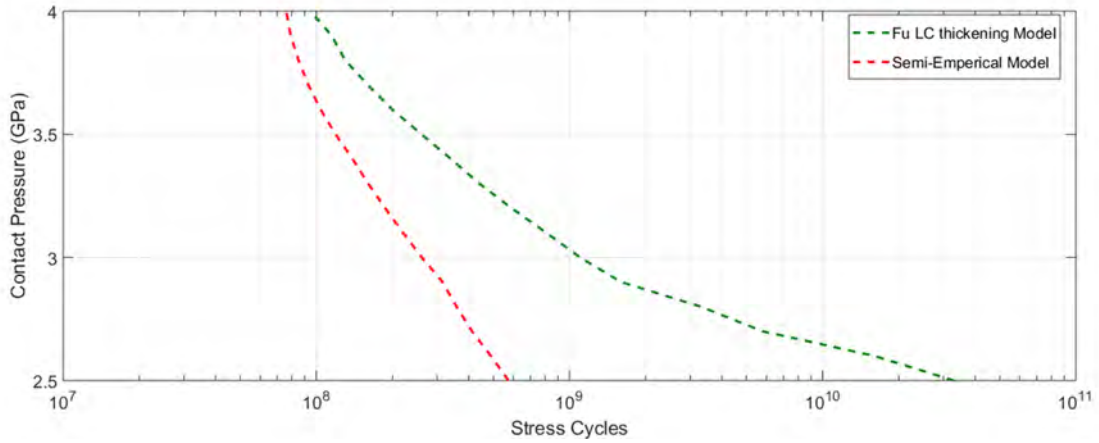

Figure 5.10: A comparison of the LAB initiation predictions made by the semi-empirical model and Fu's model [150] under a range of contact pressures.

this study show that HAB form when $LAB\%$ reaches 8%, which has been therefore used to predict HAB formation. Given that $LAB\%$ in 50CrMo4 samples (even the late stages) remain under 5%, this would explain why no HAB were observed in all 50CrMo4 samples. Figure 5.11 shows an overview of the LAB and HAB prediction curves for 100Cr6 based on the semi-empirical models developed compared to both experimental data points from this study and those from literature. It is demonstrated that the models have accurately predicted both LAB and HAB formation in 100Cr6 bearing steels in the majority of cases despite the uncertainties on their operating conditions and material heat treatment. Since the models are based on constant operating temperature and bearing rotating speed, their influence on LAB and HAB formation are not considered in these models.

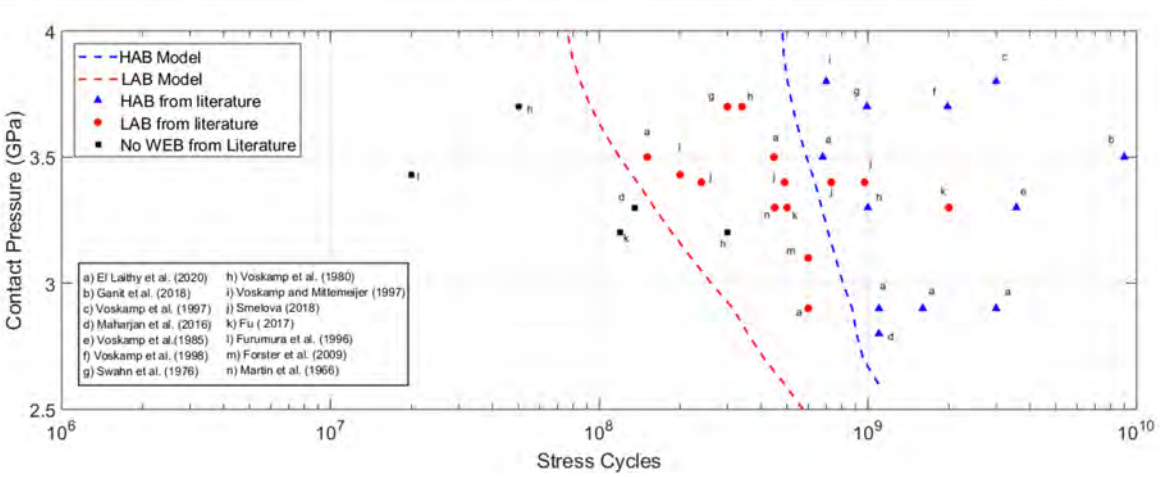

Figure 5.11: Predictions of LAB and HAB initiation based on the semi-empirical models developed in this study incorporating experimental LAB and HAB formation results from literature. Note: points marked as 'no WEB' indicates RCF tests did not result in WEB but some have had DER formed.

As discussed earlier, the bainite 100Cr6 performs similarly to the martensite

microstructure hence same models can be applied for both microstructures. Given that the low carbon steel (50CrMo4) showed a delayed WEB formation and growth compared with the 100Cr6 steel, a different prediction model is applied for each material. It it thus apparent that lowering the carbon content in the steel may significantly delay the formation of LAB due to reduction of the driving force in the material for carbon diffusion and LC thickening which consequently impedes HAB formation.

Furthermore, a comparison between literature experimental data and the semi-empirical predictive model under a certain contact pressure (3.3 GPa) is made, where the WEB formation progress model is compared in terms of the upper and lower boundaries of the WEB region. Using the y_1 and y_2 boundaries (defined by the relevant von Mises stress as described previously) as the maximum width of the WEB ($y_2 - y_1$) and comparing this to the WEB boundaries reported in literature at different cycles. The data points shown in Figure 5.12 indicate the reported WEB width as a percentage of the maximum width ($y_2 - y_1$). One of the data point in the graph shows 0% from Maharjan et al. [139] as no WEB was found to have formed under the designated conditions. It can be seen that the model has closely predicted the WEB formations under this contact pressure. The deviation observed may be attribute to the small variations from the experimental conditions, e.g. Martin et al. [79] and Swahn et al. [82] used a relatively lower operating temperature of 50 °C while the model is based on the 80 °C tests in this study. Also Fu et al. [124] tested a material with a significantly higher heat treatment (time and temperature) hence the material was softer than that in this study which may have an impact on the formation of the features.

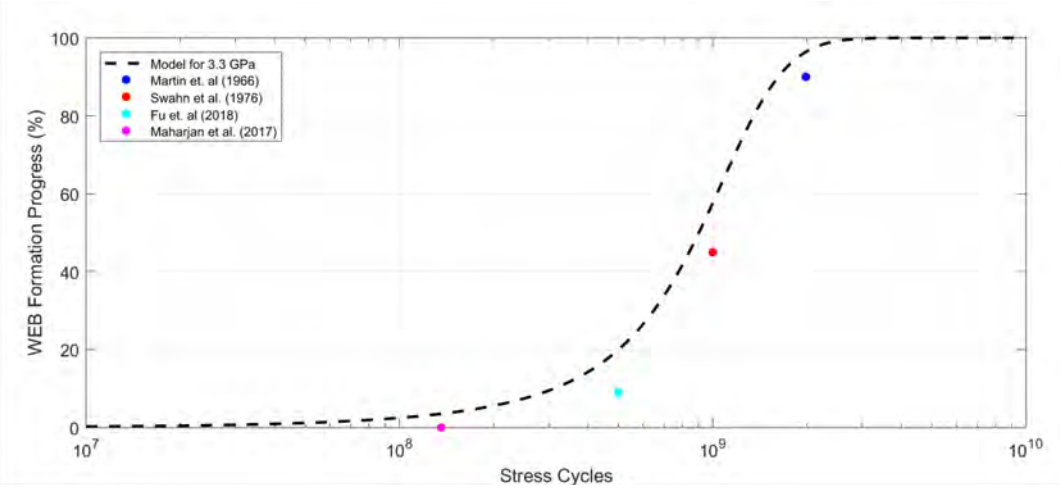

Figure 5.12: WEB formation progress from literature given as a percentage of the developed WEB within the full WEB saturation region expected is compared to the normalized $LAB\%$ evolution curve from the semi-empirical model under 3.3 GPa.

5.4 Conclusion

A large amount of experimental data obtained from the investigation of WEB formation in bearing steels provides a unique opportunity for developing a predictive model for WEB (both LAB and HAB) in this study.

Based on the density of LAB and HAB formed in the bearing steels under different contact pressures over a range of stress cycles, semi-empirical models have been proposed to predict the initiation and evolution of LAB and HAB for martensitic and bainitic 100Cr6, as well as a low carbon steel 50CrMo4, under contact pressures ranging from 2.9 GPa to 3.5 GPa. This is achieved by quantifying the area covered by the WEB network at different stages over hundreds on microns of the material subsurface, which provides a more practical overview of the material response during RCF on a global scale compared to previous models comparing the thickness of individual bands at a local scale. This study has successfully modelled the WEB features and establishing a link between LAB and HAB. The models have shown to agree extremely well with other experimental data from literature. Key conclusions from this study have been summarised below.

- Data points in this study show the growth of LAB to follow a sigmoidal pattern fitted using a Boltzmann curve fitting. The growth pattern supports the theory that WEB formation is driven by a diffusion process. However, the driver of the process may be different to the dislocation gliding model proposed in literature due to the difference in growth pattern compared to this study.

- A unified method of measuring WEB density based on von Mises stress threshold at 1300 MPa is introduced to quantify the evolution of LAB and HAB on a global scale as opposed to the LC thickness used in other models.

- A semi-empirical model based on the $LAB\%$ vs. stress cycles under a contact pressure of 2.9 GPa and 3.5 GPa is proposed to predict LAB evolution under other pressures within this range. Based on the assumption of 1% LAB is observable under LOM, initiation of LAB (when they can be seen under LOM) can also be predicted. The established model can hence predict the initiation and growth of LAB under different contact pressures and stress cycles. The model has shown to agree very well with experimental data from literature.

- Based on experimental findings that 8% LAB (area of LAB relative to a fixed reference area) would promote initiation of HAB, a semi-empirical model is established to predict the initiation of HAB over the contact pressure range of 2.9 and 3.5 GPa.

- The evolution of WEB vs stress cycles has been shown to be very similar for martensitic and bainitic 100Cr6 while the low carbon 50CrMo4 shows a significant delay in WEB formation.

Chapter 6

Mechanistic Study of DER

Following the study of the development of DER in the RCF-tested bearings in Chapter 4, this chapter focuses on investigating the formation mechanism of DER through detailed microstructural analysis. Due to its extended formation stages in martensitic 50CrMo4 and 100Cr6 bearings, the analysis on DER focuses on these two materials.

6.1 Optical Microscopy Observations

The development of DER in both 50CrMo4 and 100Cr6 over a range of stress cycles has been presented in Chapter 4 showing significant differences observed in the two steels. In 100Cr6, the samples have shown much more developed stages of WEB while the DER appeared as a sickle shape from the earliest stages recorded (591 million cycles) to the latest (3016 million cycles). In the circumferential cross section, the DER was shown to be challenging to capture which was found below the WEB (deeper in the subsurface), see details in Figure 4.3. However, DER in 50CrMo4 doesn't show that sickle shape observed like in 100Cr6 initially but appeared in the much later stage shown in Figure 4.11. The circumferential cross section of the 50CrMo4 samples best shows the recorded transformation of DER with stress cycles (Figure 4.15). It can be seen in the latest stages (2038 and 7668 million cycles in Figure 4.15e) and f) respectively) as the LAB becomes more distinguishable, the surrounding region which was initially within the DER, becomes 'brighter' while the lower boundary of the DER (at the lower boundary of the LAB), remains 'dark' under optical image. This observation would explain the sickle shape observed in the axial cross section of 100Cr6 samples and the 50CrMo4 samples at late stages. A comparison between 50CrMo4 and 100Cr6 microstructures under similar stress cycles and contact pressure (2.9 GPa) is shown in Figure 6.1. It can be seen than in 100Cr6, the WEB is heavily developed in the subsurface while the 50CrMo4 shows a developed DER stage which is heavily etched compared to the surrounding microstructure and hence, appears uniformly dark under optical microscopy.

The latest stage of the 50CrMo4 with the highest stress cycles in Figure 6.2 shows the DER area to be significantly brighter as the LAB become more developed (Figure 6.2b) while below the lower boundary of the LAB shows remains of the DER with a darker appearance. In Figure 6.2c, the same area shown in Figure 6.2b is over-etched to demonstrate the bright areas of the DER resisting etching compared to the surrounding region.

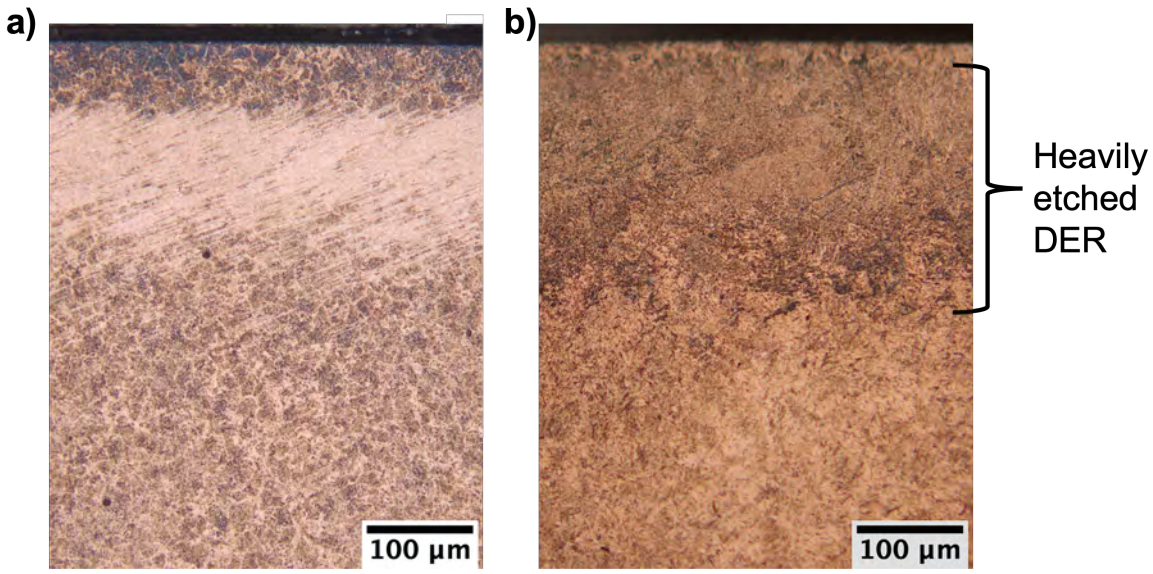

Figure 6.1: Subsurface of a) 100Cr6 bearing sample run under 2.9 GPa for 1689 million cycles showing developed WEB and b) 50CrMo4 bearing sample run under 2.9 GPa for 1626 million cycles showing developed DER which is evenly etched heavily.

Based on this observation, it appears that a similar mechanism of DER transformation occurs in both 100Cr6 and 50CrMo4 samples (see Figure 4.4, Figure 4.11e and 4.11f). However, this appears to occur much earlier in the bearing life of 100Cr6 compared to 50CrMo4. The earliest stage of 100Cr6 samples already shows the sickle shape DER while early stages of the 50CrMo4 shows the DER consisting of small dark patches which grows in size with stress cycles and becomes evenly distributed across the contact region until a transformation causing a section of the DER to become brighter which exists in the region where LAB develops.

In the next section, the DER structure is investigated using SEM to capture the transformation from early to late stage and compare the bright and darker areas observed in within the DER.

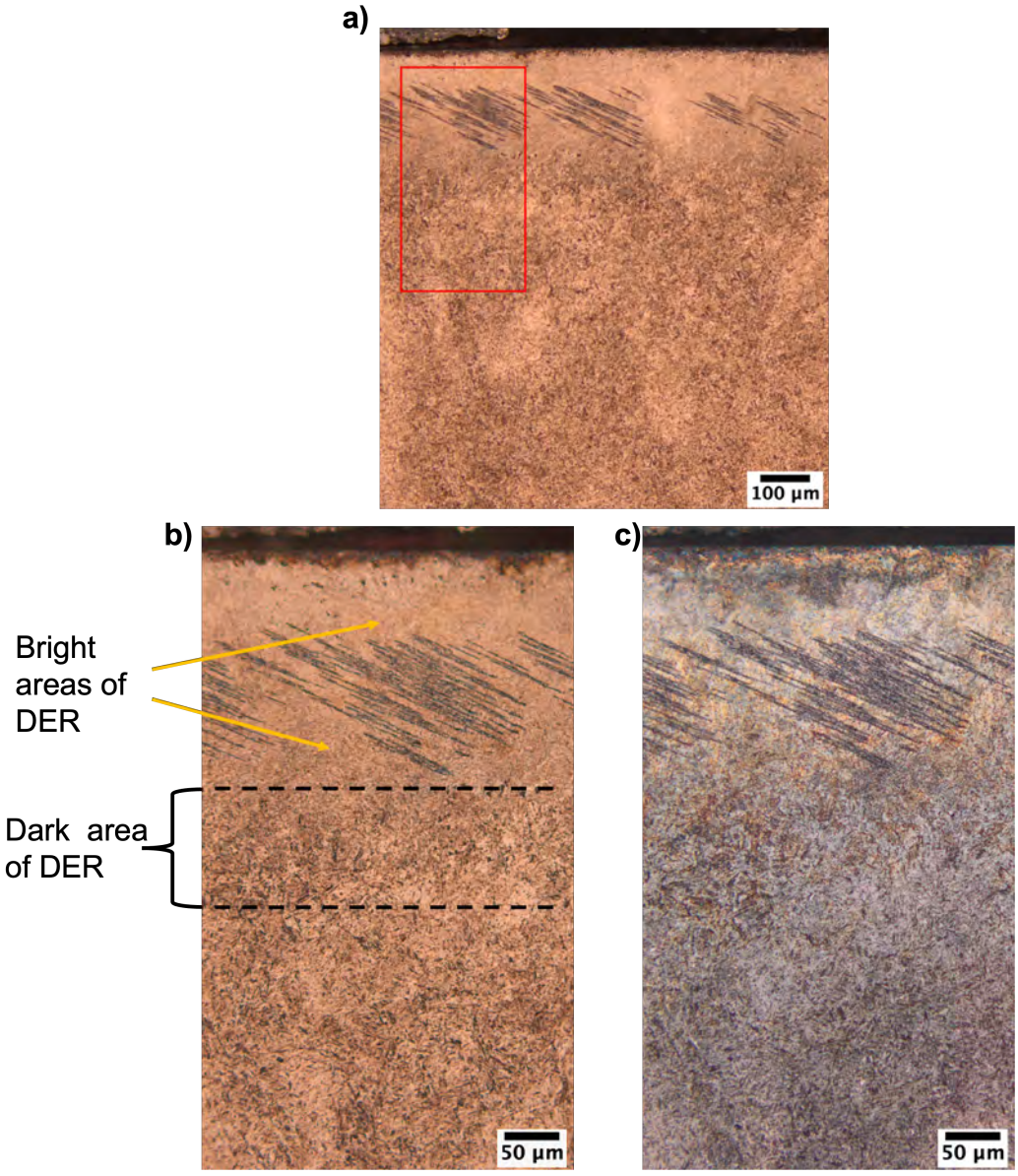

Figure 6.2: a) large scale image of late stage 50CrMo4 sample run under 2.9 GPa for 7668 million cycles showing bright areas surrounding LAB and darker areas of the DER below the lower boundary of the LAB. b) higher magnification of area highlighted in a) to show distinction between the brighter and darker areas of the DER. c) over-etch of area shown in b) indicating the brighter areas of the DER to resist etching.

6.2 SEM Analysis

The virgin samples of both bearing steels have been studied under optical microscopy and SEM as shown in Figure 6.3 to compare with the DER features developing in the RCF-tested samples. The 100Cr6 microstructure consists of martensite plates and randomly distributed spherical primary carbides while 50CrMo4 microstructure shows more of martensite lath mircostructure while no primary carbides are observed due to the low carbon content of the material [184].

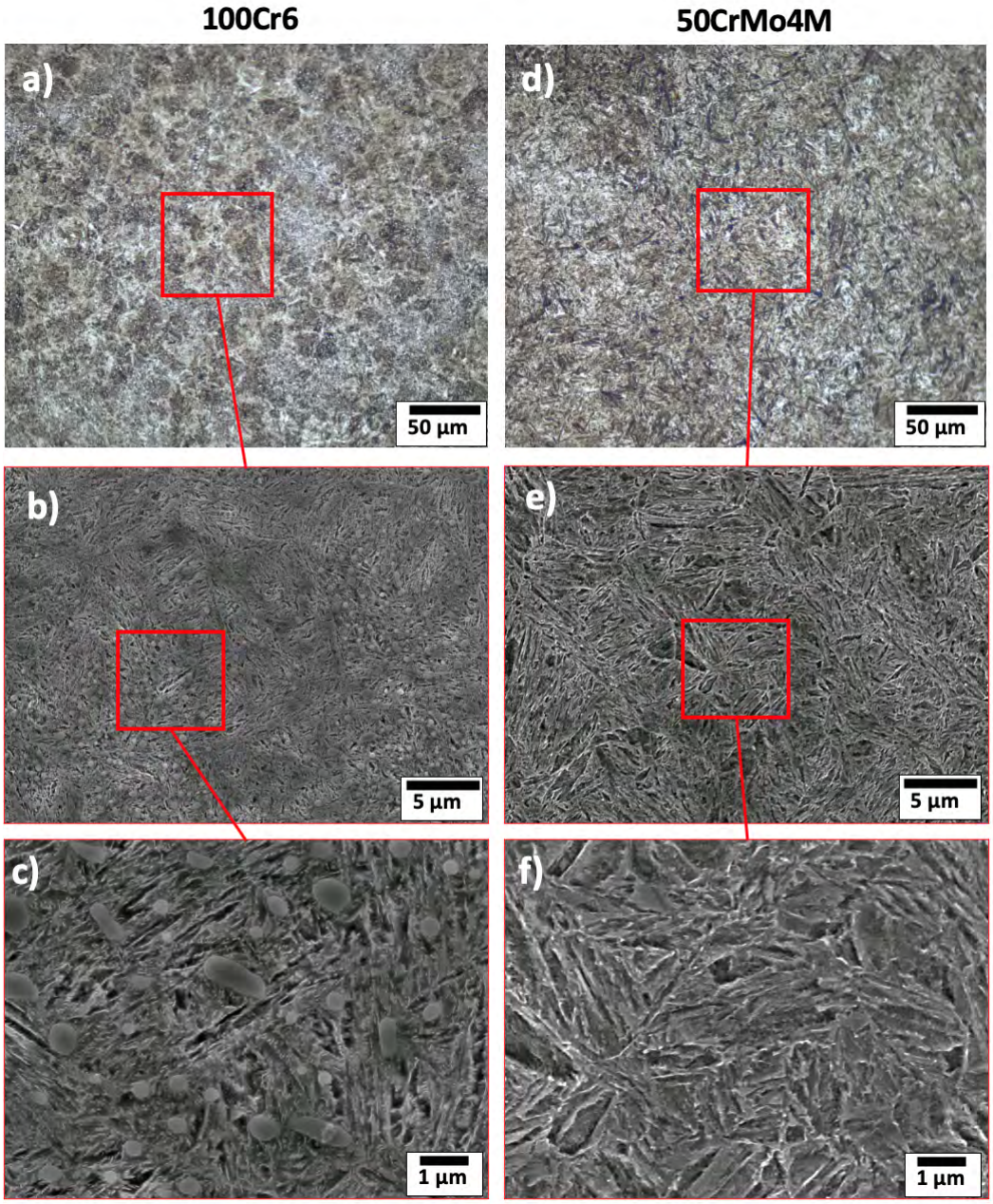

Figure 6.3: a),d) Optical images of virgin microstructure from 100Cr6 and 50CrMo4 bearing steel samples respectively. b),c) SEM images of the virgin martensitic microstructure of 100Cr6. e),f) SEM images of the virgin martensitic microstructure of 50CrMo4.

6.2.1 DER in 50CrMo4 bearings

The earliest stage of DER formation observed in the 50CrMo4 bearings was from samples tested under 2.9 GPa over 104 million cycles (see Figure 6.4a), showing dark patches after being etched. The dark etching patches show to be consisting of parallel bands at various orientations as shown in Figure 6.4b-f. Comparing with those in the developed areas of the DER (Figure 6.4b), which consists high density of the bands, those at the edge of the DER are less dense as shown in Figure 6.4c-e.

The heavily etched bands in the DER are responsible for the dark appearance under

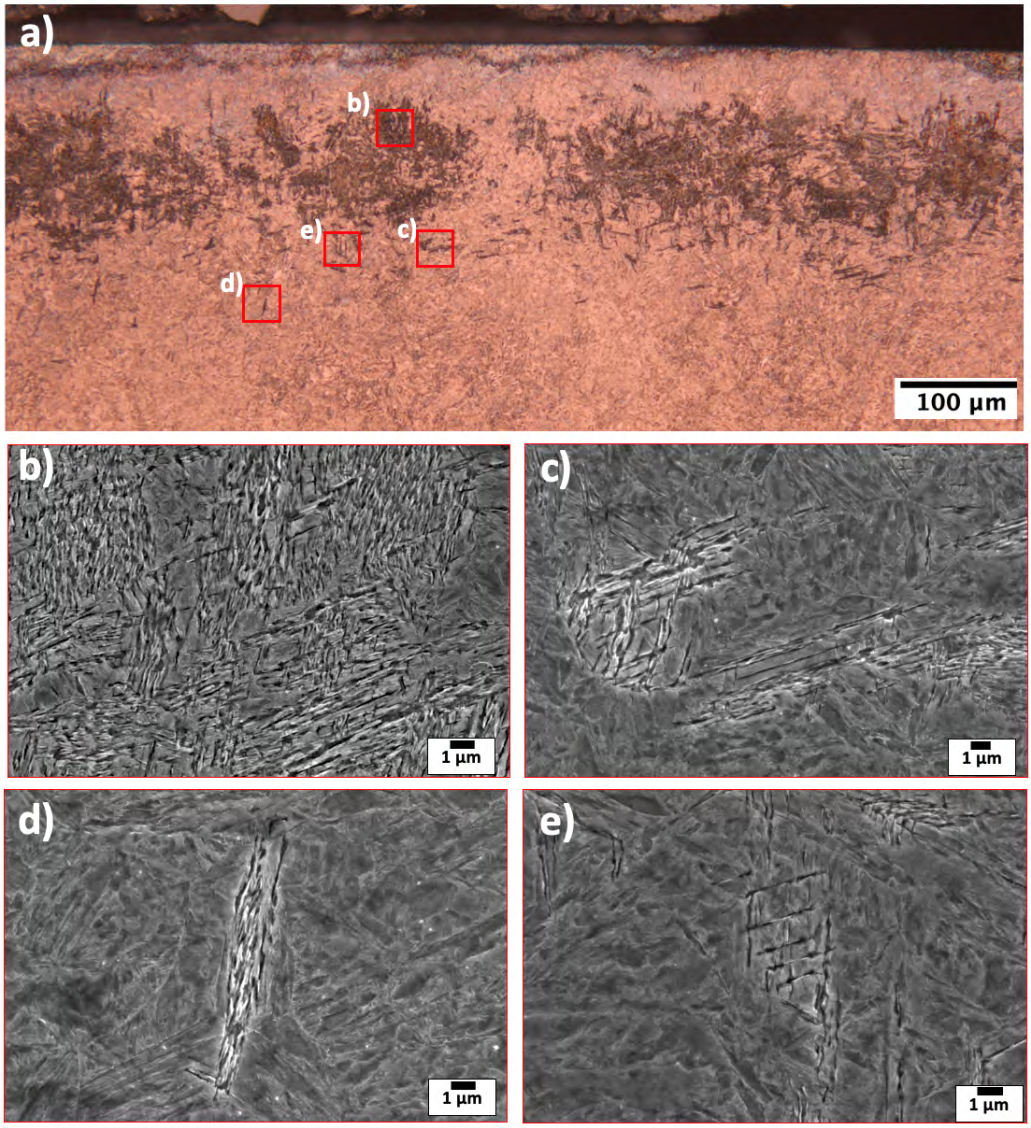

Figure 6.4: a) An optical image of DER from a 50CrMo4 sample run for 104 million cycles under 2.9 GPa. b-e) SEM images of various dark patches in the DER showing the patches consisting of various bands at multiple orientations.

optical microscopy. These bands appear to have a thickness of 30 - 100 nm and a length of up to 7 µm. About 50 million cycles later i.e more developed stages, in addition to the dark etching bands in DER, small clusters of equiaxed grains are observed in regions with dense closely-packed bands (dashed areas in Figure 6.5). Based on that equiaxed grains are observed in regions of closely-packed bands, which were observed in earlier stages (Figure 6.4c-e), it is suggested that equiaxed grains form in DER after the dark etching bands formation. However, given the complexity of the DER features, it is difficult to isolate each component to a certain number of stress cycles i.e. both dark etching bands and equiaxed grains are observed in all samples but the former is more dominant in earlier stages.

As DER develops, the density of dark patches increases and patches of different orientation start to overlap with each other, as shown in Figure 6.6 from a sample tested for

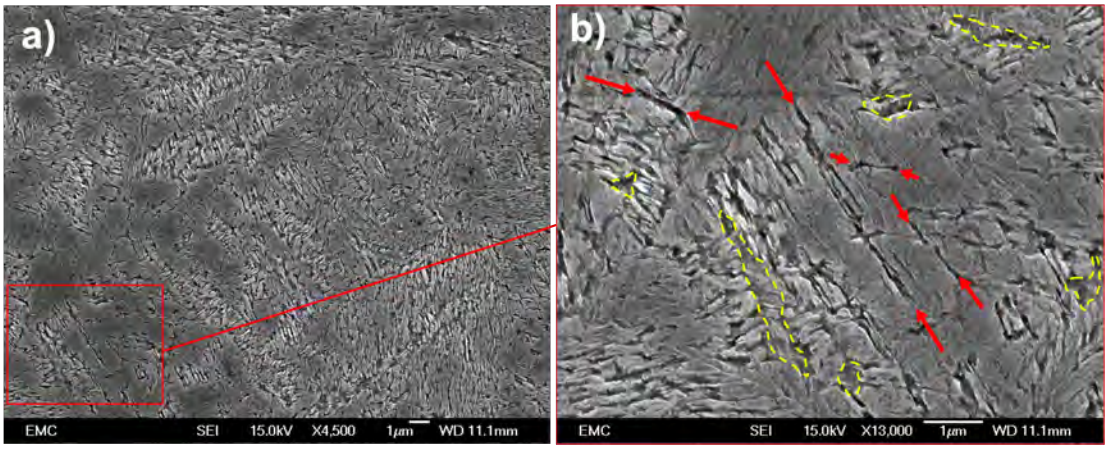

Figure 6.5: a) An SEM image of a DER patch in 50CrMo4 sample run under 2.9 GPa for 158 million cycles. b) An enlarged image of the region highlighted in a), showing the DER bands at various orientations (pointed by red arrows) and clusters of equiaxed grains (circled by yellow dashed lines).

846 million cycles under 2.9 GPa. Adjacent to the DER bands, bright structures are observed parallel to the bands with similar dimensions (see Figure 6.6b). Given that these features appear to be resistant to etching, it is proposed that they are carbide structures forming at the edges of the DER bands. However, due to their submicron sizes, it was challenging to confirm their elemental composition with EDX. Further analysis will be required to confirm its structure.

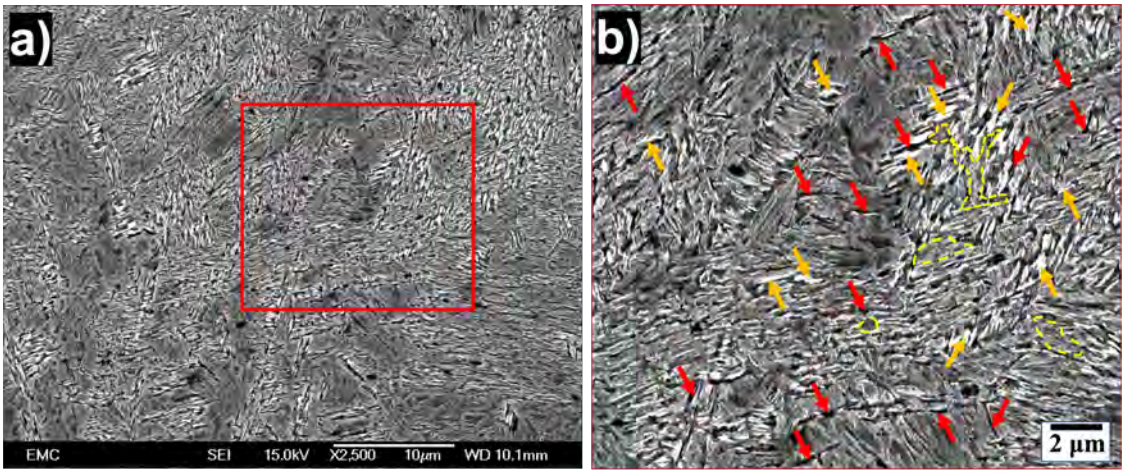

Figure 6.6: a) SEM of DER patch in 50CrMo4 sample run under 2.9 GPa for 846 million cycles showing dense DER bands overlapping. b) enlarged image of region highlighted in a) showing the DER bands at various orientations in red arrows and yellow arrow showing bright regions believed to be carbide structures. Dashed areas are regions consisting of equiaxed grains.

Unlike LAB and HAB which have distinct directionality of ∼30° and ∼80° respectively, while DER band groups intially appear to have 'random' orientations. However, further investigation has found that orientation of the band groups is not 'random' but orientates

in four main directions, see details in Figure 6.7 where DER in samples under 104 - 1626 million stress cycles are presented. The four dominant orientations of the DER bands are 15 - 25°, 70 - 85°, 95 - 110° and 130 - 160° inclined towards the rolling direction (summarised in Figure 6.7a). The four groups in different test samples are highlighted in different colours in Figure 6.7b-h. Out of the four groups, the yellow group, i.e. at 15 - 25°, is the most commonly observed orientation while the orientation group of 95 - 110° being the least common one. Nonetheless, different groups are often seen to overlap in dense regions where individual band becomes un-separable. In Figure 6.7e under a higher magnification, small regions of equiaxed grains (highlighted in dashed yellow) within a dense DER are observed

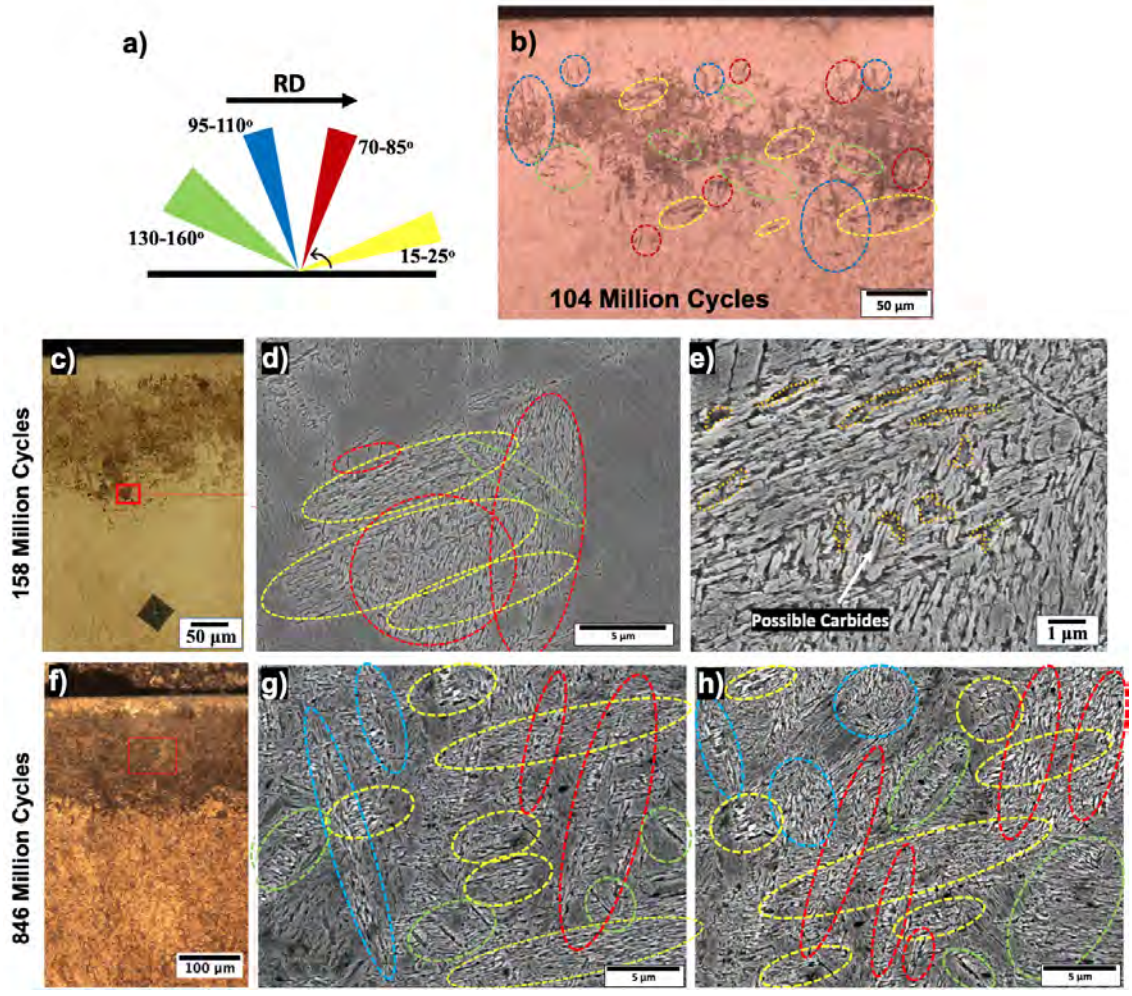

Figure 6.7: a) Different angle orientation groups of DER bands observed relative to rolling direction from 50CrMo4 samples run under 2.9 GPa. b) Optical image of DER bands from sample run for 104 million cycles with different orientation groups highlighted in colors relative to a). c) Optical image of DER from sample run for 158 million cycles. d) SEM image from region highlighted in c) showing different DER band orientations within the dark patch relative to a). e) Enlarged SEM image from the centre of d) showing equiaxed regions between the dense DER bands and possible carbides parallel to the bands. f) Optical image of DER from sample run for 846 million cycles. g,h) SEM images from region highlighted in f) showing dense DER bands at various orientation angles highlighted relative to a).

where thin nano-sized bright structures features parallel to DER bands at different orientations are also seen. Given their resistance to etching, these bright structures are believed to be carbide structures as a result of carbon migration from the ferritic DER bands to their edges where carbides nucleate.

Hence, it is demonstrated that as the DER grows in span across the subsurface and density of dark patches, the nano-sized DER bands develop from individual bands across the microstructure (Figure 6.4c-f and Figure 6.5b) into groups with dominant orientations (Figure 6.7) and eventually leading to dense clusters of closely-packed bands with bright etching-resistant structures developing parallel to the bands (assumed to be carbide-like structures). While regions of equiaxed grains also develop within such clusters.

During later stages of the DER in 50CrMo4, brightening of the dark region is seen (see Figures 6.8 and 6.9 for the 2038 and 7668 million cycles respectively), which has not been reported in literature. A comparison of the microstructures in bright and dark areas within the DER shows that the bright areas have a much finer grain structure compared to the darker area (Figure 6.8b,c and Figure 6.9b,c). While the white/etch resistant nano-structures believed to be carbides are still visible, the heavily etched DER band groups observed in earlier stages (see in Figure 6.4-6.7) are not as pronounced any more.

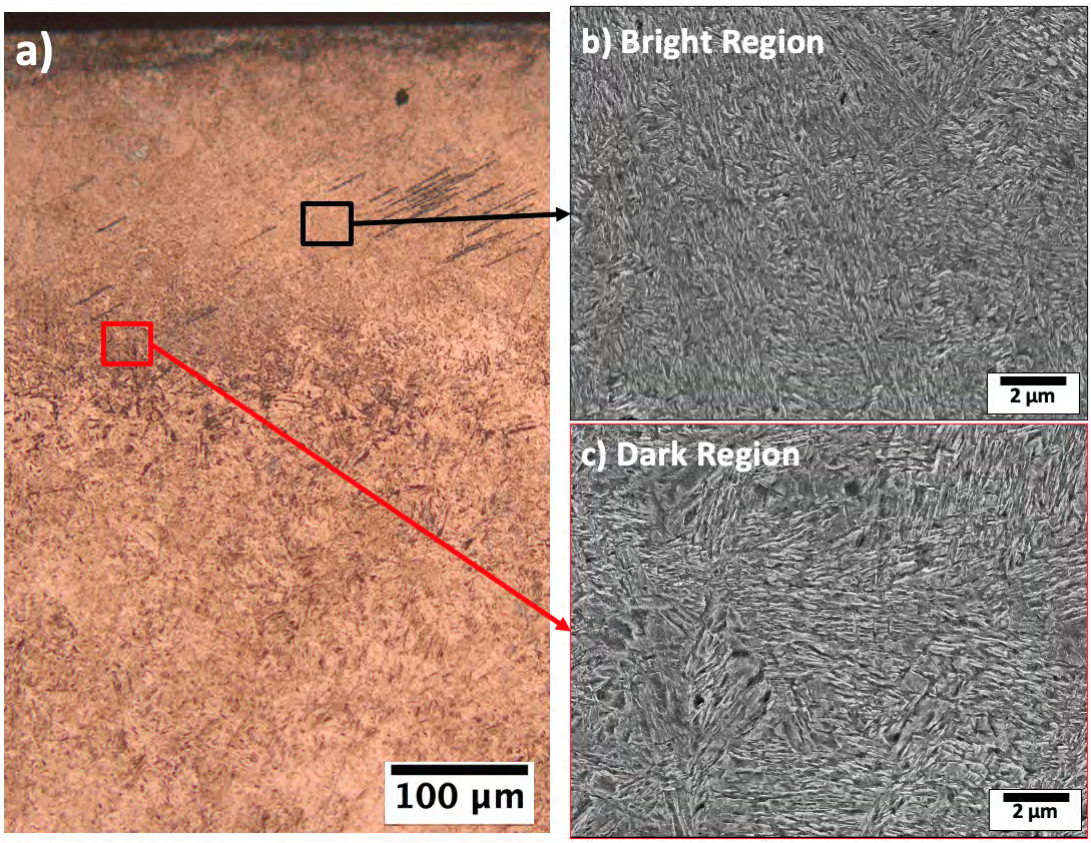

Figure 6.8: a) An Optical image from 50CrMo4 bearing run under 2.9 GPa for 2038 million cycles showing DER and LAB. b) SEM image of area from a) showing the bright portion of the DER. c) SEM image of area from a) showing the dark portion of the DER.

Instead, the microstructure in the whole original DER region appears as altered fine grains rather than the dark etching band groups observed in earlier stages. Hence it appears than there is a microstructural transformation causing the brightening of the DER in later stages through the 'removal' of the DER bands. The refined microstructure may be responsible for the enhanced resistance to etching as shown previously in Figure 6.2. A reference image is shown in Figure 6.9d to show the parent microstructure from the same sample at a depth of 700 µm from the surface i.e far away from any microstrucutral transformations investigated, highlighting the complete transformation of the parent microstructure in the DER.

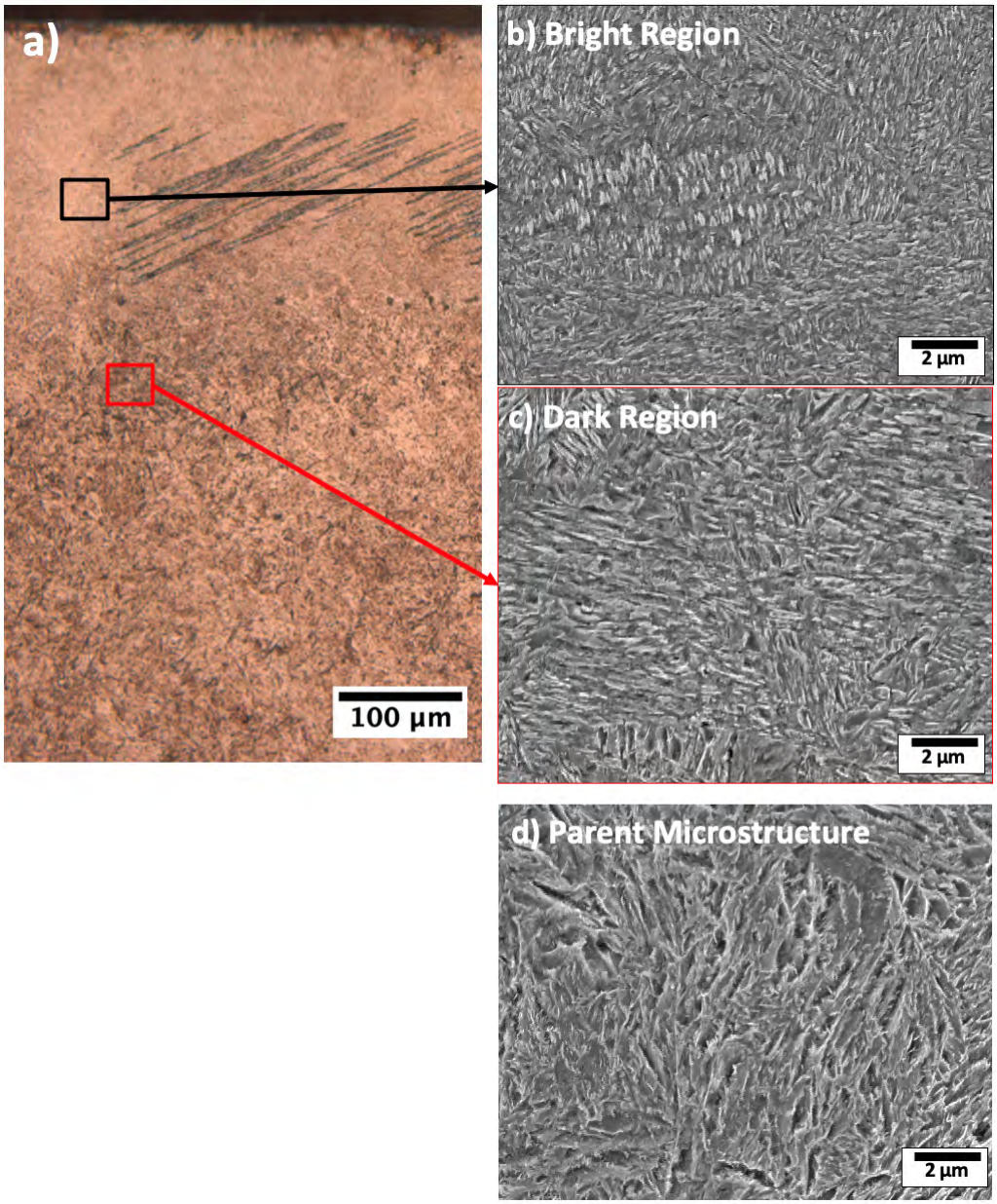

Figure 6.9: a) An Optical image from 50CrMo4 bearing sample run under 2.9 GPa for 7668 million cycles showing both DER and LAB. b) SEM image of area from a) showing the bright portion of the DER. c) SEM image of area from a) showing the dark portion of the DER. d) SEM image of parent microstructure from same sample taken at 700 µm from the surface i.e away from the maximum stress region.

6.2.2 DER in 100Cr6 bearings

In general, the DER formed in the 100Cr6 bearings as discussed in Chapter 4, is not as pronounced as that in the 50CrMo4, e.g. their density/visibility of dark patches under optical microscopy are lower. However, investigating the regions in the microstructure at similar depths, similar features are found in 100Cr6 and in 50CrMo4, such as the dark etching band groups and their orientations. Figure 6.10 shows the subsurface of 100Cr6 sample run under 2.9 GPa for 591 million cycles. Although the DER is not at pronounced as those in the early stages of 50CrMo4 specimens (up to 846 million cycles), possibly due to the much developed LAB, small areas of DER bands are observed (circled by red lines in Figure 6.10b). Since the 591 million cycle 100Cr6 bearing is the shortest test duration sample for this material obtained in this study, DER bands either below the lower boundary of the LAB or between individual LAB are examined (as shown in Figure 6.10b).

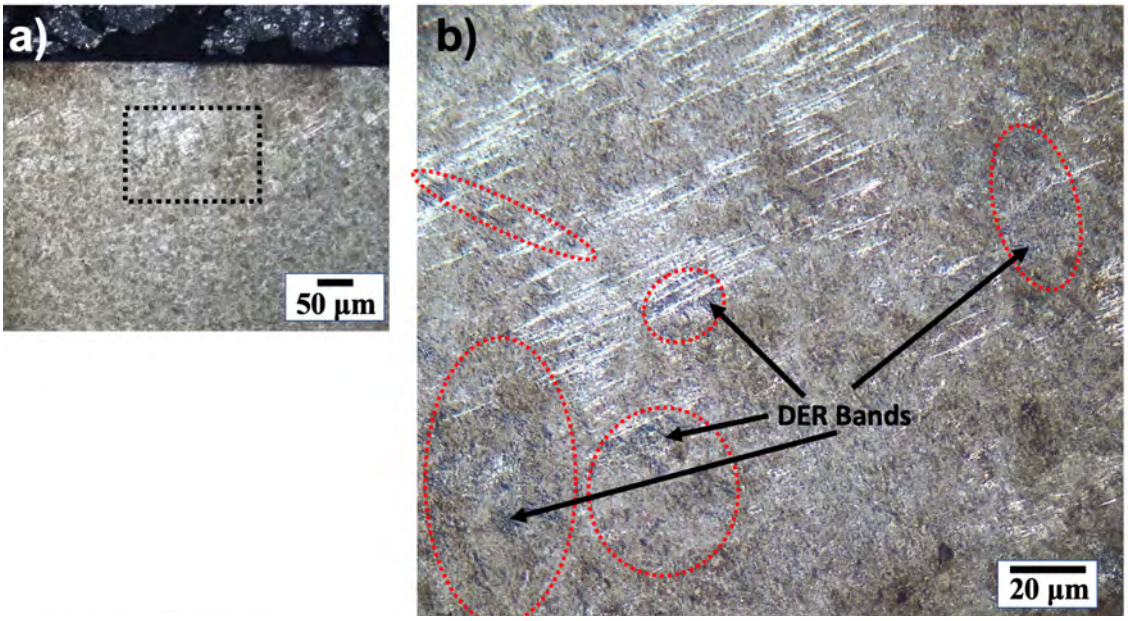

Figure 6.10: a) LOM image of subsurface of 100Cr6 sample run under 2.9 GPa for 591 million cycles. b) Enlarged area from a) showing DER bands highlighted in red at a depth below the LAB and between individual LAB.

SEM images of DER areas observed in 100Cr6 bearing under 2.9 GPa over 591 million cycles are shown in Figure 6.11. In Figure 6.11a and 6.11e, a relatively dense area of DER features is observed compared to Figure 6.11c. Hence, the distribution of DER in 100Cr6 samples is not as uniform as those in the 50CrMo4 samples, also evidenced by the etching response under LOM images shown previously. However, the orientation of the DER bands in the 100Cr6 samples are similar to the orientations observed in the low carbon steel (see in Figure 6.7). It can also be seen that the dimension of the dark etching bands ($<$ 100 nm width and $<$ 7 µm length) in 100Cr6 is similar to that in the 50CrMo4. Within dense

closely-packed DER bands parallel to each other (Figure 6.11f) and at intersections between DER bands at different orientations (Figure 6.11d and 6.11b), equiaxed grains are seen to form. Similar to that in the 50CrMo4, bright carbide structures parallel to DER bands are observed too.

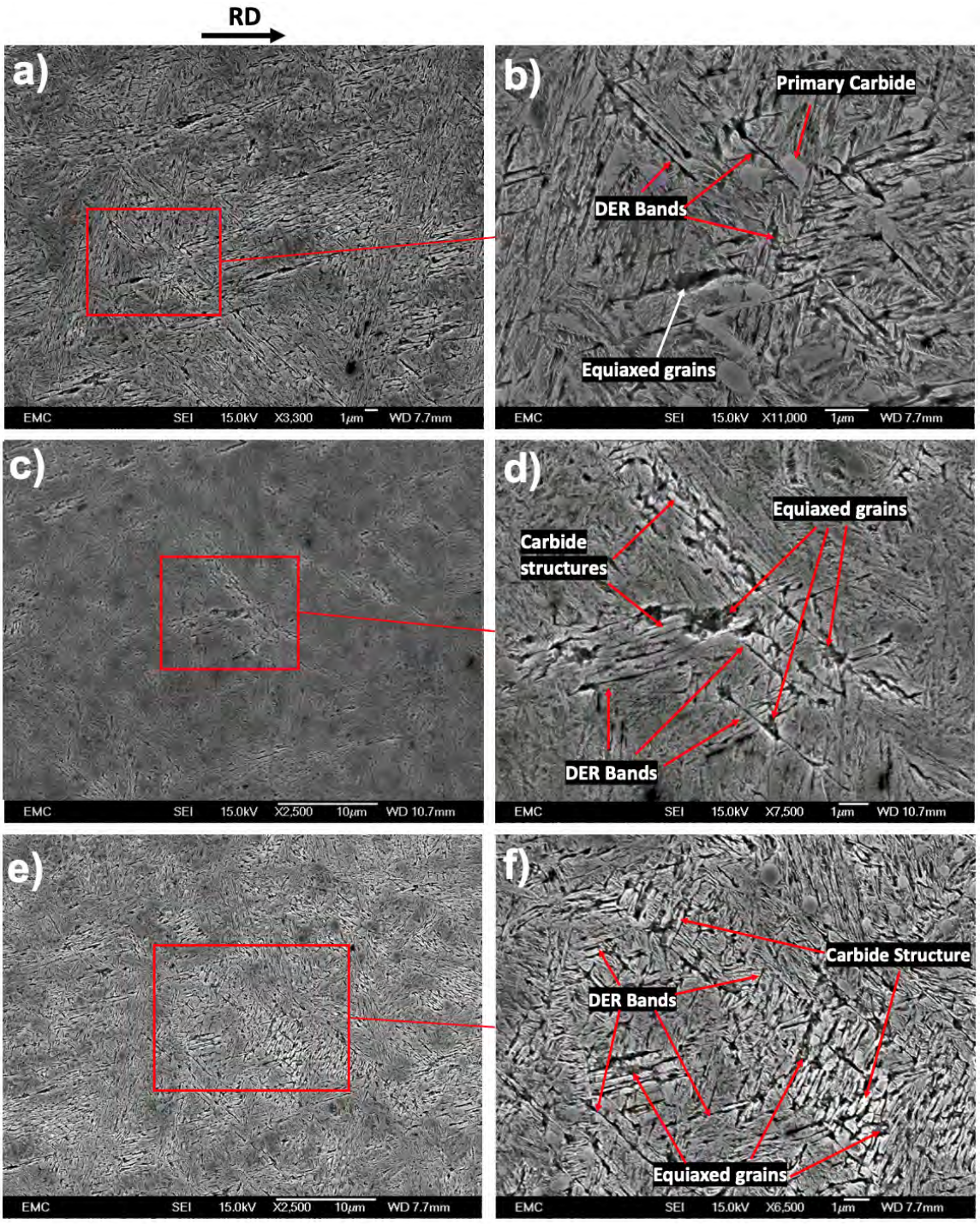

Figure 6.11: a,c) SEM images of DER areas within 100Cr6 sample run under 2.9 GPa for 591 million cycles at a depth below the lower boundary of LAB. b,d) High magnification images from a) and c) respectively showing individual DER bands, equiaxed grains and carbide structures.

At a later stage, DER are mainly found to be in between LAB as shown in Figure 6.12,

where SEM images of the bearing tested under 2.9 GPa over 3016 million cycles are shown. A similar comparison could be made in terms of orientations of the DER bands (Figure 6.12b and d). However, given that they are found surrounded by LAB (highlighted in yellow), it suggests a link between the two microstructural features. Also, carbide structures parallel to the DER bands are more pronounced and thicker in these samples comparing with those in the earlier. The etching behaviour of these carbide structures is found to be similar to the lenticular carbides of LAB discussed in Chapter 7 of this thesis. This also suggests that a similar carbide formation mechanism is observed in DER and LAB. Similar to that in the 50CrMo4, equiaxed grains are seen to have developed in regions with dense close-packed DER bands and at intersections between DER bands of different orientations (Figure 6.12b).

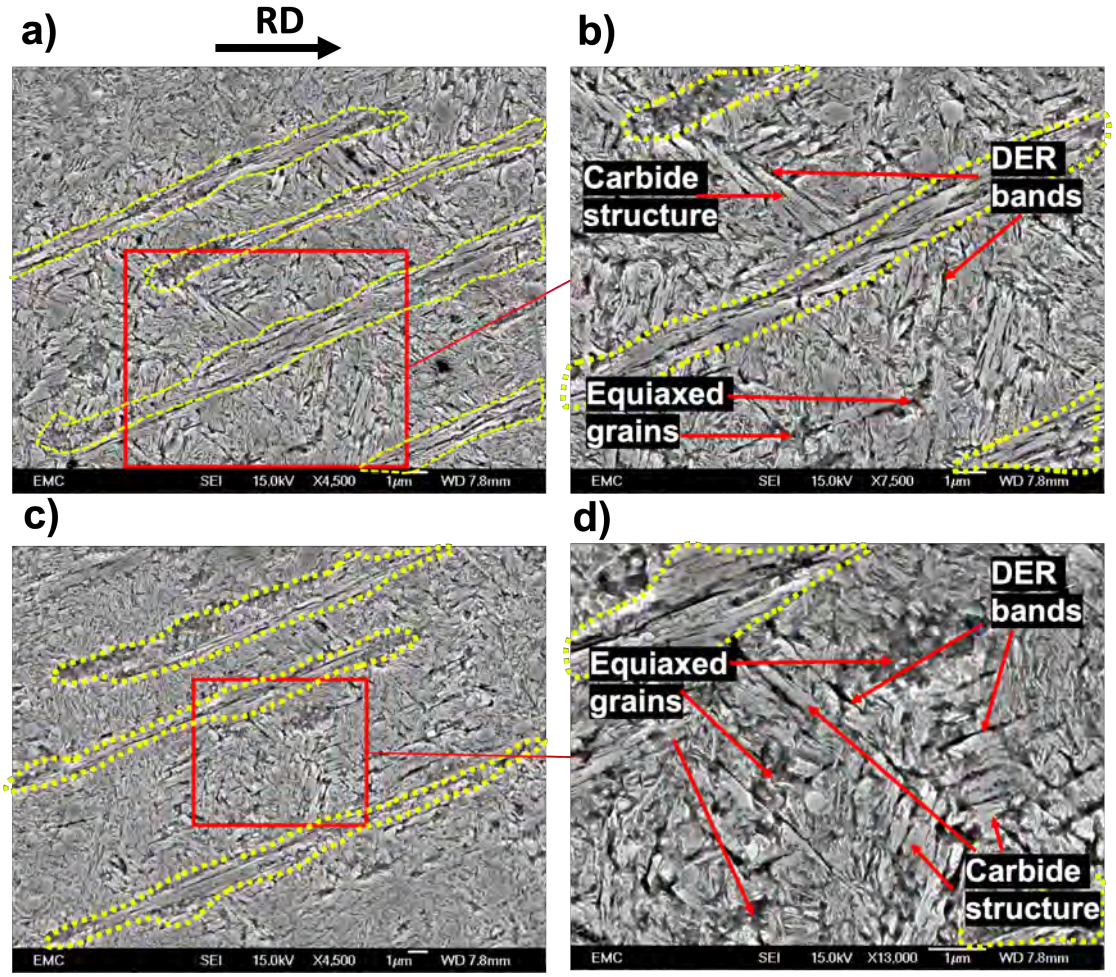

Figure 6.12: a,c) SEM images of DER areas within 100Cr6 sample run under 2.9 GPa for 3016 million cycles between LAB. b,d) high magnification images from a) and c) respectively showing individual DER bands, equiaxed grains and carbide structures. LAB are highlighted in yellow to distinguish from DER

The grain refinement observed in the 50CrMo4 during the late stages of DER has also been seen in 100Cr6 bearings (see in Figure 6.13 comparing features in the 591 and 3016 million cycles under 2.9 GPa). The dark and bright contrast in the SEM images in Figure

6.13b) and d) are correlated to refined grains and carbides due to their higher etchant resistance, suggesting DER bands breakdown and grain refinement occurring during the latest stage of DER development.

To further investigate the DER formation mechanisms, EBSD analysis has been conducted on both 50CrMo4 and 100Cr6 samples and the results are shown in the next section.

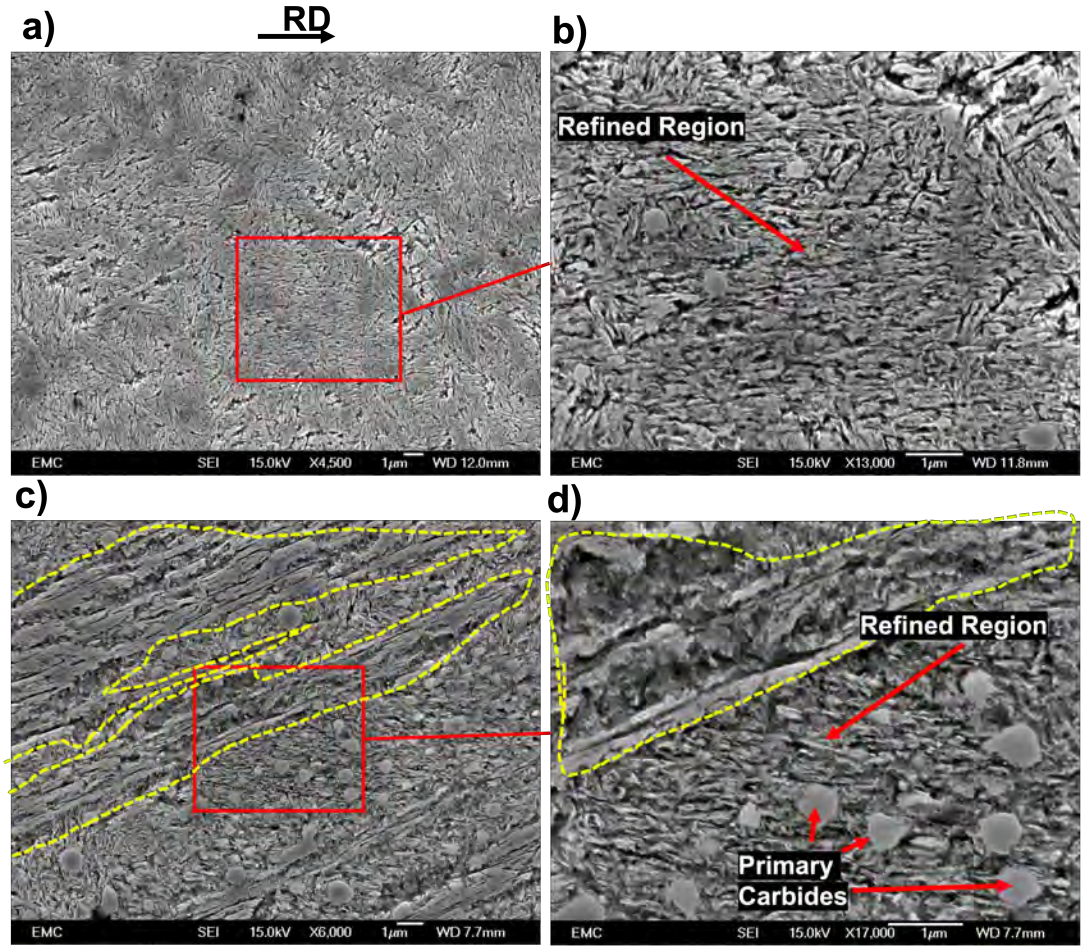

Figure 6.13: SEM images of DER in 100Cr6 samples run under 2.9 GPa for a) 591 million and c) 3016 million cycles. b, d) shows refinement of the DER microstructure in a) and c) respectively. LAB are highlighted in yellow to distinguish from DER.

6.3 EBSD Analysis of DER

Surfaces of 50CrMo4 and 100Cr6 bearing samples where DER are identified under LOM and SE SEM after nital etching are re-polished to expose an unetched surface for EBSD analysis (see experimental procedure presented in Section 3.3 above). After BSE SEM and EBSD analysis, the samples have again been re-polished and etched to capture SE SEM images for comparison. However, small variations between the BSE and SE images may be present due to the slight material removal during re-polishing.

6.3.1 EBSD analysis of DER in 50CrMo4

A variety of SEM images and EBSD maps of a 50CrMo4 virgin sample are shown in Figure 6.14, showing a typical martensite lath microstructure. The martensite laths are randomly orientated evidenced by the contrast variations in the BSE image (Figure 6.14a). Figure 6.14b shows the IPF map of the corresponding area in Figure 6.14a, where no obvious texture development is observed as expected. The IPF map has been plotted with respect to the axis that is parallel to normal direction of the bearing raceway (also for all other IPF images presented in this thesis). Figure 6.14c shows the IQ map which indicates a homogeneous distribution of strain, demonstrating sufficient surface preparation through polishing was achieved. Figure 6.14d shows a homogeneous distribution of KAM values with slightly higher values closer to the grain boundaries. This shows that the virgin martensitic steel has a homogenised strain distribution without any localised strain points. The HAGB map in Figure 6.14e shows non martensite-martensite grain boundaries such as prior-austenite grain boundaries within the microstructure. Figure 6.14f shows an SE SEM image of the re-polished and etched surface for comparison.

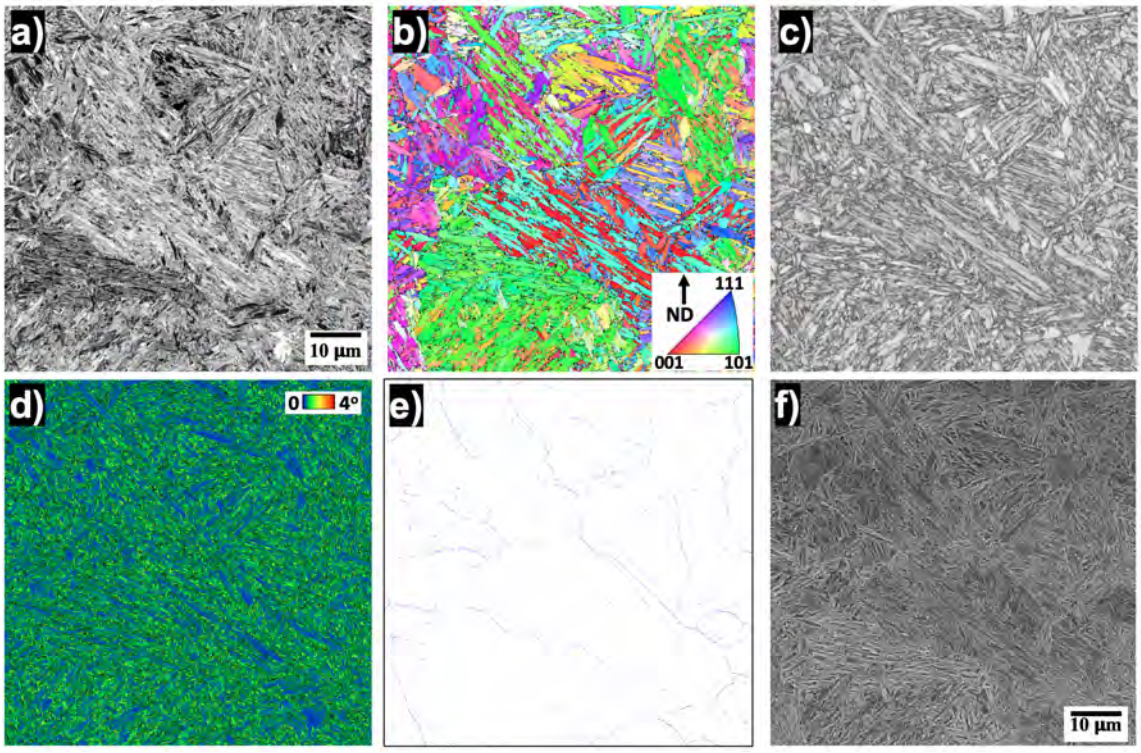

Figure 6.14: Inspection of 50CrMo4 virgin specimen through a) BSE SEM image b) IPF Map c) IQ Map d) KAM Map (100 nm, 5°) e) HAGB map and f) SE SEM image.

As discussed in Section 6.2, the earliest stage of DER formation produces dark etching band groups in the maximum shear stress region at four dominated orientations. After which, 'brightening' of the DER occurs possibly due to grain refinement. Results of the EBSD analysis of the 50CrMo4 bearing (2.9 GPa, 104 million cycles) in Figure 6.15 show that

areas of refined grains have formed in the DER possibly due to martensite fragmentation. It is also observed that the refined region (highlighted in Figure 6.15c) consists of both low misorientation equiaxed grains (likely a product of recrystallization) and relatively high misorientation grains (likely due to martensite refinement from the dense DER bands). This also suggests that the refinement of the parent martensite microstructure may have contributed to the high stress points within the refined structures due to plastic deformation, leading to recrystallization nucleation at these points and formation of equiaxed ferrite grains to release stored energy in the microstructure.

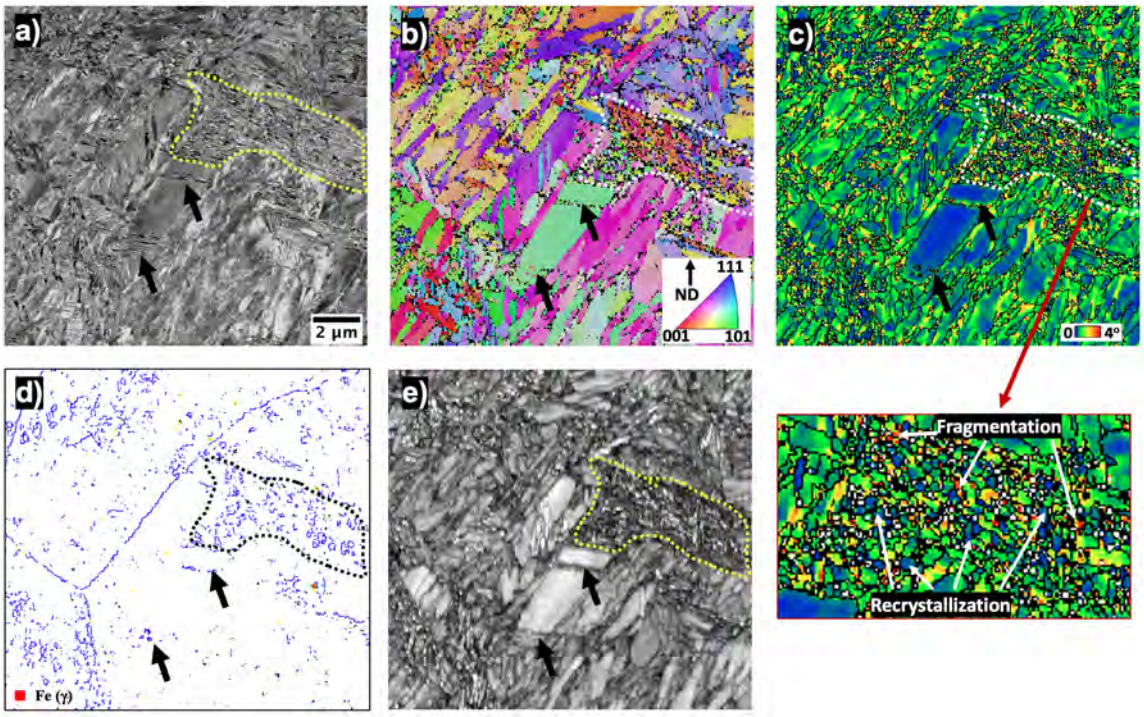

Figure 6.15: Analysis of DER in 50CrMo4 sample run under 2.9 GPa for 104 million cycles showing a) BSE SEM image b) IPF map c) KAM Map (100 nm, 5°) d) non-martensite-martensite HAGB map and e) IQ map of DER bands causing martensite fragmentation (arrow) and highlighted region of dense DER bands consisting of refined grains. Image taken at a depth of 120 µm from surface.

The martensite refinement/fragmentation and nucleation of equiaxed grains in DER are further investigated by comparing the microstructures at the upper boundary of the DER (in the subsurface 20 µm from the contacting surface) and the parent microstructure outside the vicinity of the DER in a 50CrMo4 bearing sample tested under 2.9 GPa over 158 million cycles (see Figure 6.16). Within the DER, two distinct grain structures are observed, fine grains in patches (highlighted in yellow) where dark etching bands can be seen within and the gradual fragmentation of martensite laths (highlighted in red) given their intermediate grain size between the fine grains highlighted in yellow, and the parent microstructure above the DER. Figure 6.16a shows that the fine grain patch bands (highlighted in yellow) are inclined at 140-160° to the rolling direction, which is one the four preferred angles of the

dark etching band groups discussed previously (shown in Figure 6.7). The non martensite-martensite HAGB map in Figure 6.16d shows various grain boundaries developed within the fine grain region (highlighted in yellow) while almost no boundaries are detected in the region highlighted in red, indicating an early stage of martensite fragmentation still occurring in this area. This has been further confirmed by the higher contrast in the fragmented region in the IQ map (Figure 6.16e) comparing with the lower contrast in the fine structure. This suggests that, during bearing RCF operation, a gradual process of martensite laths fragmentation to fine ferrite grains drives the formation of DER.

The structures of an early (158 million cycles) and a late (7668 million cycles) stage of DER in 50CrMo4 are compared in Figure 6.17, corresponding to a darker and brighter appearance in the LOMs respectively as shown previously in Figure 4.15. The images shown in Figure 6.17 are captured at a depth of 120 µm from the contacting surface where LAB are expected to form (discussed in Chapter 4). A refinement in DER is observed at both stages, also shown in the corresponding IPF maps in Figure 6.17b and 6.17e. However, no texture is observed across the DER region in either sample. The early stage DER also shows to contain more dark etching bands (dark needle-like structures) scattered around the LAB under the four preferred orientations as discussed above comparing with the DER in a later stage (Figure 6.17b and Figure 6.17d). While both SE SEM images in Figure 6.17c and Figure 6.17f show grain refinement, equiaxed grains appear to be much more refined at the later stage. The areas highlighted by yellow rectangles in Figure 6.17 are shown in Figure 6.18 to provide more details. The dark etching bands in the early stage DER (Figure 6.18a and Figure 6.18c) have largely changed to refined equiaxed grains in the later stage (Figure 6.18d and Figure 6.18f). This again suggests that dark etching bands formed in DER at early stages breakdown during later stages contributing to the increase of equiaxed grain formation. The remainder of etch-resistant structures in the highly refined equiaxed grain regions at later stages are suggested to be carbide structures (Figure 6.18f).

The KAM and IQ map of the areas in Figure 6.17 is shown in Figure 6.19 to illustrate the DER refinement between the two stages. Unlike the equiaxed grains of WEB which have a low misorientation [120], the fine grain structure of the DER has a relatively higher misorientation (see Figure 6.19a and 6.19c) indicating plastic deformation in these areas. The transformation of the parent microstructure to the DER could be linked to plastic deformation induced fragmentation of the martensite laths to fine grains of ferrite leading to the migration of carbon. However, at what stage the transition of martensite-ferrite occurs remains unclear. Given that bright etch-resistant structures form adjacent to DER

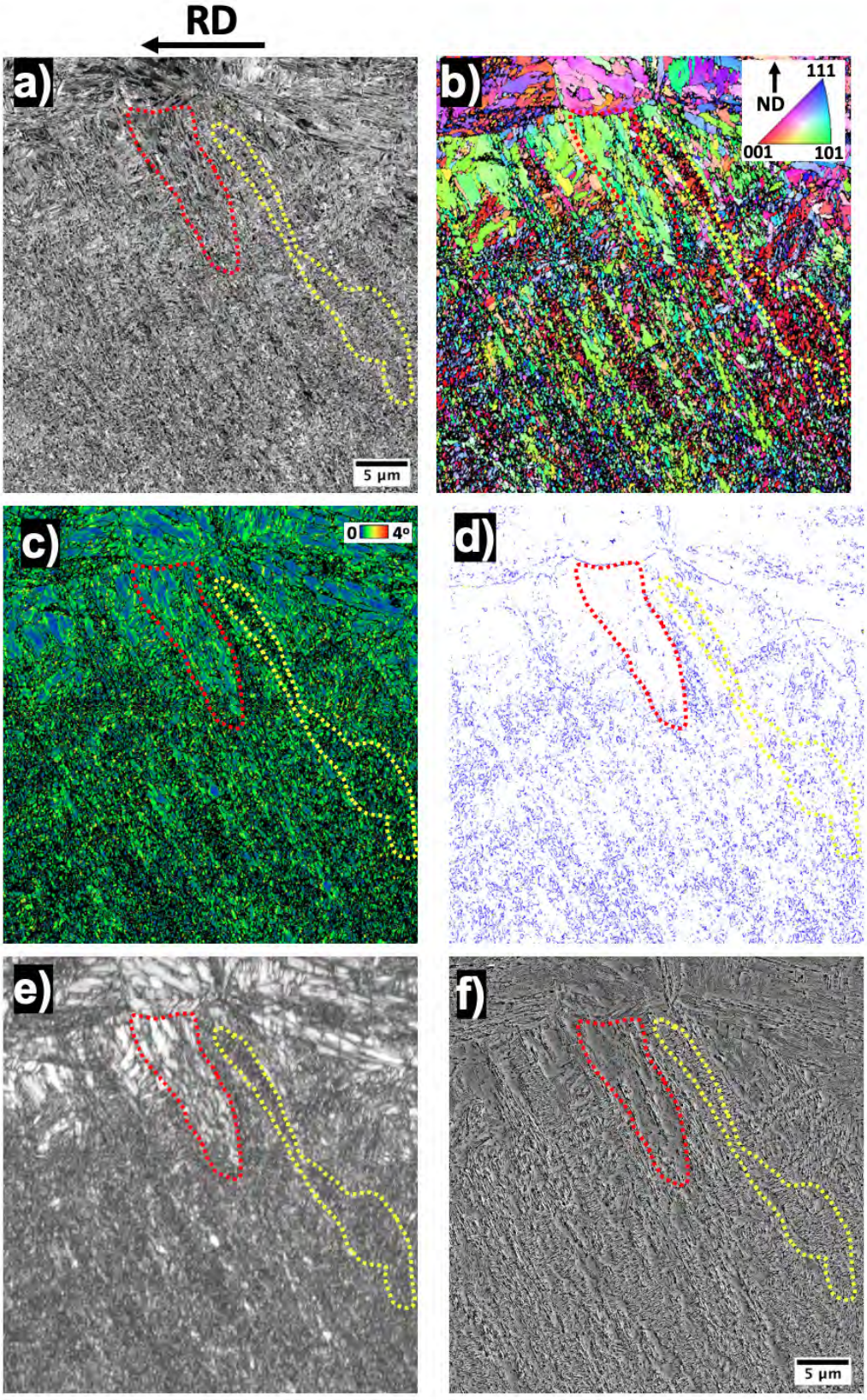

Figure 6.16: Inspection of DER in 50CrMo4 sample run under 2.9 GPa for 158 million cycles in an area located at a depth of 20 µm from the surface. Figure shows a) BSE SEM image b) IPF map with direction parallel to normal direction (ND) c) KAM map (100 nm, 5°), d) non martensite-martensite HAGB map, e) IQ map and f) SE SEM image. Patches of fine DER bands are highlighted in yellow in and area of martensite lath fragmentation is highlighted in red.

bands as being discussed previously, it is likely that the DER bands are ferrite structures after carbon migrates to the edges of these bands. The IQ map in Figure 6.19b shows that the DER regions in the early stage have a relatively high contrast compared to that of the DER at a later stage (Figure 6.19d) possibly due to the combination of finer grains and higher defects/strain accumulation during the later stages. Comparing with the early stage, more red spots are seen to scatter within the whole region (in Figure 6.19c), indicating higher misorentation due to stress build-up at these points. Since this region is where LAB would initiate, the stress points could potentially become locations for recrystallization of equiaxed grains (low misorientation grains) that initiate LAB development as a form of energy releasing process (see Chapter 7).

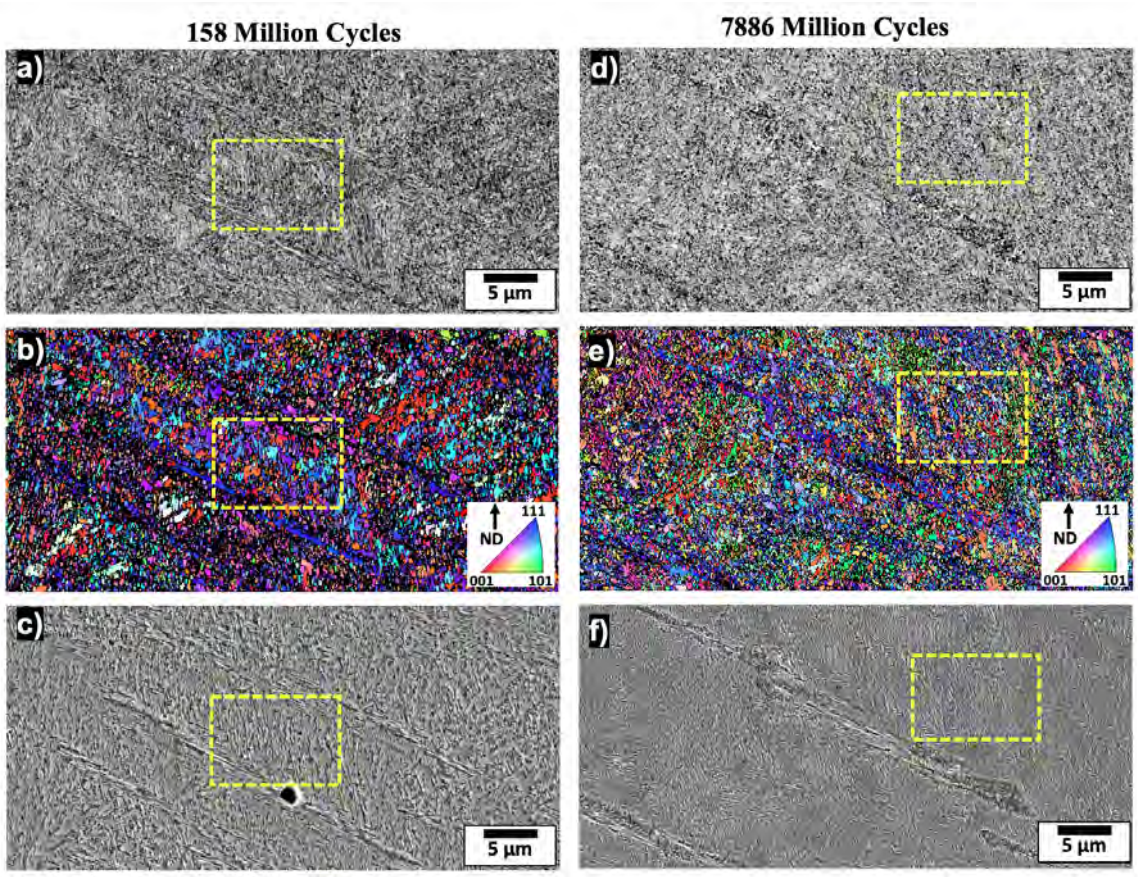

Figure 6.17: a,c) BSE and SE SEM images of DER surrounding LAB in 50CrMo4 samples run for 158 million cycles while b) shows IPF map (parallel to normal direction (ND)) of area in a) and c). d,f) BSE and SE SEM images of DER surrounding LAB in 50CrMo4 samples run for 7668 million cycles while e) shows IPF map (parallel to normal direction (ND)) of area in d) and f). Images are captured at a depth of 120 µm from the surface.

In reference to Figure 6.9, Figures 6.17-6.19 showed the 'bright regions' in the DER structure in the 50CrMo4 samples tested for 7668 million cycles under EBSD at a depth of 120 µm from the surface while Figure 6.20 shows the 'darker regions' from the same sample at 200 µm depth. DER areas in Figure 6.20 observed between LAB (circled by yellow lines) are seen to contain significantly coarser grains comparing with those seen in Figure 6.17-

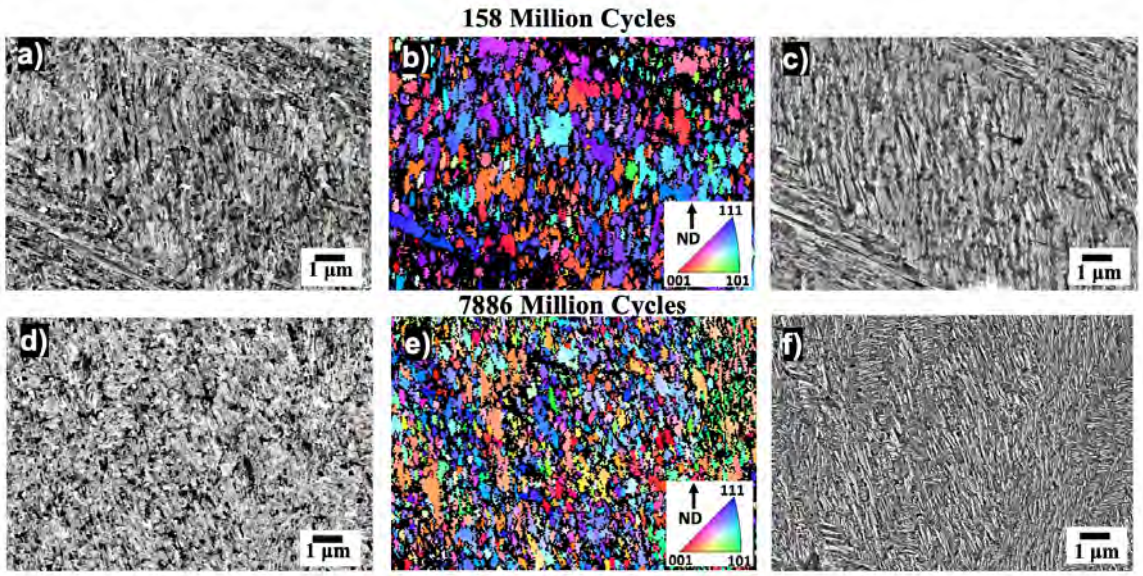

Figure 6.18: Inspection of area highlighted in Figure 6.17 through a,d) BSE SEM image b,e) IPF Map. and c,f) SE SEM

6.18d-f. These 'darker regions' also show fragmentation of martensite laths to finer grains (in reference to virgin material in Figure 6.14) but at a slower rate comparing with that in the 'bright regions' within the maximum shear stress region of the same sample. This suggests that refinement of martensite laths happens more rapidly in higher stressed regions contributing to the subsequent LAB formation.

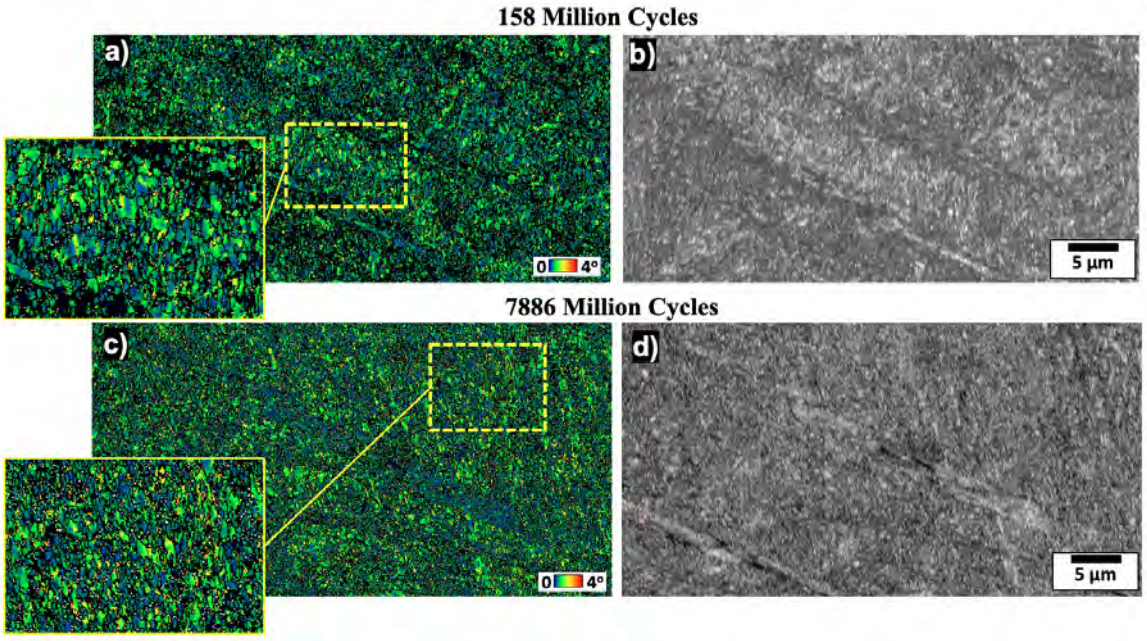

Figure 6.19: Inspection of DER areas in Figure 6.17 showing a,c) KAM map (100 nm, 5°) where high stress points (red spots) are more frequent in the later stage and b,d) IQ map.

Relationships between DER structure and prior austenite grain boundaries (PAGBs) are investigated and an example from the 158 million cycle 50CrMo4 sample is given in

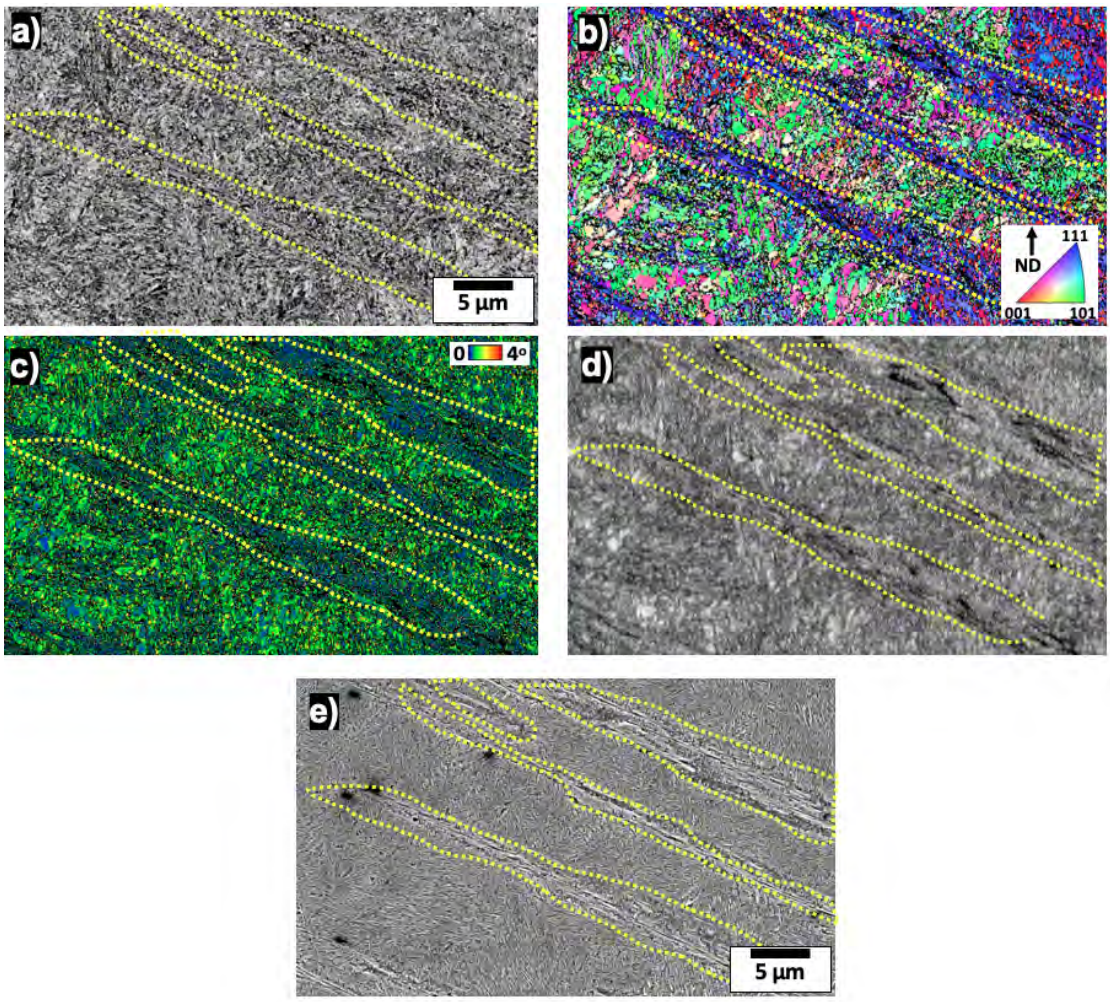

Figure 6.20: Inspection of DER in 50CrMo4 sample run under 2.9 GPa for 7668 million cycles in an area located at a depth of 200 µm from the surface. Figure shows a) BSE SEM image b) IPF map with direction parallel to normal direction (ND) c) KAM map (100 nm, 5°) d) IQ map and e) SE SEM image.

Figure 6.21. DER structures which appear as parallel bands,are highlighted in yellow under SEM images in Figure 6.21a and 6.21f while EBSD maps (Figure 6.21b and c) show these areas to consist of fine grains likely from the martensite fragmentation discussed previously. Nonetheless, these regions as shown in Figure 6.21d, appear to either accumulate around the edges of the PAGBs or grow within prior-austenite grains.

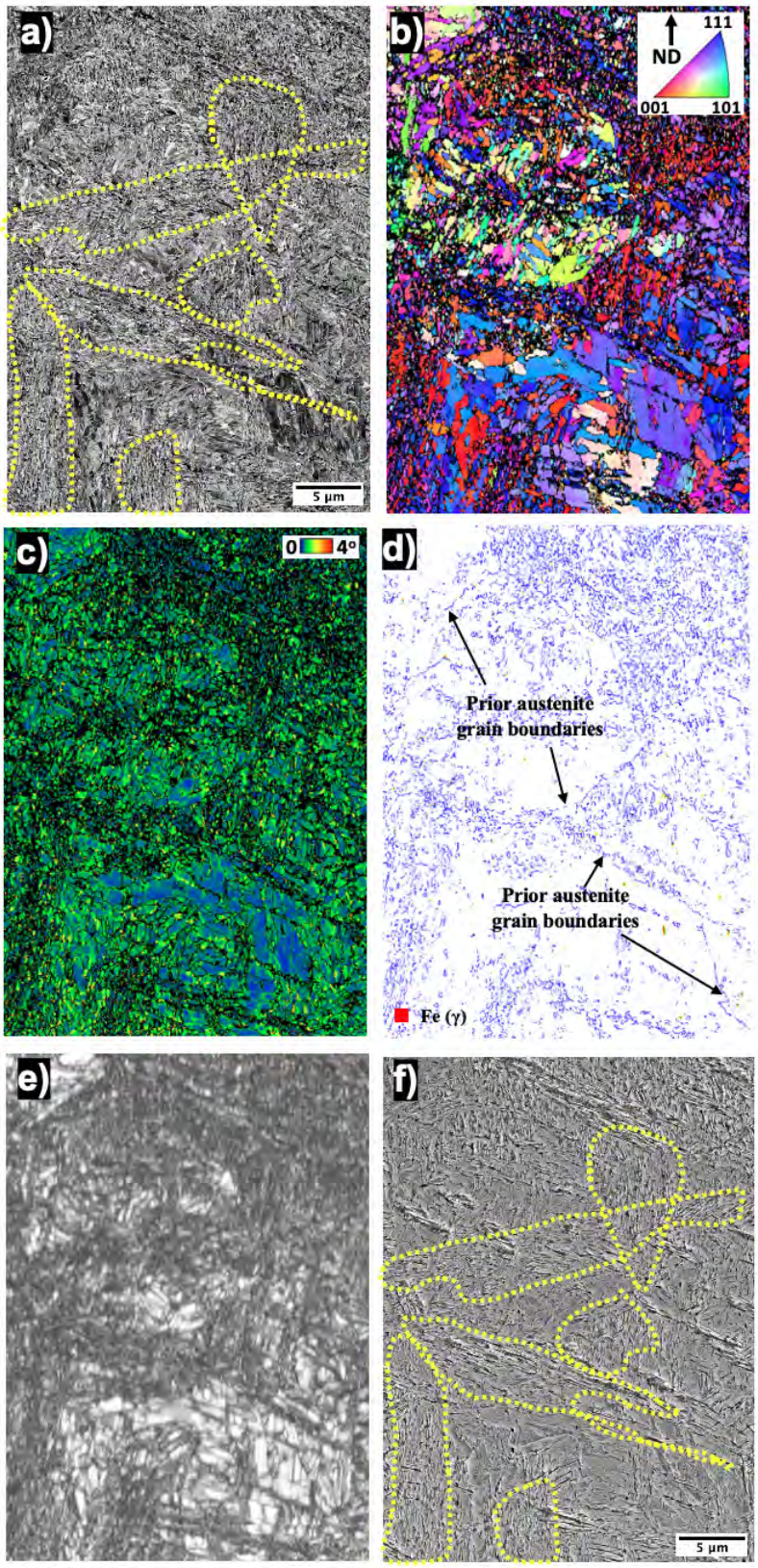

Figure 6.21: Inspection of DER in 50CrMo4 sample run under 2.9 GPa for 158 million cycles in an area located at a depth of 160 µm from the surface. Figure shows a) BSE SEM image b) IPF map with direction parallel to normal direction (ND) c) KAM map (100 nm, 5°), d) non martensite-martensite HAGB map, e) IQ map and f) SE SEM image. Patches of DER bands are highlighted in yellow in a) and f).

6.3.2 EBSD analysis of DER in 100Cr6

As being shown in a previous study, the 100Cr6 martensitic steel bearings with a similar heat treatment have no obvious texture developed without localised strain points (see SEM and EBSD images of a virgin sample in Figure 6.22) [120]. Comparing with the 50CrMo4 microstructure (Figure 6.14), which is a lath structure, the 100Cr6 martensite shows more of plate-like structures (Figure 6.22). The high carbon 100Cr6 is also shown to contain primary carbides that is not featured in the low carbon 50CrMo4 steel.

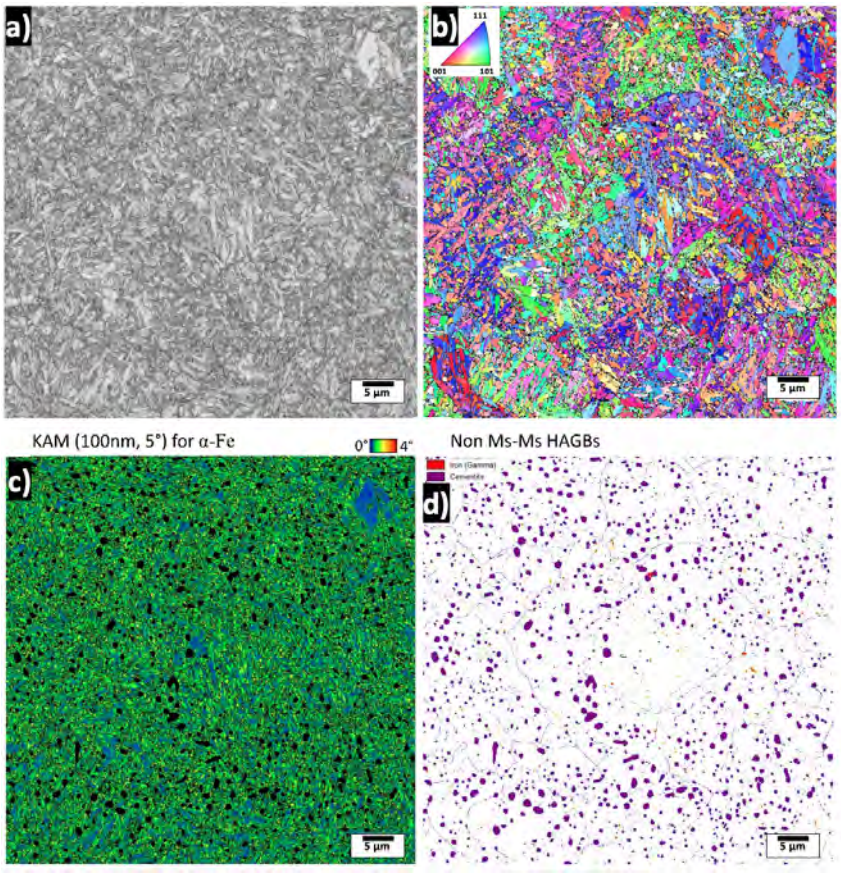

Figure 6.22: Maps of virgin 100Cr6 material obtained by the SEM/EBSD method: (a) IQ map, (b) IPF colour map with respect to rolling normal direction. c) KAM Map (100 nm, 5°) and d) non martensite-martensite HAGB map [120].

Figure 6.23 shows the DER areas at a depth of 120 µm from the surface within a 100Cr6 bearing run under 2.9 GPa for 591 million cycles, which is the shortest 100Cr6 test duration sample available to this study, where LAB formation has already started (see more details been discussed in Chapter 4). Two distinct areas are highlighted in Figure 6.23, where the area circled by a red line shows the remaining of the fragmentation of martensite evidenced by the absence of non martensite-martensite HAGBs (Figure 6.23e); and the region highlighted by the white/black ovals shows very fine DER microstructure between LAB. The latter also appears to have an inclination angle of approximately 70° to the rolling direction, which matches one of the four angles highlighted in Figure 6.7. Within

this area, regions of low misorientation grains are seen (Figure 6.23c), suggesting a form of recrystallization occurred. This supports the similar findings in the 50CrMo4 DER, i.e. it contains a mixture of low misorientation equiaxed grains as a product of recrystallization and relatively high misorientation fine grains that is a product of martensite fragmentation. Both the fragmentation of the martensite and refinement of the dark etching band microstructure may have contributed to energy build-up and creation of local stress points within DER that has led to recrystallization of equiaxed grains as a form of energy releasing process.

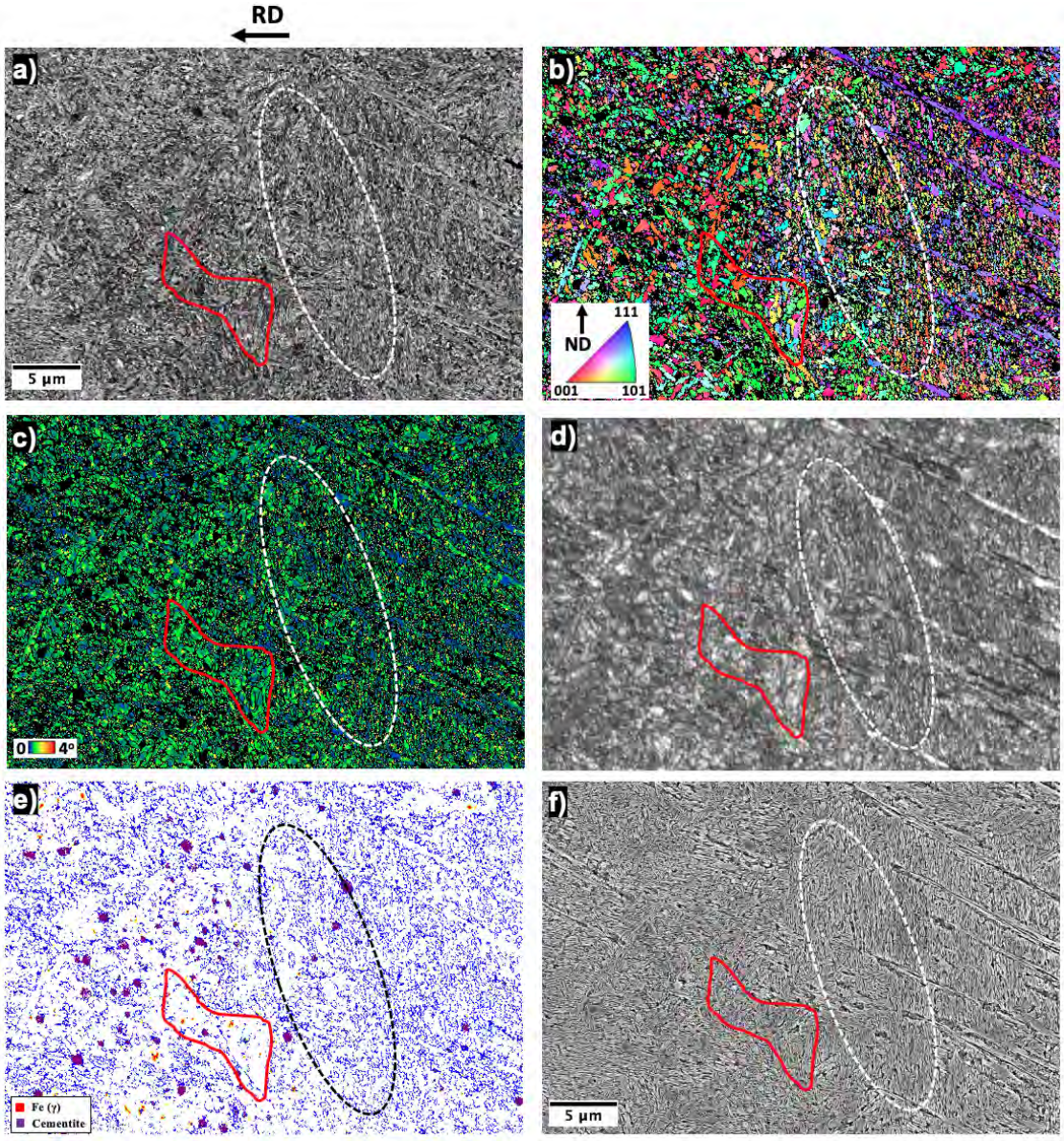

Figure 6.23: Inspection of DER in 100Cr6 sample run under 2.9 GPa for 591 million cycles in an area located at a depth of 120 µm from the surface. Figure shows a) BSE SEM image b) IPF map with direction parallel to normal direction (ND) c) KAM map (100 nm, 5°), d) IQ map e) non martensite-martensite HAGB map and f) SE SEM image. Area highlighted in red shows remains of gradual martensite fragmentation while area highlighted in white/black shows fine DER grains.

Similar to the relationships between the PAGBs and the DER structures found in 50CrMo4, recrystallised equiaxed grains are also formed at both edges of the PAGBs and within prior-austenite grains in the 100Cr6 bearings (see examples shown in Figure 6.24), although the PAGBs appear to be more preferential for the recrystallization sites than inside the prior-austenite grains.

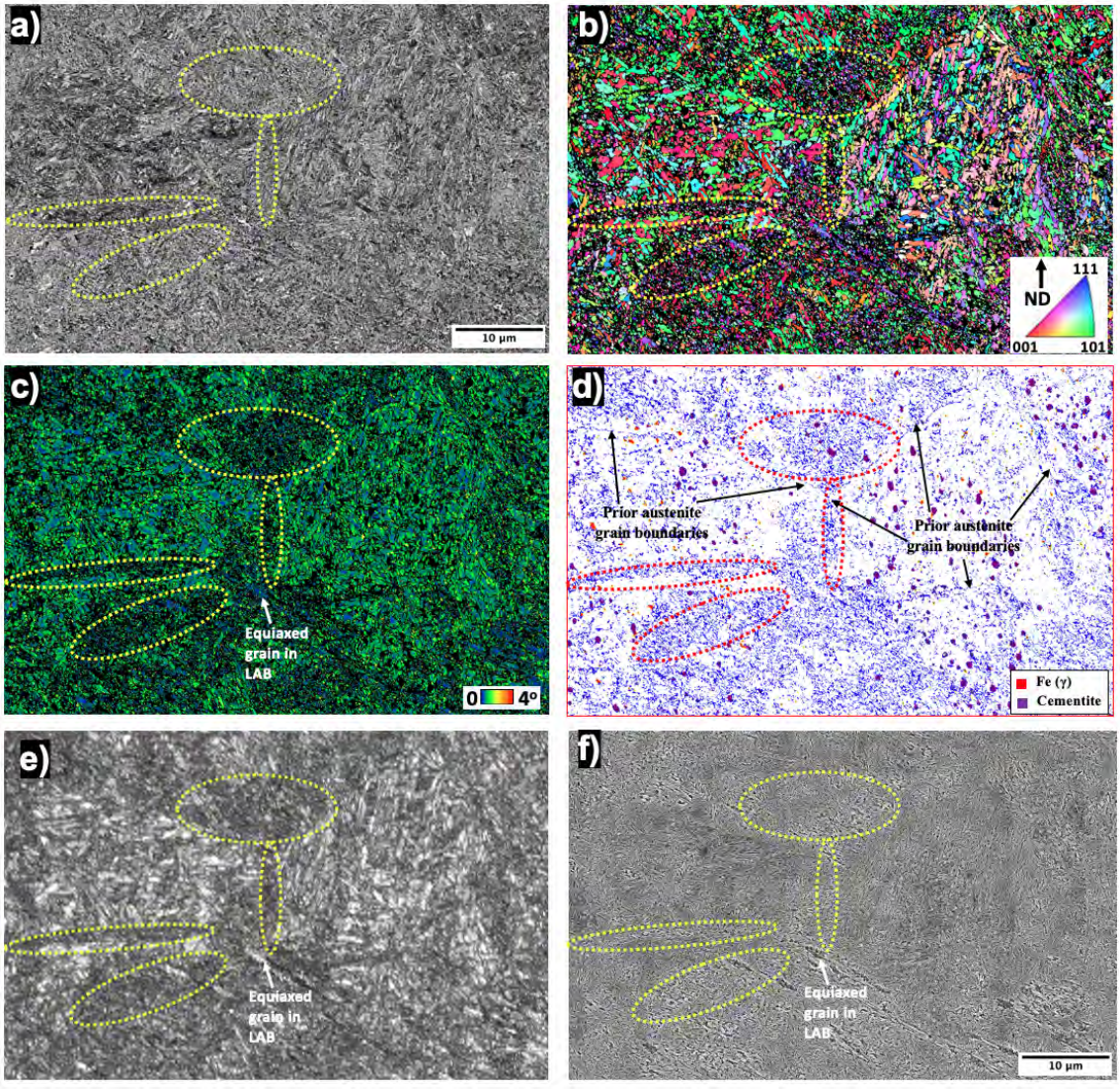

Figure 6.24: Inspection of DER area in 100Cr6 sample run under 2.9 GPa for 591 million cycles surrounding PAGB at a depth of 60 µm from the surface. Figure shows a) BSE SEM image b) IPF map with direction parallel to normal direction (ND) c) KAM map (100 nm, 5°), d) IQ map e) non martensite-martensite HAGB map. and f) SE SEM image. Area highlighted in yellow/red shows altered microstructure linked to DER in reference to PAGBs.

6.4 Nano-indentation Tests

Nano-indentation with an indent matrix of 10 x 40 with a spacing of 5 µm has been conducted on both virgin and RCF tested 50CrMo4 and 100Cr6 bearings, covering an area

from the contacting surface to a depth of 400 µm in each sample. The penetration depth was maintained at 900 nm. Figure 6.25 shows both the optical image of the indentation map and corresponding hardness measurements across the 400 µm subsurface depth for 50CrMo4 specimens run for different stress cycles (the contacting surface locates at the top of the optical images). Error bars through standard deviation has been plotted for hardness measurements at each depth interval (consisting of 10 data points each). Since the main purpose of the tests is to investigate the hardness changes in DER, locations were selected avoiding LAB interference. The results show that as stress cycles increase, an increase in hardness at a depth of 50 - 200 µm is seen, corresponding to the region that becomes 'brighter' or more resistant to etching at later stages (see the optical images of Figure 6.25d and e). The link between the higher hardness and higher etching resistance can also been linked to the refinement of the microstructure evidenced through the EBSD analysis shown in Section 6.3. The grain refinement, which contributes to the increase of hardness, results in high stress concentrations which may result in the recrystallization of equiaxed grains within the DER. This recrystallization has been shown to initiate the formation of LAB (to be discussed in Chapter 7) within the 'brighter regions' of DER. Low hardness measurements are recorded near the surface in all samples in Figure 6.25 which is likely to be an edge effect.

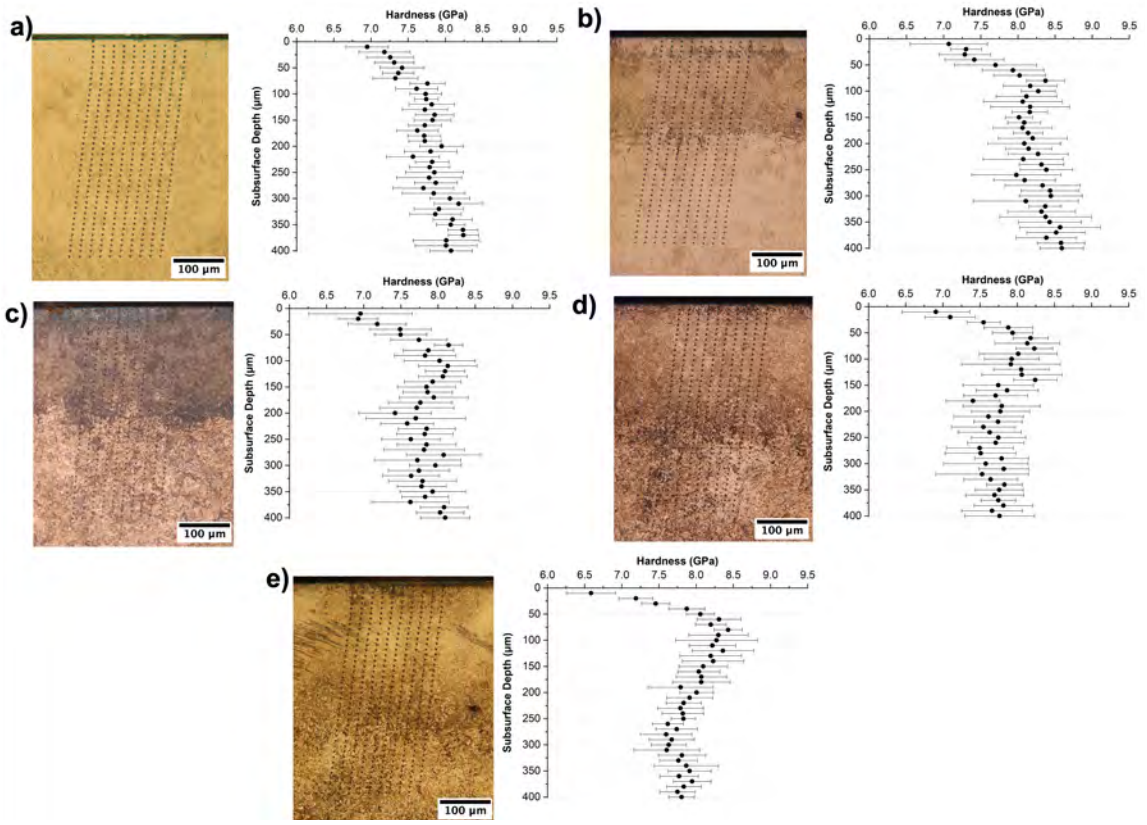

Figure 6.25: Optical image of indentation map and corresponding hardness distribution across the subsurface depth for 50CrMo4 a) virgin sample and samples run for b) 158 million cycles c) 846 million cycles d) 2038 million cycles and e) 7668 million cycles.

Similar observations are seen in the 100Cr6 specimens (see the examples given in Figure 6.26). While the DER in the 591 million cycle sample is difficult to observe under LOM, a similar depth range has been analysed for the comparison. Due to the fast development of LAB in 100Cr6, only the hardness in the 591 million cycles sample is compared with the virgin sample to avoid LAB. Similar to the 50CrMo4, a hardness increase is seen within the DER depth (away from any LAB) due to the refinement observed in the microstructure shown in the EBSD analysis.

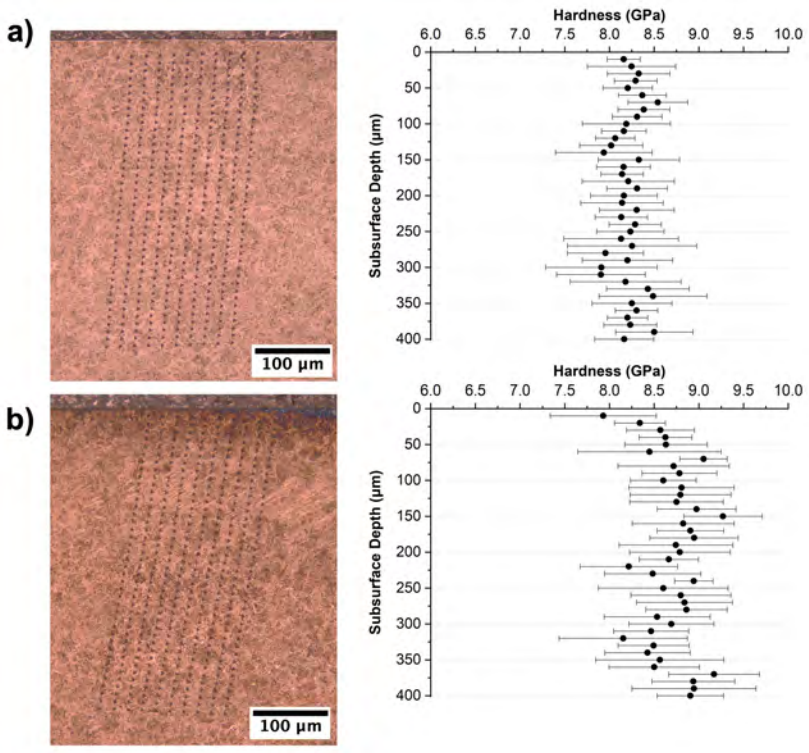

Figure 6.26: Optical image of indentation map and corresponding hardness distribution across the subsurface depth for 100Cr6 a) virgin sample b) sample run for 591 million cycles.

6.5 Discussion

It is shown that the initial stage of DER appears as individual dark etching bands with a thickness varying between 30 and 100 nm and length of up to 7 µm. The nature of these bands has been speculated for decades in literature, which have been named as ferrite microbands [137], deformation bands [80], dark needles [125], persistant slip bands [126] and elongated ferrite grains [14, 120]. The classification of these bands has been challenging due to their small dimensions. The investigation of these DER bands in this study has revealed bright structures adjacent to dark etching bands (Figure 6.4 - 6.12) resembling the etching response of lenticular carbides in WEB (to be discussed in Chapter 7), thus speculating that

these features are carbide structures. If the dark etching bands are indeed ferrite bands as suggested by literature [14, 120, 137, 150], the existence of carbide structures adjacent to the bands would suggest a carbon migration from DER ferrite bands to their edges. This contradicts the dislocation-assisted carbon migration from ferrite bands to pre-existing nano-sized tempered carbide mechanism reported in literature [150]. Based on the carbide-like structures identified in this study being adjacent to the dark etching bands within the DER, it is suggested that the carbon migration links to the formation of new carbides rather than thickening pre-existing tempered carbides. However, the role of tempered carbides in DER formation remains unclear. The fact that DER formation and development in the low carbon 50CrMo4 steel is much more pronounced that that in the high carbon 100Cr6 steel which contains a large amount of primary spherical carbides, suggests that primary carbides are not pre-requisite for DER formation. This agrees with a previous study reporting the distribution of primary carbides within the DER to remain unchanged compared to the unaltered microstructure [120].

The orientation of the dark etching bands has been reported to be random, unlike LAB and HAB that have distinct directionality at $\sim 30°$ and $\sim 80°$ respectively [124, 126, 131]. In the analysis conducted in this study, it was however discovered that the dark etching bands, which appear as parallel bands found within groups, show four dominated orientations corresponding to the rolling direction: a) 15 - 25°, b) 70 - 85°, c) 95 - 110° and d) 130 - 160°. Out of the four groups of orientation, group a) is the most commonly observed orientation followed by group b), which happen to be aligned with LAB and HAB orientations. This suggests that the orientations of the dark etching bands maybe linked to preferential slip systems in steel with some more activated than others. However the orientation features of dark etching band groups become less distinctive at later stages due to the increased dark etching band density which overlap, leading to traces of bands at other angles such as about 180° and 90°. A texture analysis was attempted to investigate the dark etching bands but was inconclusive due to the difficulties encountered in capturing the extremely small dark etching bands within the DER.

The development of DER bands is seen to correspond with the fragmentation of the parent martensite microstructure (Figure 6.15) as the dark etching bands penetrate through martensite laths. At later stages, as the dark etching bands become denser, the DER appears as dark patches under LOM similar to previous observations [120] due to them mainly consisting of heavily-etched dark etching bands. Within the dense patches of dark etching bands, a gradual grain refinement is observed (see Figure 6.15, Figure 6.16 and Figure 6.17a-c). Based on the relatively high misorientation within these refined grains, they are

likely formed through martensite fragmentation induced by plastic deformation. Within the DER patches containing dense dark etching bands, equiaxed grains with low misorientation (Figure 6.15c) are also observed and believed to be products of recrystallization nucleating at high stress points from the refinement process arising from dark etching bands development across martensite laths. Previous studies on alloys under cold rolling and compression tests have reported that deformation bands [185] and shear bands [186] are preferential sites for recrystallization nucleation due to greater dislocation density at intersections (evidenced in Figure 6.11). Shear bands subdivides the original martensite structure into finer grains, introducing more misorientation and stress points. Such a deformed structure could promote recrystallization in DER patches [171] also evidenced in Figure 6.15. This suggests that dark etching bands are a form of shear bands, which develop to cause refinement at intersection points of the dark etching bands of different orientations within the DER.

While early stage DER is shown to consist of multiple dense dark etching bands at various orientations, the bands become less pronounced during later stages due to formation of a refined microstructure (see Figure 6.17 and Figure 6.18). Given that the dark etching bands are responsible for the dark etch response observed under LOM, this would explain why the region shows to have 'brighter' or more etch-resistant areas at later stages, suggesting a breakdown of the dark etching bands occurs alongside the refinement of the original parent microstructure. A TEM investigation on adiabatic shear bands by Li et al [187] has proposed a refinement mechanism of elongated ferrite grain structures, where under high shear stress, the elongated grain (see Figure 6.27) containing clusters of entangled dislocations goes through partitioning and/or breaking down of the grain by entangled dislocation clusters and splitting and rotating of the grain respectively, leading to the formation of subgrains. The splitting may be enhanced as bands of different orientation intersect, leading to grain refinement.

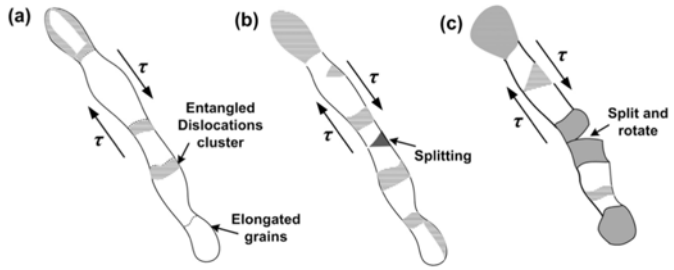

Figure 6.27: A schematic illustration of the grain refinement process (a) the elongated grain and entangled dislocation clusters at various sections; (b) grain refinement either through partitioning and breaking down the elongated subgrains by entangled dislocations clustering or through splitting and rotating the elongated subgrains into small grains; (c) subgrains formed [188].

The proposed refinement process in the DER is supported by the hardness increase evidence shown in Figure 6.25 and Figure 6.26. While the hardness of DER has been confusing in literature, e.g. a reduction reported in [82, 124] and an increase in [125, 126], it could be due to the lack of understanding of this refinement process involved in DER development, i.e. two competing mechanisms of softening due ferrite formation and carbon migration as well hardening due to refinement of parent microstructure. However, carbon redistribution has been reported to be minimal at micro-scale [120] or more observable at nano-scale [118], thus its influence on DER developed is likely to be modest when comparing the overall microstructure hardness.

The role of PAGBs on the formation of DER remains unclear as recrystallisation of equiaxed grains are found to be initiated at either the bounderies due to high dislocation densities at the PAGBs [189, 190] or within prior-austenite grains (Figure 6.21 and 6.24), which has also been reported [127].

6.6 Conclusion

The investigation of the microstructures of DER has been focused on the 50CrMo4 specimens due to the captured multiple development stages. Detailed analysis using a combination of BSE and SE SEM imaging, EBSD analysis and nanoindentation has provided evidence not only the microstructural components within DER but also how they evolve during bearing operation and their formation mechanisms from early to late stage. The conclusions of this chapter are summarized below.

- Initial stage of DER formation is the development of thin dark etching bands that grow in density in groups of different orientations. The dark appearance of the bands under LOM are due to them being heavily etched. Dark etching bands are found to grow in the parent microstructure in the highest stressed region, leading to martensite fragmentation and refinement as they become more dense. The refined microstructure is found to have an increased hardness.

- Dark etching band groups within the DER have shown to be oriented at four dominated angles inclined to the rolling direction, i.e. 15 - 25°, 70 - 85°, 95 - 110°, 130 - 160° with 15 - 25° and 70 - 85° being the most frequent orientations out of the four.

- Bright structures at the edges parallel to the DER bands are observed which show a similar etching response to lenticular carbides in WEB. These structures are therefore likely to be newly formed carbides due to carbon migration from the dark etching

bands (ferrite) rather than migrating to thicken pre-existing tempered carbides as suggested in literature.

- At later stages, the dark etching bands become less pronounced leading to a brighter appearance under LOM. This is due to the refinement process where a breakdown of the dark etching bands occur as multiple bands at various orientations intersect, leading to the development of equiaxed grains. The developed DER microstructure consists of fine grains due to martensite fragmentation and equiaxed grains with low misorientation as a product of recrystallization. High stress points formed in dense dark etching bands areas, due to martensite fragmentation and intersecting points of different dark etching bands, act as nucleation sites for equiaxed ferrite grains of low misorientations.

Findings on DER presented in this Chapter is combined with those on WEB presented in Chapter 7 for the development of a unified formation mechanism linking DER, LAB and HAB development in Chapter 8.

Chapter 7

Mechanistic Study of LAB and HAB

Following the study of the evolution and development of WEB in RCF-tested bearings under optical microscopy, detailed analysis has been conducted on the samples using SEM, TEM and APT to investigate LAB and HAB initiation and growth mechanisms. The results from the martensitic 100Cr6 samples are presented first followed by a comparison with the 50CrMo4 samples. Given the similarity in WEB development under different steel cleanliness in Chapter 4, differentiating the LAB and HAB under different steel cleanliness in this chapter is considered irrelevant, hence only the different steel alloys of 100Cr6 and 50CrMo4 is analysed.

7.1 LAB Evolution

This section presents experimental findings on LAB observed in a range of bearing samples and how the LAB evolve from early to late development stages by detailed analysis of features related to LAB. Based on the development of the three different microstructural alteration features observed (reported in [120]), i.e. equiaxed grains, elongated grains and lenticular carbides, LAB are found to develop in three stages.

7.1.1 Early Stage

Short (<10 µm in length) single LAB have been observed in samples after low stress cycles (< 1000 million cycles) in 100Cr6 bearings (Figure 7.1 a-c) as well as at the band boundaries in samples after high stress cycles (> 1000 million cycles) as shown in Figure 7.1d-i, which appear to be at their earliest stages. Although observed in different samples under different pressure and stress cycles, all LAB presented in Figure 7.1 show to have

similar characteristics, i.e. at a few µm in length and less than 1 µm in width, and the LAB consist of equiaxed ferrite grains (indicated by the red arrows in Figure 7.1). Investigation of the grain structure is given in the EBSD results presented in Section 7.4. This agrees with previous findings that LAB formation is heavily influenced by the contact pressure at the bearing contacts or subsurface shear stresses and that the density of LAB follows the distribution of the shear stresses in the subsurface, suggesting that LAB formed at the boundaries of the WEB region are at an earlier stage than those in the middle of the region. Figure 7.1e shows the growth of an equiaxed ferrite band (in length and thickness) involving a dissolution of an adjacent primary carbide (highlighted in green).

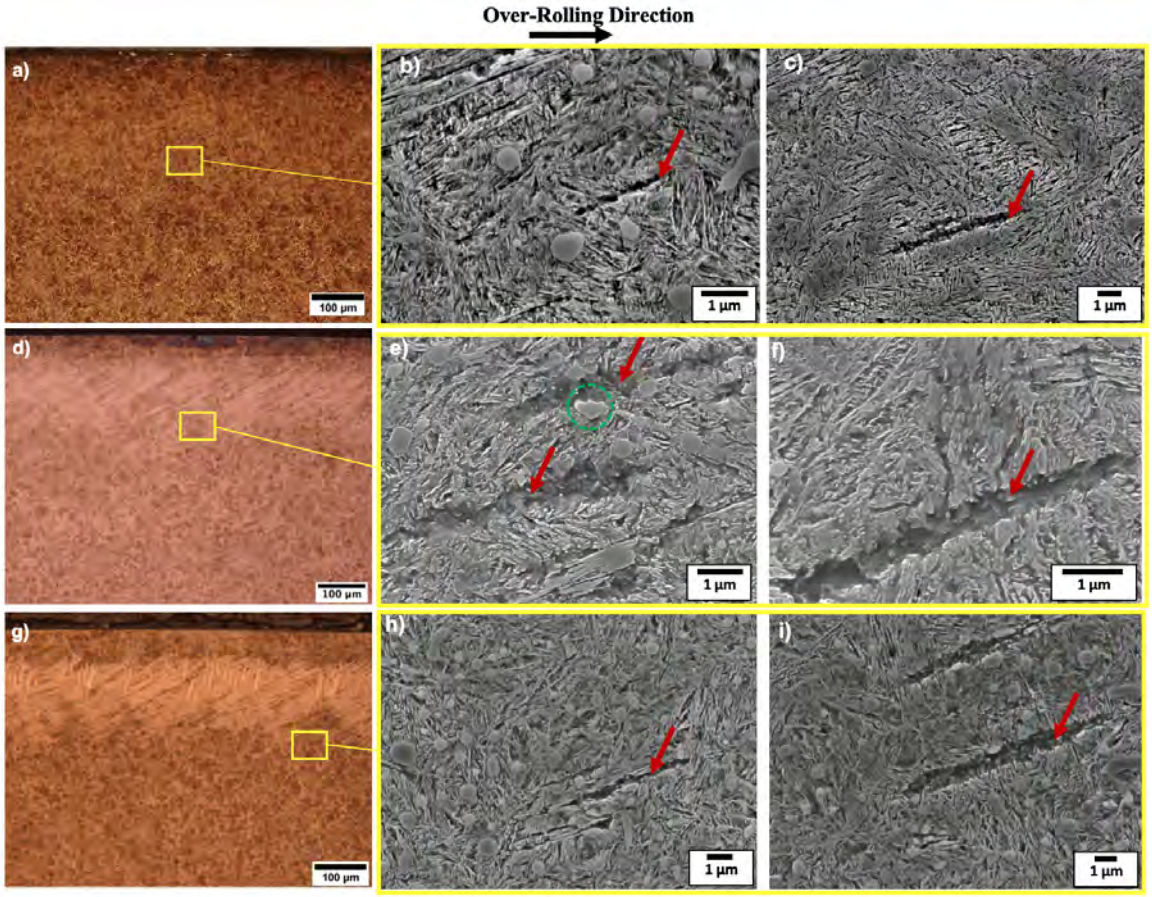

Figure 7.1: Images of early stage LAB in 100Cr6 bearings. a) in a sample under 3.5 GPa for 679 million cycles. b) and c) SEM images from the region highlighted in a). d) in a sample under 2.9 GPa for 1116 million cycles. e) and f) SEM images from the region highlighted in d) with LAB from the lower boundary of the WEB region. g) in a sample under 2.9 GPa for 3016 million cycles. h) and i) SEM images from the region highlighted in g) with LAB from the lower boundary of the WEB region. Green area shows the dissolution of a primary carbide.

7.1.2 Intermediate Stage

After the initial/early stage where LAB are very small containing only equiaxed grains, LAB are found to grow in length and width, in the meantime, elongated grains are seen to

initiate within the LAB followed by growth of elongated grains and initiation and growth of lenticular carbides adjacent to the elongated grains (see images in Figure 7.2). Thus, the intermediate stage of LAB is characterised by the formation of elongated ferrite grains and lenticular carbides within equiaxed grain bands. The elongated ferrite grains are thin needle-like structures appearing as groove or crack-like structures under SEM due to etching [120] while the lenticular carbides are the smooth bright structures adjacent to the elongated grains due to their resistance to etching, indicated by yellow arrows in Figures 7.2c and 7.2d. From the images, it is also clear that lenticular carbides nucleate from the edge of elongated grains and grow in both length and thickness adjacent to the elongated grain.

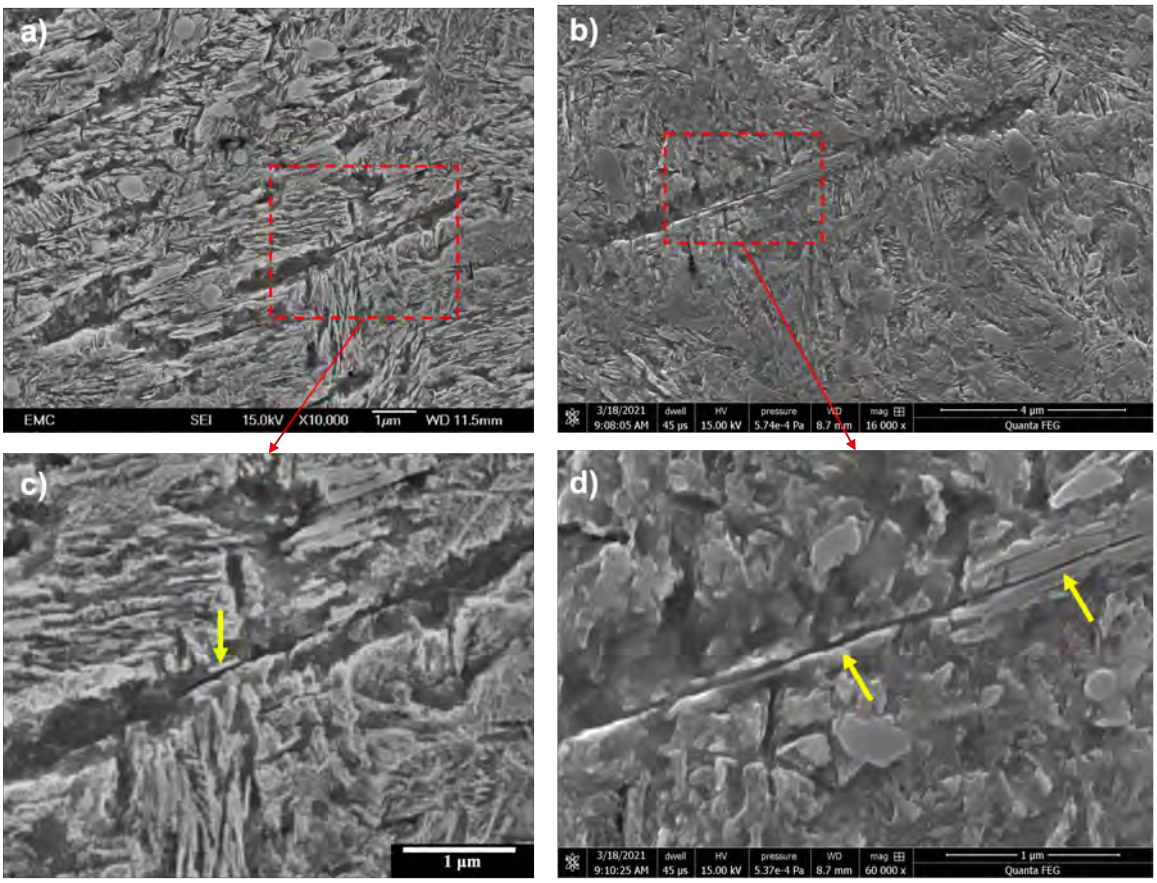

Figure 7.2: Images of intermediate stage LAB from 100Cr6 samples under 2.9 GPa for, a and c) 591 million cycles, b and d) 1116 million cycles, showing elongated ferrite grains formed in the middle of an LAB of equiaxed grains and lenticular carbides initiated adjacent to the elongated grains (in c) as well much developed lenticular carbides (in d). Yellow arrows point towards the elongated grain and lenticular carbides structures.

Over the increase of stress cycles, both elongated ferrite grains and the adjacent lenticular carbides continue to grow in the equiaxed ferrite band until a 'cotton-bud' shape is formed, where equiaxed ferrite grains form the 'heads' and the elongated ferrite grain and lenticular carbides form the stem (see Figure 7.3a-c). The lenticular carbides areas have been found to be carbon-rich from a previous study [120]. Primary carbide dissolution has been observed and is believed to be involved in the LAB formation process (see Figure 7.3d).

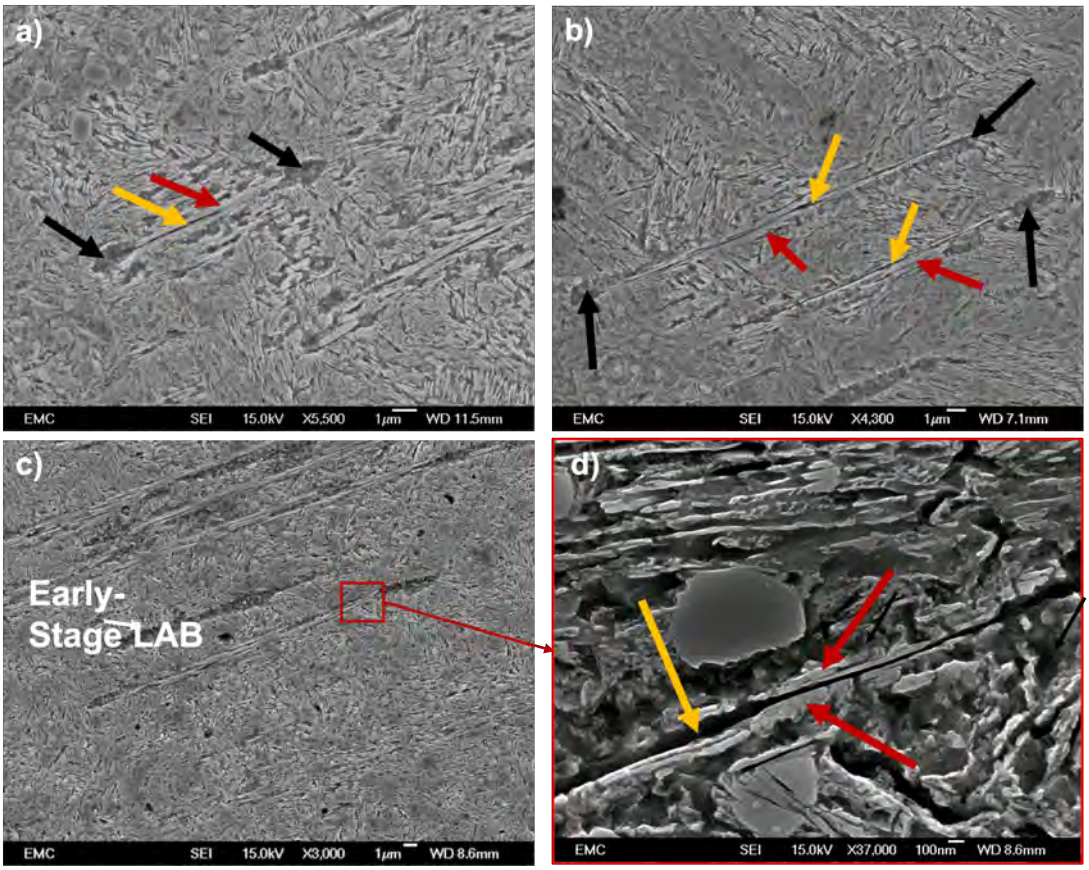

Figure 7.3: SEM images showing cotton-bud shape of LAB from 100Cr6 samples under 2.9 GPa for a) 591 million cycles b) 3016 million cycles c) 4141 million cycles, and d) a view of the elongated ferrite grain, adjacent lenticular carbides and primary carbides nearby the LAB from the area highlighted in c). Black, yellow and red arrows point to equiaxed ferrite grains, elongated ferrite grains and lenticular carbides respectively.

To study the elongated ferrite grains and lenticular carbides in 3-dimensions, manual serial sectioning has been conducted on individual LAB in a bearing sample tested under 2.9 GPa for 4141 million cycles. SEM images were taken at each stage/slice as material was removed revealing the underlying structures. The slice removed between each stage was approximately 1 µm thick and the twelve slices are shown in Figure 7.4. It is evident that lenticular carbides nucleate at the edge of the elongated ferrite grain and grow in both length and thickness along the elongated grain. A significant reduction in the thickness of the equiaxed ferrite grains in the LAB is observed in the 3rd slice (circled in green) of the series in Figure 7.4. This reduction in size appears to be the initiation of the 'cotton-bud' shape evidenced through the equiaxed grain 'cotton-bud' head on the left side. Looking from that point onwards, the emergence of a newly formed lenticular carbide becomes visible. The elongated ferrite feature (yellow arrow) is more pronounced from Figure 7.4(8) onwards as it grows across the length of the band (equiaxed ferrite region). Comparing the lenticular carbide (red arrow) and elongated ferrite (yellow arrow), it can be easily seen that the lenticular carbide grows in a pattern associated with the elongated ferrite until a thin

structure is formed in the 12th slice of the series showing in Figure 7.4 similar to that of the 'cotton-bud' stem.

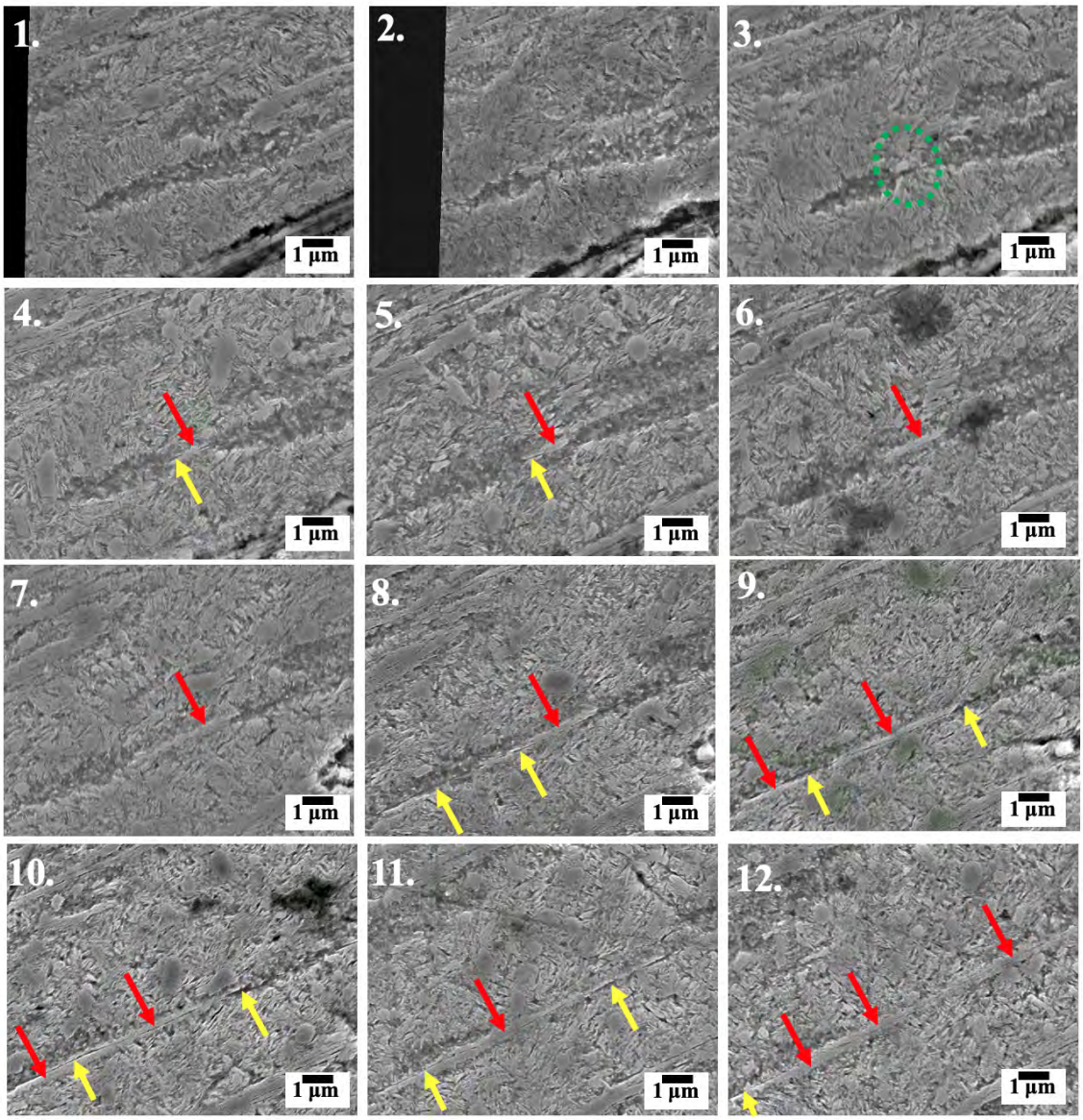

Figure 7.4: SEM images of LAB from 100Cr6 sample run under 2.9 GPa for 4141 million cycles: from 1 to 12 in the sequence of serial sectioning at ~ 1 µm thickness interval, showing the growth of lenticular carbides in both thickness and length adjacent to the elongated grain. Red arrows indicate lenticular carbide and yellow ones elongated ferrite grains.

Closer inspection of the LAB from two adjacent slices of Figure 7.4 (no. 11 and 12) presented in Figure 7.5 has shown that the lenticular carbides grow outwards from the elongated ferrite grain (See in Figure 7.5a). It also shows that lenticular carbides grow in thickness (thickness of up to 400 nm recorded in Figure 7.5) across elongated ferrite grains (with a thickness in the range of 40-100 nm) perpendicular to the length of the elongated grain at both sides (see in Figure 7.5b).

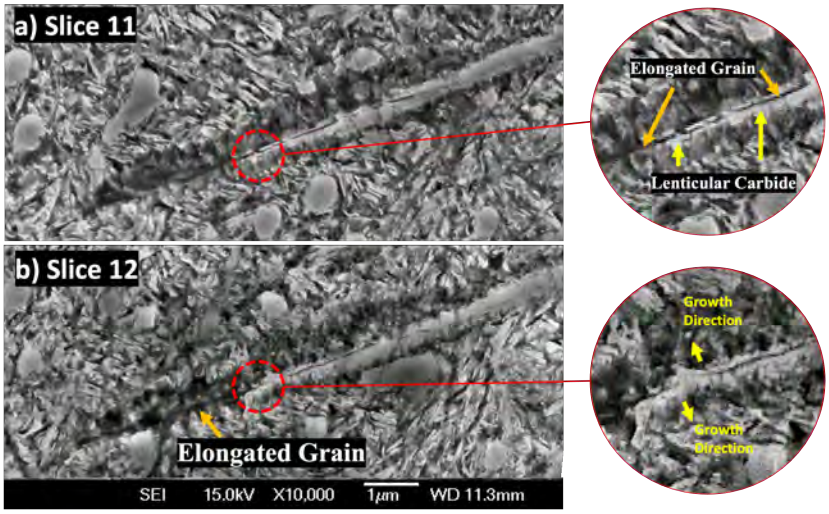

Figure 7.5: SEM images of slices no.11 and 12 in Figure 7.4, showing discontinuity of lenticular carbides growth along the elongated grain in a) and growing perpendicular to the length and at both sides of the elongated grain in b)

7.1.3 Late Stage

The LAB structures shown in Figures 7.1 to 7.5 are single or relatively small bands (at a few tens of µm in length and a couple of µm in width). At later stages, multiple single LAB grow into 'clusters' (examples given in Figure 7.6). By this stage, it is difficult to single each band out as they have grown into each other forming large LAB areas of different widths (red double arrows show the widths of these areas in Figure 7.6). The LAB clusters in Figure 7.6 are still shown to contain the three features same as those in single bands at earlier stages, i.e. equiaxed ferrite grains, elongated ferrite grains and lenticular carbides (Figure 7.6). Multiple parallel elongated ferrite grains with lenticular carbides at the their edges are observed closely packed within the equiaxed grain region of the LAB. However, no lenticular carbides are found to have formed within equiaxed ferrite grains without elongated ferrite grains. The comparison between all three constituents could be seen in Figure 7.7 where the elongated ferrite grains are shown as thin dark needles within the equiaxed region with the thickness shown in Figure 7.7b to vary from 30 to 400 nm which remains much thinner than the thickness of the equiaxed ferrite grain region which makes up most of the LAB. The size of the LAB widths ranges from 2 to 8 µm, as shown in Figures 7.6 and 7.7.

At even later stages (i.e when saturation level reported in Chapter 4 is achieved) and LAB are fully formed, especially within the region of the maximum shear stress , and no 'gap areas' are seen in the WEB region any more (see in Figure 7.8b). The whole region is fully covered by dense LAB structures. Within this area all three constituents of the LAB are observed while no remains of the parent martensite microstructure can be seen. While the LAB are found to be very dense within the maximum shear stress region, individual

LAB are still observed at the lower boundary of the WEB in the subsurface (see them in Figure 7.8c). The individual LAB in this region appear to be within observable 'cotton-bud shape' similar to those in earlier stages shown in Figure 7.2.

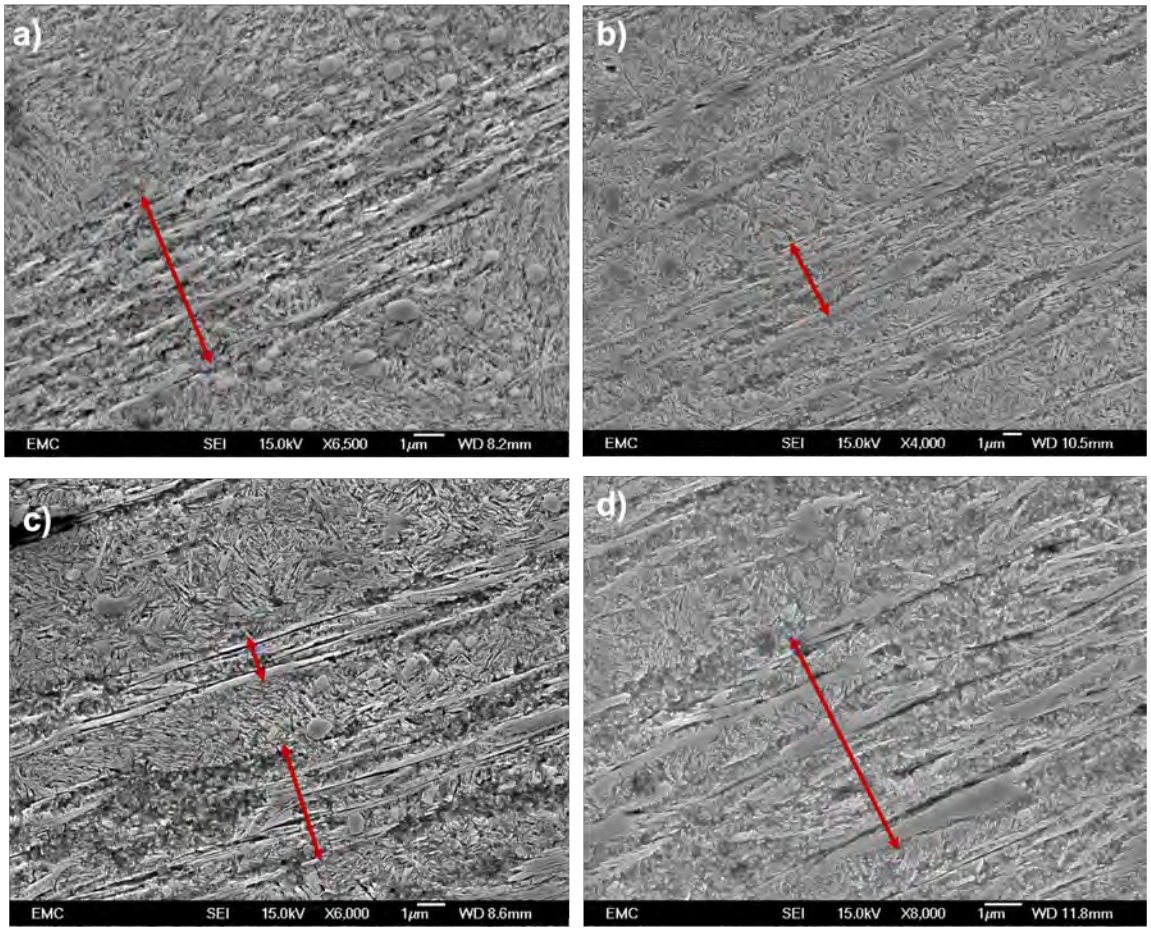

Figure 7.6: SEM images of late stage LAB from 100Cr6 samples a) under 3.5 GPa for 151 million cycles, b) under 2.9 GPa for 3016 million cycles, c) under 2.9 GPa for 4141 million cycles and, d) under 3.5 GPa for 679 million cycles. Widths of late-stage LAB are highlighted in red arrows spanning from 2-8 µm.

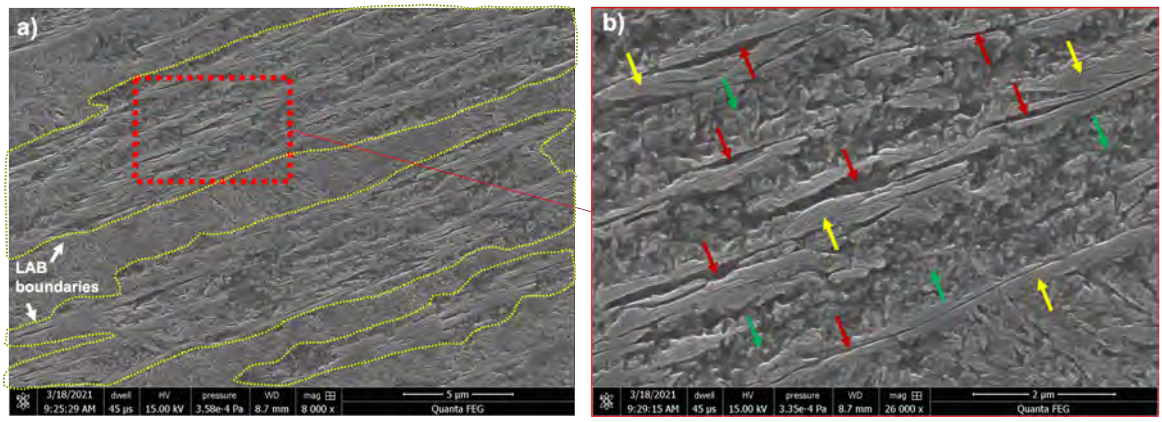

Figure 7.7: a) Thick late-stage LAB from 100Cr6 sample under 2.9 GPa for 1116 million cycles with LAB boundaries highlighted in dash lines. b) Higher magnification of late stage LAB showing all three LAB constituents. Red arrows indicate elongated grains, yellow arrows indicate lenticular carbides and green arrows are equiaxed grains.

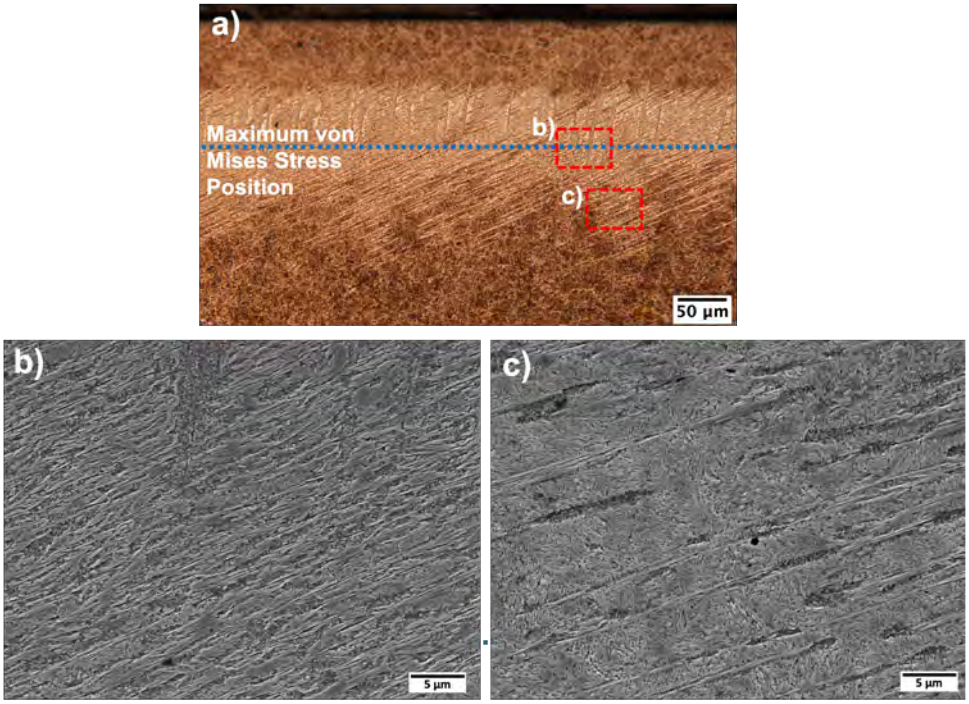

Figure 7.8: Images of late stage LAB from 100Cr6 bearing tested under 2.9 GPa for 3016 million cycles, showing a) an optical image of WEB (blue line indicates the position of the maximum stress region). b) An SEM image of WEB in the maximum shear stress region highlighted in a) where dense WEB are formed. c) An SEM image of WEB in the area highlighted in a) at the lower boundary of the WEB where less dense LAB are formed.

7.2 HAB Evolution

During the late stages of LAB, HAB are found to initiate and grow in the dense region of LAB as highlighted in Chapter 4, which coincides with the maximum shear stress region in the subsurface. Figure 7.9 shows SEM images of early stage and late stage HAB based on the number of stress cycles experienced in 100Cr6 bearings. Although, the HAB samples in Figure 7.9 are under different contact pressures, the difference in stress cycles justifies the early stage (Figure 7.9a) and late stage (Figure 7.9b) of HAB development. It is demonstrated in Figure 7.9 that HAB increase in width and length as they develop. The HAB in Figure 7.9a has been measured with a thickness reaching 1.5 µm and length of 16 µm while the later stage HAB in Figure 7.9b has a measured thickness and length of 5 µm and 70 µm respectively. Similar to LAB, the early stage HAB (Figure 7.9a) is shown to consist mainly of equiaxed ferrite grains while elongated grain structures develop later within the equiaxed band at a later stage in a similar manner (Figure 7.9b).

SEM images in Figure 7.10 show the gradual development and growth of elongated grains in a single HAB. In Figure 7.10a, the HAB at its earliest stage shows to contain only equiaxed grains, where small elongated grains appear in a larger HAB at later stages (Figure 7.10b and c) and become more pronounced as the HAB grows. It is also shown in

Figure 7.10d that multiple elongated grains may develop within an individual HAB.

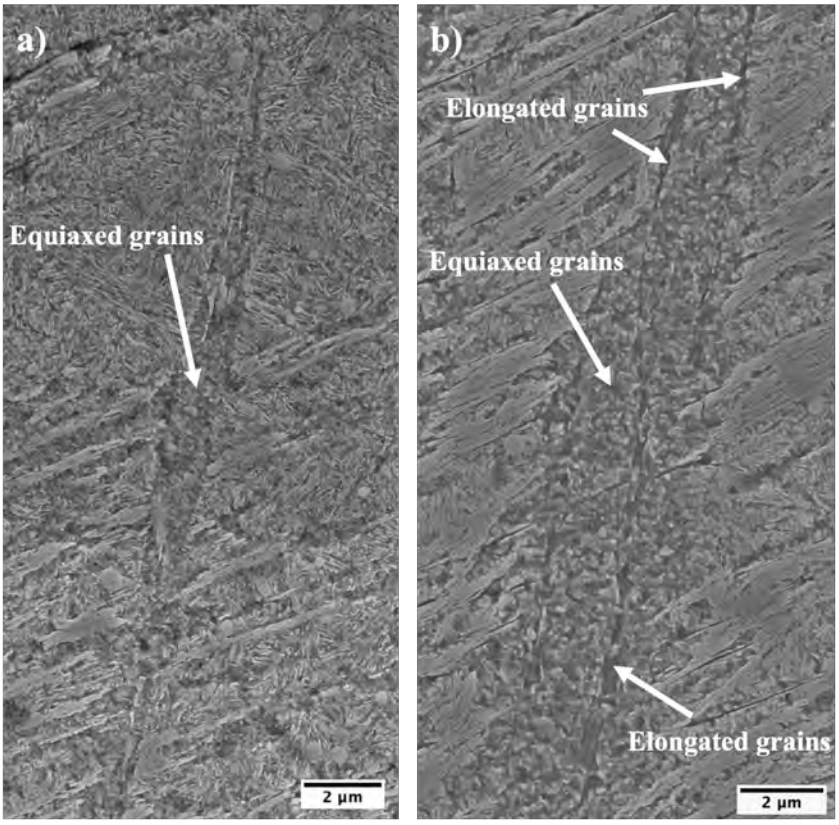

Figure 7.9: SEM images of HAB in 100Cr6 bearings a) at the early stage from a sample tested under 3.5 GPa for 671 million cycles and b) late stage from a sample tested under 2.9 GPa for 3016 million cycles.

One of the differences in the HAB evolution comparing with the LAB is that no lenticular carbides are seen to form adjacent to the elongated grains (Figure 7.10). During the early stage of HAB formation, the lenticular carbides as well as elongated grains of the LAB are still seen within the newly formed HAB (Figure 7.11a). Such pre-existing features are found to gradually dissolve within the equiaxed band during the intermediate stage (Fig. 7.11b) of HAB formation when the HAB grows in both thickness and length within the dense LAB network. Outside the HAB, these features remain unchanged. As the HAB grows, lenticular carbides in the LAB start to 'merge' at the boundary of the HAB, marking the intermediate stage of HAB formation. This suggests that the lenticular carbides in the LAB at the edge of the HAB act as carbon sinks for carbon in the HAB to migrate out of the HAB rather than forming new carbides adjacent to the elongated grains in the HAB. As the lenticular carbides grow at the edges of the HAB, they eventually merge together forming smooth and clear boundaries between the HAB's equiaxed ferrite region and the lenticular carbides (see Figure 7.11b and c). When multiple HAB form in between the LAB, as shown in Figure 7.11d, it reaches the late or final stage of HAB evolution. The distance between individual HAB is seen to be about 5 µm or less when fully developed.

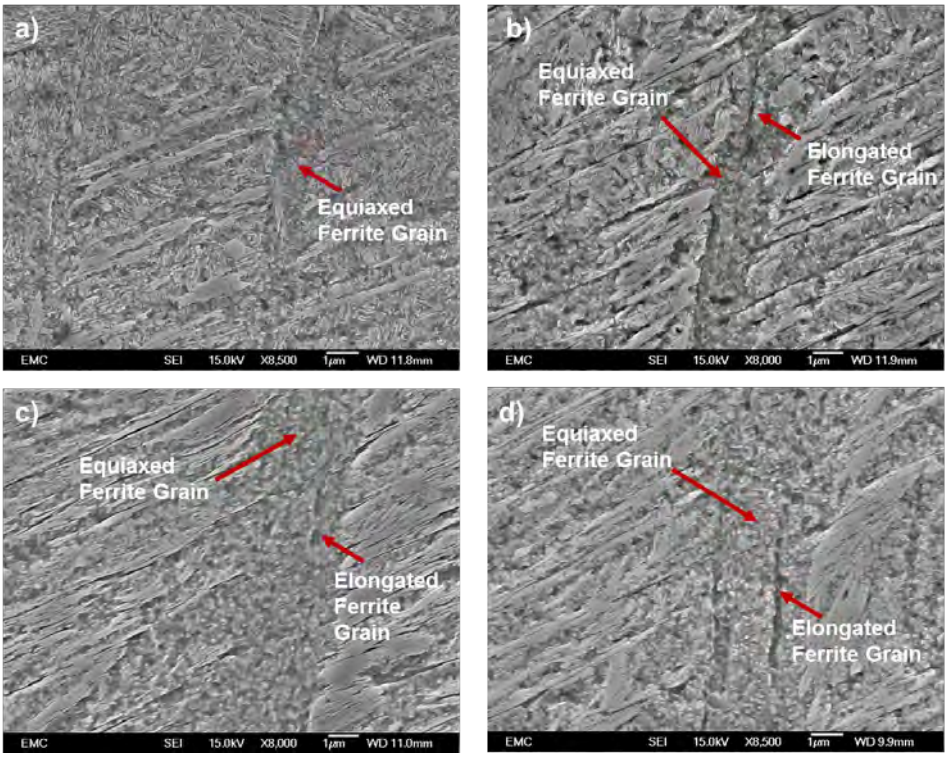

Figure 7.10: SEM images of HAB in 100Cr6 bearings tested a) under 3.5 GPa for 679 million cycles, and b, c, d) under 2.9 GPa for 1338, 3016 and 4141 million cycles respectively, showing the development of equiaxed ferrite and elongated ferrite grains during the HAB formation.

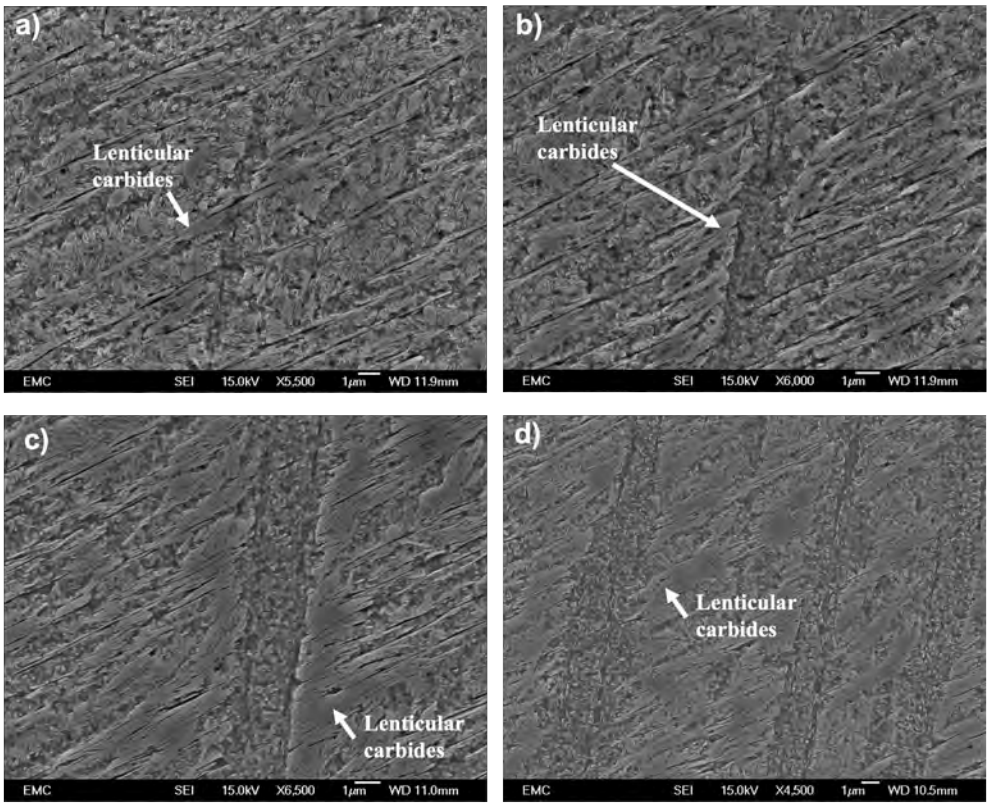

Figure 7.11: SEM images of HAB from 100Cr6 bearing samples tested under 2.9 GPa for a) 1116, b) 1338, c and d) 3016 million cycles, showing the evolution of HAB from early (a) to intermediate (b) and late (c and d) stages and surrounding lenticular carbides.

7.3 LAB in 50CrMo4

The formation process of LAB is significantly slower in 50CrMo4 bearings compared to that in the 100Cr6 ones under similar operating conditions as highlighted in Chapter 4. This has resulted in less LAB detected in the 50CrMo4 bearings in comparison. Given that HAB formation is proposed to develop under dense closely-packed LAB (see Chapter 4 and 5), this would explain why no HAB have been observed in the 50CrMo4 samples available to this study.

LAB evolution in 50CrMo4 has been investigated in this section similar to the previous results in this chapter recording the evolution of LAB in 100Cr6 samples. A similar LAB evolution stages has been observed, including the initiation stage of single LAB with equiaxed grains (Fig. 7.12a), intermediate stage when elongated grain and lenticular carbides co-grow (Fig. 7.12b and c) and the latest stage when clusters of LAB form (Fig. 7.12d). Comparing with the 100Cr6 bearings, all LAB formation stages experienced much higher stress cycles (Figure 7.12) due to the slow responses of the material to RCF.

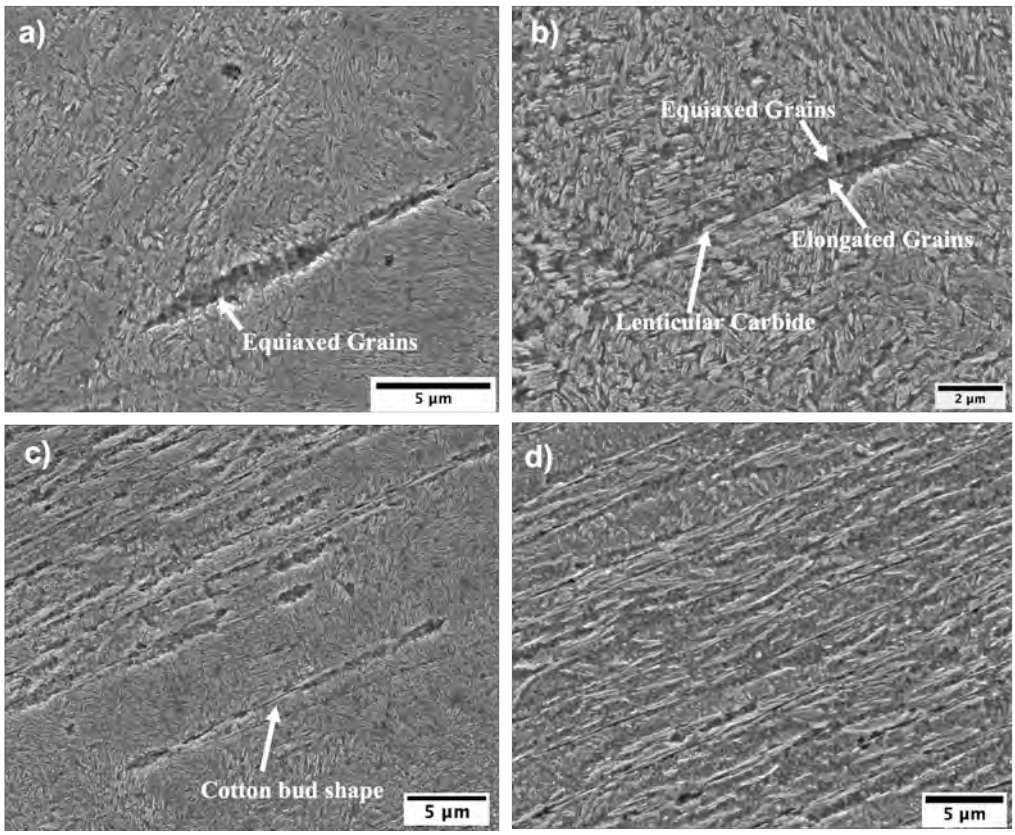

Figure 7.12: SEM images of LAB from 50CrMo4 bearing samples tested under 2.9 GPa for a) 846, b)1626, c) 2038 and d) 7668 million cycles, showing a) early stage LAB consisting on equiaxed grains. b) elongated grains and lenticular carbide within the equiaxed grain band. c) intermediate stage LAB showing cotton-bud shape. d) late stage LAB consisting on multiple elongated grains and lenticular carbides within a region of equiaxed grains.

7.4 EBSD Analysis of WEB

To confirm the grain structures during WEB evolution, HAB and LAB formed in a range of samples (mainly focused on 100Cr6 samples) have been analysed using EBSD. The results are presented as evidence to support findings from the SEM investigation shown previously. For EBSD analysis, an unetched surface is required to achieve the required surface finish. BSE SEM imaging of the features is conducted in this section showing orientation contrasts rather than SE imaging which requires an etched surface. It should be noted that all IPF and KAM maps in this section consist of points indexed as bcc with CI > 0.1.

7.4.1 HAB

HAB investigation has been conducted on the 100Cr6 bearing specimen run for 3016 million cycles under 2.9 GPa to analyse fully developed HAB and their formation at late stages. Figure 7.13 presents a series of SEM/EBSD images of fully formed HAB, including a BSE and a SE image, a KAM map, an IQ map, an IPF map and a HAGB map. To see more details, the areas highlighted in Figure 7.13 are presented in Figure 7.14 at a higher resolution. While it is hard to identify elongated grains in the HAB in the BSE images, they can be easily identified in the SE SEM image, KAM, IQ, IPF and HAGB maps (in both Figures 7.13 and 7.14). The grain boundaries in the HAGB map (Figure 7.14e) clearly show a difference in grain structure between the elongated ferrite grains and the surrounding equiaxed grains in the HAB where the former is much larger in size and has the long axis parallel to the band orientation ($\sim 30^\circ$ for LAB and $\sim 80^\circ$ for HAB). Also, the equiaxed grains in the HAB have shown to have relatively low misorientation (Figure 7.13c and 7.14c) compared to the elongated grains and surrounding microstructure. Equiaxed grains also show a relatively high IQ contrast (Figure 7.13d and 7.14d), evidenced by the higher brightness comparing with that of the surrounding microstructures except the elongated grains, indicating regions with relatively lower local strain, dislocation density and defects as a typical outcome of recrystallization in deformed materials in response to build-up of stored energy [171]. Since newly formed ferrite phases typically would have lower internal strains comparing with martensite [170], a higher IQ contrast is shown for them. This also provides the evidence supporting the hypothesis that equiaxed grains are ferritic and are formed likely due to recrystallization [120]. From Figure 7.13b, a general alignment of the grain structures with a <111> axis approximately parallel to the normal direction (ND), particularly the elongated grains, is seen. Also, the equiaxed grains appear to have a larger variation in grain orientations comparing with the elongated grains (Figure 7.14b). It should be noted that the lenticular carbides have not been indexed under EBSD analysis

(appear black in EBSD maps) due to the carbide crystallite size being smaller than the special resolution of this EBSD.

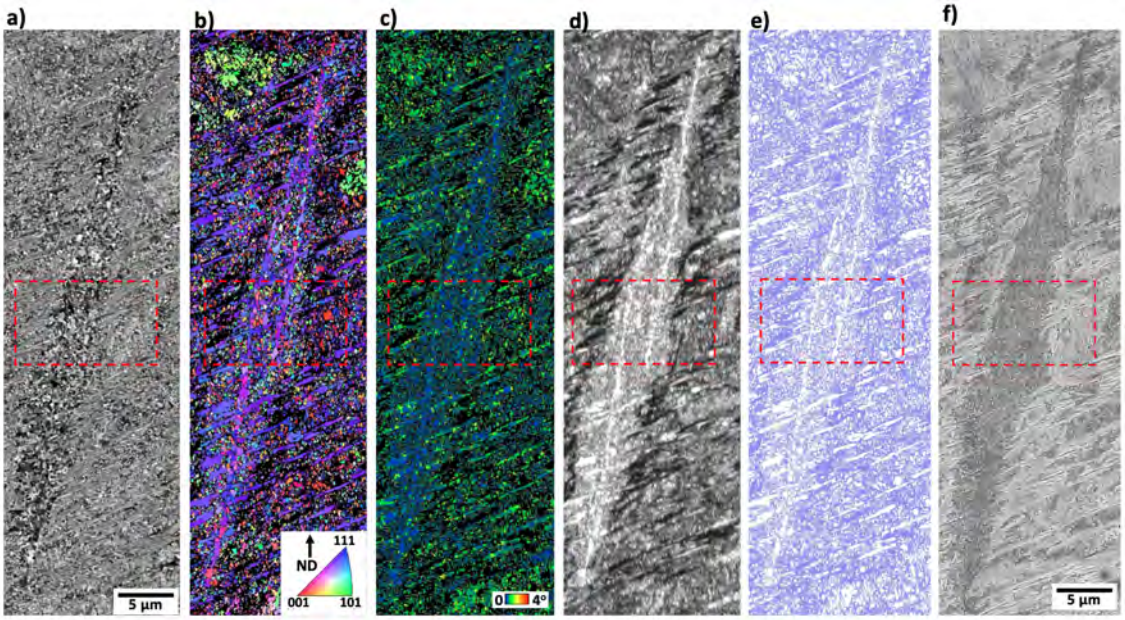

Figure 7.13: Characterisation of HAB in 100Cr6 bearing sample tested under 2.9 GPa for 3016 million cycles with developing elongated grain showing a) BSE SEM image b) IPF map showing directions parallel to normal direction c) KAM map (100 nm, 5°) d) IQ Map e) HAGB map (blue line indicates grain boundaries with misorientations ≥ 15°) and f) SE SEM image

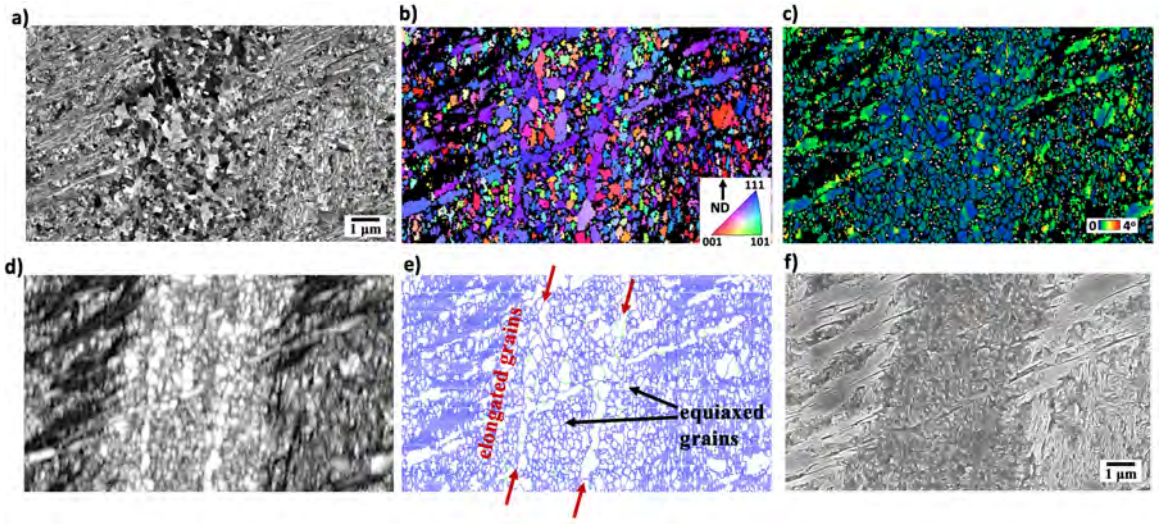

Figure 7.14: SEM images of the area highlighted in Figure 7.13 showing a) BSE SEM image b) IPF map showing directions parallel to normal direction c) KAM map (100 nm, 5°) d) IQ Map e) HAGB map (blue line indicates grain boundaries with misorientations ≥ 15°) and f) SE SEM image.

Figure 7.15 presents another HAB within the same 100Cr6 sample (2.9 GPa 3016 million cycles), showing a fully formed elongated grain of about 8 µm in length within the HAB comparing with those less developed in Figure 7.13. This elongated grain has a more distinct texture (uniform colour in the IPF map in Figure 7.15b) and is much bigger comparing with

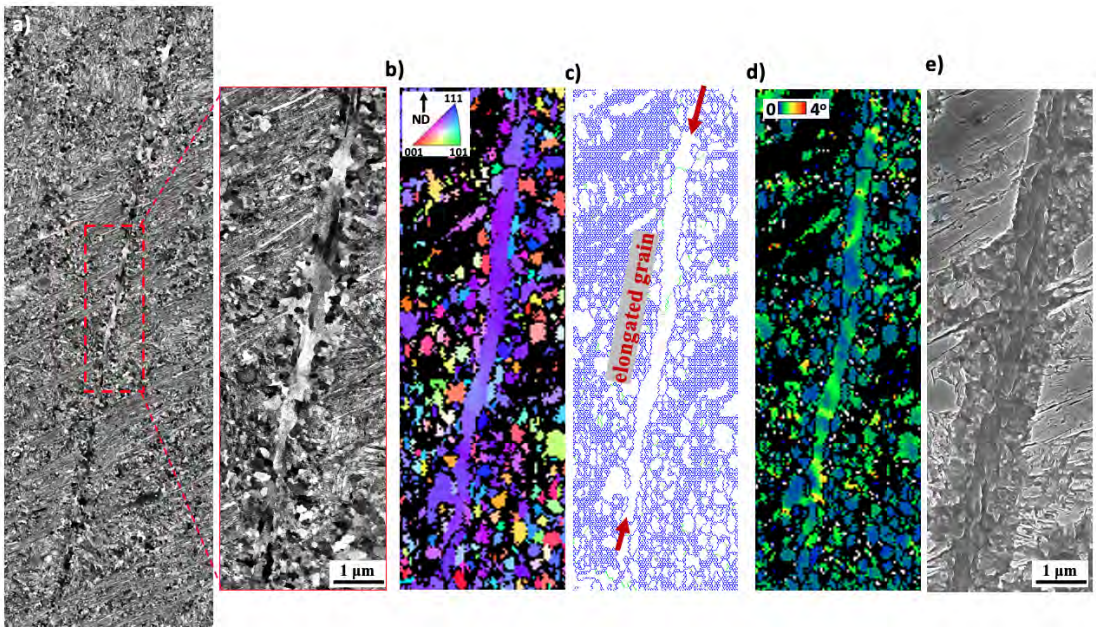

Figure 7.15: Characterisation of a late-stage HAB with developed elongated grain in a 100Cr6 bearing sample tested under 2.9 GPa for 3016 million cycles. a) BSE SEM image b) IPF map showing directions parallel to normal direction c) HAGB map (blue line indicates grain boundaries with misorientations $\geq 15°$) d) KAM map (100 nm, 5°) and e) SE SEM image

the surrounding equiaxed grains that range in size from 100-300 nm based on those in Figures 7.14 and 7.15 at various grain orientations. Comparing the structures of the elongated grains in the two HAB shown in Figures 7.14b,7.14e and Figures 7.15b and 7.15c, elongated grains at the less developed stage (Figure 7.14) consist of multiple coarse grains of various orientations while at later stage (Figure 7.15) it consists of a single large, elongated grain under a more uniform orientation. This suggests elongated grains formed from equiaxed grains through a grain rotation and coalescence process. The fully developed elongated grain also shows to have a build-up of misorientation in the coarser elongated grain (Figure 7.15d) as the green scale becomes more dominant across the elongated grain that is likely due to deformation arising from shearing effect through the plastic deformation of the newly formed coarse grain.

7.4.2 LAB

Figure 7.16 presents a series of SEM/EBSD images showing an early stage (solid circle) and a relatively late stage (dashed circle) LAB in a 100Cr6 bearing sample tested under 2.9 GPa for 3016 million cycles. Similar to the HAB, the equiaxed grains appear as grains with various orientations (Figure 7.16b) and a relatively high IQ contrast compared to the surrounding matrix (Figure 7.16d) and low misorientation (Figure 7.16c). The elongated grains are shown to be much coarser compared to the equiaxed grain and with an apparent

texture close to <111> axis parallel to the normal direction (ND) similar to findings in the HAB. The higher misorientation of the elongated grains comparing with the equiaxed grains shown in the KAM map (Figure 7.16c) evidenced from the transition from blue to green scale suggests that the grains are under the influence of a shearing component that contributes to the deformation of the grains.

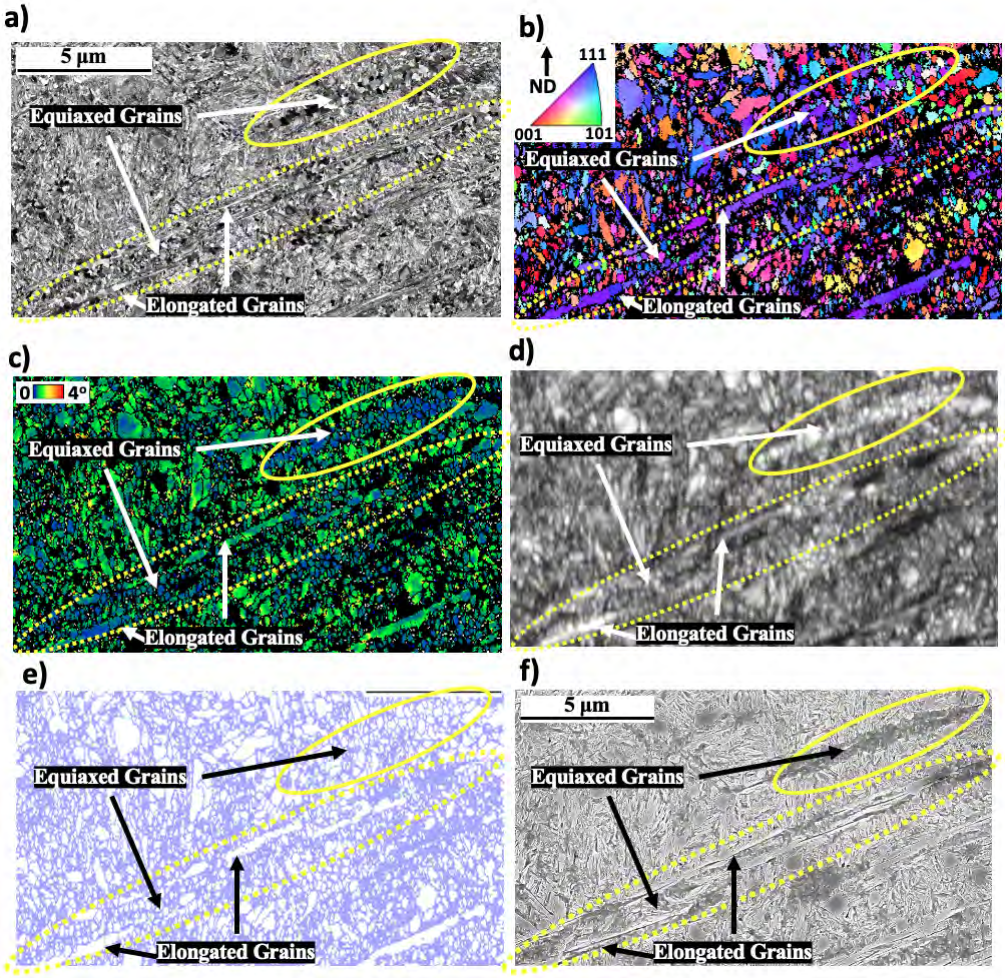

Figure 7.16: Images of LAB in a 100Cr6 bearing sample tested under 2.9 GPa for 3016 million cycles. a) BSE SEM image b) IPF map c) KAM map (100 nm, 5°) d) IQ map of region e) HAGB map (blue line indicate grain boundaries with misorientations $\geq 15°$) and f) SE SEM image. Solid circle highlights an early stage LAB consisting of only equiaxed grains while the dashed circle highlights a late-stage LAB consisting of both equiaxed and multiple elongated grains. Lenticular carbides remain unindexed in the EBSD maps and hence appears black adjacent to the elongated grains.

Similar results are found in the intermediate stage LAB with the cotton-bud shape (see Figure 7.17), where the heads consist of equiaxed grains of varied orientations (red arrow) while the stem consists of coarser elongated grains with a preferred orientation similar to the HAB. However, looking at the middle of the stem (pointed by the yellow arrow in Figure 7.17b), the elongated grain is not a single fully connected grain, i.e. different from the elongated grain shown in Fig. 7.15b. This again suggests an alignment/rotation and

coalescence of the equiaxed grains to elongated grains transition. At the top left corner of the images in Figure 7.17, a cluster of late stage LAB are also seen, which contain much more developed elongated grains (thicker and longer) than those in the cotton-bud LAB at intermediate stage while the bottom right corner shows an early stage LAB with the lenticular carbide nucleating parallel to the elongated grain within the equiaxed band (Figure 7.17e).

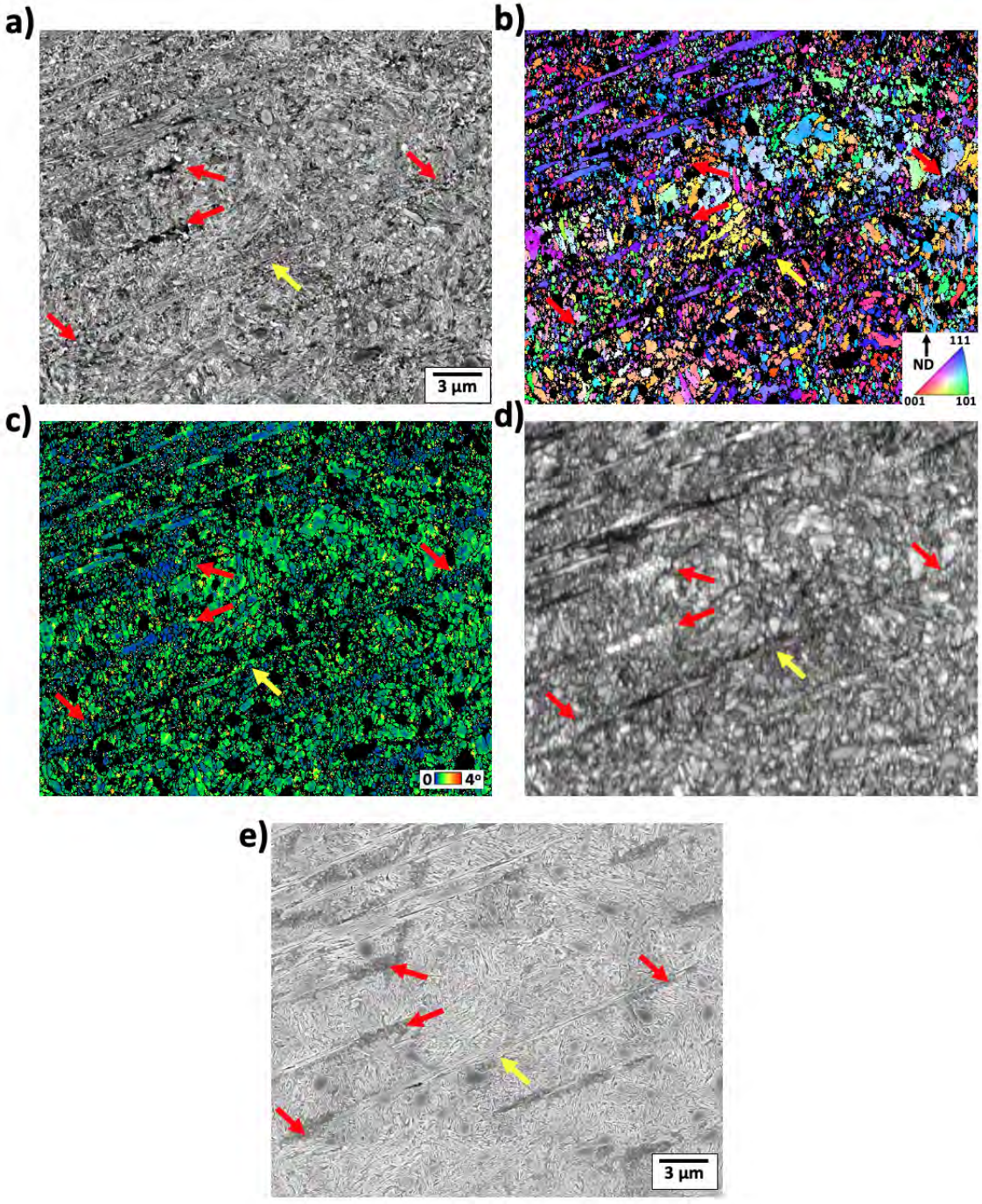

Figure 7.17: Characterization of LAB in 100Cr6 bearing sample run at 2.9 GPa for 3016 million cycles. a) BSE SEM image b) IPF map c) KAM map (100 nm, 5°) d) IQ map of region of LAB and e) SE SEM image. Red arrows indicate the heads of the cotton bud LAB, yellow arrows indicate the stem.

A comparison of the LAB in 50CrMo4 under EBSD (Figure 7.18) has shown similar results to 100Cr6 samples. The LAB were captured from 50CrMo4 sample run for 7668 million cycles under 2.9 GPa. Given the relatively slower growth rate of LAB in 50CrMo4 bearings, the latest stage sample has been selected to investigate LAB development stages in this material. Figure 7.18 shows an early stage LAB consisting mainly of equiaxed grains in the center of the captured area showing the same characteristics observed in 100Cr6, i.e. relatively low misorientation (Figure 7.18c), various grain orientations (Figure 7.18b) and high IQ contrast (Figure 7.18d). Later stages of the LAB could also be seen in the bottom left corner of the images in Figure 7.18 where elongated grains have developed within the equiaxed ferrite band similar to those shown in 100Cr6 samples. A modest increase in the grain misorientation could be observed compared to the surrounding equiaxed grains while a more distinct texture is observed where a <111> axis is approximately parallel to the normal direction (ND). The results have shown that the development of LAB in the two steels follows similar stages although the development in the 50CrMo4 is a much slower process comparing with that in the 100Cr6 steels.

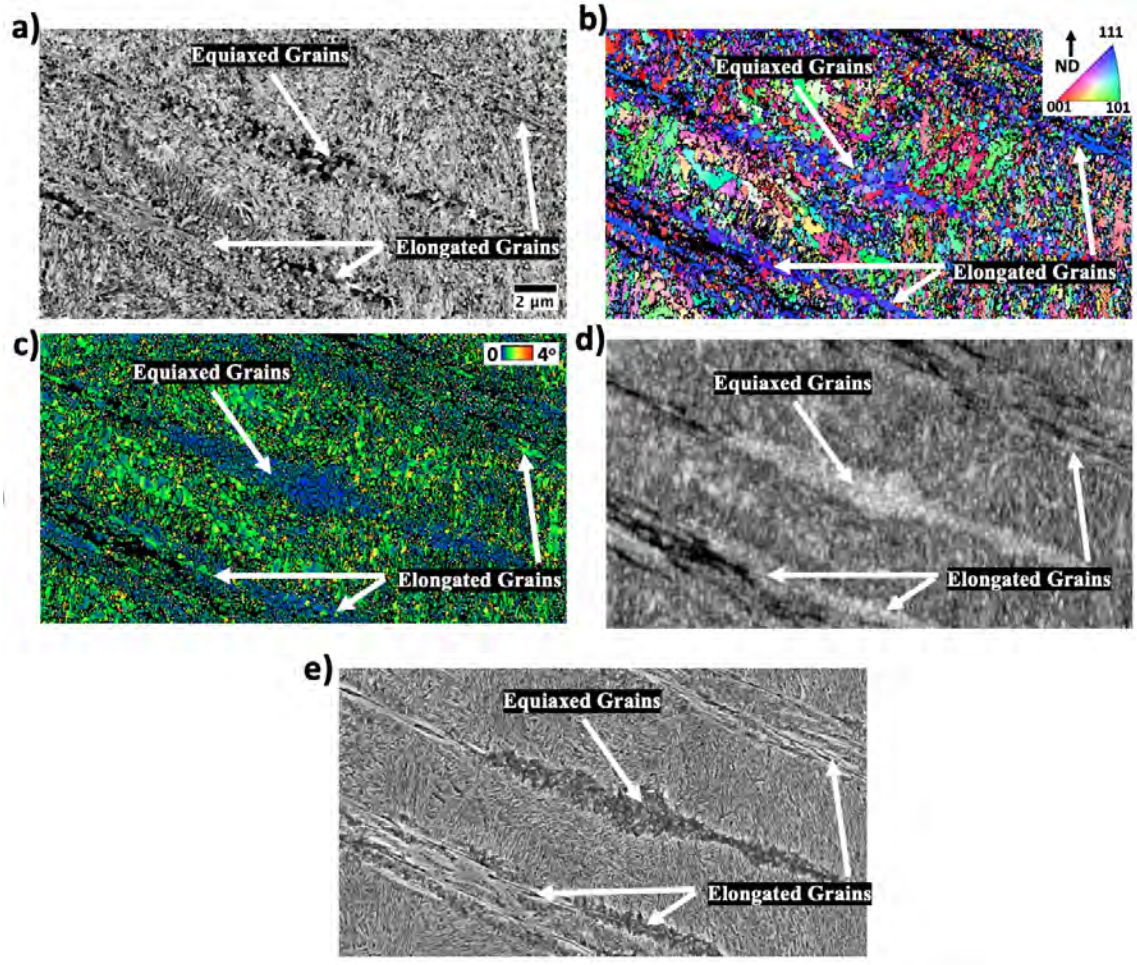

Figure 7.18: Characterization of LAB in a 50CrMo4 bearing sample run at 2.9 GPa for 7668 million cycles. a) BSE SEM image b) IPF map c) KAM map (100 nm, 5°) d) IQ map of region of LAB and e) SE SEM image.

7.5 Nano-indentation

The mechanical properties of WEB constituents, including equiaxed grains, elongated grains and lenticular carbides, are investigated by measuring their nano-hardness. Two sets of nano-indentation tests have been performed. The first was an array of 30 × 35 indents with a 1 µm spacing between two adjacent indents, which was carried out on an unetched surface from a 100Cr6 bearing sample tested under 2.9 GPa for 4141 million cycles. After the analysis, the surface was then etched to identify the microstructural features and compare with the colour map generated from the indentation matrix.

Figure 7.19a shows an SEM image of the area containing LAB and HAB in the subsurface of the 100Cr6 sample after being indented then etched with nital. The nano-indents are visible and can be correlated with the hardness map shown in Figure 7.19b. It shows that the ferrite bands, in the HAB, containing both elongated and equiaxed grains, have a lower hardness comparing with that of the parent martensite matrix and the lenticular carbides, with the lenticular carbides being the hardest feature in the area. The hardness of the lenticular carbides is found to be similar to that of spherical primary carbides seen at the top of the image in Figure 7.19a. Furthermore, the softest regions within the bands is shown to correspond to the positions of the elongated grains possibly due to grain coarsening (Hall--Petch effect) as observed from the EBSD results. Due to the close proximity of the indents

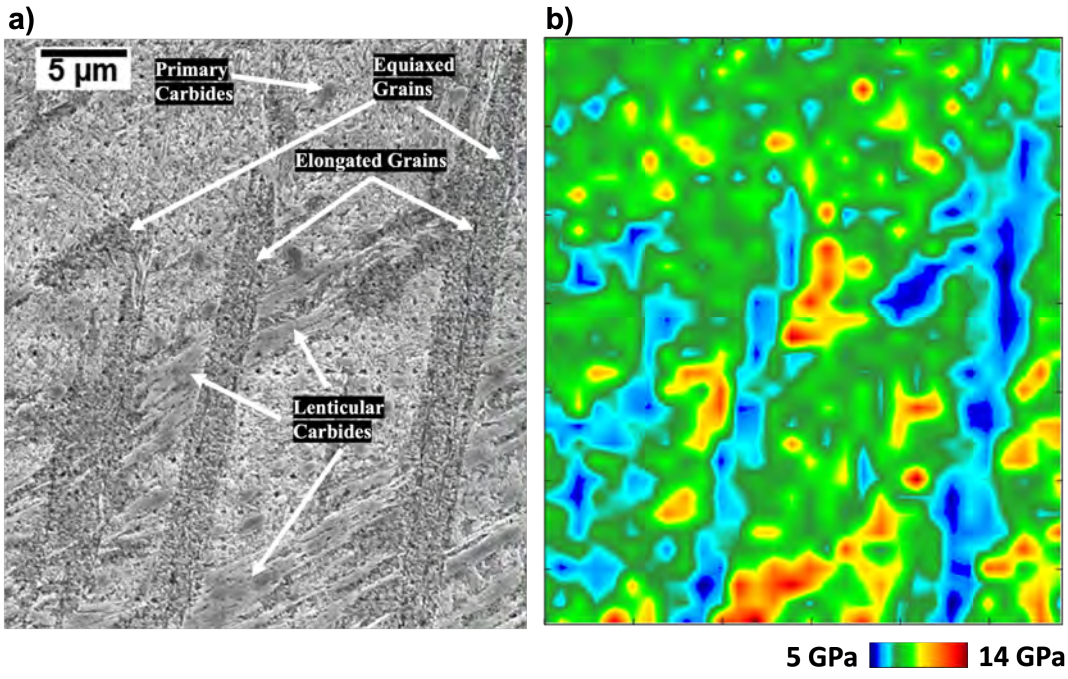

Figure 7.19: a) An SEM image of an area in the subsurface of a 100Cr6 bearing tested under 2.9 GPa for 4141 million cycles, showing LAB and HAB features. b) A hardness color map from a nano-indentation test on an area with LAB and HAB features shown in a) to indicate significant variations in hardness.

shown in Figure 7.19, any given hardness value may have been influenced by surrounding indents. Hence, the results are shown in Figure 7.19 in the form of a color map rather than recorded hardness values to be considered as qualitative measurements for comparing the relative hardness of the features only. An example of the load displacement curves obtained for the ferrite and carbide structures in Figure 7.19 is shown in Appendix D.

To obtain quantitative measurements, a second nano-hardness test was then conducted with an indent matrix of 10 x 46 with a spacing of 3 µm between adjacent indents, see an SEM image showing locations of the indent in the WEB in Figure 7.20. The penetration depth of the indentation was kept at 50 nm to provide indents small enough to be positioned fully

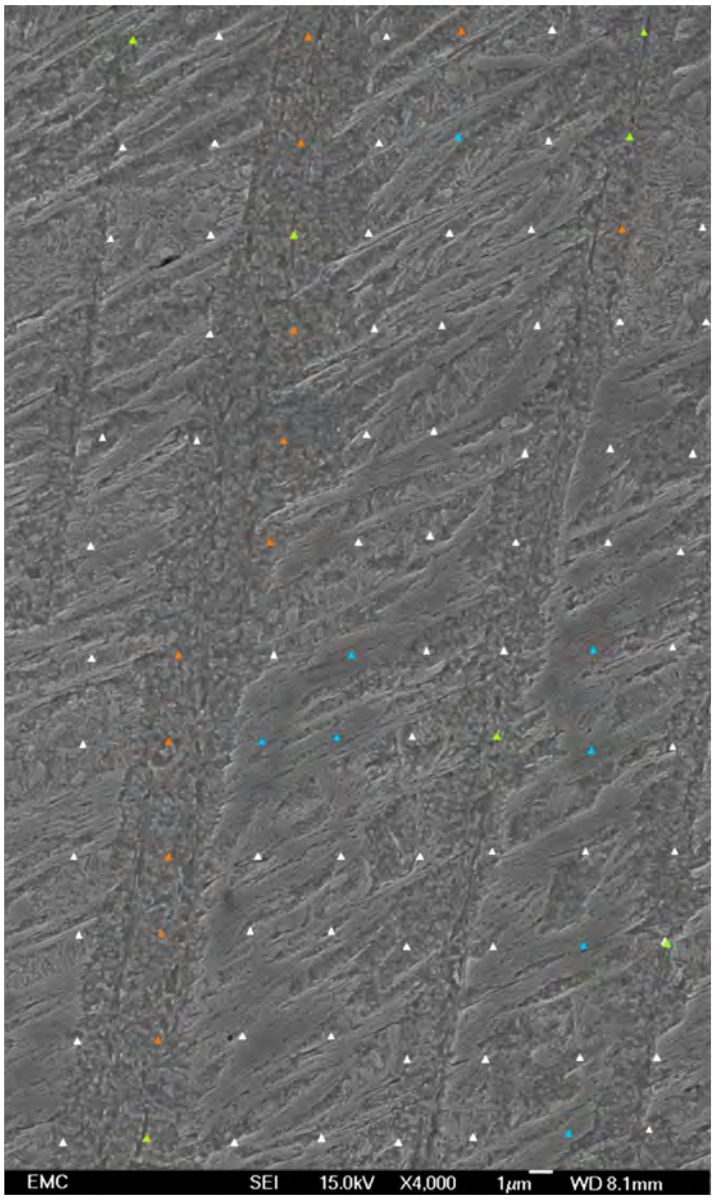

Figure 7.20: An SEM image of the etched surface post the nano-indentation test with 3 µm spacing and 50 nm indent depth on a bearing sample tested under 2.9 GPa for 4141 million cycles. Orange, blue and green triangles indicate positions of the indents in equiaxed ferrite grains, lenticular carbides and elongated grains respectively.

within each constituent of the WEB. The analysis of these micro-features at this scale makes it possible to determine hardness of the equiaxed ferrite grains, elongated ferrite grains and the lenticular carbides. The 'indents' on the SEM map were graphically added on the SEM image of the etched surface after indentation to show the position of each indent clearly and the corresponding microstructural features. A minimum of 10 measurements were taken for each constituent and the averaged hardness values are shown in Table 7.1. It shows that the hardness follows: lenticular carbides > martensite matrix > equiaxed grains > elongated grains.

Table 7.1: A summary of the averaged nano-hardness values and their standard deviations for the three WEB constituents and the parent steel matrix.

	Hardness (GPa)
Equiaxed grains	5.04 ± 0.8
Elongated grains	4.40 ± 1.1
Lenticular carbides	9.67 ± 1.9
Parent Matrix	7.1 ± 1.9

7.6 Interfacial Energy of LCs

To understand the transition from LAB to HAB, the interfacial energy of lenticular carbides within LAB and at the edges of HAB under fully developed conditions are compared. Carbide dissolution is driven by a significant energy build-up which destabilises carbides [191–193]. The free energy build-up driving carbide dissolution could arise from i) interfacial energy, ii) difference in binding energy between C-Fe in the carbide and C-dislocation and, iii) elastic energy increase in heavily dislocated regions [192].

The interfacial energy of the carbides (E_{LC}) can be determined from Equation 7.1 [194], where γ is the specific interfacial energy per unit area between ferrite and carbide, V_m is the molar volume of the carbide and $\frac{dSA}{dV}$ is the ratio between the surface area of carbide/ferrite and the volume of the carbides. This equation indicates that the change in interfacial energy of carbides is proportional to the surface area to volume ratio of the carbides. Hence a comparison between the surface-volume ratios of the lenticular carbides in a dense LAB region and in a HAB region can provide an insight to the ratio of interfacial energy between the two features.

To do so, an area of fully developed (late-stage) LAB and and area of HAB of same size in 100Cr6 bearing run for 3016 million cycles have been selected for the comparison. Figure 7.21 shows SEM images of the initial selected areas (a and d for LAB and HAB respectively). Based on findings in this study where HAB develops in areas with dense LAB, it is assumed

that the LAB region in Figure 7.21a would eventually transition to the region shown in 7.21d as HAB develop if tested for long enough. Using a mask on the original SEM images (Figure 7.21a and d), carbides in the LAB and HAB are highlighted (Figure 7.21 b and e). By extending the depth by 44 µm (the average depth of developed LAB measured via serial sectioning and recorded in Table 5.1), a 3D model of the carbides is created for the LAB (Figure 7.21c) and HAB (Figure 7.21f), which have been used to determine the $\frac{dSA}{dV}$ of the lenticular carbides for the two cases. ImageJ is used for both the construction of the 3D model, and the measurement of the surface area and volume of the 3D model (carbides) in both cases.

$$E_{LC} = \gamma \times V_m \times \frac{dSA}{dV} \tag{7.1}$$

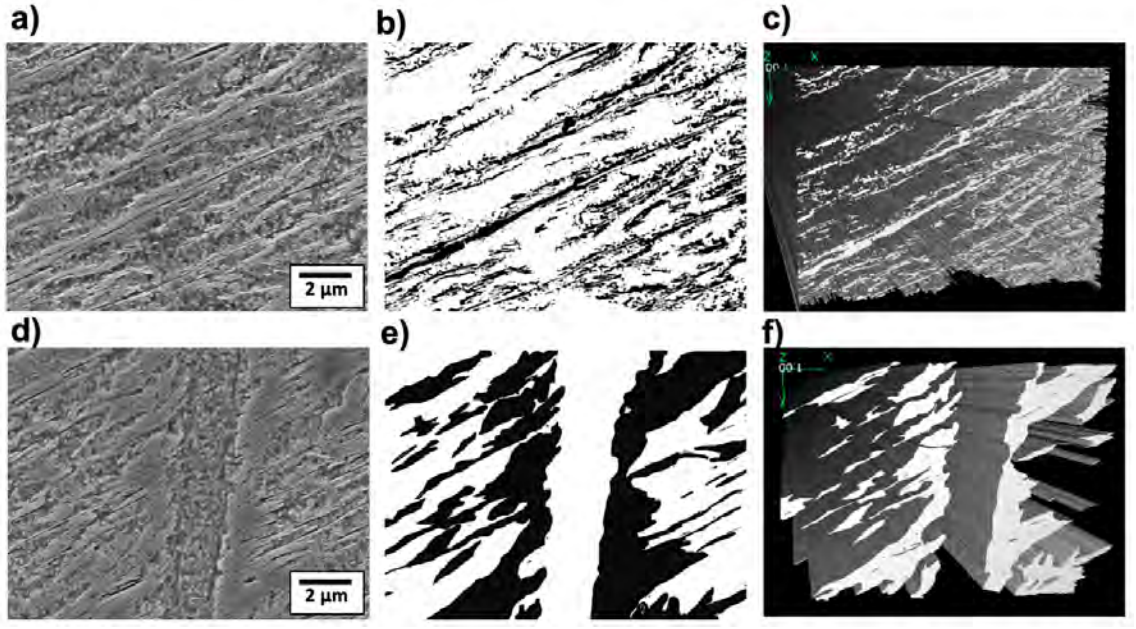

Figure 7.21: Images of LAB (a-c) and HAB (d-f) in 100Cr6 bearing sample tested under 2.9 GPa for 3016 million cycles. a) and d) SEM images, b) and e) after mask is applied to a and b, highlighting the carbides in the area, c) and f) re-constructed 3D images of b) and e), showing carbides in the area (average depth of 44 µm is applied).

Table 7.2: A summary of the volume and surface area measurements of LCs in the LAB and HAB shown in Figure 7.21

	LCs associated with LAB	**LCs associated with HAB**
Volume (µm^3)	4,994	5,376
Surface Area (µm^2)	203,003	34,588
Surface Area / Volume Ratio $\frac{dSA}{dV}$ (µm^{-1})	40.65	6.43

A significant reduction in $\frac{dSA}{dV}$ of approximately 6 times is seen between LAB to HAB transition, indicating that the free-energy build-up associated with the LCs growth during

the LAB development is a potential driver for the HAB formation. The breakdown of LCs in LAB to form HAB has significantly reduced the overall free energy in the region.

7.7 FIB/TEM Analysis

To further investigate the LAB structure, a FIB/TEM analysis is conducted on a 100Cr6 bearing sample run under 2.9 GPa for 3016 million cycles, where late stage LAB are observed. The FIB milling was conducted on the LAB in the axial cross section of the bearing (see Figure 7.22). This would result in the surface of the TEM lamella to coincide with a circumferential cross section of the bearing raceway which is similar to the LAB SEM images presented in this Chapter. After lifted out from the sample, the TEM lamella was welded onto a tooth of a copper grid, followed by final milling to the thickness of 80 nm for imaging.

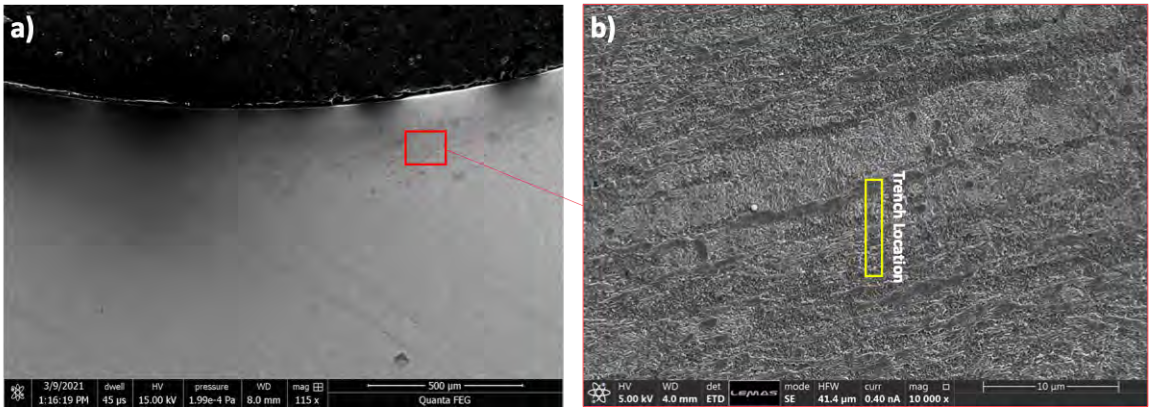

Figure 7.22: a) Axial surface of 100Cr6 bearing surface from sample run for 2.9 GPs under 3016 million cycles and b) location of area where the trench was milled using FIB to create the TEM lamella.

The overall TEM lamella is shown in Figure 7.23 with the rolling direction (RD) marked on the image for reference. The bright spot visible in the image is caused by a damage in the specimen during handling. Equaixed grains at various orientations (based on their varied contrast) are observed across the lamella while groups of elongated grains at 30° inclined to the RD are also seen in the image. To confirm the equiaxed and elongated grains, the sample has been examined in a number of titling angles (see images in Figure 7.24). The top right images in Figure 7.24 show elongated grains embedding in equiaxed grains with a thickness of approximately 100 nm while the images in the bottom row show multiple parallel elongated grains less than 50 nm in thickness. These thin elongated grains are similar to that observed under BSE SEM within lenticular carbides (see Figure 7.16 for comparison). Within the equiaxed grains observed in the bottom of Figure 7.24, there also appears to be grains elongated slightly with a directionality similar to that of LAB.

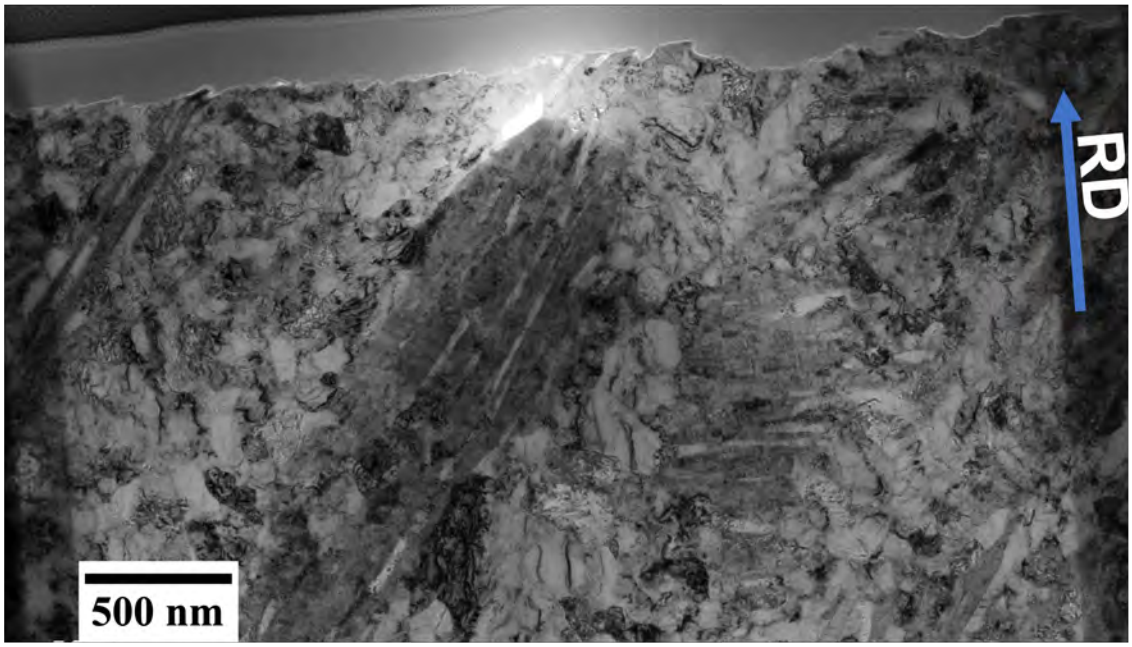

Figure 7.23: a) Axial surface of bearing surface b) location of area where the trench was milled using FIB to create the TEM lamella.

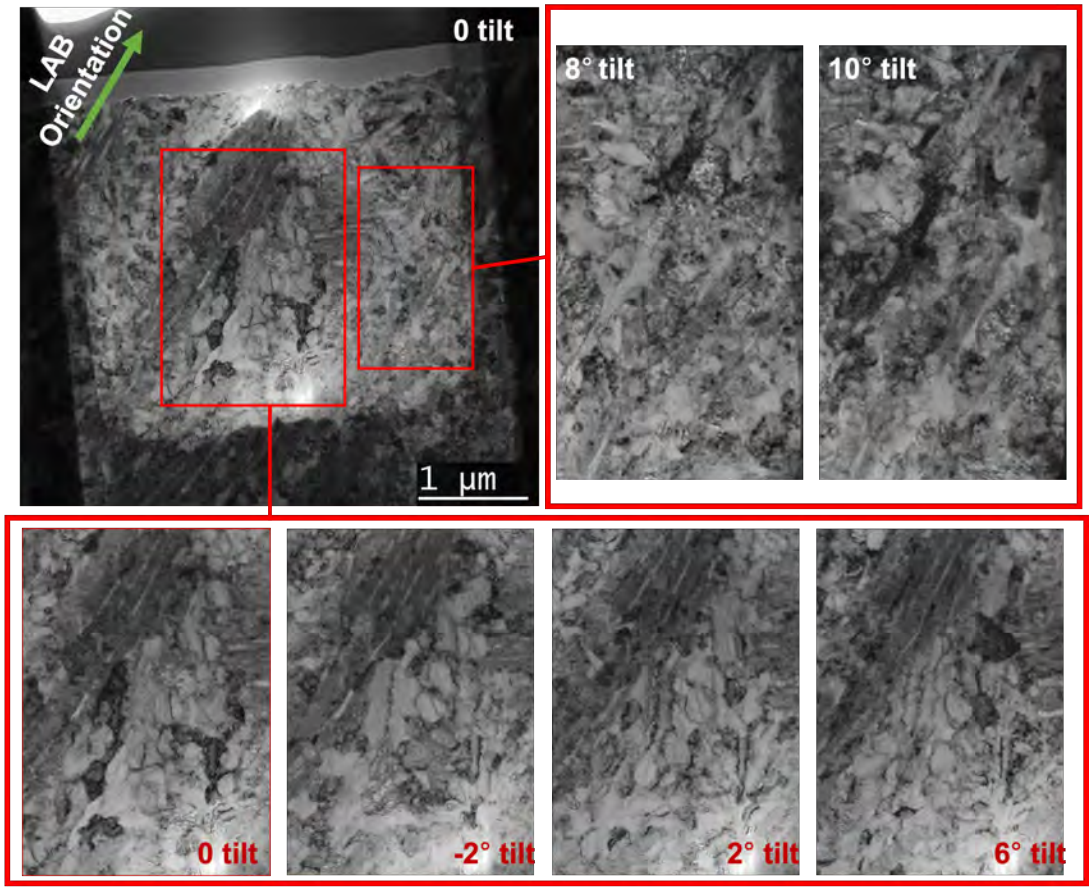

Figure 7.24: Different tilting angles of specimen at regions to highlight equiaxed and elongated grains in lamella.

Elemental analysis of an area within the lamella is shown in Figure 7.25, showing that lenticular carbides are both carbon and chromium rich, which contradicts the hypothesis

of lenticular carbide being free of chromium [120, 124]. Nonetheless, the carbon depleted region which has been suspected to be ferrite band is found to be parallel to the carbon rich band of lenticular carbide. However, the carbide structure in Figure 7.25 is seen not to be one large carbide but appears to be consist of columns of carbon rich and depleted regions, see Figure 7.26 for a closer look.

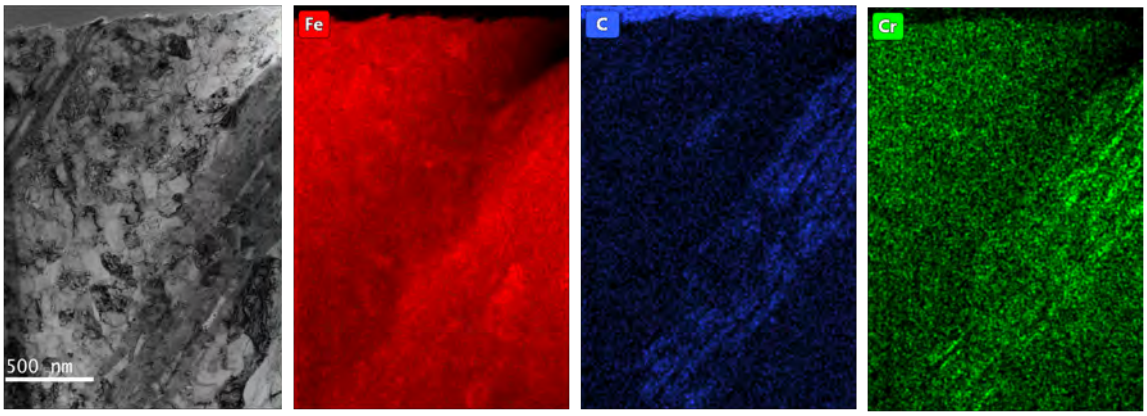

Figure 7.25: TEM image and EDX mapping of Fe, C and Cr elements across LAB consisting of ferrite and lenticular carbide.

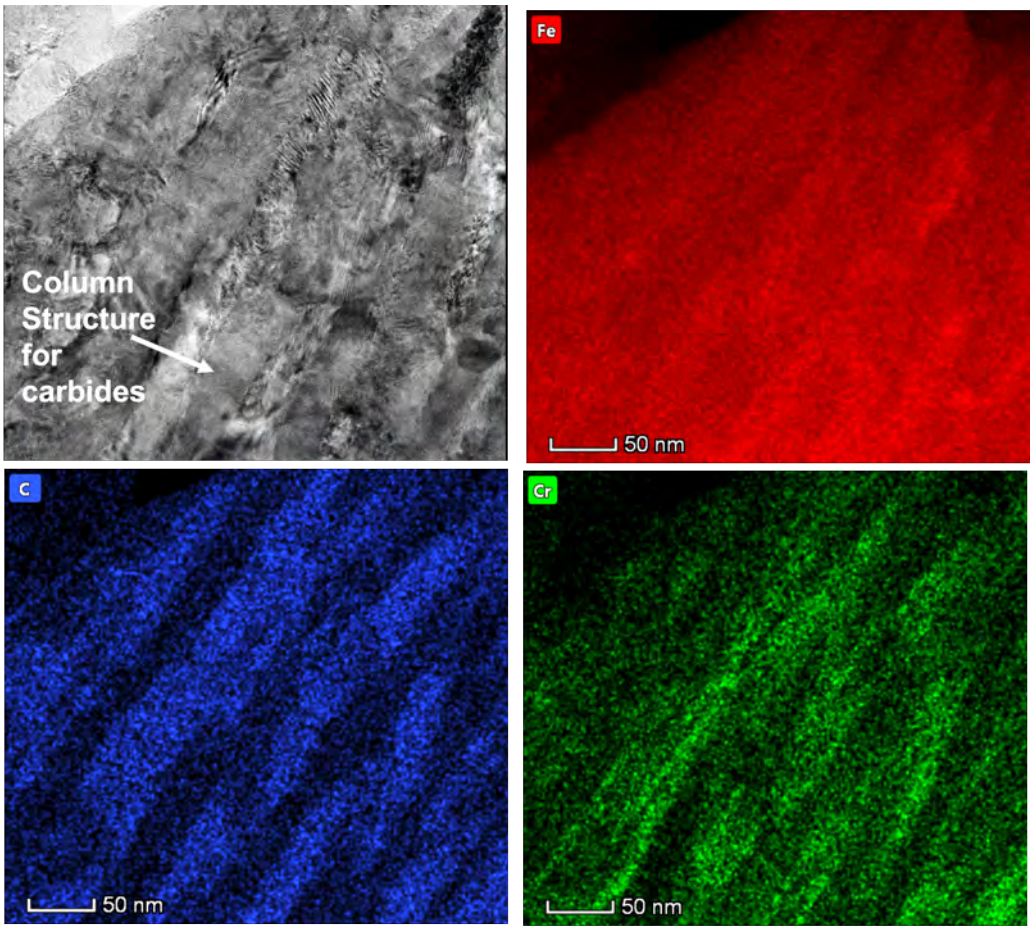

Figure 7.26: TEM image and EDX mapping of Fe, C and Cr elements across lenticular carbide region from Figure 7.25 consisting of carbon depleted elongated grains and carbon rich rows in between.

The carbide structure is clearly seen to consist multiple rows of elongated carbon free grains and parallel columns of carbon rich structures in Figure 7.26. The carbon-free bands of elongated grains show to have a thickness of below 50 nm, and within the bands, contrast variation is seen in the TEM image in Figure 7.26, indicating plastic deformation occurred in these elongated grains. These are in agreement with the results obtained from the KAM maps presented in Section 7.4. Within the carbon rich bands, columns perpendicular to the band orientation are observed (see arrow in Figure 7.26) similar to observations made by other researchers [120, 124]. This suggests that lenticular carbides develop as small crystallites at the edges of the elongated ferrite grains and grow in length and thickness until the coalesce into the lenticular shape commonly observed under SEM.

However, another LAB area has shown to contain carbon rich structures without the chromium rich feature observed above, see TEM image and elemental maps of LAB in Figure 7.27. The elongated grain in Figure 7.27a shows to contain a modest amount of carbon at the edges of the elongated grains suggesting this is an early stage of LC formation (Figure 7.27c) but the chromium distribution in this area appears to be more homogeneous unlike that shown in Figure 7.26. This suggests that at early stages of LC formation, carbon migrates and accumulates at the edges of elongated grains however the role of chromium in LC formation is unclear. This agrees with the SEM observations in this study where LC nucleation occurs at the edges of elongated grains.

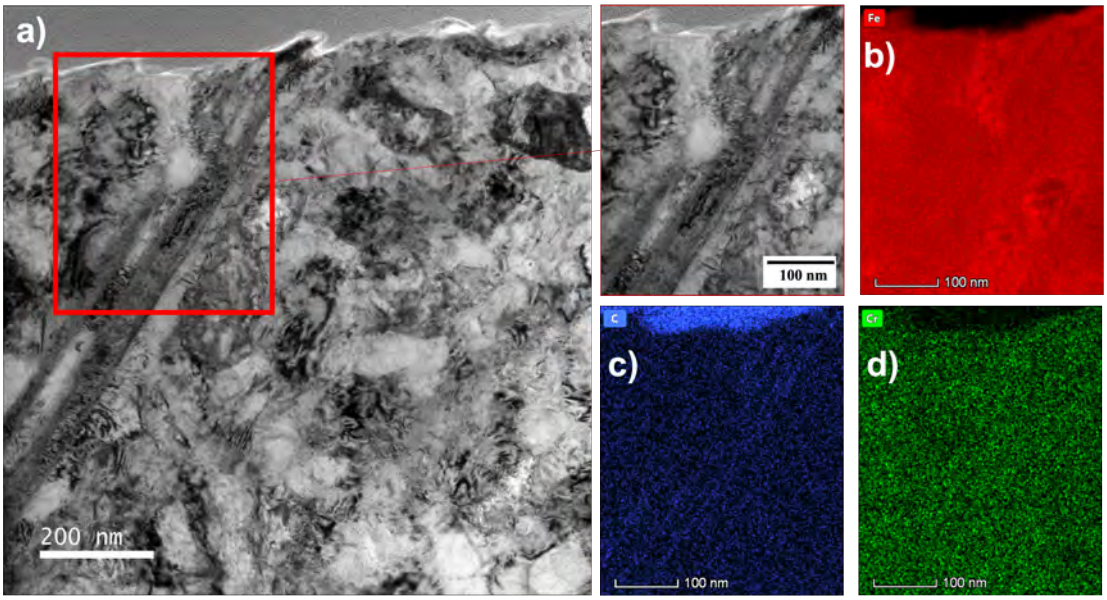

Figure 7.27: a) TEM image elongated grain in LAB. EDX mapping of area highlighted in red in a) showing the elemental distribution of b) Fe c) C and d) Cr.

Diffraction patterns of different regions within the TEM lamella are presented in Figure 7.28 to investigate their crystal structures within LAB. Area A and Area C, consisting mainly of equiaxed grains, show a diffraction pattern of ferrite, while Area D, consisting of

elongated grains, also shows a ferrite diffraction pattern. The coarser size of the elongated grain comparing with the equiaxed grains is evidenced by the more spaced spots pattern shown in Area D comparing with those in Area A and C. Area B, consisting of elongated grains and lenticular carbides, shows to contain a polycrystalline microstructure with a diffraction pattern that links to both cementite and ferrite. This further confirms that the carbon depleted areas shown in Figure 7.26 are indeed ferrite grains and the carbon-rich areas are carbides with a cementite structure. The polycrystalline diffraction pattern of the carbides also supports the theory where the carbides develop as small crystallites that coalesce as they develop as shown in Figure 7.26. Details on the diffraction patterns measured and compared in Figure 7.28 can be seen in Appendix E.

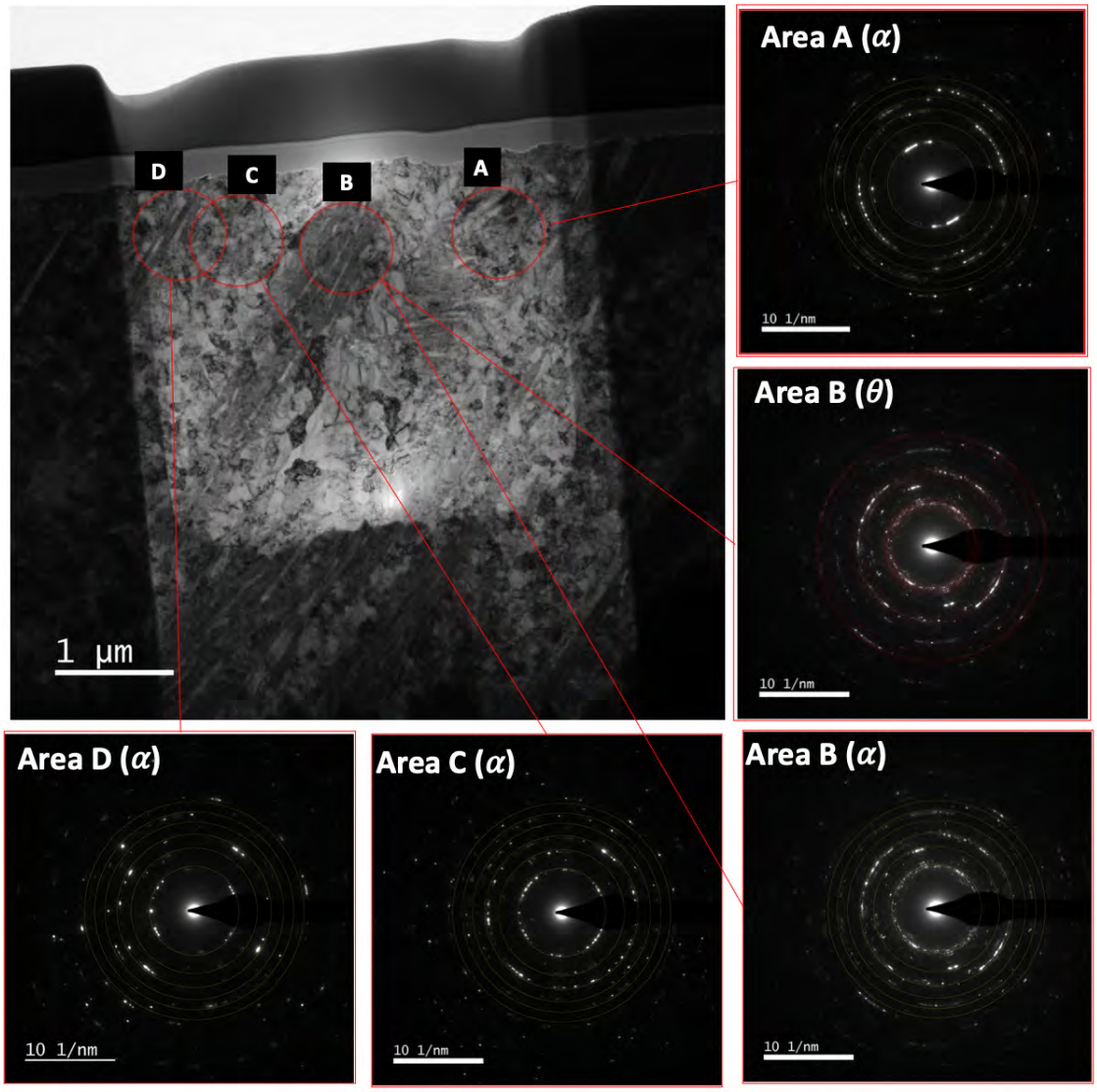

Figure 7.28: a) Different areas across the LAB in TEM sample that has been analysed using SAED. For each area, ring patterns for the close packed planes of BCC ferrite (α) in yellow and orthorhombic cementite (θ) in red are drawn for reference to the diffraction pattern. Area A,C and D show ferrite phase while Area B shows a mixture of ferrite and cementite.

7.8 FIB/APT Analysis

To investigate carbon distributions in LAB and elucidating their formation mechanisms, FIB/APT analysis has been conducted on a sample from the 100Cr6 bearing tested under 2.9 GPa over 3016 million cycles, a late LAB stage sample. An overview of the procedure is shown in Figure 7.29, where an optical image of a circumferential cross section (Figure 7.29a) identifies the region of analysis and an SEM image (Figure 7.29b) shows three lift out areas (Tip A, B and C) and that the area contains lenticular carbides, elongated and equiaxed grains. The specimens were firstly milled and sharpened using FIB until shaped into a sharp needle with a 50 nm diameter (see an example shown in Figure 7.29c), which is then analysed by APT to provide details of elemental distribution in the needles.

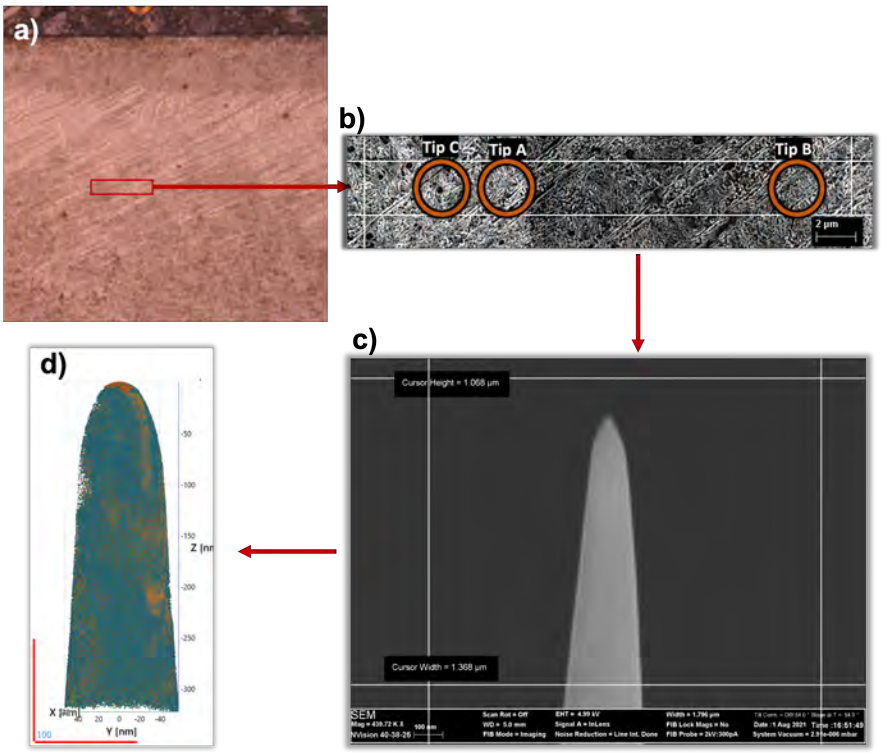

Figure 7.29: a) optical image of WEB in 100Cr6 sample run under 2.9 GPa for 3016 million cycles. b) SEM image of LAB area showing the location of the FIB/APT lift-outs c) Needle obtained after lift-out at set locations in b). c) Example of 3D atomic map of elemental distribution in needle.

7.8.1 APT Specimen A

The 3D elemental distribution of carbon in Specimen A is shown in Figure 7.30. An isosurface carbon concentration of 0.36% of a 5 nm thick slice of the 3D model is shown in Figure 7.30a where grain boundaries (high carbon concentrations) of equiaxed ferrite grains can be clearly seen. Carbon is found to be depleted inside equiaxed grains. In Figure 7.30b, the full 3D model is shown with an isosurface carbon concentration of 15% which is typically

used to identify carbide locations. Irregular shaped carbides of sizes between a few nm and 100 nm are observed in Figure 7.30b. Comparing with a 2D slice of the model in Figure 7.30c, it shows these carbides are located at ferrite grain boundaries.

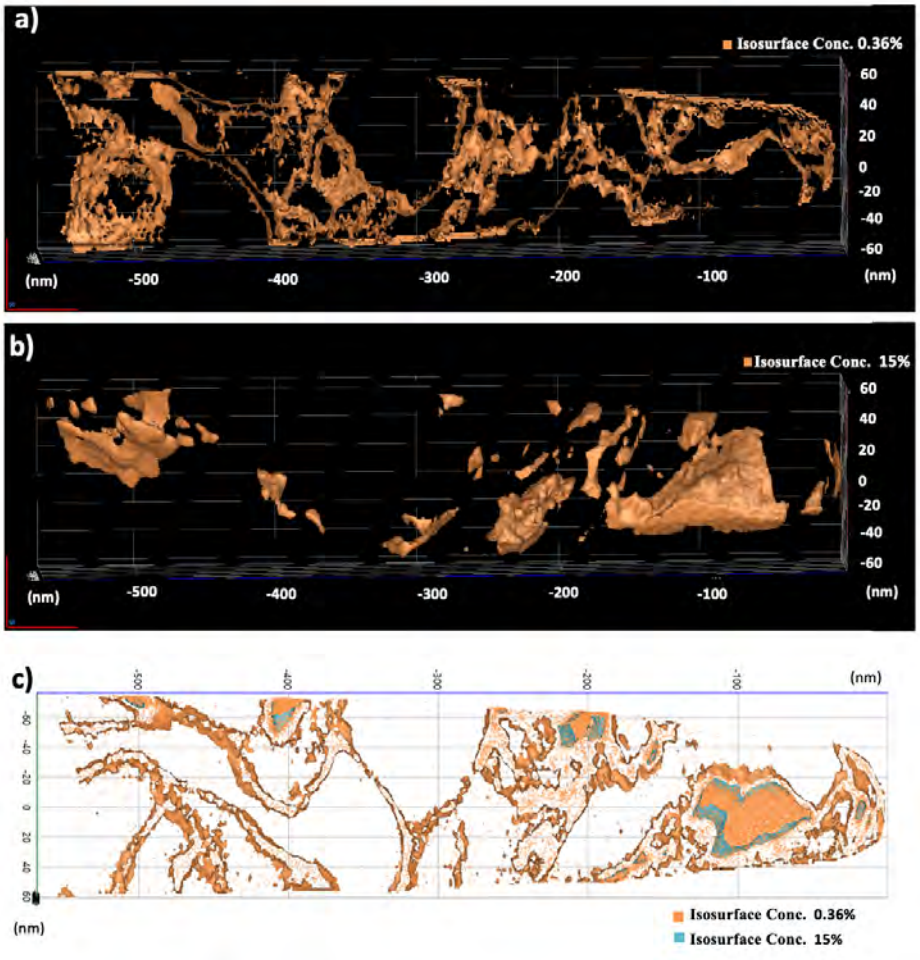

Figure 7.30: a) Slice of the 3D model of showing the isosurface carbon concentration of 0.36% in the volume, corresponding to grain boundaries of ferrite grains. b) Full 3D model of the volume showing carbon concentration isosurface of 15%, corresponding to carbides within the region. c) A 2D slice showing isosurface carbon concentrations of 0.36% (yellow) and 15% (blue), showing carbides positions across grain boundaries.

Proxigrams have been plotted in Figure 7.31 to examine carbon distributions across grain boundaries highlighted in the isosurface carbon concentration of 0.36% shown in Figure 7.31a. Carbon and chromium atomic concentrations at a number of grain boundaries have been measured and the values are shown in Figure 7.31b and c) respectively. It shows that the carbon concentration varies from an average of around 0.15 at% at inside of the grains to about 2 at% at the grain boundary, while the chromium distribution remains relatively unchanged across the grain boundaries as expected. GB 1 and GB 5 show a slight increase in Cr, which has been discarded due to the errors associated in that region.

Proxigrams across ferrite/carbide interfaces (identified in Figure 7.30) are plotted in Figure 7.32, showing a carbon concentration of about 23 at% that is similar to that

previously reported in lenticular carbide structures [124]. The gradual increase in carbon concentration across the carbide interface in Figure 7.32b is evidence of a diffusion mechanism causing the growth of the carbides. Maximum carbon concentration detected in the carbides is similar to that of cementite (25 at%). However, the chromium concentration appears to vary significantly between the carbides, e.g. they are much higher in carbides 4, 6 and 7. This is suggested to be caused by the slow diffusion rate of Cr comparing with that of C, as well as whether LAB form in the proximity of a pre-existing primary carbide $(Fe,Cr)_3C$ that has dissolved. The irregular shaped carbides of various sizes may be individual crystallites growing due to carbon migration and later coalesce to form the lenticular carbide shape observed under SEM.

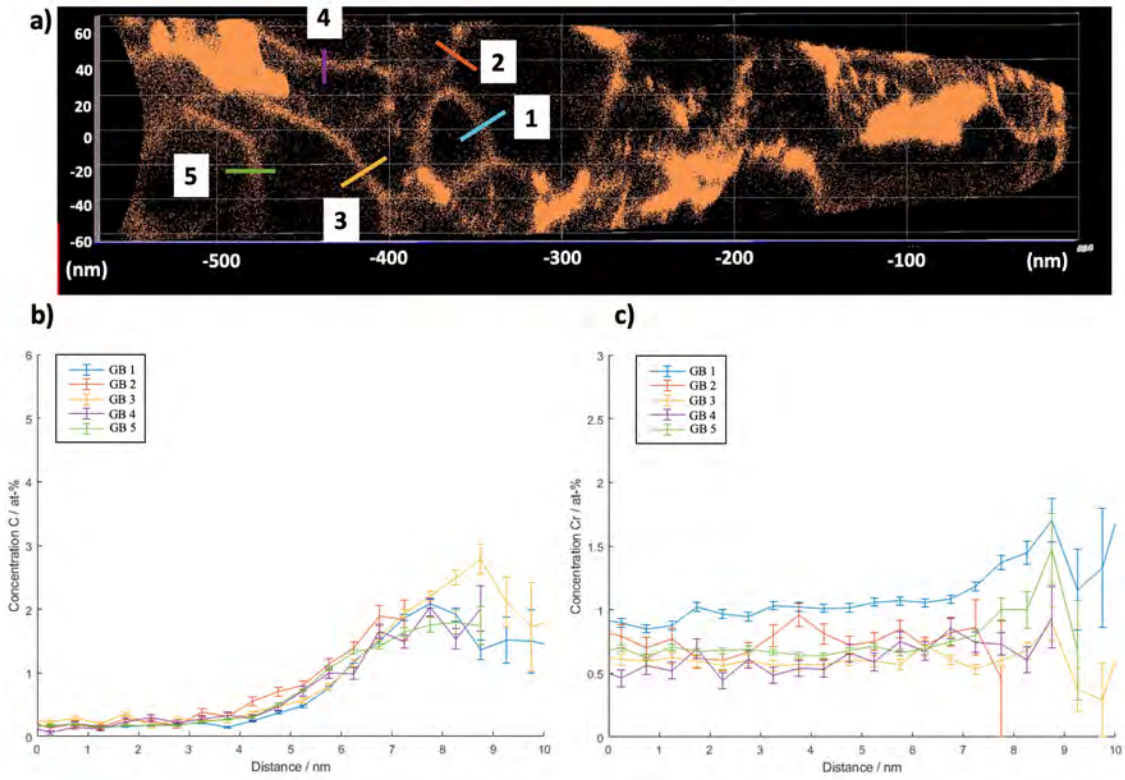

Figure 7.31: a) Slice of the 3D model showing the position of grain boundaries (GB) where proxigrams are taken to measure b) carbon concentration (at%) and c) chromium concentration (at%) variation from grain interior to grain boundary of different locations highlighted in a).

Within the equaixed grains observed in the sample, some grains appear to show a very faint carbon atom scattering between GBs, highlighted in Figure 7.33a, resembling dissolving GBs. The 1D elemental concentration profiles across the three highlighted areas show a modest increase in carbon reaching up to 0.6 at% (Figures 7.33 b-d). Although this is much lower than the 2 at% at the grain boundaries (Figure 7.31), the slight increase of carbon within the grains suggests that a grain boundary dissolving process might be occurring while adjacent grains coalescence during the transition of equiaxed to elongated grains (discussed

in Section 7.4). The corresponding chromium concentrations show limited changes (Figures 7.33e-g) with a minor increase at location B, which is similar to that shown in Figure 7.31.

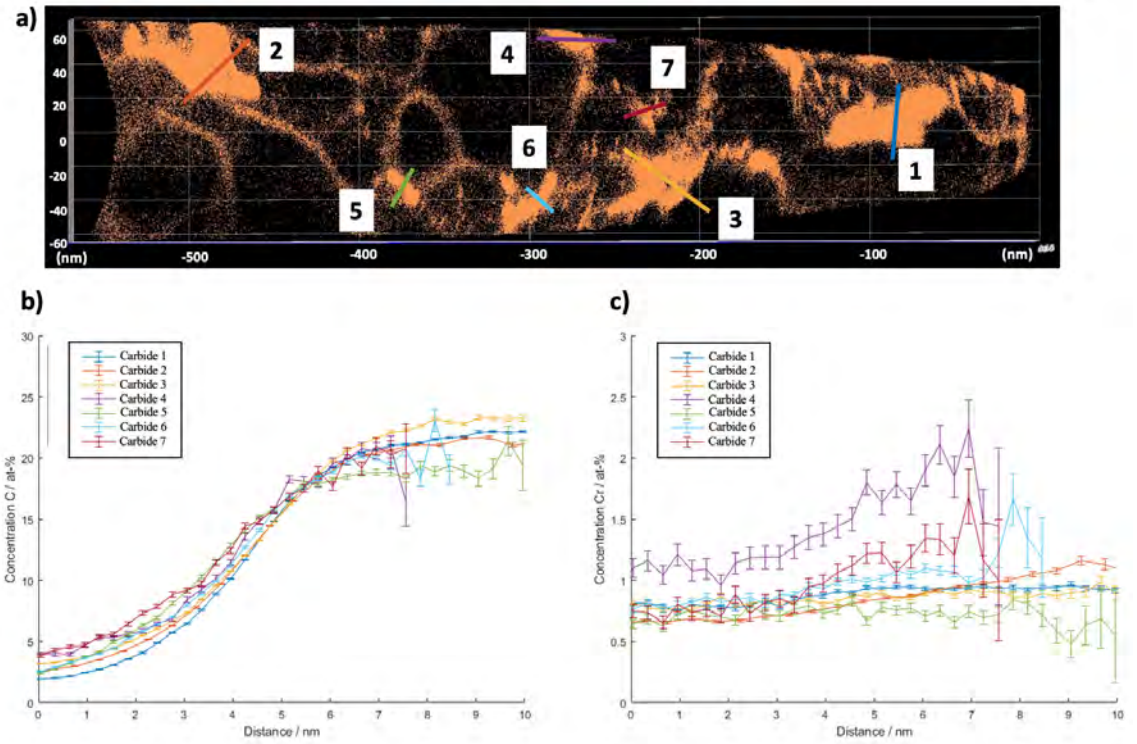

Figure 7.32: a) Slice of the 3D model showing the position of carbides where proxigrams are taken to measure b) carbon concentration (at%) and c) chromium concentration (at%) across carbide/ferrite interface of different locations highlighted in a).

7.8.2 APT Specimen B

Similar analysis has been conducted on Specimen B and the results are shown in Figures 7.34-7.36 for comparison. The isosurface carbon concentration of 0.36 at% of a 5 nm thick slice of the 3D carbon map (Figure 7.34a) shows coarser grains than those in specimen A (Figure 7.30) with a mixture of equiaxed and elongated grains. Figure 7.34b of the isosurface carbon concentration of 15 at% across the whole 3D volume shows large intact carbides between two elongated grains. It should be noted that this specimen is slightly smaller than Specimen A which can be observed by the scale bars in Figure 7.30 and Figure 7.34.

The carbon concentrations across the carbides are shown in Figure 7.35, where Carbide 1 and Carbide 2 show to contain 22 at% and 18 at% respectively. The 22 at% is similar to the composition of the irregular shaped carbides observed in specimen A (Figure 7.32b), confirming the composition of carbides. The slightly lower concentration observed in Carbide 2 is likely due to that the location of this carbide is at the edge of the dataset cut-out position, which may not reflect the true composition. Interestingly, a small enrichment of chromium

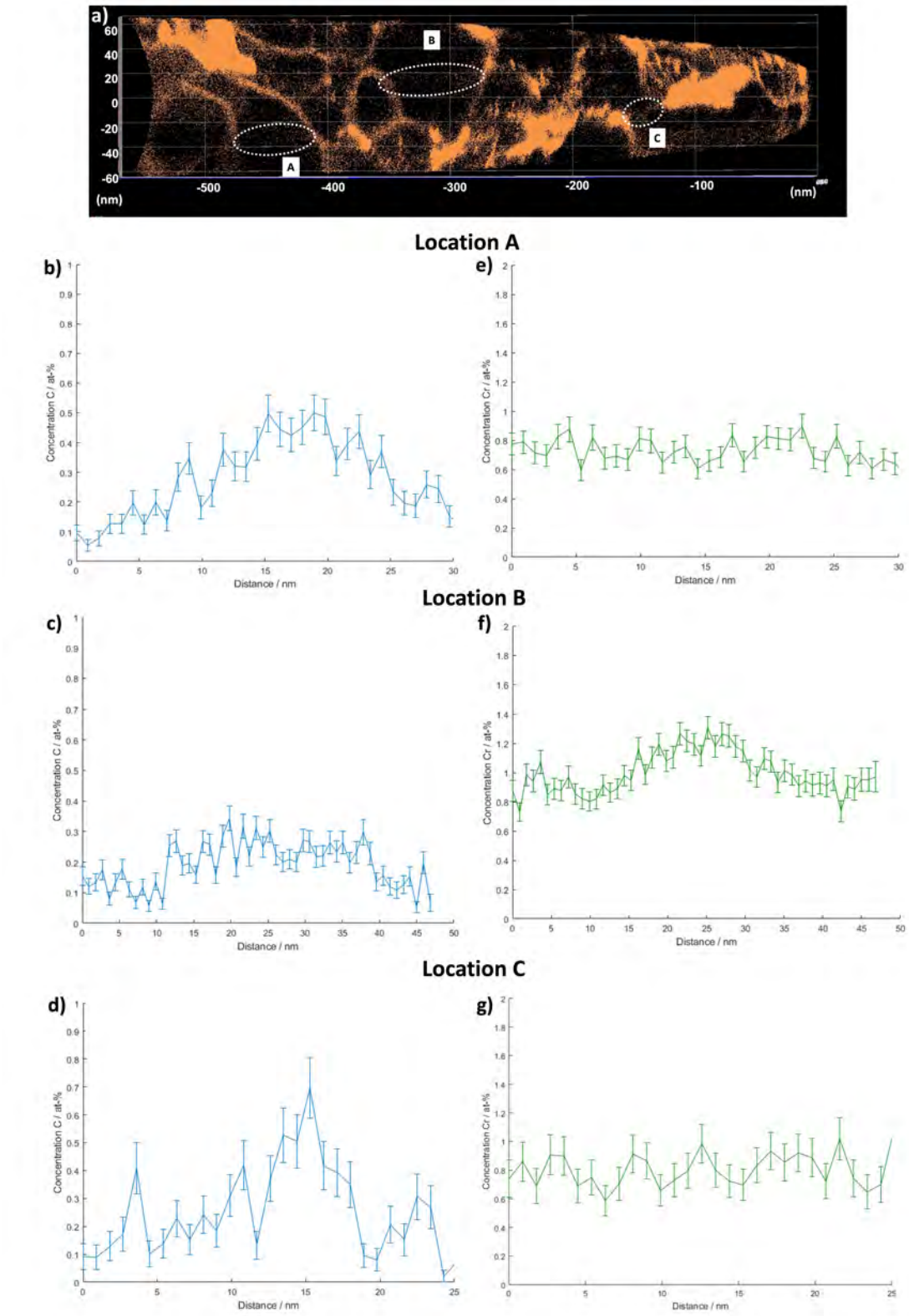

Figure 7.33: a) Slice of the 3D model of showing three different positions of grain boundary elimination due to grain coalescence. b-d) Carbon concentration and e-f) chromium concentration variation (at%) across dissolving grain boundaries at different locations highlighted in a).

is seen in both carbide structures (Figure 7.35d and e) although their distributions do not align with the carbon distributions, suggesting that chromium may be attributed to residual chromium atoms locally present from dissolved pre-existing primary carbides as previously discussed. A higher carbon concentration of up to 5 at% at grain boundaries is observed in proxigrams shown in Figure 7.36. No chromium has been detected in these cases (Figure 7.36), which backs up the discussions for Figure 7.31c.

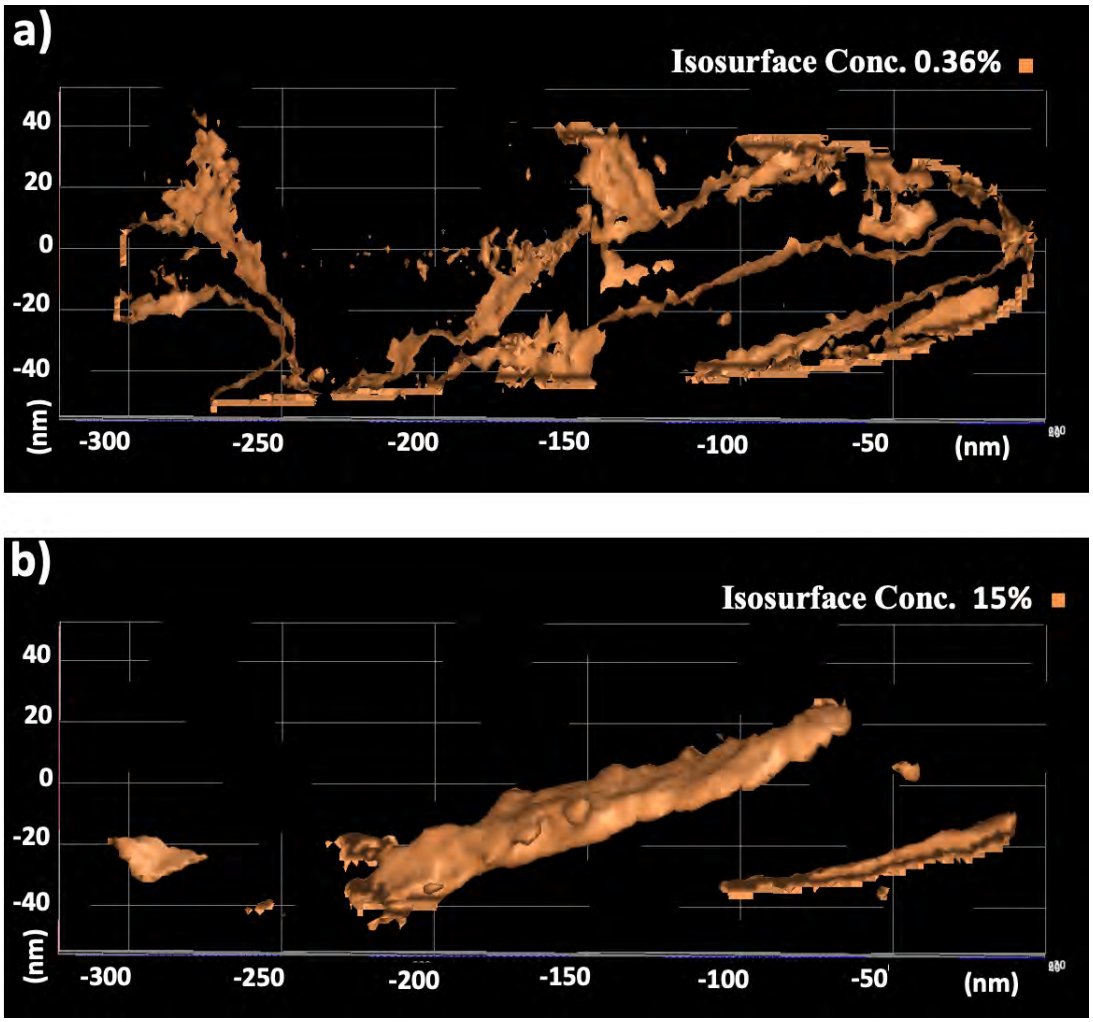

Figure 7.34: a) Slice of the 3D model of showing the isosurface carbon concentration of 0.36% in the volume, corresponding to ferrite grain boundaries. b) Full 3D model of the volume showing carbon concentration isosurface of 15 at%, corresponding to carbides within the region.

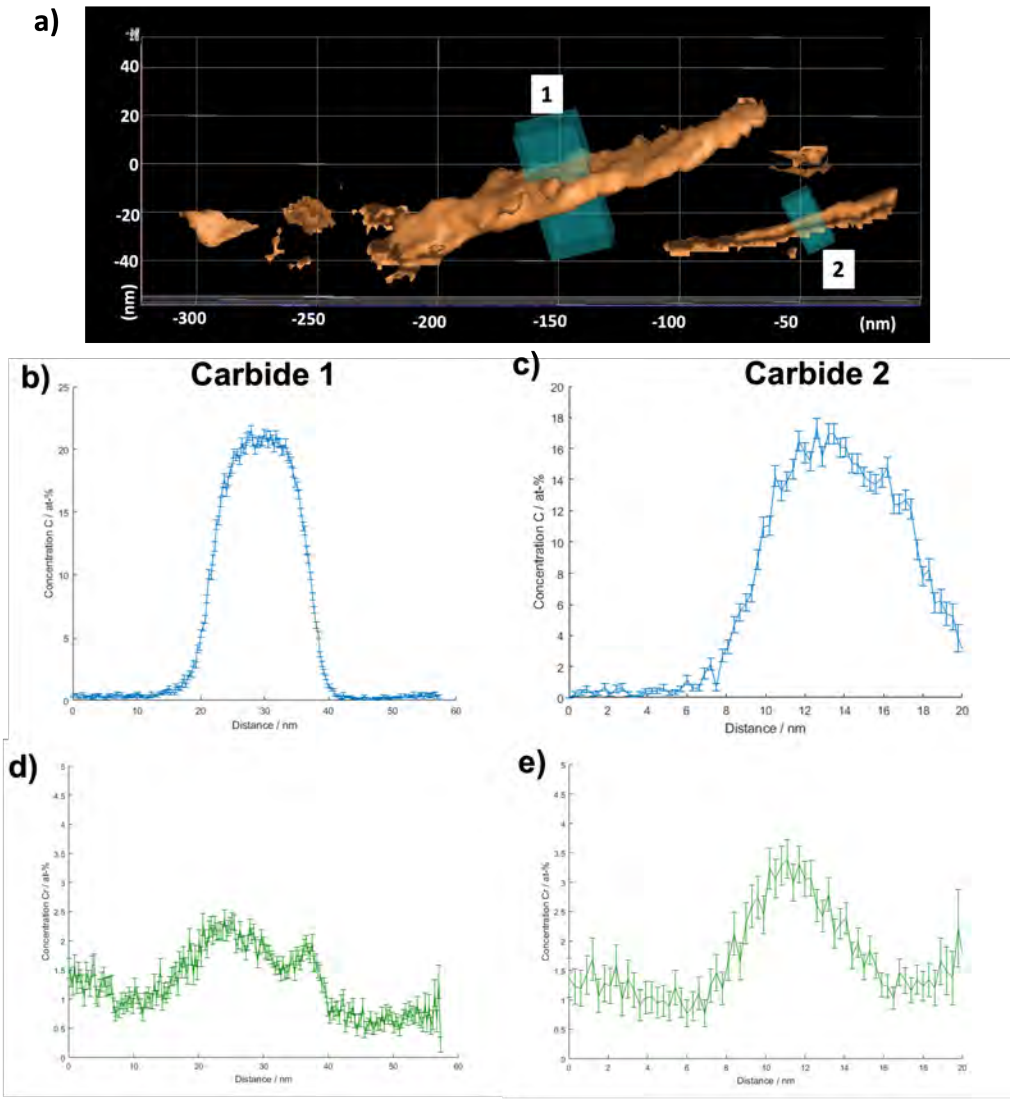

Figure 7.35: a) Slice of the 3D model of 15 at% isosurface carbon concentration showing the position (1 and 2) of carbides where proxigrams are taken. b,c) Carbon concentration variation (at%) and d,e) chromium concentration variation (at%) across ferrite/carbide interface of different locations highlighted in a).

7.8.3 APT Specimen C

The analysis on Specimen C has been focused on the areas of 'dissolving' grain boundaries, as shown in Figure 7.37a, where ferrite grains coarser than those in Specimens A and B are seen as well as more planer features. The grain boundaries and carbon structures can be observed based on the carbon concentration and planer shape shown in isosurface carbon map of 0.36 at% in Figure 7.37b. The fact that no carbon is detected in the isosurface carbon concentration of 3 at% (Figure 7.37c) suggests that this specimen was embedded in ferrite band at a junction of different ferrite grain boundaries with no carbides detected. An interesting observation is that the grain boundaries to the left of the images (Figures 7.37a and b) appear to contain more dispersed carbon atoms than that to the right.

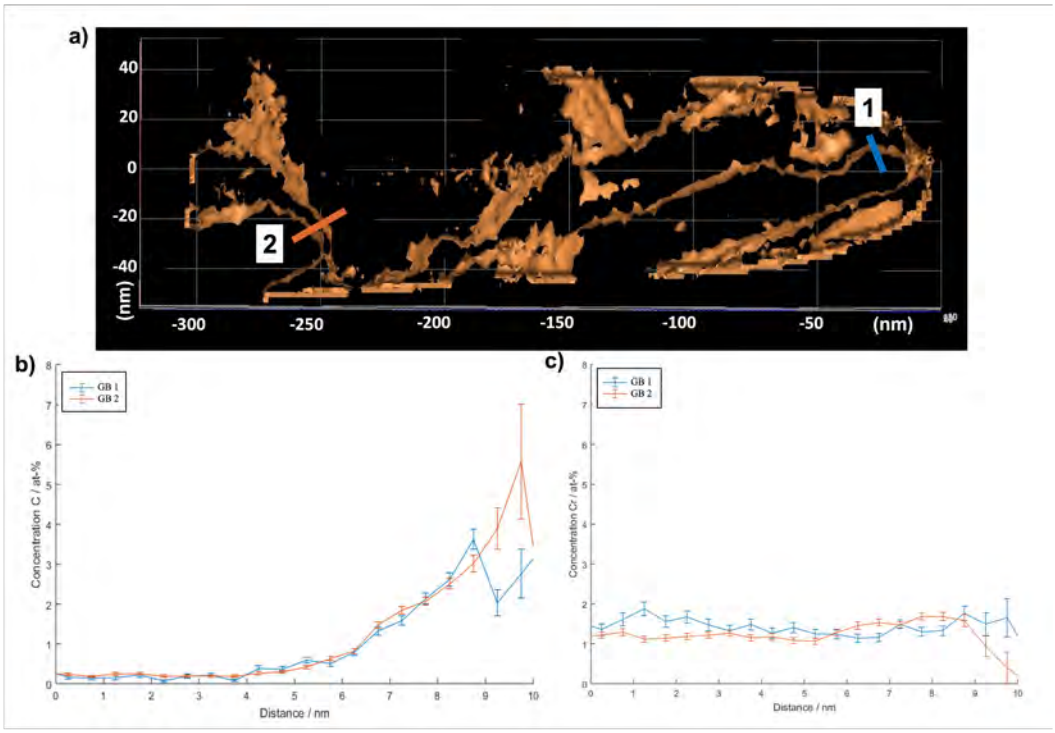

Figure 7.36: a) Slice of the 3D model of 0.36 at% isosurface carbon concentration showing the position (1 and 2) of grain boundaries where proxigrams are taken. b) Carbon concentration variation (at%) and c) chromium concentration variation (at%) across grain boundary of different locations highlighted in a).

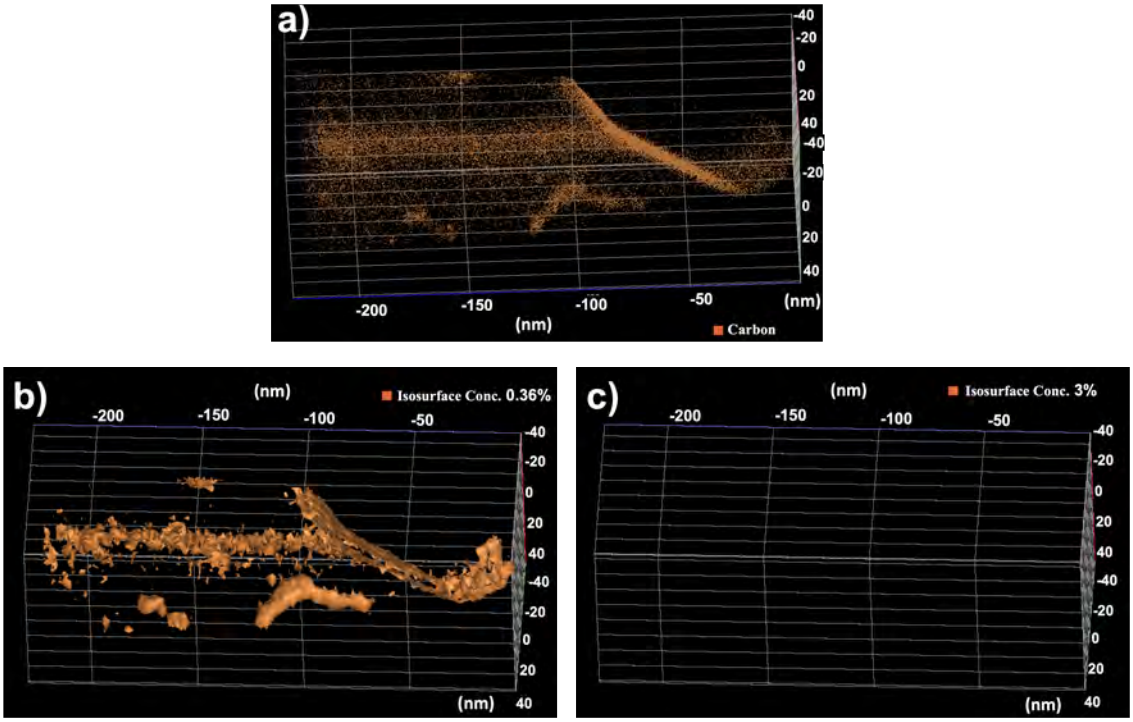

Figure 7.37: a) Carbon atom distribution across 5 nm thick slice of specimen C volume. Slice of the 3D model showing isosurface carbon concentration of b) 0.36 at% and c) 3 at%.

A comparison of the carbon distributions at those different grain boundaries has shown that the grain boundaries with more scattered carbon atoms have much lower carbon

concentrations (0.6 at% at position 1 in Figure 7.38) similar to findings in Specimen A (Figure 7.33). The other grain boundaries in Figure 7.38 show carbon concentrations of up to 3.5 at% at positions 2, 3 and 4, which resemble the other grain boundary carbon levels (up to 5 at%) discussed in Figure 7.31 and 7.36. Based on the relatively low carbon content and the dispersed carbon distribution in GB 1, it is suggested that that GB 1 is a dissolving grain boundary, likely due to coalescence of adjacent grains as discussed from Section 7.4 where carbon that was originally segregated at the grain boundary is released.

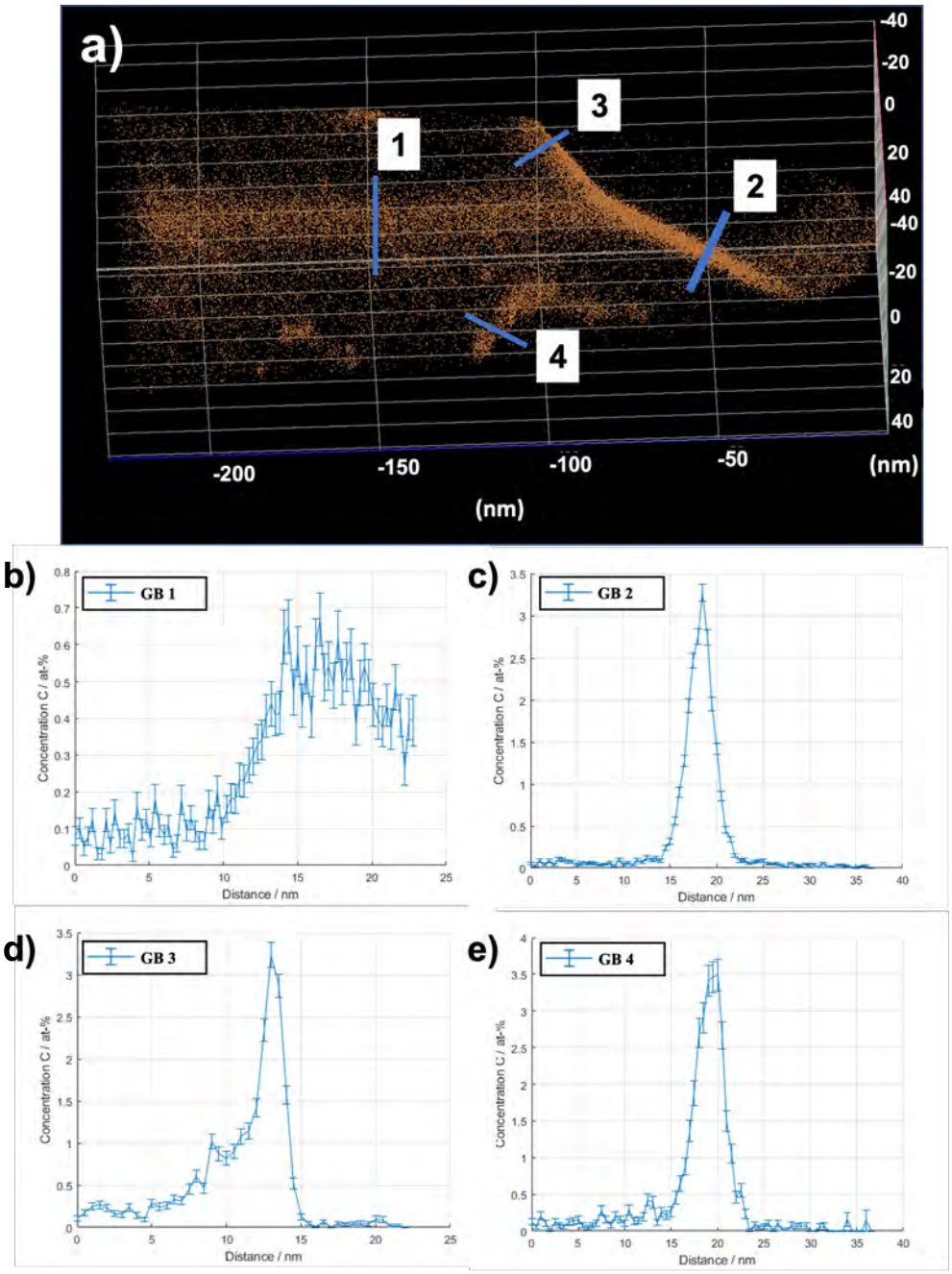

Figure 7.38: a) Location of different grain boundaries (GB) where carbon distribution is measured across. Proxigrams showing the carbon distribution across b) GB 1 c) GB 2 c) GB 3 and d) GB 4.

7.9 Discussion

This study has shown that WEB (both LAB and HAB) consist of three main constituents: equiaxed grains, elongated grains and lenticular carbides. The first stage of microstructural alteration in the formation of LAB is found to be the formation of very small bands of equiaxed ferrite grains (Figure 7.1). Over the increase of stress cycles during this stage, the bands grow in both thickness and length to up to 1-2 µm width and 10 µm in length. EBSD analysis has shown these bands have a higher IQ contrast compared to the surrounding matrix, suggesting a lower number of defects, such as strains and dislocations, in the bands and ferrite regions [170]. Coupled with the relatively low misorientation of the equiaxed grains shown in the KAM maps, this provides a strong evidence that these grains are ferritic and likely formed due to recrystallization.

Nucleation sites of recrystallized grains arise in regions of microstructure with relatively high dislocations. Recrystallisation occurs as a way of energy release following the energy build-up in the region due to local plastic deformation. LAB are found to form after DER development (as discussed in [4]) through a recrystallization process at stress build-up points within DER due to a martensite refinement process (discussed in Chapter 6). Due to difficulties in observing DER under LOM, especially at late stages where LAB are developed e.g. in the 100Cr6 as oppose to the 50CrMo4 samples in this study, some have reported LAB formation without DER in softer steels (hardness lower than 720 HV) [124, 139]. However, as shown in Chapter 6, the dark etch response which is caused by the dark etching bands may have broken down and hence be difficult to observe under LOM. A detailed examination e.g. using SEM, may be required to further confirm this in the future. However if LAB can indeed develop in steel without DER, it would suggest a different form of energy build-up rather than the parent grain refinement and dark etching band intersection mechanisms proposed in this study. While the recrystallization stages during LAB formation is linked to the stress points caused within the DER, the nucleation of HAB via a second recrystallization stage process is believed to be correlated with the lenticular carbides of the LAB, demonstrated by the substantial interfacial energy reduction during the transition from LAB to HAB. It has also shown that the equiaxed grains in LAB cause breakdown of pre-existing microstructure such as primary carbides within the bands (as shown in Figure 7.3d).

Various studies have investigated the influence of plastic deformation on cementite dissolution in steel microstructures and the factors influencing the stability of the carbides. The driving force for carbide dissolution in the microstructure is the supply of energy that is sufficient to destabilize the carbide. This energy could arise from the interfacial energy

that increases the Gibbs free energy of the carbide [191]. The interfacial energy is heavily dependent on the surface area to volume ratio $\frac{dSA}{dV}$ of the carbide. Shapes with a low $\frac{dSA}{dV}$ demonstrate a lower interfacial energy and greater stability, which explains why primary carbides are typically spherical. As shown in Table 7.2, the thin,long and densely packed lenticular carbides in the late stage LAB have a much higher $\frac{dSA}{dV}$ ratio (6 times) comparing that of the lenticular carbides surrounding HAB. Therefore a transition from LAB to HAB would make the carbides much more stable structures. It has also been reported that ferrite/carbide interfaces are preferential sites for dislocation pile-up, causing an increase in the interaction energy which can exceed the binding energy of C-Fe leading to the break of C-Fe bonds in carbides [192, 193], hence the subsequent recrystallisation (HAB nucleation) is a way of reducing the overall energy in the system. This also explains why HAB initiates from the dense region of LAB as highlighted in Chapter 4.

The equiaxed ferrite grains developed in LAB or HAB appear to have led to the formation of elongated grains within, with a preferential orientation close to a <111> direction // ND, similar to the findings from a previous study [120] and typically observed in cold rolled steel. However, during the early stages, elongated ferrite grains appear as small slightly distorted individual grains that are coarser than the surrounding equiaxed grains (Figure 7.16 and Figure 7.14) showing small variations in their orientations. Later in HAB, multiple grains started to align and elongate at approximately 80° to the rolling direction (see in Figure 7.15), showing coalescence of the individual grains into a longer elongated grain. During this process, grain rotation/coalescence appears to have occurred (also demonstrated by the carbon concentration variations in the APT analysis). A similar process has been reported in nanocrystalline metals when plastic deformation results in texture development through rotation of adjacent grains across preferential slip systems and eventually leads to coalescence as a form of grain growth (illustrated in Figure 7.39)[195–199]. Within a grain pair, due to plastic deformation one grain rotates to align with the adjacent grain resulting in the reduction of the initial high-angle grain boundary AB in Figure 7.39a to a low angle grain boundary in Figure 7.39b and eventually coalescence of the grains as shown in Figure 7.39c through the elimination of the adjacent grain boundary between the two grains. This is believed to be a form of recovery in the microstructure driven by the reduction of the boundary energy of the system [195, 196]. This explains the formation of the elongated grains shown in Figure 7.14 where the initial individual grains coarser than the equiaxed grains with a similar grain orientation (after rotation) have grown (coalescence) into longer grains (the elongated grains) as shown in Figure 7.15. Within the $\sim$ 8 µm elongated grain, some low-angle grain boundaries are still visible (green lines in Figure 7.15c) suggesting a possible transition from high-to-low angle grain boundaries and eventually fully coalescence.

It has been previously proposed that elongated grains found in both LAB and HAB show a $< 111 > \{112\}$ slip system aligned with the long axis of both bands (30° and 80° to the rolling direction respectively) [120]. This is similar to findings from this study that show plastic deformation of the equiaxed regions in WEB occurs through grain rotation towards preferential slip systems that are likely aligned with the shearing component responsible for the LAB and HAB orientations. The alignment of grains results in a form of recovery through the elimination of common grain boundaries and grain growth thus the formation of elongated grains. This is also evidenced from TEM analysis where grains embedded within the equiaxed ferrite grains show an elongation pattern in the LAB orientation. The proposed alignment of the elongated grains with a shear component is based on the higher deformation observed compared to the surrounding more randomly orientated equiaxed grains (see KAM maps in Figures 7.14-7.18). It is worth noting that, the elongated grains in LAB and HAB are different as lenticular carbides form adjacent to the elongated grains in LAB but not in HAB. Given that lenticular carbides at the edge of HAB are observed to thicken and merge into clear boundaries (Figure 7.11), a migration of carbon within the HAB that was released during the breakdown of the pre-existing lenticular carbides within to the remaining carbides at the edges of the HAB is proposed which acts as carbon sinks. This depletes the equiaxed band prior to the formation of elongated grains, hence no new lenticular carbides are formed in HAB unlike LAB.

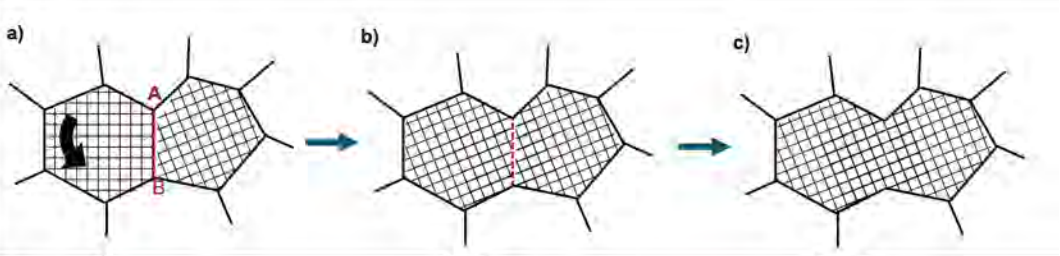

Figure 7.39: An illustration of the grain rotation and coalescence theory due to plastic deformation in nanocrystalline materials, showing a) rotation of one of two adjacent grains with a high-angle grain boundary, b) the high-angle grain boundary become a low-angle grain boundary after the grain rotation and c) fully coalesced grains resulting in a coarser and elongated grain.

The coarse grains of the elongated grains are also evidenced from the nano-indentation analysis, where they show to have a lower hardness comparing with the surrounding equiaxed grains. The overall hardness of the LAB and HAB is lower than that of the martensitic parent matrix, suggesting ferritic structures. Hardness values of equiaxed grains and lenticular carbide in WEB reported by Smelova et al. [120] being 4.2 - 6 GPa and 9 - 11 GPa respectively are similar to those obtained in this study (5.04 ± 0.8 GPa and 9.67 ±1.9 GPa respectively), however a much smaller indentation size has been used in this study to ensure

that the indents were obtained in individual features such as equiaxed and elongated grains without overlapping with neighbouring microstructures. It is also interesting to see that the primary carbides have a similar hardness to the lenticular carbides (shown in Figure 7.19) or carbon-rich areas as reported in [120].

Diffraction pattern and EDX analysis of the lenticular carbides (Figure 7.25-7.28) provide evidence that it consists of a polycrystalline orthorhombic cementite structure, which clarifies the debates in literature as what structure these carbides consist of [4, 8, 79, 117, 141]. It is shown in Figure 7.26 that the lenticular carbides consists of columns of carbide crystallites with the long axis perpendicular to the LAB orientation, supporting the current theory of carbon migration from the ferrite band to the edges of the band where carbides nucleate. However, different to previous studies [117, 141, 150], the carbide nucleation is linked to the elongated ferrite grains rather than the overall ferrite band containing both equiaxed and elongated ferrite grains. This is evidenced from Figure 7.26 where rows of both carbon-depleted regions (elongated ferrite grains) and carbon-rich regions (carbides) are stacked. Figure 7.27 shows slight carbon accumulation at the edges of the elongated grains rather than the surrounding equiaxed grains which suggests the possible nucleation site for the lenticular carbides which is also supported from the SEM study in this section.

The atomic distribution of carbon investigated through APT has shown the carbide structures within the LAB to consist of about 23 at% which is similar to previous findings [124] using EELS and similar to the theoretical carbon composition of cementite (25 at%). However it is interesting to observe within both EDX and APT analysis, some carbide structures show traces of chromium where previous studies have reported lenticular carbides to be chromium depleted [120, 138], although the chromium distributions within these carbides are not fully embedded across (see Figure 7.35). This suggests that rather than being a deformed state of primary carbides, considering the slow diffusion rate of chromium, it is likely that the probability of chromium embeds within the lenticular carbide may be associated with the possibility of a pre-existing primary carbide dissolving in the same location. While carbon may diffuse across either through dislocation migration or temperature diffusion, chromium will likely remain due to the slow diffusion rate and hence, may become embedded in new carbides nucleating within its proximity. This would explain why similar carbides with similar carbon contents show variations in chromium contents.

The grain boundaries within LAB show an average carbon concentration varying from 2 to 3.5 at% with the exception of GB 2 in Figure 7.36 which showed a concentration of 5 at%. For comparison, reports have suggested grain boundaries in white etching cracks

(WECs) have a carbon concentration at the grain boundary ranging from 2-5at% [188] while another study have reported up to 14 at% [200]. However, WECs have a finer equaixed grain structure of 10-50 nm [188, 200] while grains in LAB have been observed to exceed 100 nm in this study. This may lead to an overall higher carbon content in WEC volume compared to WEB due to more grain boundaries. Nonetheless, irregular shaped carbides in the LAB shown in the APT investigation with sizes exceeding 100 nm are not typically observed in WEC [166, 188, 200, 201] as they appear more uniformly distributed across the grain boundary network in WECs compared to the LAB in this study where carbide formation is observed at grain boundaries. Hence it appears carbide formation in the equiaxed ferrite grains of WEB is more evident compared to that in WEC which may be due to the grain size. Evidence in Figure 7.32 and Figure 7.38a shows potential dissolving of grain boundaries leading to carbon dispersion which could be a consequence of rotation/coalescence of equiaxed grains.

7.10 Conclusion

The investigation of the microstructure of WEB (including both LAB and HAB) formed in ACBBs has been conducted using a range of characterisation techniques using SEM, EBSD, nanoindentation, FIB/TEM, EDX and FIB/APT techniques. Detailed analysis has provided evidence of the three main constituents in LAB and HAB being equiaxed grains, elongated grains and lenticular carbides. The samples tested over a range of stress cycles have enable the elucidating of LAB and HAB evolution mechanisms from early to late stages and their possible drivers. Findings in this chapter have been used to propose a unified formation mechanism which is presented in Chapter 8. The conclusions of this chapter are summarized below:

- LAB form in three stages: at the early stage, bands of equiaxed ferrite grains develop within the maximum shear stress region. As the equiaxed ferrite band grows in length and thickness, the intermediate stage shows elongated ferrite grains developing within these bands due to plastic deformation accompanied by the nucleation of lenticular carbides at the edges of the elongated grains. These carbides grow in thickness across the equiaxed ferrite grains of the LAB. At the latest stage multiple densely packed bands form and merge together leading to large regions of LAB completely altering the parent microstructure. Towards the latest stage of LAB formation, regions of equiaxed grains form within dense LAB areas while lenticular carbides break down, leading to the initiation of HAB.
- HAB is observed initially as a band of equiaxed ferrite grains developing within regions

of dense late stage LAB where pre-existing features such as the LAB constituents (elongated grains, lenticular carbides) gradually breakdown as the equiaxed HAB grows in length and thickness. During later stages, HAB show elongated grains being developed within the equiaxed bands similar to LAB, however without being accompanied by the lenticular carbide nucleation adjacent to the elongated grains. The lenticular carbides at the edges of the HAB appear to continue thickening and merging into clear boundaries of the HAB. This is believed to be due to migration of carbon within the HAB that was released during the breakdown of the lenticular carbides within to the remaining carbides at the edges of the HAB which acts as carbon sinks.

- Evidence suggests that the formation of equiaxed ferrite grains in both LAB and HAB is a result of recrystallization to release the energy-build-up in the system during RCF. Lenticular carbides in fully developed LAB show to be less stable with a high surface-volume ratio. This has led to the transformation to those in HAB achieving more stable geometries through the reduction of interfacial energy of the carbides. A similar energy build-up in the initial microstructure is believed to contribute to the initiation of the LAB recrystallization stage where the refined microstructure in the DER and the intersection of dense closely-packed DER bands results in stress points resulting in a recrystallization process (equiaxed ferrite grain of LAB).

- The formation of elongated grains within the recrystallized equiaxed ferrite grains in LAB and HAB is a form of recovery due to plastic deformation induced grain rotation and coalescence driven by the reduction of the overall grain boundary. In LAB, the elimination of grain boundaries results in the release of carbon and its accumulation at the grain boundaries of the elongated grains resulting in the nucleation of lenticular carbides rather than carbon migration across the whole equiaxed ferrite band. Carbides have been found to develop across grain boundaries in the LAB while carbon accumulation has been recorded at the edges of elongated grains prior to carbide formation. In HAB, lenticular carbides formed during LAB formation (adjacent to HAB) act as carbon sinks driving carbon migration from the equiaxed grains to the carbides. This depletes the equiaxed band prior to the formation of elongated grains, hence no new lenticular carbides are formed in HAB unlike LAB.

Chapter 8

Unified Formation Mechanisms for DER, LAB and HAB

The first stage of microstructural alterations due to RCF is the formation of the DER which first appears as DER bands developing in parent microstructures (Figure 8.1b). These have been given different names in literature such as ferrite microbands [137] , deformation bands [80], dark needles [125], persistant slip bands [126] and elongated ferrite grains [14, 120]. Nonetheless, these bands appear to have smooth etch-resistant structures at their edges that are similar to those lenticular carbides found in WEB at larger scale. This suggests that similar to LAB, carbide-like structures develop at the edge of these dark etching bands within the DER which could be related to dislocation rearrangement under applied cyclic stress within the bands (Figure 8.1b). These bands grow in density across the maximum shear stress region in patches ('randomly orientated' groups of bands with similar orientation, see in Figure 6.7), resulting in the dark etch response observed in LOM. As the dark etching bands grow, a refinement process is observed within the DER area through fragmentation of martensite laths especially in the maximum shear stress region (Figure 8.1c). At a late stage, the dark etching bands are seen to disappear (less frequently observed) while more and more equiaxed/fine grains are formed in the region (brightening due to higher hardness). This is suggested also due to breakdown of dark etching bands at band intersections (Figure 8.1d).

The refined microstructure in DER is shown to consist of various high stress points which lead to recrystallization of fine equiaxed ferrite grains (Figure 8.2b) evidenced by the EBSD analysis results (Figure 6.15), where low misorientation grains are seen surrounding high stress points of the refined microstructure. The recrystallization of equiaxed ferrite grains is also seen to nucleate at intersections of dark etching bands (Figure 8.2c) as evidenced in Figure 6.11. The development of equiaxed grains leads to initiation of LAB. However, it

remains unclear why the equiaxed ferrite bands grow at the distinct directionality of 30° to the rolling direction.

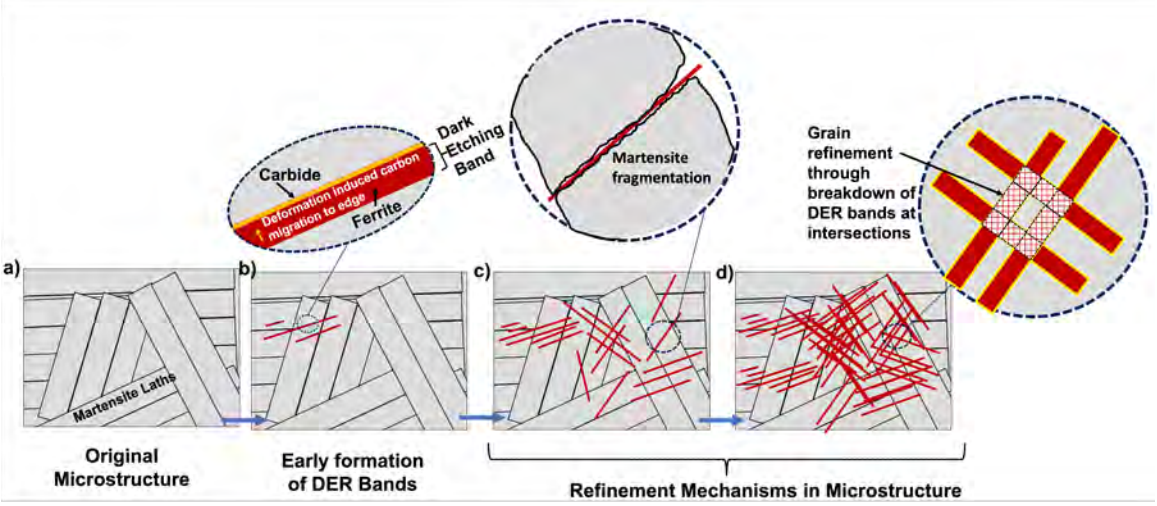

Figure 8.1: Schematic of microstructural alteration stages in DER showing a) original microstructure consisting of martensite laths. b) Development of DER bands in parent microstructure which consist of carbide-like structure at the edge likely due to carbon migration across the DER band. c) More DER bands develop at different orientations which result in the fragmentation of martensite laths leading to refinement of the region. d) DER bands become dense leading to dark patches where the DER bands eventually breakdown due to intersections between different DER bands at different orientations.

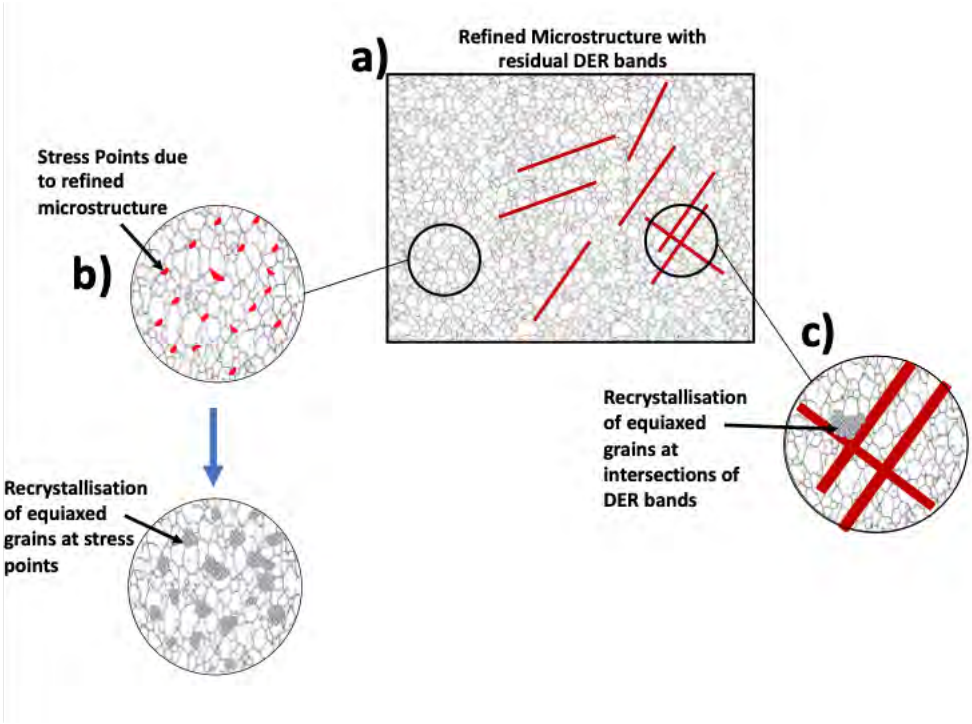

Figure 8.2: a) Schematic of late stage DER consisting of refined microstructure resulting from the refinement mechanisms in Figure 8.1 and remaining DER bands still intact. b) Stress points due to refined microstructure due to martensite fragmentation becoming nucleation sites for recrystallization and equiaxed ferrite grain formation. c) Recrystallization of equiaxed ferrite grains nucleating at intersections of dark etching bands.

The initial or early stage of LAB is characterized by the formation of equiaxed ferrite grains as a band that grows in length and thickness (Figure 8.3a and 8.3b). This is later followed by the formation of elongated ferrite grains within the equiaxed grain band (Fig. 8.3c) and the lenticular carbides forming adjacent to the elongated grains. The growth of both the elongated ferrite grains and the lenticular carbides in equiaxed ferrite grain bands results in the commonly observed 'cotton-bud' shape bands formation (Figure 8.3d). The cotton-bud shape has 'heads' consisting of equiaxed grain and the 'stem' of elongated ferrite grains and lenticular carbides. For larger equiaxed ferrite grain bands, multiple elongated grains surrounded by lenticular carbides may develop within the band parallel to each other which is considered the late stage of LAB (Figure 8.3e).

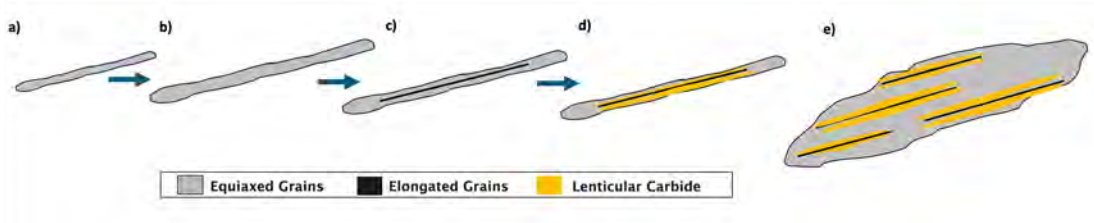

Figure 8.3: A schematic showing LAB evolution from the initial stage as a small band consisting equiaxed grain (a) growing in length and thickness (b). During the intermediate stage (c), elongated grains develop within the equiaxed grained band and eventually lenticular carbides nucleate at the edge of the elongated grains and grows leading to the cotton-bud shape shown in (d). At the latest stage, LAB multiplies forming dense LAB areas showing in (e).

It has been suggested in literature that lenticular carbides nucleate at the edges of the equiaxed grained LAB [4, 8, 14, 80, 82, 117, 123, 124, 131, 143, 150]. However, SEM evidence of LAB at different stages in this study have shown that lenticular carbides originate at the edges of elongated ferrite grains rather than the edges of equiaxed grain bands due to plastic deformation as a form of recovery. TEM analysis has also shown that lenticular carbides are parallel to carbon-depleted elongated ferrite grains (not at the edges of equiaxed grain bands).

A possible explanation for the nucleation of the lenticular carbides at these sites could be explained by the grain rotation-coalescence theory discussed previously. APT analysis has shown that carbon segregates at equiaxed grain boundaries and is depleted within each grain due to the incompatibility of the carbon with the ferrite matrix [166, 200]. The rotation/coalescence theory is supported by the texture developed in the grains from EBSD analysis and the dissolving grain boundaries shown in the APT results where carbon is seen to disperse across grains. Hence during the transformation of equiaxed to elongated ferrite grains, the elimination of adjacent grain boundaries during coalescence would release the segregated carbon atoms leading to a diffusion of carbon towards the grain boundaries of

the newly formed elongated ferrite grain which would have a higher carbon concentration compared to the carbon concentration in the grain boundaries of the initial equiaxed grains (Figure 8.4). This has thus led to lenticular carbides nucleation at the edges of the elongated grains once enough carbon has accumulated during coalescence. The carbon diffusion in this instance may be driven by dislocation-assisted carbon diffusion or free carbon diffusion [150].

Results in this study suggest that current theoretical models in literature assuming lenticular carbide nucleation through carbon migration across the whole equiaxed ferrite band [4, 14, 117, 150] provide an overestimation of LAB initiation (as discussed in Chapter 5). Since carbide nucleation is actually caused by carbon migration from elongated grains of 20-300 nm thickness rather than across the equiaxed bands of an order of magnitude thicker, the formation of LAB is predicted to be earlier than the old models. It has also been observed that multiple elongated grains may develop in large equiaxed grain regions forming multiple carbides adjacent to the elongated grains, confirming that the diffusion distances used in previous LAB prediction models are far too large. However, after the nucleation of the lenticular carbides, they grow in thickness and typically exceeds the thickness of the elongated ferrite grains. This suggests that once the carbide nucleates, they act as a carbon sink driving carbon migration from the equiaxed ferrite grains within the band possibly by the dislocation-assisted diffusion mechanism [150]. It is therefore important to differentiate between the nucleation stage of the lenticular carbide and the growth of the carbide afterwards. A schematic of the formation of elongated grains and lenticular carbides in LAB is shown in Figure 8.4.

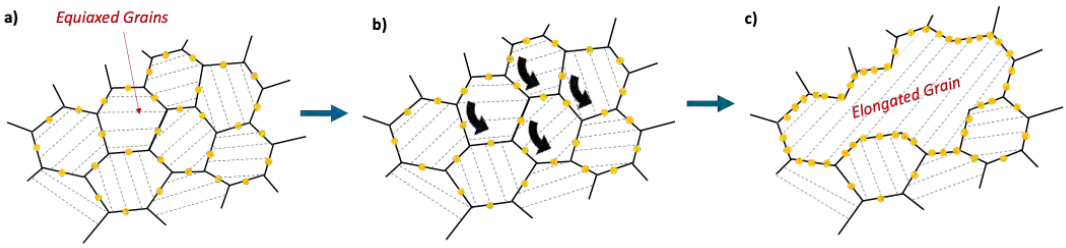

Figure 8.4: A schematic of the formation of elongated grains and lenticular carbides in LAB. a) Equiaxed grains of various orientations in LAB with carbon segregated at grain boundaries. b) Grain rotation and coalescence in LAB leading to formation of elongated grains. c) A fully developed elongated grain where carbon in the elongated grain boundaries due to coalescence have migrated to the boundaries of the elongated grains leading to nucleation of lenticular carbides. Yellow marks indicate carbon.

Looking at the HAB which form later in bearing life, a similar sequence is observed starting with the formation of equiaxed ferrite grains (Figure 7.9a, Figure 7.10a and Figure 7.11a) followed by the formation of elongated grains within similar to that during LAB development (Figure 7.10b-d). A schematic of the different stages of HAB formation is

shown in Figure 8.5. The high IQ contrast and low misorientation (Figure 7.13) suggests the equiaxed grains are products of recrystallization similar to that of LAB. A noticeable difference between the LAB and HAB is the absence of carbide forming at the edge of elongated grains in HAB. While elongated grains are the nucleation sites for lenticular carbides in LAB, the pre-existing dense lenticular carbide areas around the HAB act as carbon sinks as observed in Figure 7.11. Lenticular carbides in LAB breakdown and dissolve forming new equiaxed grains (imitation of HAB) while thickening of the carbides at the edges of HAB continues (Figure 7.11c and 7.11d). As discussed above, the driver of the formation of equiaxed grains for HAB (initial stage HAB) is proposed to be the high interfacial energy of the close-packed lenticular carbides in dense LAB which is released via recrystallization to break down the lenticular carbides into more stable structures in HAB (Figure 8.5b-c).

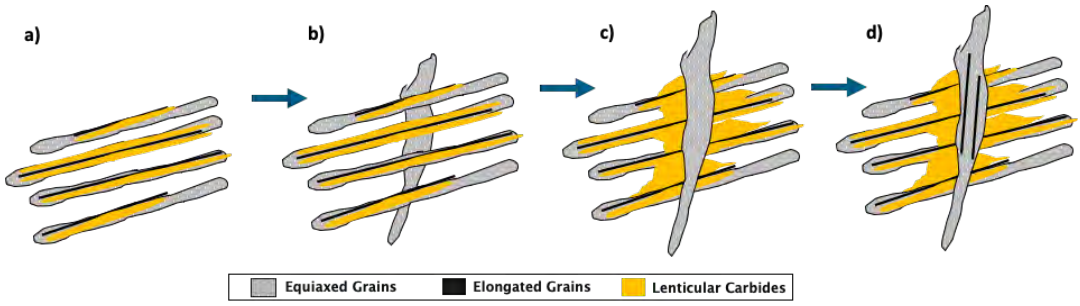

Figure 8.5: A schematic showing the HAB evolution process starting from a) dense LAB region, b) equiaxed HAB forming in region with dense close-packed LAB, c) breakdown of pre-existing features such as lenticular carbides within the HAB and the carbides thicken/merge at the HAB edge making clear boundary. d) Elongated grains develop gradually within the equiaxed grains of HAB.

Based on the SEM observations, the dissolution of the pre-existing lenticular carbides of the LAB within the HAB would result in free carbon released migrating to the carbides outside the HAB (see Figure 8.6) causing the observed thickening at the HAB boundaries. This suggests that the lenticular carbides act as carbon sinks which attract carbon from the equiaxed grains to the carbide given the incompatibility of carbon in the ferrite matrix of the band while the HAB acts as diffusion channels. It was shown in Table 7.2 that such a breakdown of the lenticular carbides and the migration of carbon to the residual lenticular carbides at HAB edges results in a more stable carbide network of a reduced surface-volume ratio, supporting the proposed mechanism during the second recrystallization stage taking place during HAB formation.

In LAB, even though the lenticular carbides are shown to nucleate at the edges of elongated grains, they are typically larger in thickness compared to the elongated grains. This suggests that after nucleation, it is likely that these carbides act as carbon sinks for excess carbon in the equiaxed ferrite bands and hence keep growing in thickness across the

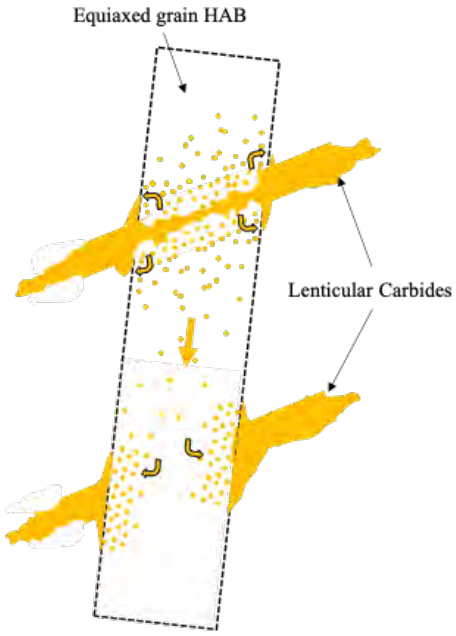

Figure 8.6: A schematic showing the breakdown of lenticular carbides within HAB (transition from Fig. 8.5b-c). The resulting free carbon in the HAB later migrates to remaining lenticular carbides at the edge which act as carbon sinks and the HAB becomes a sort of diffusion channel. Arrows indicate the direction of migration of excess free carbon in the band

equiaxed ferrite grains. A major difference between the two bands is that no new lenticular carbides develop with the elongated grains of the HAB unlike the LAB. This could be explained by the surrounding microstructure of both LAB and HAB during initiation. For LAB, it is seen in Figure 7.3d that primary carbides in the path of the equiaxed ferrite bands dissolve which likely results in carbon accumulation within the bands. This is an expected observation during recrystallization where pre-existing features breakdown during the formation of new grains. This suggests that pre-existing features such as primary carbides, tempered carbides or even the martensitic matrix all of which typically have a relatively higher carbon content dissolve within the equiaxed grains of the band leading to carbon build-up in the LAB. Once the elongated grains develop, lenticular carbides nucleate which then acts as carbon sinks to reduce the carbon accumulation within the band [150]. Prior to the nucleation of the lenticular carbide from the elongated grains, there are no obvious carbon sinks leading to the carbon saturation of the band.

Initial carbon build-up in the equiaxed grains in a HAB is likely to originate from the breakdown of lenticular carbides within LAB. However, it can be seen from the early formation stage, HAB are surrounded by multiple LAB (consisting of lenticular carbides) which can attract carbon from the equiaxed grains of the HAB prior to the formation of elongated ferrite grains due to deformation. This is evidenced from Figure 7.11 where continuous thickening of the lenticular carbides at the edges of the HAB can be seen (see

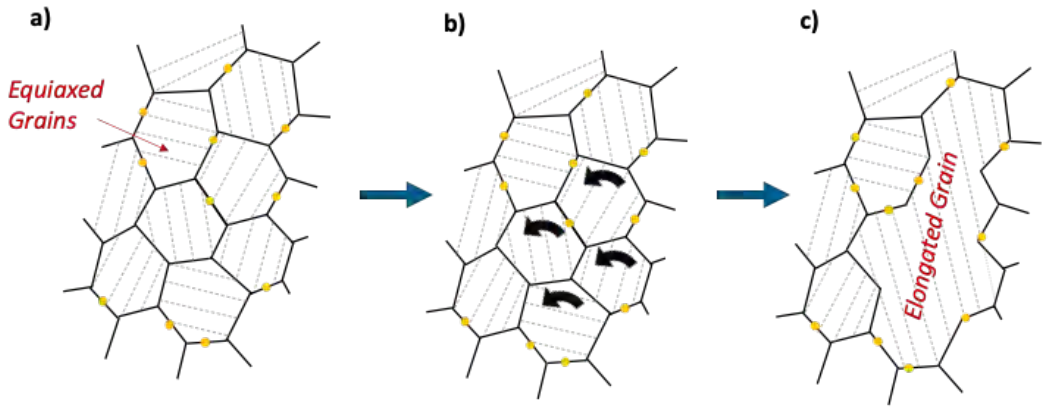

Figure 8.7: A schematic of an elongated grain formation in a HAB. a) equiaxed grains of various orientations in HAB with carbon segregated at grain boundaries but less carbon compared to the LAB in Figure 8.4a. b) Grain rotation and coalescence in HAB leading to formation of elongated grains. c) Fully developed elongated grain where no significant carbon has been released during grain coalescence. Yellow marks indicate carbon and hence carbon build-up at the edges of the elongated grain is not sufficient for carbide nucleation.

schematic in Figure 8.5b-c and Figure 8.6). Hence when the elongated grains develop in HAB, there is no significant carbon accumulation at the edges of the newly formed elongated grains to result in nucleation of new lenticular carbides. An earlier study has suggested through microprobe analysis that HAB have a lower carbon content compared to LAB, which supports this theory that there is less carbon accumulation in the HAB equiaxed grains than the LAB equiaxed grains when the elongated grains develop [4, 128]. A schematic of the formation of elongated grains in the relatively carbon depleted equiaxed grains of the HAB is shown in Figure 8.7. The texture associated with the elongated grains in both LAB and HAB shows an approximate <111> axis parallel to the normal direction, which is in agreement with previous findings [120], which additionally reported a $< 111 > \{112\}$ slip system parallel to the long axis of the elongated grains. This suggests the grain rotation (texturing) is likely driven by a stress component acting in the orientation of $\sim 30°$ and $80°$ for LAB and HAB respectively causing the alignment of preferential slip systems with the stress component.

The proposed formation mechanism has established a link between all three RCF-induced microstructural alterations which have been observed for decades forming sequentially but their dependence on each other and their formation mechanisms remained unclear. While this model has successfully established a link between all three features, certain aspects remain yet unclear such as the orientation of which the recrystallized equiaxed grains of the LAB and HAB (more distinctive orientation than equiaxed grains in DER) grow and the stress component responsible for the rotation/coalescence of equiaxed grains to form elongated grains. Modelling of uniaxial testing conducted by Chen et al. [202] has shown

that activation of slip systems conforms with the highest Schmid factor in each grain which is influenced by the grain orientation. Given that the elongated grains with an established texture are more deformed (based on KAM maps) compared to the surrounding equiaxed grains which have more heterogeneous orientations suggests a maximum Schmid factor associated with the LAB and HAB orientations.

Chapter 9

DER/WEB Link with Bearing Failure

In this Chapter, the potential influence on the formation of DER and WEB on bearing failure is investigated to determine how the features may influence the durability of the bearing steel. In this section, samples from martensitic 100Cr6 bearings have been investigated including one bearing with surface pitting and several bearings without any surface damages of a range of stress cycles.

9.1 The failed bearing

The 100Cr6 bearing failed after being RCF tested for 885 million cycles under a contact pressure of 3.5 GPa and temperature of 80° (similar to all other tests in this project). A large pit/spall is observed on the surface of the inner ring of this bearing (see Figure 9.1a), where crack networks are seen in the subsurface (in a circumferential section). Micro-cracks adjacent and parallel to LAB are observed in Figures 9.1c-e, especially propagating through interfaces between lenticular carbides and ferrite phases, which happen to be planes of weakness in the microstructure being hard-soft material interfaces.

Since these micro-cracks are unlikely the spall initiation locations based on the size of the pit, it is difficult to confirm the role of LAB in crack initiation stage. However, from the shape and position of the large crack across the WEB region, it is likely that LAB played a role in the crack propagation especially at the weak plane of the ferrite-carbide interface due the big difference in their hardness (Chapter 7).

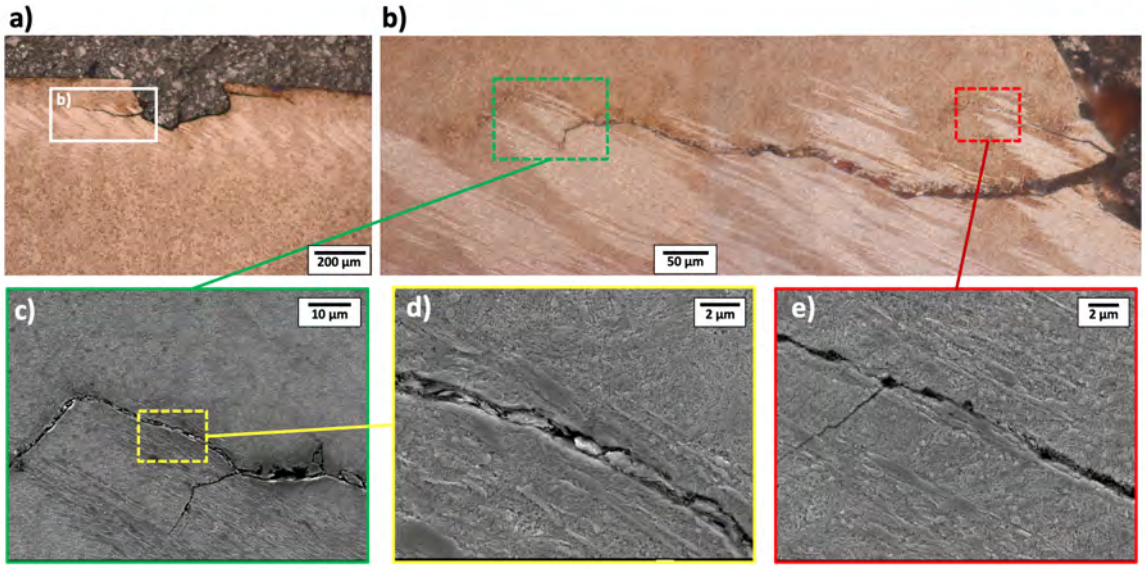

Figure 9.1: a) Optical image of micro pit in failed 100Cr6 sample run for 885 million cycles for 3.5 GPa. b) Optical image of crack connected to pit. c) SEM image of micro-crack tip showing interaction between crack position and LAB features. d) Enlarged SEM image from d) showing crack propagating between ferrite grains and lenticular carbides of LAB. e) SEM image of micro-crack parallel to lenticular carbide of LAB.

9.2 Non-failed Bearings

In this section, the subsurface of non-failed bearing samples (i.e. no surface damage observed) is investigated to determine the impact of subsurface microstructural alterations (DER/WEB) on the integrity of the steel microstructure during RCF. Interactions between WEB and non-metallic inclusions (NMIs) observed in those bearings are reported in this section along with voids/cracks observed in individual LAB in late-stage samples, i.e. when WEB are fully formed as discussed in Chapter 4.

9.2.1 Subsurface cracks/voids in LAB

Voids have been observed in LAB in several bearing samples of various stress cycles without surface damages (shown in Figures 9.2 – 9.5). Figure 9.2 shows examples of voids/micro-cracks parallel to LAB involving removal of lenticular carbides and ferrite in the 100Cr6 bearing of 4141 million cycles, which contains fully formed LAB. The cracks shown in Figures 9.2a and c) are over 10 µm in length and about 1-2 µm in width while the one in Figure 9.2b is of less than 2 µm in length and approximately 500 nm in width.

It is however not possible to confirm whether the voids were a by-product of the metallographic preparation or an etching artefact or indeed formed inside the material prior to being examined due to the nature of the microstructural alterations developing within the microstructure. Nonetheless, even if they are a result of surface preparation, it would still

suggest that LAB in the subsurface, especially the lenticular carbides-ferrite interfaces, as planes of weakness, has a significant impact on the integrity of the microstructure. However, based that similar voids have mainly been found in the late stage samples (e.g. the 100Cr6 bearings run for 4141 million cycles and 3016 million cycles under 2.9 GPa), it suggests that they are likely naturally occurring features. Voids are observed in both the region with the highest density of LAB and at the depth where the LAB are more separated (see Figure 7.8) as shown in Figure 9.3.

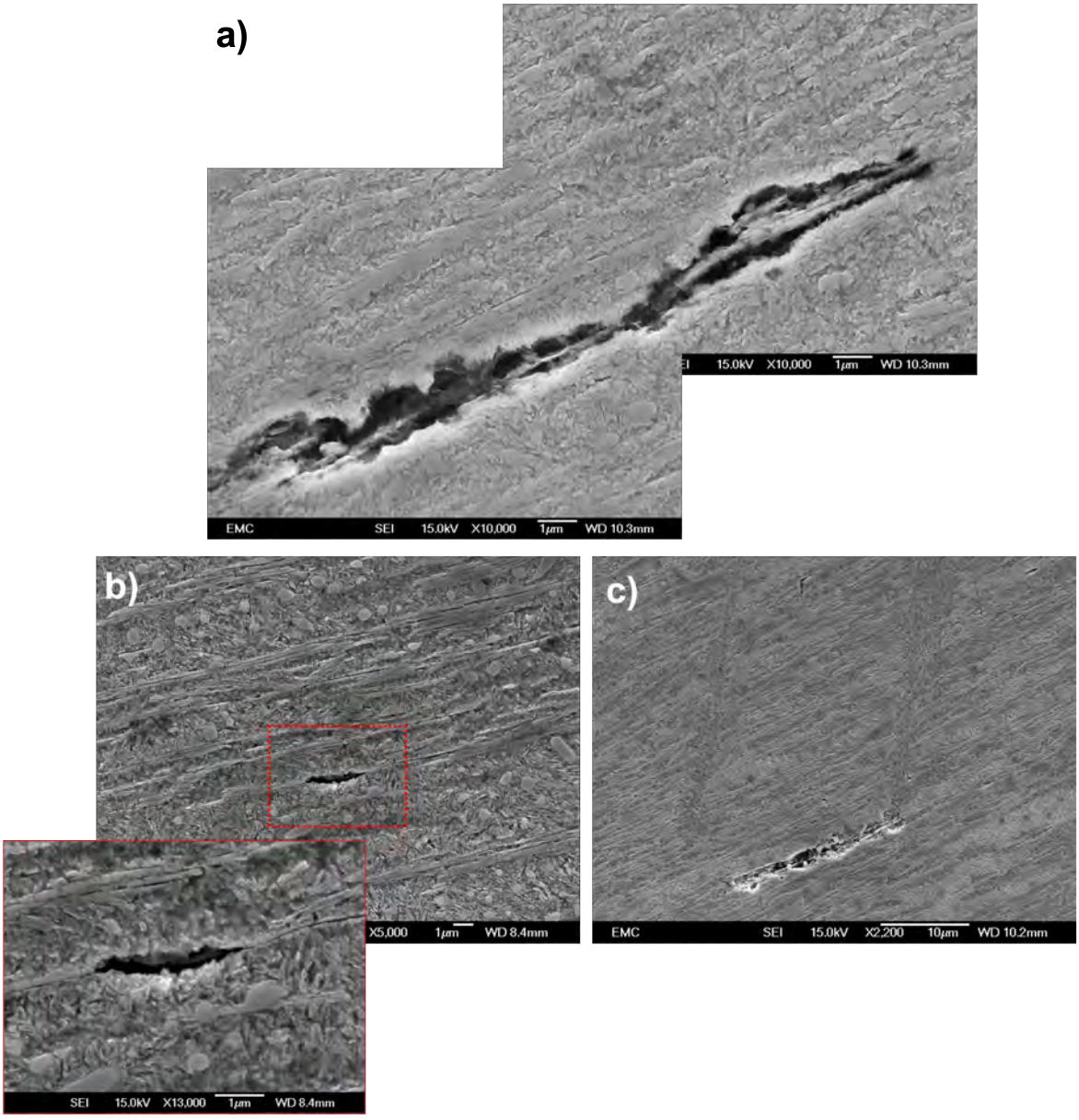

Figure 9.2: a) Different voids observed across LAB in 100Cr6 sample run for 4141 million cycles under 2.9 GPa.

Serial sectioning through a large single LAB in the 4141 million cycle 100Cr6 sample (see in Figure 9.4) has been conducted to investigate the nature of these voids. Voids at the edge of WEB area with less dense or individual LAB have been selected to avoid complications.

Materials were removed at 1 µm intervals for 12 µm depth. The optical images of the 12 slides are shown in Figure 9.4, indicating a continuity of the voids throughout the whole depth of 12 µm. This coupled with the void dimensions getting smaller with serial sectioning suggests this is unlikely to be an artefact of etching. It is interesting to note that across the sections shown in Figure 9.4, the void is mainly surrounding the edge of a lenticular carbide in the middle of the LAB while the width of the void spreads across the ferrite band. While it may be possible for the relatively brittle lenticular carbides being removed during polishing, the fact that the void spans over the 12 µm thickness of sectioning suggests it could be a naturally occurring artefact.

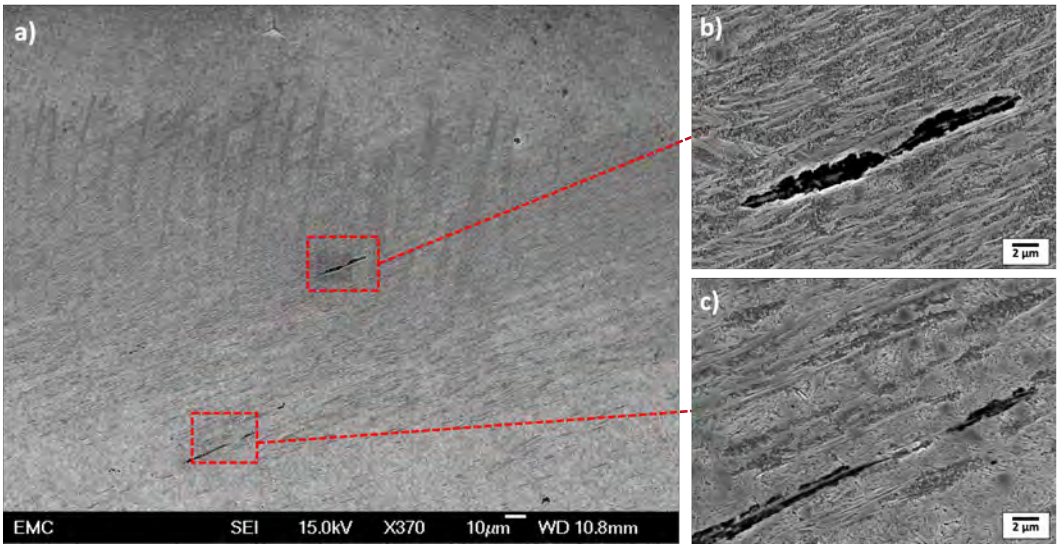

Figure 9.3: a) Different voids observed across LAB in 100Cr6 sample run for 4141 million cycles under 2.9 GPa in a) dense region of LAB and b) region with more sparse LAB.

Figure 9.5 shows multiple voids have been developed within a large area of LAB, typically at the interfaces of lenticular carbides and ferrite grains.Since similar voids have not been observed in low stress cycle bearings, it is suggested that voids are developed at late stage WEB formations as a consequence of mechanical loading on weak planes between the ferrite-lenticular carbide or a consequence of potential volume change associated with the microstructural transformation of martensite to ferrite, which is associated with a reduction in volume. While it remains unclear which factor is the main cause of voids, it is clear that the plane between the lenticular carbide and ferrite grains are planes of weakness that can impact the integrity of the microstructure. This effect becomes more detrimental at late stages as its density increases. It is also interesting that all the WEB related voids observed are linked to the LAB rather than the HAB. This may be linked to the proposed formation mechanism, where the LAB is associated with a build-up of energy in the microstructure while the HAB stage is a form of energy release. Void/crack formation is also shown in Figure 9.6 parallel to the lenticular carbide of the LAB in an earlier stage sample run for

1116 million cycles under 2.9 GPa. However, given the proximity of the LAB with a MnS inclusion, potential influence of the inclusion on the void formation could not be excluded.

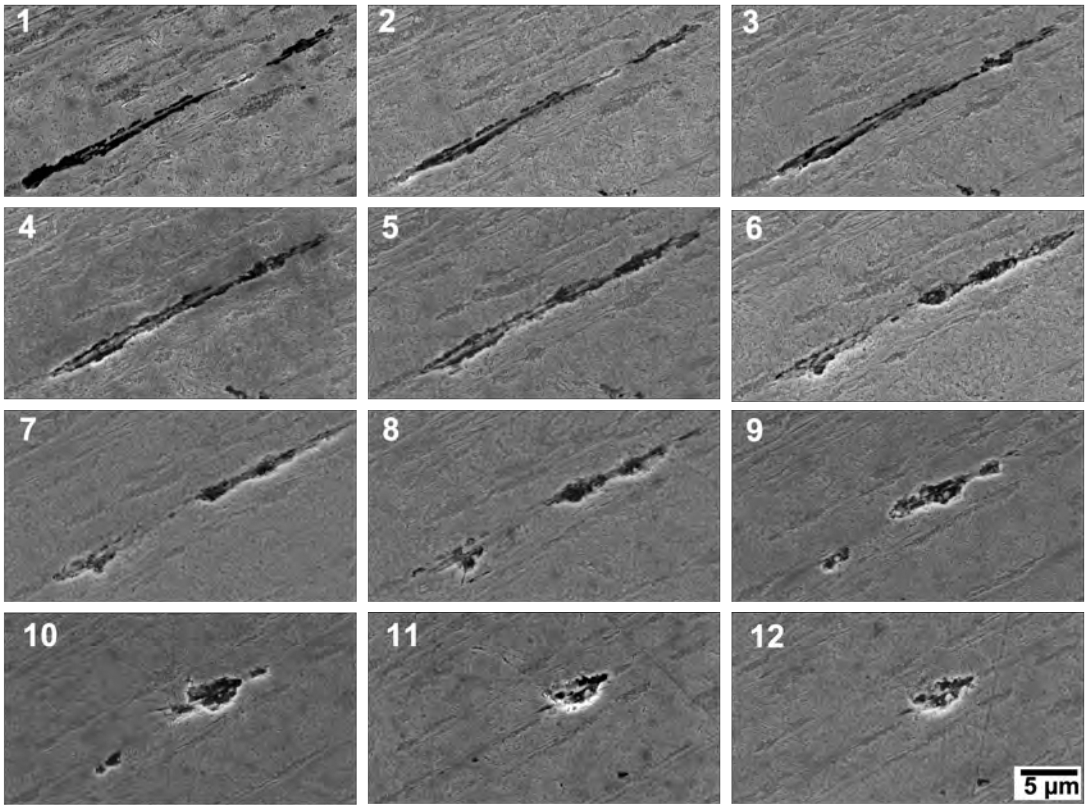

Figure 9.4: Serial sectioning of void in Figure 9.3 at 1 µm intervals from 100Cr6 sample run under 2.9 GPa for 4141 million cycles.

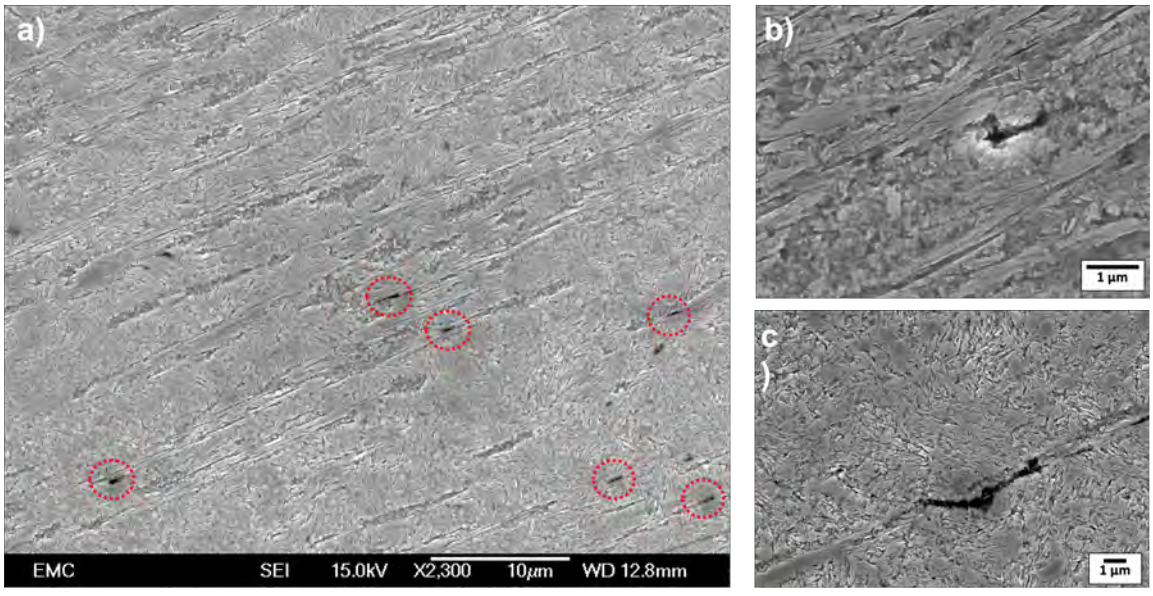

Figure 9.5: SEM images from 100Cr6 sample run under 2.9 GPa for 3016 million cycles showing a) multiple sub-micron voids observed across different LAB. b) Enlarged SEM images of individual voids.

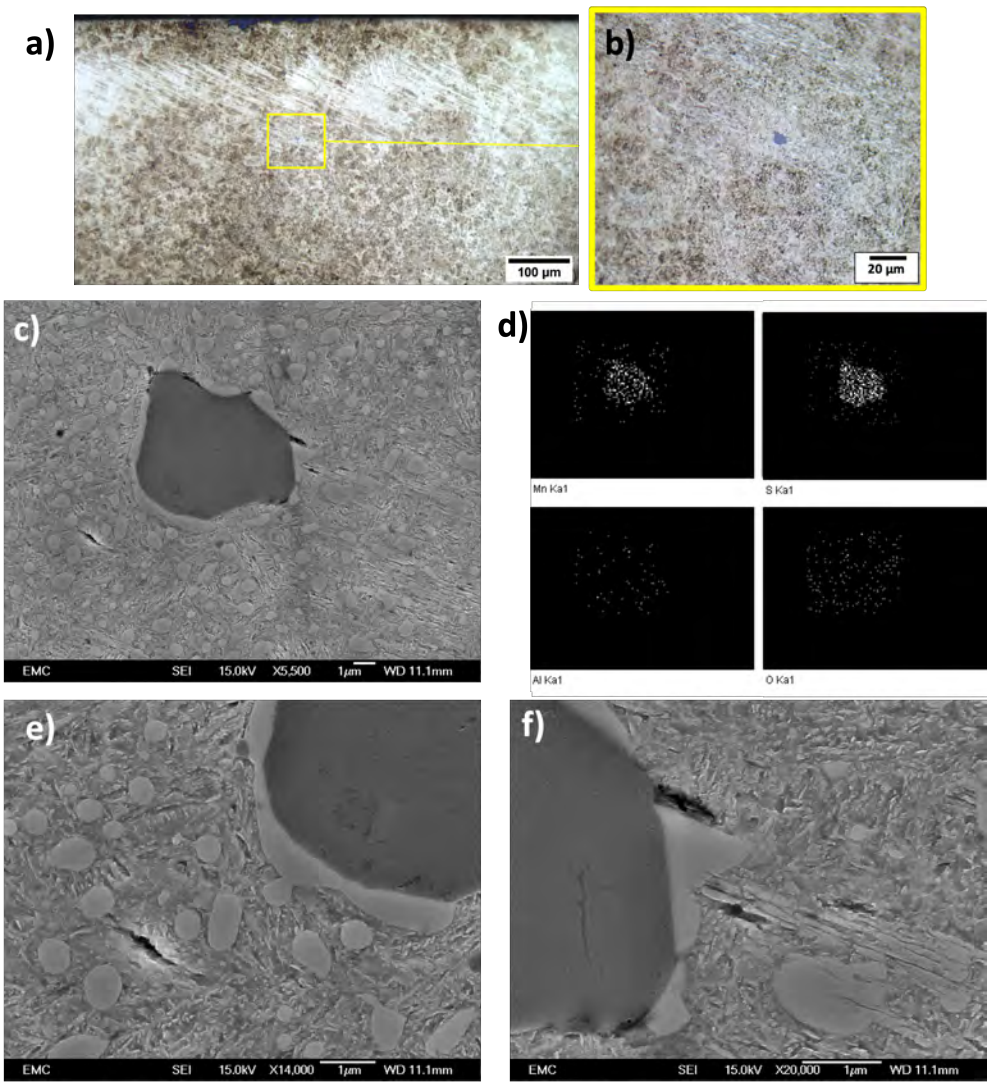

Figure 9.6: a,b) Optical images of the subsurface of bearing run for 1116 million cycles under 2.9 GPa highlighting position of inclusion. c) SEM image of MnS inclusion and surrounding crack/voids. d) EDX elemental map of inclusion in c). e,f) Nicro-cracks captured within the vicinity of the inclusion and boundary of lenticular carbides from LAB.

9.2.2 Non-Metallic Inclusions

Interactions between inclusions and WEB have been investigated in this section to study their influence on the material integrity. Figure 9.7 shows inclusions embedded within the region of dense LAB and HAB from 100Cr6 sample run under 2.9 GPa for 4141 million cycles. While the inclusion in Figure 9.7a is alumina, Figure 9.7b shows traces of Al, O and S, indicating the inclusion consists of alumina. However, since Mn was not investigated, it is unclear whether MnS is also present. Nonetheless, both inclusions in Figure 9.7 show a sort of deformation pattern aligned with the LAB orientation which suggests the LAB may influence the cohesion of the inclusions with the surrounding microstructure.

Figure 9.8 shows multiple inclusions recorded in 100Cr6 samples over various stress cycles within a depth ranging from 60-250 µm which lies within the region of WEB formation. An

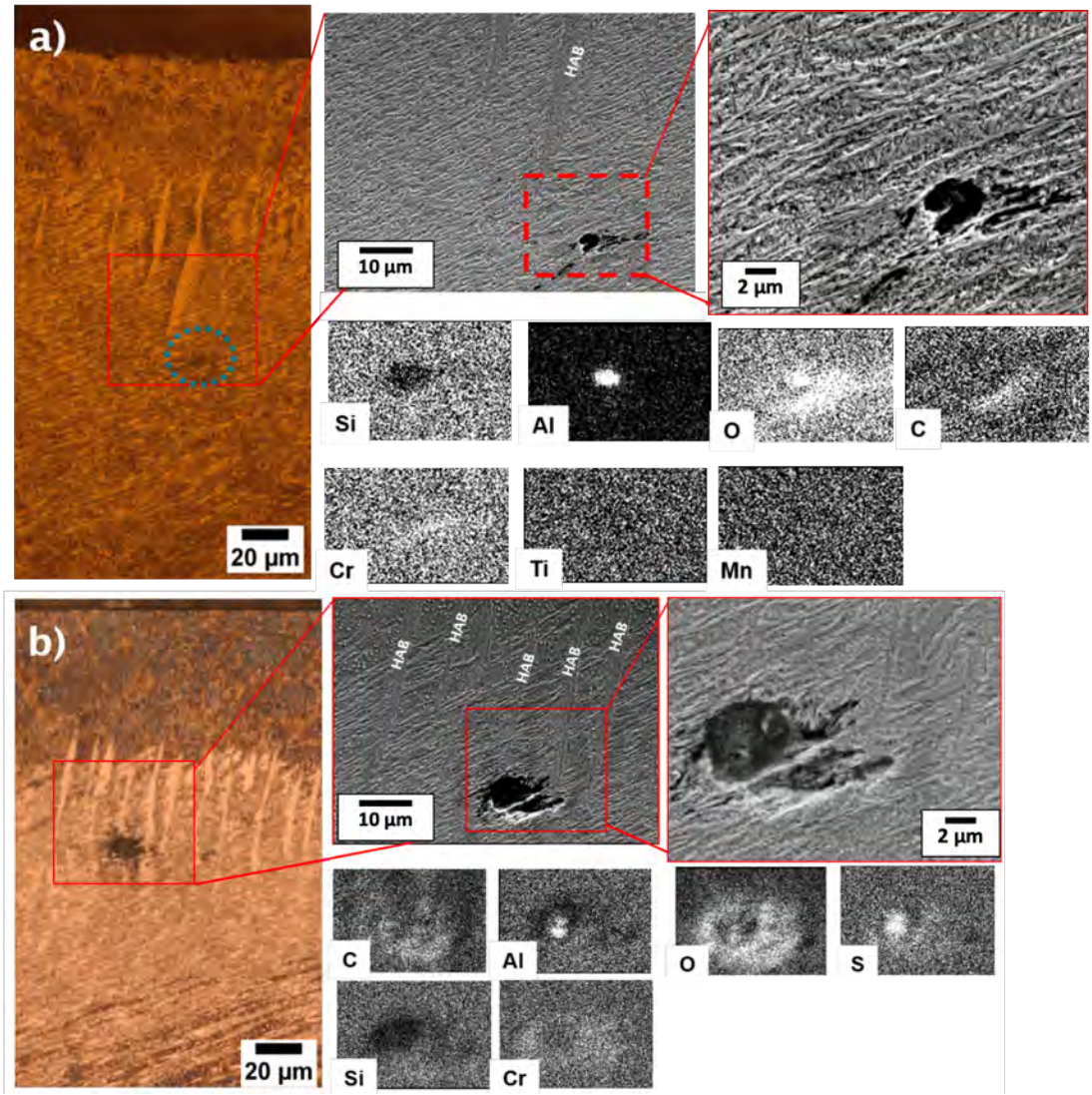

Figure 9.7: LOM, SEM images and EDX analysis of inclusions found within WEB from 100Cr6 sample run under 2.9 GPa for 4141 million cycles.

alumina inclusion shown in Figure 9.8a is positioned within both LAB and HAB and it is interesting to observe cracks within the inclusion parallel to both band orientations. A similar observation is seen in Figure 9.8c where a crack in the MnS inclusion is seen stemming from a LAB at the edge. This highlights a possibility of WEB growing through NMIs and initiating cracks within WEB when inclusions are in close proximity. All inclusions shown in Figure 9.8 (both alumina and MnS) appear to have de-bonded from the surrounding microstructure where LAB have developed. It is also interesting to observe in Figure 9.8a,b,e and f) that the cracks are parallel to the LAB.

At other sites, voids are observed possibly due to removal of the inclusions during polishing (see Figure 9.9), which also suggests that de-bonding of the inclusions may have contributed to final bearing failure. This loss of coherence and void formation may be linked to the potential reduction in lattice volume during the transformation of martensite

to ferrite. Nonetheless, the direction of the void formation around inclusions within LAB suggests a potential stress/strain component along the weak planes of the LAB drive the formation and growth of the voids. It is interesting that the void shape in Figure 9.9a,c resembles that associated with butterflies. However, no microstructural transformations is observed being developed along the crack other than LAB. It is thus suggested that inclusions do not play a significant role in the formation of LAB, and void/cracks develop at inclusions within LAB is a consequence of LAB development while pre-existing inclusions happened to be in its path.

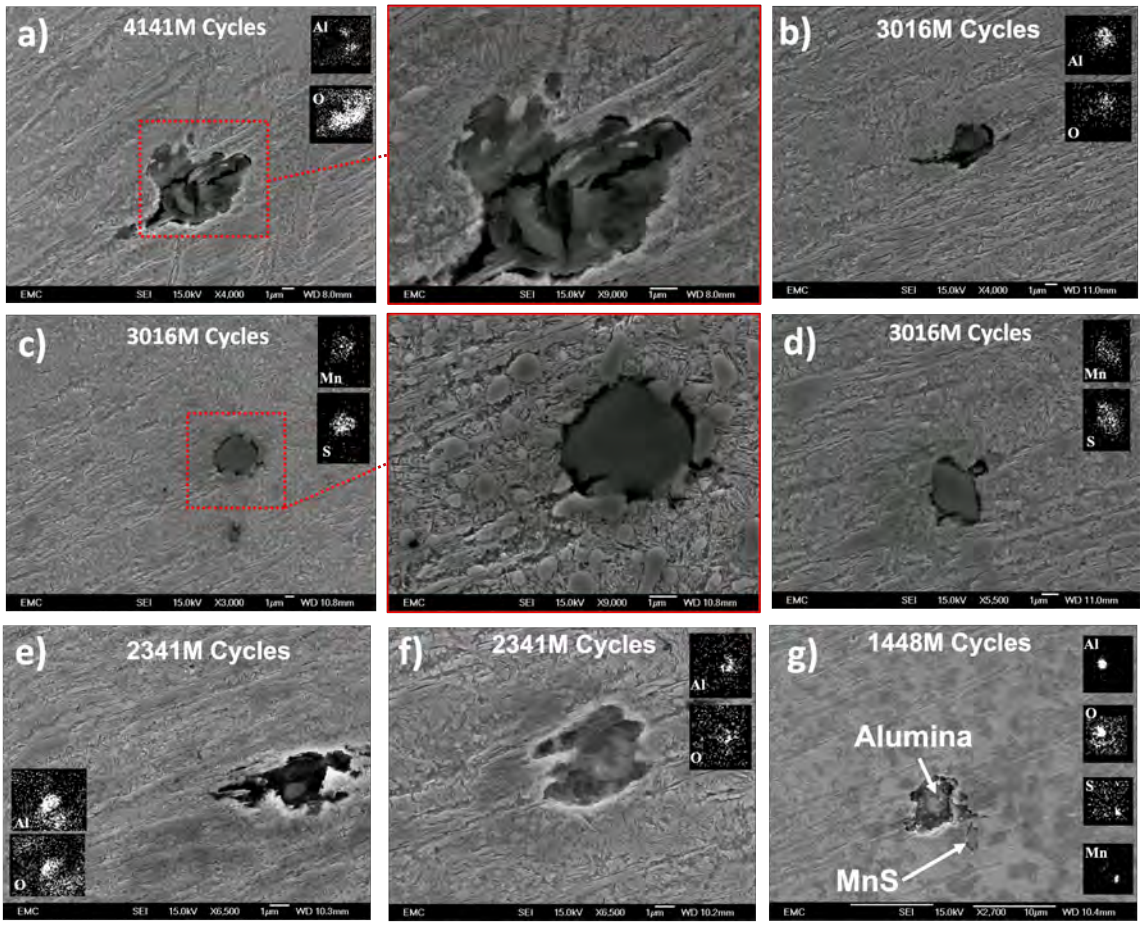

Figure 9.8: SEM images and EDX elemental maps of different inclusions located within the vicinity of WEB from different samples run at various stress cycles under 2.9 GPa. a-f) Samples within 100Cr6 marensite parent microstructure while g) is from 100Cr6 bainite microstructure. a,c) Micro-cracks developing within the cracks at orientations parallel to surrounding LAB and HAB while b,d-g) show a loss of coherence of the inclusion/microstructure interface when surrounded by LAB.

To exclude the potential influence of etching on void formation, subsurface of a latest stage 100Cr6 sample run for 4141 million cycles under 2.9 GPa is investigated in a polished but unetched condition (see Figure 9.10), where an artefact of voids similar to that in Figure 9.9 is observed, supporting the finding of void formation around inclusions within the vicinity of LAB (same depth) where the void orientation is also similar to that of LAB.

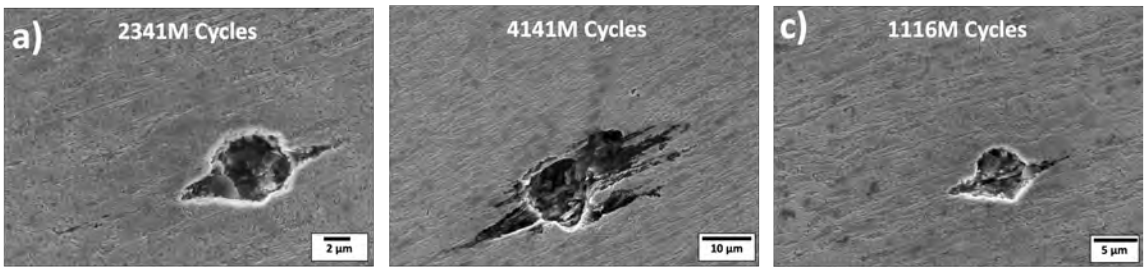

Figure 9.9: SEM image of defects in the etched surface where the inclusion within the WEB has been removed due to void formation parallel to LAB and loss of coherency with the microstructure.

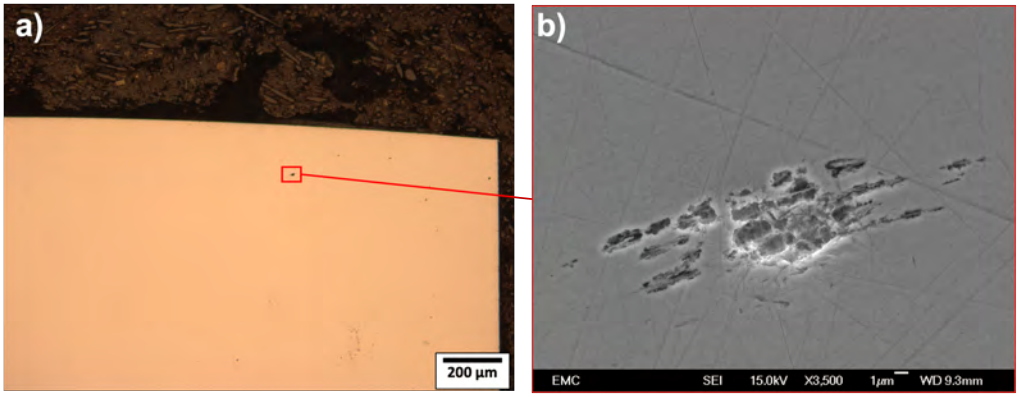

Figure 9.10: a) Optical image of unetched subsurface of sample run for 4141 million cycles under 2.9 GPa. b) SEM image of void captured within the depth range of LAB in the sample where inclusion has been removed.

Figure 9.11 presents inclusions captured from two different samples at a depth of over 700 µm, i.e away from any microstructural transformations in the subsurface or away from the maximum shear stress region. Both inclusions in this figure show a better coherence with the surrounding microstructure compared to the inclusions located within WEB. The influence of LAB on void formation around inclusions can be confirmed by comparing these in Figure 9.11 with those in Figure 9.8 and Figure 9.9.

9.3 Discussion

Study investigating the influence of DER and WEB on bearing failure is scarce in literature. While it is commonly reported that DER and WEB impact the integrity of the steel microstructure, the contribution of these features on final failure was unclear. It has been shown by Martin et al. [79] through artificial fracture that cracks propagated across the whole subsurface as a straight line with the exception of the subsurface region with WEB where the crack orientation varied across the LAB. This suggests a possible plane of weakness across the boundary of the WEB. This is similar to findings from the failed sample in this study where cracks from the micro-pit can be seen to have propagated across the LAB

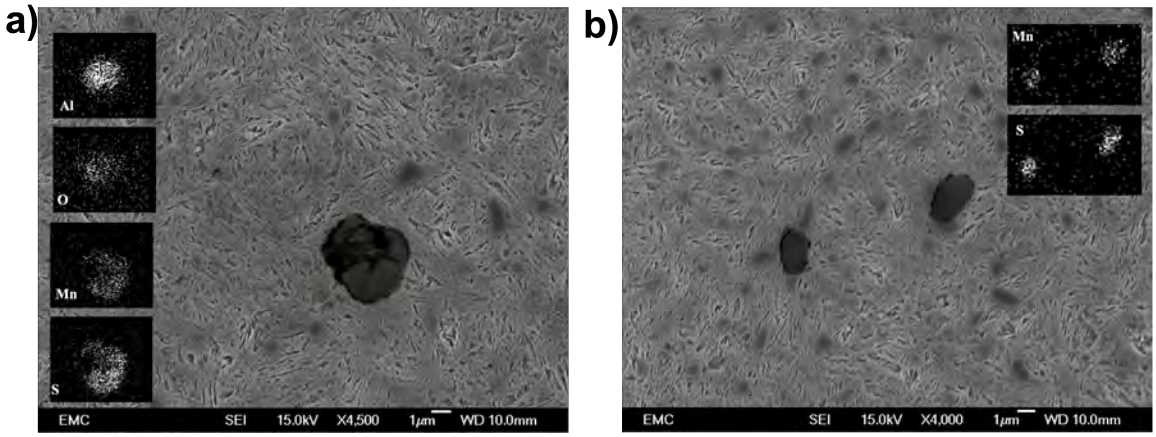

Figure 9.11: a) SEM and EDX map of an inclusion believed to be a mixture of MnS and Alumina from sample run 2341 million cycles. b) SEM and EDX map of MnS inclusion from sample run for 3016 million cycles. Both inclusions are captured at a depth of over 700 µm from the surface.

and particularly the ferrite/lenticular carbide interface. As discussed in Chapter 7, this is due to the difference in hardness between the two constituents of LAB. Images of a crack propagating below WEB and towards WEB parallel to LAB has also been reported by Maharjan et al.[139]. However no detail is given showing that cracks propagate at the interface of lenticular carbides - ferrite grains in LAB. Voskamp [30] reported that the bottom of the surface pitting area in samples with LAB shows more a rough surface while pitting in samples without LAB presents a smoother bottom due to the crack propagating across the LAB boundaries in the former case. However, given the late stage of the pit recorded in this chapter, no correlation between the pit shape and LAB can be established.

In non-failed samples, voids have been observed in various samples under a range of stress cycles at lenticular carbide/ferrite interface in LAB. While this may be naturally occurring damage in the material, the potential influence of surface polishing or etching cannot be excluded. Nonetheless, based on the commonality of the voids observed it is strongly suggested that these are indeed planes of weakness, which is in agreement with that discussed in literature [5, 8]. Using serial sectioning, voids have been seen to span for over 12 µm providing more evidence for the suggested subsurface defects not being generated during polishing.

The interaction between LAB/HAB and inclusions is an interesting observation that has not been discussed in literature. Microstructural alteration interactions with inclusions have only been studied through the formation of butterflies/WEAs [155]. The findings in this study suggest that LAB and HAB may be interacting with inclusions that are in its growth path resulting voids and de-bonding of inclusions from their surrounding matrix. Cracks have been seen to develop within both alumina and MnS inclusions where either LAB or

HAB has developed across it (see Figure 9.8a and Figure 9.8c). While void formation has also been observed in multiple inclusions at an orientation parallel to LAB.

Voids development at edges of inclusions (Figure 9.8a and Figure 9.9) resembles that voids/cracks observed in butterflies. This suggests that the interaction between WEB and inclusions may contribute to bearing failure. The loss of coherence of the inclusion with the surrounding microstructure could be due to the volume reduction associated with martensite-ferrite transformation, which in some specimens, has led to the inclusion being removed during polishing (Figure 9.9 and Figure 9.10). This loss of coherence may lead to void development across weak planes in the LAB leading to the void shapes shown in Figure 9.8a and Figure 9.9. However, it should be noted that all inclusion interactions with the WEB in this study is from inclusions with a diameter below 10 µm, which is lower than those typically associated with butterflies where inclusion diameters of over 20 µm have been typically reported [164, 169].

9.4 Conclusion

Contributions of the microstructural alterations towards bearing failures have been investigated in this chapter. Bearing samples with and without surface damages have been examined and the conclusions are summarised below:

- Crack networks are found under pitting areas in a failed bearing sample, showing that LAB are preferential sites for crack propagation, and the interfaces between ferrite bands and lenticular carbides in LAB act as a plane of weakness for crack propagation. However, a detailed investigation comparing the propagation rate of cracks in samples with and without WEB would be interesting to quantify how they influence bearing lives.

- Multiple voids have been observed parallel to LAB in various samples which appear mainly concentrated at the interface between the ferrite band and lenticular carbide. However, it remains unclear whether these voids are naturally occurring due to the microstructural transformation process, possibly due to volume reduction during martensite ferrite transformation or whether they are damage from polishing. However, given that these voids are over 12 µm in depth from the polished surface suggests they may be naturally occurring features. Nonetheless, in both cases, this suggests the weak plane across the LAB making the bearing sample susceptible to failure.

- LAB and HAB penetrating through inclusions (both alumina and MnS) is shown

to results in micro-cracks across the inclusion parallel to the WEB orientation which suggests a possible stress/strain orientation in the region causing material deformation in this orientation. The coherence of the inclusions and the surrounding altered microstructure is also seen to reduce leading to voids and cracks at the edges of the inclusions parallel to LAB in a manner similar to crack observations captured in butterflies. The interaction between WEB and inclusions is also shown to be potential sites for bearing failure. While inclusions play no obvious role in the formation of the WEB, they may contribute to final failure if the WEB grow across inclusions within its proximity. This loss of coherence has led to inclusions being removed from the material due to surface preparation.

Chapter 10

Conclusions and Future Work

This chapter provides an overview of the main findings and conclusions of this study, followed by recommendations for future work to advance the relevant research fields.

10.1 Overview

The formation of subsurface microstructural alterations known as dark etching region (DER) and white etching bands (consisting of both low angle bands (LAB) and high angle bands (HAB)) has been investigated systematically across different bearing steels to examine the growth rate of the features under different conditions, where a semi-empirical model has been established to predict the formation of WEB. Detailed studies on all three features at micro, nano and atomic scale have explored their evolutions leading to the establishment of their formation mechanisms as well as links between all three features. This study has also examined the possible contributions of the microstructural alterations on subsurface induced bearing RCF failures.

In this thesis, a combination of techniques has been used to examine the initiation, formation and growth of DER, LAB and HAB and their influence on crack development in bearing steels. Initially, the development of all three features has been examined under optical microscopy to examine in detail the progression of all three features under a range of stress cycles. This includes identifying the subsurface region location where each feature develops and the area consumed in the subsurface by each feature across different stages of bearing life. The influence of contact pressure (2.9 GPa and 3.5 GPa) has also been examined for a 100Cr6 through hardened martensitic bearing steel. The development of these features has also been investigated and compared with bearings of two other steels, i.e. a 100Cr6 bainite and a 50CrMo4 martensite steel. Two cleanliness grades of the 100Cr6 martensite steel bearings have been examined to study influence of steel cleanliness or non-metallic

inclusions on DER/WEB development. To further understand the true structure of WEB, a serial sectioning on LAB and HAB has been conducted. Based on the statistics of the features found from a collection of LAB and HAB measured in a range of bearing samples as well as the serial sectioning results, a true 3D model of WEB has been established.

Based on the findings on the development of LAB and HAB (Chapter 4), a semi-empirical model has been developed to predict the initiation and growth of LAB and HAB in 100Cr6 and 50CrMo4 bearing steel (Chapter 5). This model has been based on subsurface stress thresholds and growth patterns of WEB observed under LOM for a range of stress cycles. A comparison with literature has shown that this model can predict the development of LAB and HAB for a range of contact pressures more accurately.

A detailed mechanistic study has then been conducted on the DER (Chapter 6) and on the WEB consisting of both LAB and HAB (Chapter 7) using SE, BSE SEM imaging, EBSD, FIB/TEM, EDX, FIB/APT and nanoindentation. The microstructure of the subsurface bearing steel from untested (virgin) to DER initiation and evolution over stress cycles has been studied to determine its formation mechanism. The DER mechanistic study (Chapter 6) focuses on the 50CrMo4 martensite bearing steel due to its extended development stage comparing with that in other steels. Similar studies on the initiation and growth of LAB and HAB in the 100Cr6 have been conducted, which have been compared with the LAB in 50CrMo4 where HAB were not observed to form after over 7000 million cycles of testing. The results show that the DER and WEB formation mechanisms in both 50CrMo4 and 100Cr6 are similar, leading to the establishment of a unified formation mechanism for DER/LAB/HAB (Chapter 8).

Lastly, the influence of WEB on bearing failures has been investigated (Chapter 9) through the analysis of one failed bearing as well as a number of bearings at their late stages of life without surface spall observed. Voids have been found within LAB in a number of cases and interactions between WEB and inclusions have also been observed to de-bond the inclusions from their surrounding microstructure.

10.2 Conclusions

This section provides the conclusion of this study showing the major findings gained from the analysis of DER, LAB and HAB. The conclusions are summarised below.

- The distribution of WEB formation density correlates well with the distribution of the principal shear stress and von Mises stress in all samples investigated. They initiate in the maximum stress region and grow towards the upper and lower boundaries of

the stresses in the subsurface. WEB formation is seen to saturate between 1500-2000 million stress cycles under 2.9 GPa at the depth equivalent to that of the von Mises stress of 1300 MPa. DER formation and distribution have however shown to correlate with the distribution of orthogonal shear stress and it grows in density and its span across the depth in subsurface with the increase of stress cycles. No correlation is found with residual stress distribution in the subsurface for DER or WEB.

- The influence of material microstructure on WEB formation, e.g. martensite or bainite 100Cr6, is non-existing, while low carbon steel 50CrMo4 significantly prolongs the formation of DER thus delays the initiation and growth of LAB. Steel cleanliness grades, i.e. cleanliness A and cleanliness B 100Cr6, show little influence on the DER and WEB formation.

- Serial sectioning of WEB has shown that LAB and HAB have a similar average length but HAB are significantly thicker and can span upto one-third of the width of the contact between the ball and raceway. The serial sectioning has also provided evidence that HAB initiate from dense LAB area.

- A semi-empirical model has been developed based on the data obtained from a large number of RCF experiments in this study. Comparing with models in literature, this semi-empirical model provides a more accurate prediction for both LAB and HAB development. The model also shows that HAB initiate only when a certain density of LAB is reached after sufficient amount of stress cycles.

- Early stages of DER are found to be consist of 'randomly oriented' dark etching band groups (less than 100 nm in thickness), which are actually in four dominated orientations of 15 - 25° , 70 - 85° , 95 - 110° and 130 - 160°, where the two angles groups of 15 - 25° and 70 - 85° towards the rolling direction being the most prominent. The density of dark etching band groups/patches increases with stress cycles till refinement starts. The refinement results in formation of 'brighter' regions within DER, due to the increased hardness of finer grains that resist to etching.

- At the late stages, dark etching bands are observed to breakdown at bands intersection leading to high stress points, which become nucleation sites for recrystallization of equiaxed ferrite grains that initiate LAB. The fine microstructures in DER during the late stages consist of both fine grains from martensite fragmentation and recrystallized equiaxed ferrite grains.

- Equiaxed grains recrystallised in DER grow in a shape of thin bands oriented at about 30° towards the rolling direction in both length and thickness becoming the early stage

LAB, i.e. individual single low angle bands. As the single bands grow, elongated ferrite grains are found to develop within the bands. This is accompanied by migration of carbon from equiaxed grains to the edges of the newly formed elongated grain forming lenticular carbides. The carbides show a cementite structure and continue grow in thickness away from the elongated grain and across the equiaxed grains, which act as a carbon sink. Later, single low angle bands grow into densely packed bands and merge into each other leading to large regions of LAB fully consuming the parent microstructure.

- HAB initiates as a band of equiaxed ferrite grains within densely packed LAB region through the second stage of recrystallization, where elongated grains and lenticular carbides of the LAB gradually breakdown. HAB grow in length and thickness with increase of stress cycles, leading to the formation of elongated grains within HAB similar to that in LAB. However, no new lenticular carbides adjacent to the new elongated grains is observed to form in HAB. Instead, the lenticular carbides in LAB (at the edges of the HAB), acting as carbon sink during this process, continue to thicken and merge together creating clear boundaries at the edges of HAB.

- Formation of elongated grains within the recrystallized equiaxed ferrite grains in LAB and HAB is a form of recovery due to plastic deformation induced grain rotation and coalescence driven by the reduction of the overall grain boundary. The elimination of grain boundaries under this process releases segregated carbon that later migrates to the edges of elongated grains in LAB to nucleate lenticular carbides.

- A unified formation mechanism is proposed for DER, LAB and HAB where a link between the three features is established. RCF microstructural transformation is found to be a cycle of energy build-up and release in the microstructure. The first stage is the formation of DER (consisting of dark etching bands), where grain refinement and recrystallization of equiaxed ferrite grains at high stress points develop. Although the causes remain unclear, the equiaxed grains grow at an orientation of $\sim 30^{\circ}$ to the rolling direction marking the start of LAB. As LAB grows, a dense network of LAB forms, where a high density of unstable lenticular carbides leads to another build-up of stress points in the microstructure. The second recrystallization stage (HAB) is the second energy release process where the lenticular carbides are broken down into more stable geometries with a lower surface area to volume ratio.

- Interfaces between lenticular carbides and ferrite bands are shown to be a plane of weakness in the microstructure that plays a significant role in crack propagation and

final RCF failures. However, its influence on crack initiation remains uncertain. The observation of LAB and HAB growing through inclusions at their vicinity, development of micro-cracks in inclusions parallel to WEB orientation and de-bonding of inclusions from the surrounding microstructure, suggests that WEB may contribute to subsurface induced bearing failures.

10.3 Future Work

Based on the studies performed in this thesis, the following work are suggested to be conducted in the future to further the research of this topic:

- The stages of microstructural transformation for DER, LAB and HAB have been successfully captured in this study by characterising the evolution of different constituent of the three features and growth patterns. However a greater understanding on the drivers for the distinct orientations of DER bands, LAB and HAB is required as it remains an unsolved puzzle. Modelling of local microstructures prior to the formation of the particular feature might help develop a more accurate simulation of the stress/strain distribution in the material and locally where the microtractural alteration forms. For example, establish an accurate model of the refined microstructure with dark etching bands may help understand the stress distribution in DER prior to LAB formation, or the energy build-up required to initiate the recrystallization associated with LAB initiation. For HAB, modelling the densely packed lenticular carbide in LAB rather than using the parent microstructure may help incorporate the right parameters influencing its formation and its particular orientation.

- An investigation in measuring the magnitude and orientation of strains locally across the bands using a combination of digital image correlation and FIB (DIC-FIB) on LAB and HAB may help better understand the strain values associated with the transformations.

- The role of WEB with the initiation of subsurface cracks remains unclear. A potential investigation of non-destructive techniques of non-failed samples containing WEB could help determine whether void develop naturally across the LAB at the ferrite/carbide interface. In this project, although Barkhausen noise analysis and neutron diffraction had been attempted, both were unfortunately unsuccessful due to low resolution achieved. The use of x-ray imaging (Zeiss 160 kVp Versa 510) has also proven to be difficult again due to the limited resolution for the high density of the

steel specimens thus voids could not be detected.

- Using high resolution techniques, such as TEM, to capture the dark etching bands in their early stages could help better understand the type of band developed and hence determine the root cause of the bands formation. Although difficult, the investigation of the bright structures (structure and elemental composition) adjacent to the dark etching bands would help confirm whether they are newly formed carbides rather than pre-existing tempered carbides.

- A full comparison between the DER, LAB and HAB with other microstructural alterations in bearings such as WECs and butterflies/WEA could help further the research of material transformations due to RCF and the conditions leading to their formation. This would be interesting if all features can be captured under the same operating conditions.

References

[1] M. El Laithy, L. Wang, T. J. Harvey, and B. Vierneusel, "Semi-empirical model for predicting LAB and HAB formation in bearing steels," *International Journal of Fatigue*, p. 106230, 2021.

[2] M. El Laithy, L. Wang, T. J. Harvey, and B. Vierneusel, "Re-investigation of dark etching regions and white etching bands in SAE 52100 bearing steel due to rolling contact fatigue," *International Journal of Fatigue*, vol. 136, p. 105591, 2020.

[3] M. El Laithy, L. Wang, T. J. Harvey, B. Vierneusel, M. Correns, and T. Blass, "Further understanding of rolling contact fatigue in rolling element bearings-a review," *Tribology International*, vol. 140, p. 105849, 2019.

[4] A. Warhadpande, F. Sadeghi, and R. D. Evans, "Microstructural alterations in bearing steels under rolling contact fatigue part 1—historical overview," *Tribology Transactions*, vol. 56, no. 3, pp. 349–358, 2013.

[5] J.-H. Kang, B. Hosseinkhani, and P. E. Rivera-Díaz-del Castillo, "Rolling contact fatigue in bearings: multiscale overview," *Materials Science and Technology*, vol. 28, no. 1, pp. 44–49, 2012.

[6] J. Kang, *Mechanisms of microstructural damage during rolling contact fatigue of bearing steels*. PhD thesis, University of Cambridge, 2014.

[7] R. Ahmed, "Rolling contact fatigue," *ASM handbook*, vol. 11, pp. 941–956, 2002.

[8] F. Sadeghi, B. Jalalahmadi, T. S. Slack, N. Raje, and N. K. Arakere, "A review of rolling contact fatigue," *Journal of tribology*, vol. 131, no. 4, p. 041403, 2009.

[9] T. A. Harris and M. N. Kotzalas, *Advanced concepts of bearing technology: rolling bearing analysis*. CRC Press, 2006.

[10] T. A. Harris and M. N. Kotzalas, *Essential concepts of bearing technology*. CRC press, 2006.

[11] A. Jones, "Metallographic observations of ball bearing fatigue phenomena," in *Symposium on testing of bearings*, ASTM International, 1947.

[12] H. Muro and N. Tsushima, "Microstructural, microhardness and residual stress changes due to rolling contact," *Wear*, vol. 15, no. 5, pp. 309–330, 1970.

[13] H. Bhadeshia, "Steels for bearings," *Progress in materials Science*, vol. 57, no. 2, pp. 268–435, 2012.

[14] I. Polonsky and L. Keer, "On white etching band formation in rolling bearings," *Journal of the Mechanics and Physics of Solids*, vol. 43, no. 4, pp. 637–669, 1995.

[15] M. Sluiter, "Phase stability of carbides and nitrides in steel," *MRS Online Proceedings Library Archive*, vol. 979, 2006.

[16] M.-H. Evans, *White structure flaking failure in bearings under rolling contact fatigue*. PhD thesis, University of Southampton, 2013.

[17] H. Bhadeshia, "Martensite and bainite in steels: transformation mechanism & mechanical properties," *Le Journal de Physique IV*, vol. 7, no. C5, pp. C5–367, 1997.

[18] K. Tsubota, T. Sato, Y. Kato, K. Hiraoka, and R. Hayashi, "Bearing steels in the 21st century," in *Bearing steels: into the 21st century*, ASTM International, 1998.

[19] Y. Hirotsu and S. Nagakura, "Crystal structure and morphology of the carbide precipitated from martensitic high carbon steel during the first stage of tempering," *Acta Metallurgica*, vol. 20, no. 4, pp. 645–655, 1972.

[20] C.-B. Ma, T. Ando, D. Williamson, and G. Krauss, "Chi-carbide in tempered high carbon martensite," *Metallurgical Transactions A*, vol. 14, no. 6, pp. 1033–1045, 1983.

[21] H. Borchers and K. Doffin, "Kinetik der bildung des karbids Fe2C in stahl 100Cr6," *steel research international*, vol. 40, no. 6, pp. 493–498, 1969.

[22] A. S. Irwin, W. J. Anderson, and W. J. Derner, "Review and critical analysis: Rolling-element bearings for system life and reliability," 1985.

[23] E. V. Zaretsky, "Rolling bearing steels - a technical and historical perspective," *Materials Science and Technology*, vol. 28, no. 1, pp. 58–69, 2012.

[24] R. Baughman, "Effect of hardness, surface finish, and grain size on rolling-contact fatigue life of M-50 bearing steel," *Journal of Basic Engineering*, vol. 82, no. 2, pp. 287–294, 1960.

[25] E. V. Zaretsky, "Selection of rolling-element bearing steels for long-life applications," in *Effect of Steel Manufacturing Processes on the Quality of Bearing Steels*, ASTM International, 1988.

[26] C. Ooki, "Improving rolling contact fatigue life of bearing steels through grain refinement," tech. rep., SAE Technical Paper, 2004.

[27] C. Sidoroff, P. Dierickx, and P. M. Perez, "Modeling of retained austenite transformation in bearing steels," *NTN technical review*, no. 83, pp. 60–66, 2015.

[28] M. Holzweissig, M. Uslu, H. G. Lambers, D. Canadinc, and H. Maier, "A comparative analysis of austenite-to-martensite and austenite-to-bainite phase transformation kinetics in steels," *Materials Research Letters*, vol. 1, no. 3, pp. 141–147, 2013.

[29] D. H. Herring, "A discussion of retained austenite," tech. rep., Industrial Heating, 2005.

[30] V. A. Pieter, *Microstructural changes during rolling contract fatigue: Metal fatigue in the subsurface region of deep groove ball bearing inner rings.* PhD thesis, Delft University of Technology, 1997.

[31] E. Zaretsky, "Rolling bearing and gear materials," *Tribology for aerospace applications*, pp. 325–451, 1997.

[32] G. Johnston, T. Andersson, E. Amerongen, and A. Voskamp, "Experience of element and full-bearing testing of materials over several years," in *Rolling contact fatigue testing of bearing steels*, ASTM International, 1982.

[33] G. Krauss, "Steels: heat treatment and processing principles," *ASM International, 1990,*, p. 497, 1990.

[34] M. Paladugu and R. S. Hyde, "Influence of microstructure on retained austenite and residual stress changes under rolling contact fatigue in mixed lubrication conditions," *Wear*, vol. 406, pp. 84–91, 2018.

[35] H. Böhmer and R. Eberhard, "Microstructural optimisation of bearing steels for operation under contaminated lubrication by using the experimental method of dented surfaces," in *Bearing steel technology*, ASTM International, 2002.

[36] P. Walker, "Improving the reliability of highly loaded rolling bearings: the effect of upstream processing on inclusions," *Materials Science and Technology*, vol. 30, no. 4, pp. 385–410, 2014.

[37] E. S. Alley and R. W. Neu, "Microstructure-sensitive modeling of rolling contact fatigue," *International Journal of Fatigue*, vol. 32, no. 5, pp. 841–850, 2010.

[38] F.-J. Ebert, "Fundamentals of design and technology of rolling element bearings," *Chinese Journal of Aeronautics*, vol. 23, no. 1, pp. 123–136, 2010.

[39] R. Baum, K. Böhnke, T. Boeckers, and H. Klemp, "Properties of through hardening bearing steels produced by bof blowing metallurgy and by electric arc furnace with ladle metallurgy," *Steel Research*, vol. 58, no. 9, pp. 432–438, 1987.

[40] J. Akesson, "SKF rolling bearing steels-properties and processes," *Ball Bearing Journal*, vol. 217, p. 32, 1983.

[41] Y. Murakami and H. Usuki, "Quantitative evaluation of effects of non-metallic inclusions on fatigue strength of high strength steels. ii: Fatigue limit evaluation based on statistics for extreme values of inclusion size," *International Journal of Fatigue*, vol. 11, no. 5, pp. 299–307, 1989.

[42] T. B. Lund, "Sub-surface initiated rolling contact fatigue—influence of non-metallic inclusions, processing history, and operating conditions," *Journal of ASTM International*, vol. 7, no. 5, pp. 1–12, 2010.

[43] M. Dinkel and W. Trojahn, "Influence of sulfur inclusion content on rolling contact fatigue life," in *Bearing Steel Technologies: 10th Volume, Advances in Steel Technologies for Rolling Bearings*, ASTM International, 2014.

[44] K. Hashimoto, K. Hiraoka, K. Kida, and E. Costa Santos, "Effect of sulphide inclusions on rolling contact fatigue life of bearing steels," *Materials science and Technology*, vol. 28, no. 1, pp. 39–43, 2012.

[45] S. Li, "Effects of inclusions on very high cycle fatigue properties of high strength steels," *International Materials Reviews*, vol. 57, no. 2, pp. 92–114, 2012.

[46] R. Kiessling and I. of Metals, *Non-metallic inclusions in steel. Part 5.* London : Institute of Metals, 1989. "Book number 411."–T.p. verso.

[47] N. K. Arakere, N. Branch, G. Levesque, V. Svendsen, and N. H. Forster, "Rolling contact fatigue life and spall propagation of AISI M50, M50NiL, and AISI 52100, part II: stress modeling," *Tribology Transactions*, vol. 53, no. 1, pp. 42–51, 2009.

[48] T. Sakai, Y. Sato, and N. Oguma, "Characteristic S–N properties of high-carbon–chromium-bearing steel under axial loading in long-life fatigue," *Fatigue & Fracture of Engineering Materials & Structures*, vol. 25, no. 8-9, pp. 765–773, 2002.

[49] A. Evans, "The role of inclusions in the fracture of ceramic materials," *Journal of Materials Science*, vol. 9, no. 7, pp. 1145–1152, 1974.

[50] W. Leslie, "Inclusions and mechanical properties," *Mechanical Working and Steel Processing XX*, pp. 3–50, 1982.

[51] A. Ghosh, *Secondary steelmaking: principles and applications.* CRC Press, 2000.

[52] G. Auclair, F. Ruby-Meyer, R. Meilland, and P. Rocabois, "Cleanliness assessment: a critical review and a real need to predict rolling contact fatigue behaviour," in *Bearing Steels: Into the 21st Century*, ASTM International, 1998.

[53] W. Duckworth and E. Ineson, "The effects of externally introduced alumina particles on the fatigue life of EN24 steel," *Clean steel*, vol. 77, pp. 87–103, 1963.

[54] J. Lankford, "(e) effect of oxide inclusions on fatigue failure," *International Metals Reviews*, vol. 22, no. 1, pp. 221–228, 1977.

[55] P. Thornton, "The influence of nonmetallic inclusions on the mechanical properties of steel: A review," *Journal of Materials Science*, vol. 6, no. 4, pp. 347–356, 1971.

[56] M. Atkinson, "The influence of nonmetallic inclusions on the fatigue properties of ultra-high-tensile steels," *J. Iron Steel Inst*, vol. 195, p. 64, 1960.

[57] K. Tanaka and T. Mura, "A theory of fatigue crack initiation at inclusions," *Metallurgical Transactions A*, vol. 13, no. 1, pp. 117–123, 1982.

[58] K. Hashimoto, T. Fujimatsu, N. Tsunekage, K. Hiraoka, K. Kida, and E. C. Santos, "Effect of inclusion/matrix interface cavities on internal-fracture-type rolling contact fatigue life," *Materials & Design*, vol. 32, no. 10, pp. 4980–4985, 2011.

[59] L. Zhang and B. G. Thomas, "Inclusions in continuous casting of steel," in *XXIV National Steelmaking Symposium, Morelia, Mich, Mexico*, vol. 26, p. 28, Citeseer, 2003.

[60] Olympus, "Non-metallic inclusion analysis in steel." https://www.olympus-ims.com/en/applications/nmi-analysis/, 2016. [Last Accessed 13th Jul 2018].

[61] S. Seetharaman, A. McLean, R. Guthrie, and S. Sridhar, *Treatise on process metallurgy*, vol. 2. Elsevier, 2013.

[62] Deutsches Institut für Normung, "Microscopic examination of special steels using standard diagrams to assess the content of non-metallic inclusions,," tech. rep., International Organization for Standardization, 1985.

[63] A. Voskamp, "Material response to rolling contact loading," *Journal of tribology*, vol. 107, no. 3, pp. 359–364, 1985.

[64] M.-H. Evans, A. Richardson, L. Wang, and R. Wood, "Serial sectioning investigation of butterfly and white etching crack (WEC) formation in wind turbine gearbox bearings," *Wear*, vol. 302, no. 1-2, pp. 1573–1582, 2013.

[65] G. Stachowiak and A. W. Batchelor, *Engineering tribology*. Butterworth-Heinemann, 2013.

[66] K. L. Johnson, *Contact Mechanics*. Cambridge University Press, 1985.

[67] E. V. Zaretsky, "Rolling bearing life prediction, theory, and application," tech. rep., 2013.

[68] N. Tsushima, K. Maeda, H. Nakashima, and H. Kashimura, "New steels now in use for automotive rolling element bearings," in *Bearing Steels: Into the 21st Century*, ASTM International, 1998.

[69] E. Ioannides, "An analytical formulation for the life of rolling bearings," *Acta Polytechnica Scandinavica, Mechanical Engineering Series*, 1999.

[70] J. Tao, T. Hughes, H. Evans, R. Snidle, N. Hopkinson, M. Talks, and J. Starbuck, "Elastohydrodynamic lubrication analysis of gear tooth surfaces from micropitting tests," *Journal of tribology*, vol. 125, no. 2, pp. 267–274, 2003.

[71] G. Lundberg and A. Palmgren, "Dynamic capacity of rolling bearings," *Polytechnica Scandinavica. Mechanical Engineering Series*, vol. 1, no. 3, pp. 1–52, 1947.

[72] G. E. Totten, *Handbook of hydraulic fluid technology*. CRC Press, 2011.

[73] W. Greenert, "The toroid contact roller test as applied to the study of bearing materials," *Journal of Basic Engineering*, vol. 84, no. 1, pp. 181–189, 1962.

[74] H. Fessler and E. Ollerton, "Contact stresses in toroids under radial loads," *British journal of applied physics*, vol. 8, no. 10, p. 387, 1957.

[75] G. Moyar and J. Morrow, "Relation of fatigue to pitting failure of surfaces in rolling contact," *Appl. Mech. Rep*, vol. 565, 1958.

[76] N. Popinceanu, E. Diaconescu, and S. Cretu, "Critical stresses in rolling contact fatigue," *Wear*, vol. 71, no. 3, pp. 265–282, 1981.

[77] K. Fujita and A. Yoshida, "Surface durability of case-hardened nickel-chromium steel rollers under pure rolling and sliding-rolling contacts," *Wear*, vol. 52, no. 1, pp. 37–48, 1979.

[78] J. Martin and A. Eberhardt, "Identification of potential failure nuclei in rolling contact fatigue," *Journal of Basic Engineering*, vol. 89, no. 4, pp. 932–942, 1967.

[79] J. Martin, S. Borgese, and A. Eberhardt, "Microstructural alterations of rolling—bearing steel undergoing cyclic stressing," *Journal of Basic Engineering*, vol. 88, no. 3, pp. 555–565, 1966.

[80] J. Bush, W. Grube, and G. Robinson, "Microstructural and residual stress changes in hardened steel due to rolling contact," *Transactions of the ASM*, vol. 54, pp. 390–412, 1961.

[81] G. Vasilca and V. Raszillier, "A study of dark etching area (DEA) type structure modification of material and hertzian contact area induced by ball bearing type motion," *Wear*, vol. 19, no. 1, pp. 1–15, 1972.

[82] H. Swahn, P. Becker, and O. Vingsbo, "Martensite decay during rolling contact fatigue in ball bearings," *Metallurgical transactions A*, vol. 7, no. 8, pp. 1099–1110, 1976.

[83] V. Bhargava, G. Hahn, and C. Rubin, "Rolling contact deformation, etching effects, and failure of high-strength bearing steel," *Metallurgical Transactions A*, vol. 21, no. 7, pp. 1921–1931, 1990.

[84] A.Voskamp and E.Mittemeijer, "Crystallographic preferred orientation induced by cyclic rolling contact loading," *Metallurgical and Materials transactions A*, vol. 27, no. 11, pp. 3445–3465, 1996.

[85] A. M. Group, J. Merwin, and K. Johnson, "An analysis of plastic deformation in rolling contact," *Proceedings of the Institution of Mechanical Engineers*, vol. 177, no. 1, pp. 676–690, 1963.

[86] S. Turteltaub and A. Suiker, "Transformation-induced plasticity in ferrous alloys," *Journal of the Mechanics and Physics of Solids*, vol. 53, no. 8, pp. 1747–1788, 2005.

[87] N. Arakere and G. Subhash, "Work hardening response of M50-NiL case hardened bearing steel during shakedown in rolling contact fatigue," *Materials Science and Technology*, vol. 28, no. 1, pp. 34–38, 2012.

[88] R. Vegter and J. Slycke, "The role of hydrogen on rolling contact fatigue response of rolling element bearings," *Journal of ASTM international*, vol. 7, no. 2, pp. 1–12, 2009.

[89] A. Bower and K. Johnson, "Plastic flow and shakedown of the rail surface in repeated wheel—rail contact," in *Mechanics and Fatigue in Wheel/Rail Contact*, pp. 1–18, Elsevier, 1991.

[90] G. Hahn, V. Bhargava, and Q. Chen, "The cyclic stress-strain properties, hysteresis loop shape, and kinematic hardening of two high-strength bearing steels," *Metallurgical Transactions A*, vol. 21, no. 2, p. 653, 1990.

[91] J. Williams, "The influence of repeated loading, residual stresses and shakedown on the behaviour of tribological contacts," *Tribology International*, vol. 38, no. 9, pp. 786–797, 2005.

[92] S. Kulkarni, G. Hahn, C. Rubin, and V. Bhargava, "Elasto-plastic finite element analysis of three-dimensional pure rolling contact above the shakedown limit," *Journal of Applied Mechanics*, vol. 58, no. 2, pp. 347–353, 1991.

[93] G. Popescu, G. E. Morales-Espejel, B. Wemekamp, and A. Gabelli, "An engineering model for three-dimensional elastic-plastic rolling contact analyses," *Tribology transactions*, vol. 49, no. 3, pp. 387–399, 2006.

[94] K. D. Van and M. Maitournam, "Steady-state flow in classical elastoplasticity: applications to repeated rolling and sliding contact," *Journal of the Mechanics and Physics of Solids*, vol. 41, no. 11, pp. 1691–1710, 1993.

[95] M. M.-H. Yu, B. Moran, and L. M. Keer, "A direct analysis of three-dimensional elastic-plastic rolling contact," *Journal of tribology*, vol. 117, no. 2, pp. 234–243, 1995.

[96] C.-C. Yu, B. Moran, and L. Keer, "A simplified direct method for cyclic strain calculation: repeated rolling/sliding contact on a case-hardened half plane," *Journal of tribology*, vol. 118, no. 2, pp. 329–334, 1996.

[97] C. Sakae and L. Keer, "Application of direct method for a nonlinear-kinematic-hardening material under rolling/sliding line contact: constant ratchetting rate," *Journal of the Mechanics and Physics of Solids*, vol. 45, no. 9, pp. 1577–1594, 1997.

[98] M. Yu, B. Moran, and L. Keer, "A direct analysis of two-dimensional elastic-plastic rolling contact," *Journal of tribology*, vol. 115, no. 2, pp. 227–236, 1993.

[99] E. Melan, "Der spannungszustand eines mises-henckys chen kontinuums bei veraderlicher belastung," *Sitzber Akad. Wiss. Wien Iia*, vol. 147, pp. 73–87, 1938.

[100] W. Koiter, "A new general theorem on shakedown of elastic-plastic structures," *Proc. Koninkl. Ned. Akad. Wet. B*, vol. 59, pp. 24–34, 1956.

[101] D. Pham and D. Weichert, "Shakedown analysis for elastic-plastic bodies with limited kinematic hardening," in *Proceedings of the Royal Society of London A: Mathematical, Physical and Engineering Sciences*, vol. 457, pp. 1097–1110, The Royal Society, 2001.

[102] Y. Jiang, B. Xu, and H. Sehitoglu, "Three-dimensional elastic-plastic stress analysis of rolling contact," *Journal of tribology*, vol. 124, no. 4, pp. 699–708, 2002.

[103] A. M. Kumar, G. T. Hahn, and C. A. Rubin, "A study of subsurface crack initiation produced by rolling contact fatigue," *Metallurgical Transactions A*, vol. 24, no. 2, p. 351, 1993.

[104] A. Voskamp and E. Mittemeijer, "The effect of the changing microstructure on the fatigue behaviour during cyclic rolling contact loading," *Zeitschrift für Metallkunde*, vol. 88, no. 4, pp. 310–320, 1997.

[105] H.-J. Christ, C. Sommer, H. Mughrabi, A. Voskamp, J. Beswick, and F. Hengerer, "Fatigue behaviour of three variants of the roller bearing steel sae 52100," *Fatigue & Fracture of Engineering Materials & Structures*, vol. 15, no. 9, pp. 855–870, 1992.

[106] A. N. Lari, *Residual Stresses: Technology–Applications–Effects*. Elsevier, 2014.

[107] D. Morris, F. Sadeghi, Y.-C. Chen, C. Wang, and B. Wang, "Effect of residual stresses on microstructural evolution due to rolling contact fatigue," *Journal of Tribology*, vol. 140, no. 6, 2018.

[108] S. S. Creţu and N. Popinceanu, "The influence of residual stresses induced by plastic deformation on rolling contact fatigue," *Wear*, vol. 105, no. 2, pp. 153–170, 1985.

[109] E. Zaretsky, R. Parker, and W. Anderson, "A study of residual stress induced during rolling," *Journal of Lubrication Technology*, vol. 91, no. 2, pp. 314–318, 1969.

[110] R. Parker, D. Reichard, and E. Zaretsky, "Residual stress and subsurface hardness changes induced during rolling contact," 1968.

[111] A. Voskamp, R. Österlund, P. Becker, and O. Vingsbo, "Gradual changes in residual stress and microstructure during contact fatigue in ball bearings," *Metals Technology*, vol. 7, no. 1, pp. 14–21, 1980.

[112] R. Scott, R. Kepple, and M. Miller, "The effect of processing-induced near-surface residual stress on ball bearing fatigue," *Rolling contact phenomena*, vol. 1, pp. 301–316, 1962.

[113] F. Sadeghi and P. C. Sui, "Internal stresses in elastohydrodynamic lubrication of rolling/sliding contacts," *Journal of tribology*, vol. 111, no. 1, pp. 180–187, 1989.

[114] D. McLean, *Mechanical Properties of Metals*. John Wiley and sons, 1962.

[115] B. Wielke, "Hysteresis loop of an elastic-plastic $\lambda/2$ oscillator," *physica status solidi (a)*, vol. 23, no. 1, pp. 237–244, 1974.

[116] M. Hempel and E. Houdremont, *Beitrag zur Kenntnis der Vorgänge bei der Dauerbeanspruchung von Werkstoffen*. Verlag Stahleisen, 1953.

[117] J. Buchwald and R. Heckel, "An analysis of microstructural changes in 52100 steel bearings during cyclic stressing," *ASM Transactions Quarterly*, vol. 61, pp. 750–756, 1968.

[118] H. Fu, W. Song, E. I. Galindo-Nava, and P. E. Rivera-Díaz-del Castillo, "Strain-induced martensite decay in bearing steels under rolling contact fatigue: modelling and atomic-scale characterisation," *Acta Materialia*, vol. 139, pp. 163–173, 2017.

[119] A. Bhattacharyya, G. Subhash, and N. Arakere, "Evolution of subsurface plastic zone due to rolling contact fatigue of M-50 NiL case hardened bearing steel," *International Journal of Fatigue*, vol. 59, pp. 102–113, 2014.

[120] V. Šmeļova, A. Schwedt, L. Wang, W. Holweger, and J. Mayer, "Electron microscopy investigations of microstructural alterations due to classical rolling contact fatigue (RCF) in martensitic AISI 52100 bearing steel," *International Journal of Fatigue*, vol. 98, pp. 142–154, 2017.

[121] K. Sugino, K. Miyamoto, M. Nagumo, and K. Aoki, "Structural alterations of bearing steels under rolling contact fatigue," *Transactions of the Iron and Steel Institute of Japan*, vol. 10, no. 2, p. 98, 1970.

[122] D. Morris, F. Sadeghi, Y.-C. Chen, C. Wang, and B. Wang, "A novel approach for modeling retained austenite transformations during rolling contact fatigue," *Fatigue & Fracture of Engineering Materials & Structures*, vol. 41, no. 4, pp. 831–843, 2018.

[123] R. Österlund and O. Vingsbo, "Phase changes in fatigued ball bearings," *Metallurgical Transactions A*, vol. 11, no. 5, pp. 701–707, 1980.

[124] H. Fu, *Microstructural alterations in bearing steels under rolling contact fatigue*. PhD thesis, University of Cambridge, 2017.

[125] H. Muro and N. Tsushima, "Microstructural, microhardness and residual stress changes due to rolling contact," *Wear*, vol. 15, no. 5, pp. 309–330, 1970.

[126] S. Echeverri Restrepo, S. Ooi, P. Yan, P. Andric, R. Vegter, and J. Lai, "Dark etching regions under rolling contact fatigue: a review," *Materials Science and Technology*, vol. 37, no. 4, pp. 347–376, 2021.

[127] V. Rumpf, *A study on microstructural alterations in white etching cracks, dark etching region, and white etching bands in rolling contacts*. PhD thesis, University of Southampton, 2018.

[128] J. Beswick, "Measurement of C levels in structurally transformed SAE 52100 ball-bearing steel by microprobe analysis," *Praktische Metallographie*, vol. 12, no. 4, pp. 200–206, 1975.

[129] A. Muroga and H. Saka, "Analysis of rolling contact fatigued microstructure using focused ion beam sputtering and transmission electron microscopy observation," *Scripta metallurgica et materialia*, vol. 33, no. 1, 1995.

[130] D. Scott, B. Loy, and G. Mills, "Paper 10: metallurgical aspects of rolling contact fatigue," in *Proceedings of the institution of mechanical engineers, conference proceedings*, vol. 181, pp. 94–103, SAGE Publications Sage UK: London, England, 1966.

[131] O. Zwirlein and H. Schlicht, "Rolling contact fatigue mechanisms—accelerated testing versus field performance," in *Rolling contact fatigue testing of bearing steels*, ASTM International, 1982.

[132] H.-K. Lorösch, "Influence of load on the magnitude of the life exponent for rolling bearings," in *Rolling contact fatigue testing of bearing steels*, ASTM International, 1982.

[133] N. Mitamura, H. Hidaka, and S. Takaki, "Microstructural development in bearing steel during rolling contact fatigue," vol. 539, pp. 4255–4260, 2007.

[134] J.-H. Kang, B. Hosseinkhani, R. H. Vegter, and P. E. Rivera-Díaz-del Castillo, "Modelling dislocation assisted tempering during rolling contact fatigue in bearing steels," *International Journal of Fatigue*, vol. 75, pp. 115–125, 2015.

[135] T. Lund, "Structural alterations in fatigue-tested ball- bearing steel," *Jernkontorets Ann*, vol. 153, no. 7, pp. 337–343, 1969.

[136] H. Schlicht, "Material properites adapted to the actual stressing in a rolling bearing," *Ball and roller bearing engineering*, vol. 1, pp. 24–29, 1981.

[137] A. King and J. O'Brien, "Microstructural alterations in rolling contact fatigue," in *Advances in Electron Metallography: Vol. 6*, ASTM International, 1966.

[138] H. Fu and P. E. Rivera-Díaz-del Castillo, "Evolution of white etching bands in 100Cr6 bearing steel under rolling contact-fatigue," *Metals*, vol. 9, no. 5, p. 491, 2019.

[139] N. Maharjan, W. Zhou, and Y. Zhou, "Microstructural study of bearing material failure due to rolling contact fatigue in wind turbine gearbox," in *Proceedings of the international symposium on current research in hydraulic turbines, Kathmandu University, Dhulikhel, Nepal*, vol. 14, 2016.

[140] K. Johnson, *Formation of shear bands in ball-bearing races*. University of Cambridge Department of Engineering, 1988.

[141] H. Swahn, P. Becker, and O. Vingsbo, "Electron-microscope studies of carbide decay during contact fatigue in ball bearings," *Metal Science*, vol. 10, no. 1, pp. 35–39, 1976.

[142] H. Fu, E. Galindo-Nava, and P. Rivera-Díaz-del Castillo, "Modelling and characterisation of stress-induced carbide precipitation in bearing steels under rolling contact fatigue," *Acta Materialia*, vol. 128, pp. 176–187, 2017.

[143] S. Borgese, "A study of the growth mechanism of lenticular carbides in cyclically stressed 52100 steel," *Journal of Lubrication Technology*, vol. 92, no. 1, pp. 54–58, 1970.

[144] P. Becker, "Metallography of structural-changes in ball-bearing steels caused by rolling-contact fatigue," in *Ultramicroscopy*, vol. 2, pp. 113–113, 1976.

[145] T. Ochi and Y. KUSANO, "Change in microstructure and properties in the rolling contact fatigue oi bearing steel," 1999.

[146] A. H. Cottrell and B. Bilby, "Dislocation theory of yielding and strain ageing of iron," *Proceedings of the Physical Society. Section A*, vol. 62, no. 1, p. 49, 1949.

[147] S. Ganti, B. Turner, M. Kirsch, D. Anthony, B. McCoy, H. Trivedi, and V. Sundar, "Three-dimensional (3D) analysis of white etching bands (WEBs) in AISI M50 bearing steel using automated serial sectioning," *Materials Characterization*, 2018.

[148] J. Lyman, "A shear-stress normal-strain cycle relation to fatigue in bending, torsion, and rolling contact," *Journal of Lubrication Technology*, vol. 92, no. 4, pp. 567–571, 1970.

[149] A. Warhadpande, F. Sadeghi, and R. D. Evans, "Microstructural alterations in bearing steels under rolling contact fatigue: Part 2—diffusion-based modeling approach," *Tribology Transactions*, vol. 57, no. 1, pp. 66–76, 2014.

[150] H. Fu and P. E. Rivera-Díaz-del Castillo, "A unified theory for microstructural alterations in bearing steels under rolling contact fatigue," *Acta Materialia*, vol. 155, pp. 43–55, 2018.

[151] E. Orowan, "Mechanical strength properties and real structure of crystals," *Z. Kristallogr*, vol. 89, no. 3/4, pp. 327–343, 1934.

[152] W. Holweger, M. Wolf, D. Merk, T. Blass, M. Goss, J. Loos, S. Barteldes, and A. Jakovics, "White etching crack root cause investigations," *Tribology Transactions*, vol. 58, no. 1, pp. 59–69, 2015.

[153] A. Greco, S. Sheng, J. Keller, and A. Erdemir, "Material wear and fatigue in wind turbine systems," *Wear*, vol. 302, no. 1-2, pp. 1583–1591, 2013.

[154] F. Gutiérrez Guzmán, M. O. Oezel, G. Jacobs, G. Burghardt, C. Broeckmann, and T. Janitzky, "Influence of slip and lubrication regime on the formation of white etching cracks on a two-disc test rig," *Lubricants*, vol. 6, no. 1, p. 8, 2018.

[155] M. Evans, "White structure flaking (WSF) in wind turbine gearbox bearings: effects of 'butterflies' and white etching cracks (WECs)," *Materials Science and Technology*, vol. 28, no. 1, pp. 3–22, 2012.

[156] M.-H. Evans, L. Wang, H. Jones, and R. Wood, "White etching crack (WEC) investigation by serial sectioning, focused ion beam and 3-D crack modelling," *Tribology International*, vol. 65, pp. 146–160, 2013.

[157] A. Richardson, M.-H. Evans, L. Wang, R. Wood, M. Ingram, and B. Meuth, "The evolution of white etching cracks (WECs) in rolling contact fatigue-tested 100Cr6 steel," *Tribology letters*, vol. 66, no. 1, pp. 1–23, 2018.

[158] A. M. Diederichs, A. Schwedt, J. Mayer, and T. Dreifert, "Electron microscopy analysis of structural changes within white etching areas," *Materials Science and Technology*, vol. 32, no. 16, pp. 1683–1693, 2016.

[159] F. Manieri, K. Stadler, G. E. Morales-Espejel, and A. Kadiric, "The origins of white etching cracks and their significance to rolling bearing failures," *International Journal of Fatigue*, vol. 120, pp. 107–133, 2019.

[160] A. Grabulov, *Fundamentals of rolling contact fatigue*. PhD thesis, Delft University of Technology, 2010.

[161] P. Becker, "Microstructural changes around non-metallic inclusions caused by rolling-contact fatigue of ball-bearing steels," *Metals Technology*, vol. 8, no. 1, pp. 234–243, 1981.

[162] K. Hiraoka, M. Nagao, and T. Isomoto, "Study on flaking process in bearings by white etching area generation," *Journal of ASTM International*, vol. 3, no. 5, pp. 1–7, 2006.

[163] A. Grabulov, R. Petrov, and H. Zandbergen, "EBSD investigation of the crack initiation and TEM/FIB analyses of the microstructural changes around the cracks formed under rolling contact fatigue (RCF)," *International Journal of Fatigue*, vol. 32, no. 3, pp. 576–583, 2010.

[164] A. Grabulov, U. Ziese, and H. Zandbergen, "TEM/SEM investigation of microstructural changes within the white etching area under rolling contact fatigue and 3-D crack reconstruction by focused ion beam," *Scripta Materialia*, vol. 57, no. 7, pp. 635–638, 2007.

[165] W. Solano-Alvarez and H. Bhadeshia, "White-etching matter in bearing steel. part ii: distinguishing cause and effect in bearing steel failure," *Metallurgical and Materials Transactions A*, vol. 45, no. 11, pp. 4916–4931, 2014.

[166] H. K. Danielsen, F. G. Guzmán, K. V. Dahl, Y. Li, J. Wu, G. Jacobs, G. Burghardt, S. Fæster, H. Alimadadi, S. Goto, *et al.*, "Multiscale characterization of white etching cracks (WEC) in a 100Cr6 bearing from a thrust bearing test rig," *Wear*, vol. 370, pp. 73–82, 2017.

[167] A. M. Diederichs, S. Barteldes, A. Schwedt, J. Mayer, and W. Holweger, "Study of subsurface initiation mechanism for white etching crack formation," *Materials Science and Technology*, vol. 32, no. 11, pp. 1170–1178, 2016.

[168] L. Morsdorf, D. Mayweg, Y. Li, A. Diederichs, D. Raabe, and M. Herbig, "Moving cracks form white etching areas during rolling contact fatigue in bearings," *Materials Science and Engineering: A*, vol. 771, p. 138659, 2020.

[169] M.-H. Evans, "An updated review: white etching cracks (WECs) and axial cracks in wind turbine gearbox bearings," *Materials Science and Technology*, vol. 32, no. 11, pp. 1133–1169, 2016.

[170] L. Ryde, "Application of ebsd to analysis of microstructures in commercial steels," *Materials science and technology*, vol. 22, no. 11, pp. 1297–1306, 2006.

[171] K. K. Alaneme and E. A. Okotete, "Recrystallization mechanisms and microstructure development in emerging metallic materials: A review," *Journal of Science: Advanced Materials and Devices*, vol. 4, no. 1, pp. 19–33, 2019.

[172] I. Manika and J. Maniks, "Effect of substrate hardness and film structure on indentation depth criteria for film hardness testing," *Journal of Physics D: Applied Physics*, vol. 41, no. 7, p. 074010, 2008.

[173] G. Tang, *Indentation analysis and mechanical modeling of multilayered composites*. PhD thesis, University of New Mexico, 2009.

[174] M. U. Abdullah, Z. A. Khan, and W. Kruhoeffer, "Evaluation of dark etching regions for standard bearing steel under accelerated rolling contact fatigue," *Tribology International*, vol. 152, p. 106579, 2020.

[175] R. Errichello, R. Budny, and R. Eckert, "Investigations of bearing failures associated with white etching areas (WEAs) in wind turbine gearboxes," *Tribology Transactions*, vol. 56, no. 6, pp. 1069–1076, 2013.

[176] V. Šmeļova, A. Schwedt, L. Wang, W. Holweger, and J. Mayer, "Microstructural changes in white etching cracks (WECs) and their relationship with those in dark etching region (DER) and white etching bands (WEBs) due to rolling contact fatigue (RCF)," *International Journal of Fatigue*, vol. 100, pp. 148–158, 2017.

[177] R. Osterlund, O. Vingsbo, L. Vincent, and P. Guiraldenq, "Butterflies in fatigued ball-bearings-formation mechanisms and structure," *Scandinavian Journal of Metallurgy*, vol. 11, no. 1, pp. 23–32, 1982.

[178] J.-H. Kang, B. Hosseinkhani, C. Williams, M. Moody, P. Bagot, and P. Rivera-Díaz-del Castillo, "Solute redistribution in the nanocrystalline structure formed in bearing steels," *Scripta Materialia*, vol. 69, no. 8, pp. 630–633, 2013.

[179] W. Liu, "The failure analysis of the repeat geartooth breakage in a 40 MW steam turbine load gearbox and the butterfly in the carburized case," *Engineering Failure Analysis*, vol. 46, pp. 9–17, 2014.

[180] W. Davies and K. Day, "Surface fatigue in ball bearings, roller bearings, and gears in aircraft engines," in *Proc. Symp. on 'Fatigue in rolling contact', London, UK*, pp. 23–40, 1963.

[181] Y. Murakami, M. Naka, A. Iwamoto, and G. Chatell, "Long life bearings for automotive alternator applications," tech. rep., SAE Technical Paper, 1995.

[182] N. Kino and K. Otani, "The influence of hydrogen on rolling contact fatigue life and its improvement," *JSAE review*, vol. 24, no. 3, pp. 289–294, 2003.

[183] W. Solano Alvarez, *Microstructural degradation of bearing steels.* PhD thesis, University of Cambridge, 2015.

[184] G. Krauss, "Martensite in steel: strength and structure," *Materials science and engineering: A*, vol. 273, pp. 40–57, 1999.

[185] Q. Luan, J. Wang, Y. Huang, D. S. Balint, and J. Jiang, "How would the deformation bands affect recrystallization in pure aluminium?," *Materials & Design*, vol. 209, p. 109960, 2021.

[186] Y. Tian, O. I. Gorbatov, A. Borgenstam, A. V. Ruban, and P. Hedström, "Deformation microstructure and deformation-induced martensite in austenitic Fe-Cr-Ni alloys depending on stacking fault energy," *Metallurgical and materials transactions A*, vol. 48, no. 1, pp. 1–7, 2017.

[187] S.-X. Li, P.-C. Zhao, Y.-N. He, and S.-R. Yu, "Microstructural evolution associated with shear location of aisi 52100 under high strain rate loading," *Materials Science and Engineering: A*, vol. 662, pp. 46–53, 2016.

[188] Y. Li, M. Herbig, S. Goto, and D. Raabe, "Formation of nanosized grain structure in martensitic 100Cr6 bearing steels upon rolling contact loading studied by atom probe tomography," *Materials Science and Technology*, vol. 32, no. 11, pp. 1100–1105, 2016.

[189] G. Gao, R. Liu, K. Wang, X. Gui, R. Misra, and B. Bai, "Role of retained austenite with different morphologies on sub-surface fatigue crack initiation in advanced bainitic steels," *Scripta Materialia*, vol. 184, pp. 12–18, 2020.

[190] R. Singh, A. Singh, P. K. Singh, and D. K. Mahajan, "Role of prior austenite grain boundaries in short fatigue crack growth in hydrogen charged rpv steel," *International Journal of Pressure Vessels and Piping*, vol. 171, pp. 242–252, 2019.

[191] J.-H. Kang and P. Rivera-Díaz-del Castillo, "Carbide dissolution in bearing steels," *Computational Materials Science*, vol. 67, pp. 364–372, 2013.

[192] V. Gavriljuk, "Decomposition of cementite in pearlitic steel due to plastic deformation," *Materials Science and Engineering: A*, vol. 345, no. 1-2, pp. 81–89, 2003.

[193] J. Languillaume, G. Kapelski, and B. Baudelet, "Cementite dissolution in heavily cold drawn pearlitic steel wires," *Acta Materialia*, vol. 45, no. 3, pp. 1201–1212, 1997.

[194] X. Sauvage, J. Copreaux, F. Danoix, and D. Blavette, "Atomic-scale observation and modelling of cementite dissolution in heavily deformed pearlitic steels," *Philosophical Magazine A*, vol. 80, no. 4, pp. 781–796, 2000.

[195] F. J. Humphreys and M. Hatherly, *Recrystallization and related annealing phenomena*. Elsevier, 2012.

[196] D. Moldovan, D. Wolf, S. R. Phillpot, and A. J. Haslam, "Grain rotation as a mechanism of grain growth in nanocrystalline materials," *Trends in Nanoscale Mechanics*, pp. 35–59, 2003.

[197] S. Bobylev and I. Ovid'ko, "Stress-driven rotations of high-angle grain boundaries in nanocrystalline materials," *Reviews on Advanced Materials Science*, vol. 35, no. 1/2, pp. 25–38, 2013.

[198] I. A. Ovid'ko, "Plastic deformation mechanisms in nanocrystalline metallic materials," *Journal of the Mechanical Behavior of Materials*, vol. 22, no. 3-4, pp. 81–88, 2013.

[199] B. Chen, L. Zhu, Y. Xin, and J. Lei, "Grain rotation in plastic deformation," *Quantum Beam Science*, vol. 3, no. 3, p. 17, 2019.

[200] Y. Li, M. Herbig, S. Goto, and D. Raabe, "Atomic scale characterization of white etching area and its adjacent matrix in a martensitic 100Cr6 bearing steel," *Materials Characterization*, vol. 123, pp. 349–353, 2017.

[201] D. Mayweg, L. Morsdorf, X. Wu, and M. Herbig, "The role of carbon in the white etching crack phenomenon in bearing steels," *Acta Materialia*, vol. 203, p. 116480, 2021.

[202] P. Chen, S. Mao, Y. Liu, F. Wang, Y. Zhang, Z. Zhang, and X. Han, "In-situ EBSD study of the active slip systems and lattice rotation behavior of surface grains in aluminum alloy during tensile deformation," *Materials Science and Engineering: A*, vol. 580, pp. 114–124, 2013.

[203] H. Bhadeshia, "Cementite," *International Materials Reviews*, vol. 65, no. 1, pp. 1–27, 2020.

Appendix A

The calculations mentioned in this section have been taken from Stachowiak and Batchelor [65] and Johnson [66]. The elliptical contact area formed due to the contact between the rolling element (ball) and inner ring raceway which is given by the semimajor axis (a) in the y direction and semiminor axis (b) in the x direction. Equation for calculating a and b is shown in Equation 10.1 and 10.2 respectively, while the contact area labels can be seen in Figure 10.1.

$$a = k_1 \left(\frac{3NR'}{E'} \right)^{\frac{1}{3}} \tag{10.1}$$

$$b = k_2 \left(\frac{3NR'}{E'} \right)^{\frac{1}{3}} \tag{10.2}$$

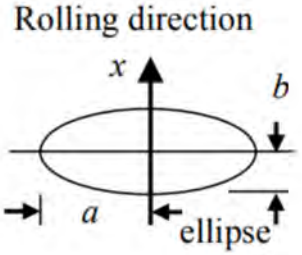

Figure 10.1: Schematic of elliptical contact area.

The reduced radius of curvature R' and reduced Young's modulus E' is determined using Equation 10.3 - 10.8. Details of all the notations used is shown in Table 10.1.

$$\frac{1}{R'} = \frac{1}{R_x} + \frac{1}{R_y} \tag{10.3}$$

$$\frac{1}{R_x} = \frac{1}{R_{ax}} + \frac{1}{R_{bx}} \tag{10.4}$$

$$\frac{1}{R_y} = \frac{1}{R_{ay}} + \frac{1}{R_{by}} \tag{10.5}$$

$$\frac{2}{E'} = \frac{1 - {v_1}^2}{E_1} + \frac{1 - {v_2}^2}{E_2} \tag{10.6}$$

For rolling elements that are spherical (ball), the radius is the same in both directions, hence $R_{ax} = R_{ay}$, therefore the contact coefficient k_0 can be calculated using Equation 10.7 which is then used in Figure 10.2 to determine the k_1 and k_2 coefficients graphically.

$$k_0 = \frac{\left(\frac{1}{R_{bx}} - \frac{1}{R_{by}} \right)}{\left(\frac{1}{R_{ax}} + \frac{1}{R_{ay}} + \frac{1}{R_{bx}} + \frac{1}{R_{by}} \right)} \tag{10.7}$$

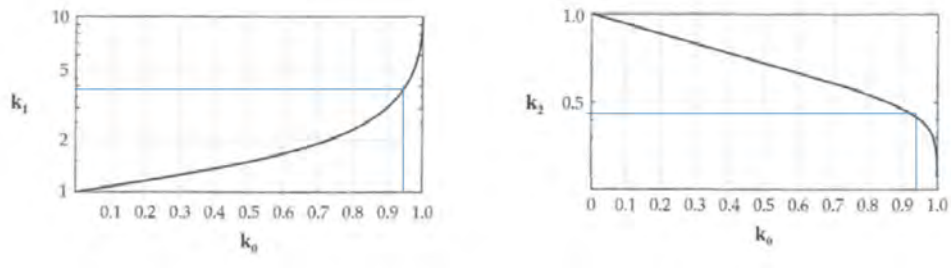

Figure 10.2: Graphs used to determine k_1 and k_2 based on calculated k_0 value.

Given the RCF-tested bearings in this study are axially loaded, the normal load on the inner

ring N used for the calculations is determined through the Equation 10.8.

$$N = \frac{\frac{F_a}{n}}{\sin\left(\frac{(180-\alpha)\pi}{180}\right)} \tag{10.8}$$

The maximum contact pressure P_0 can then be calculated using Equation 10.9:

$$P_0 = \frac{3N}{2\pi ab} \tag{10.9}$$

Table 10.1: Details of notations used in this section.

R'	Reduced radius of curvature (m)
R_x	Reduced radii of curvature in the x-direction (m)
R_y	Reduced radii of curvature in the y-direction (m)
R_{ax}	Radius of curvature of the rolling element (ball) in x direction (m)
R_{ay}	Radius of curvature of the rolling element (ball) in y direction (m)
R_{bx}	Radius of curvature of inner raceway in x direction (m)
R_{ay}	Radius of curvature of inner raceway in y direction (m)
k_0, k_1, k_2	Contact coefficients
E'	Reduced Young's modulus (Pa)
E_1	Young's modulus of rolling element (Pa)
E_2	Young's modulus of raceway (Pa)
N	Normal load acting on inner ring (Pa)
P_0	Maximum contact pressure (Pa)
F_a	Axial load acting on bearing (N)
n	number of rolling elements in bearing
α	Contact angle (degrees)

Subsurface Stresses:

The normal principal stresses σ_x, σ_y and σ_z are calculated using Equations 10.10 - 10.12 from Johnson [66].

$$\frac{\sigma_x}{P_0} = \frac{2b}{e^2 a}\left(\Omega_x - \nu\Omega'_x\right) \tag{10.10}$$

$$\frac{\sigma_y}{P_0} = \frac{2b}{e^2 a}\left(\Omega_y - \nu\Omega'_y\right) \tag{10.11}$$

$$\frac{\sigma_z}{P_0} = -\frac{b}{e^2 a}\left(\frac{1-T^2}{T}\right) \tag{10.12}$$

$$\Omega_x = -\frac{1}{2}(1-T) + \zeta\{F(\phi,e) - E(\phi,e)\} \tag{10.13}$$

$$\Omega'_x = 1 - \left(\frac{a^2 T}{b^2}\right) + \zeta\{\left(\frac{a^2}{b^2}\right)E(\phi,e) - F(\phi,e)\} \tag{10.14}$$

$$\Omega_y = \frac{1}{2} + \frac{1}{2T} - \left(\frac{a^2 T}{b^2}\right) + \zeta\{\left(\frac{a^2}{b^2}\right)E(\phi,e) - F(\phi,e)\} \tag{10.15}$$

$$\Omega'_y = -1 + T + \zeta\{F(\phi,e) - E(\phi,e)\} \tag{10.16}$$

$$T = \left(\frac{b^2+z^2}{a^2+z^2}\right)^{\frac{1}{2}} \tag{10.17}$$

$$\zeta = \frac{z}{a} = \cot\phi \tag{10.18}$$

$$e = 1 - \left(\frac{b^2}{a^2}\right)^{\frac{1}{2}} \tag{10.19}$$

The elliptical integrals of first kind F(ϕ,e) and second kind E(ϕ,e) are determined using Equations 10.20 and 10.21.

$$F(\phi, e) = \int_0^{\phi} \frac{d\phi}{\sqrt{1 - e^2 (\sin \phi)}} \tag{10.20}$$

$$E(\phi, e) = \int_0^{\phi} \sqrt{1 - e^2 (\sin \phi)}\, d\phi \tag{10.21}$$

Once, the principal stresses are calculated, the von Mises σ_{vM} stress can be calculated using Equation 10.22, where from the three principal stresses calculated follow the sequence of $\sigma_I < \sigma_{II} < \sigma_{III}$.

$$\sigma_{vM} = \sqrt{\frac{(\sigma_I - \sigma_{II})^2 + (\sigma_{II} - \sigma_{III})^2 + (\sigma_{III} - \sigma_I)^2}{2}} \tag{10.22}$$

The principal shear stress τ_{45} is calculated in Equation 10.23. The orthogonal shear stress τ_0 analysed in this thesis is in the xz plane (y=0) based on the coordinates shown in Figure 10.1. Hence the orthogonal shear stress τ_{xz} is determined using Equation 10.24 across depth z at the location of the maximum stress value when x=0.87b.

$$\tau_{45} = \frac{\sigma_{III} - \sigma_I}{2} \tag{10.23}$$

$$\tau_{xz} = -\frac{ax}{b^2}\left(\frac{z}{b}\right)^2 \frac{\left(\left(1 + \frac{\lambda_1}{b^2}\right)\frac{\lambda_1}{b^2}\right)^{-1.5}\left(1 + \frac{\lambda_1}{b^2}\right)^{-0.5}}{\left(\frac{bx}{b^2+\lambda_1}\right)^2 + \left(\frac{bz}{\lambda_1}\right)^2} \tag{10.24}$$

Where λ_1 is the positive root of Equation 10.25:

$$\frac{x^2}{a^2 + \lambda} + \frac{y^2}{b^2 + \lambda} + \frac{z^2}{\lambda} = 1 \tag{10.25}$$

The subsurface stresses for the bearing samples in this study tested under contact pressure P_0 of 2.9 GPa is shown in Figure 10.3.

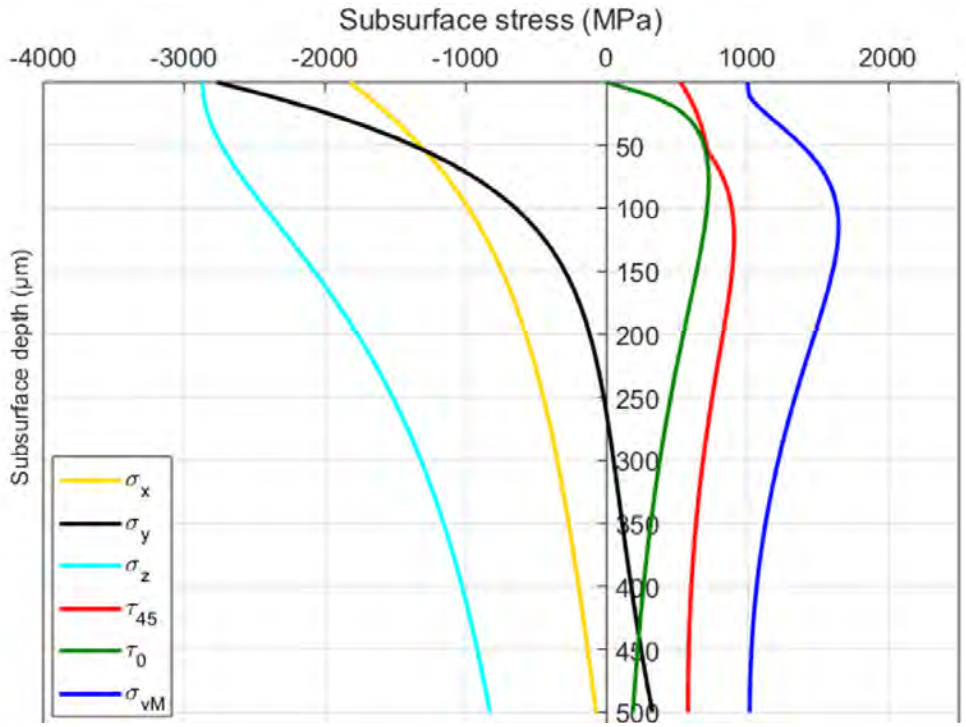

Figure 10.3: Subsurface stress distribution vs depth.

Appendix B

100Cr6 Martensite, Cleanliness A, 2.9 GPa

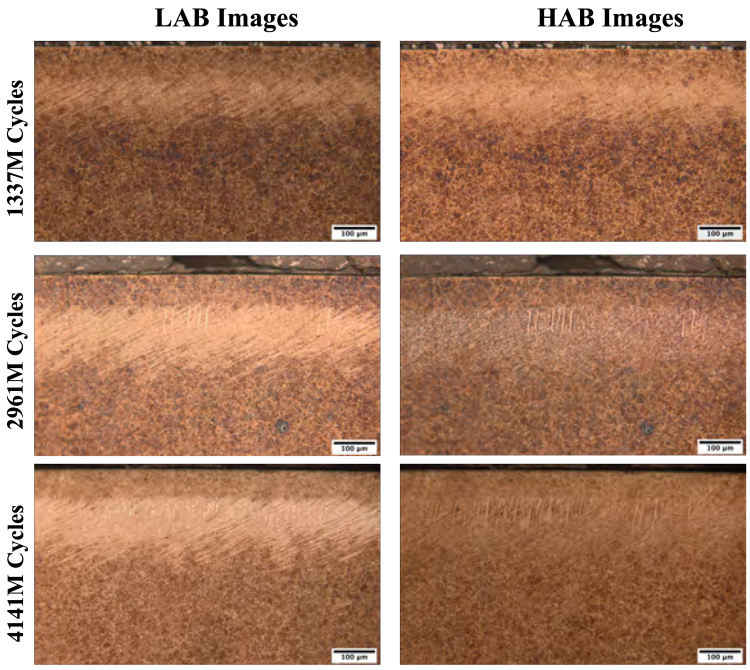

100Cr6 Bainite, Cleanliness B, 2.9 GPa

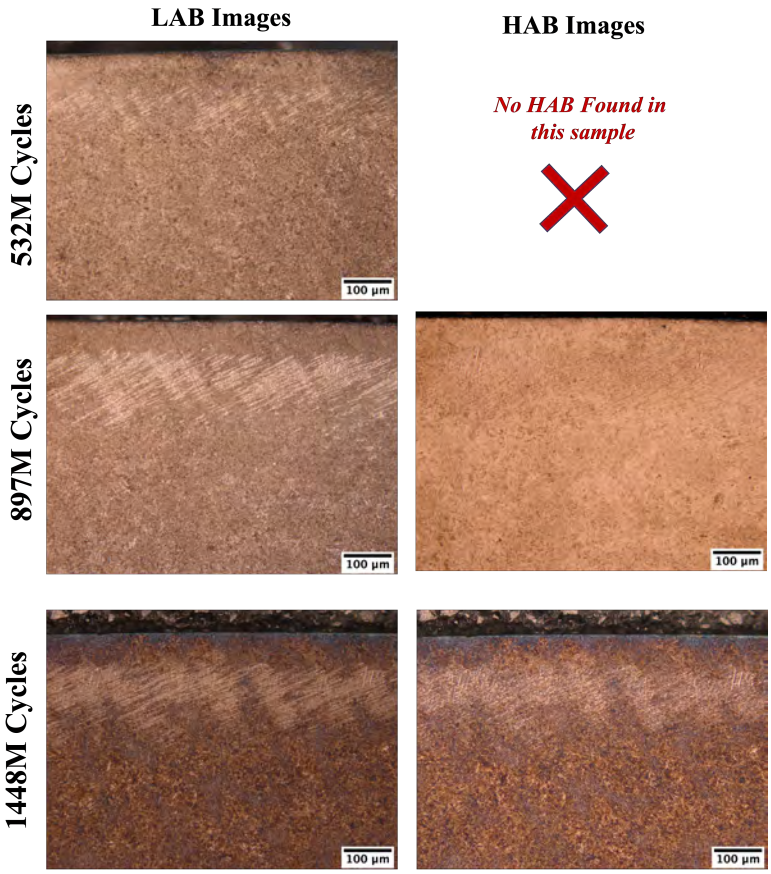

Appendix C

Logarithmic regression is conducted using equation 10.26 to determine the trend line for different variables.

$$y = A + Bln(x) \tag{10.26}$$

Where y is the contact pressure (GPa) and x is the variable being analysed (which is x_0 and dx as discussed in Chapter 5). The constants A and B are determined using equations 10.27 and 10.28 respectively.

$$A = \overline{y} - B\overline{ln(x)} \tag{10.27}$$

$$B = \frac{S_{xy}}{S_{xx}} \tag{10.28}$$

The sum of square values of S_{xx} and S_{xy} can be determined using equations 10.29 and 10.30 below.

$$S_{xx} = \sum [ln(x_i)]^2 - n \cdot \overline{ln(x)}^2 \tag{10.29}$$

$$S_{xy} = \sum ln(x_i)y_i - n \cdot \overline{ln(x)} \cdot \overline{y} \tag{10.30}$$

Using the values of x_0 for 2.9 GPa and 3.5 GPa shown in Table 5.1 would give A = 445 and B = -21.5. While using the values of dx for 2.9 GPa and 3.5GPa would give the values A = -20.34 and B=1.2. Hence Replacing the constant values back into Equation 10.26, the x variable (x_0 or dx) can be determined for different contact pressures (y value) as shown in Figure 10.4.

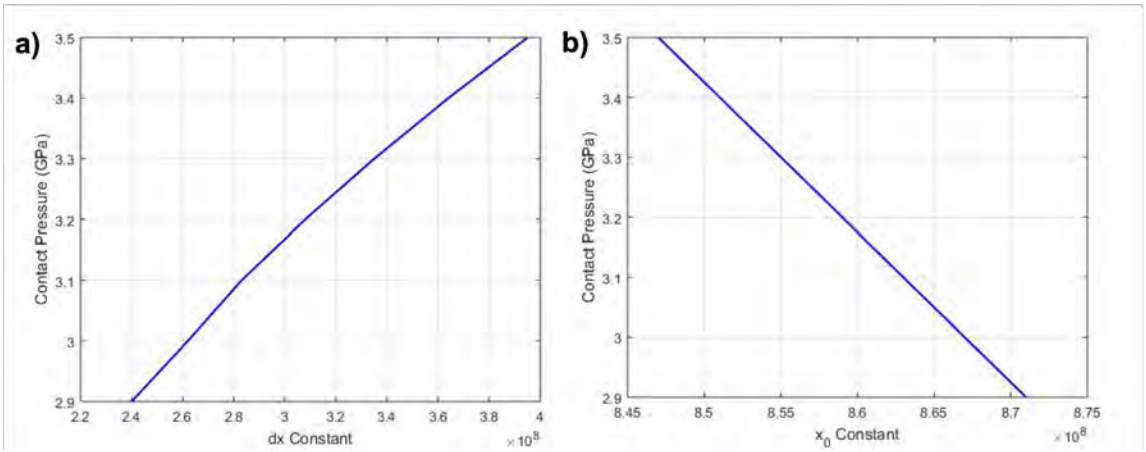

Figure 10.4: Graphs showing how a) dx and b) x_0 vary with contact pressure based on logarithmic regression.

Appendix D

Figure 10.5 below shows the location of the indents selected (labelled A-D) to plot the load-displacement graphs for each feature for comparison.

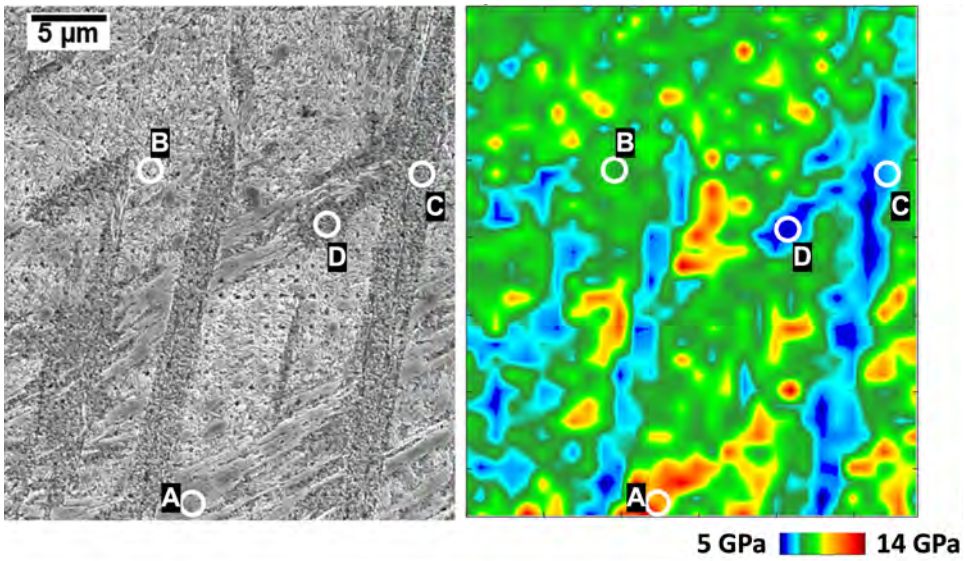

Figure 10.5: SEM and hardness map from Figure 7.19 where locations are circled to indicate the position of the indents used to plot the load-displacement graph.

In Figure 10.5, Indent from region A is selected to represent the lenticular carbides, B corresponds to the parent matrix (martensite), region C for equiaxed ferrite grains and region D for elongated ferrite grains. The load-displacement curves from the 4 indents are shown in Figure 10.6.

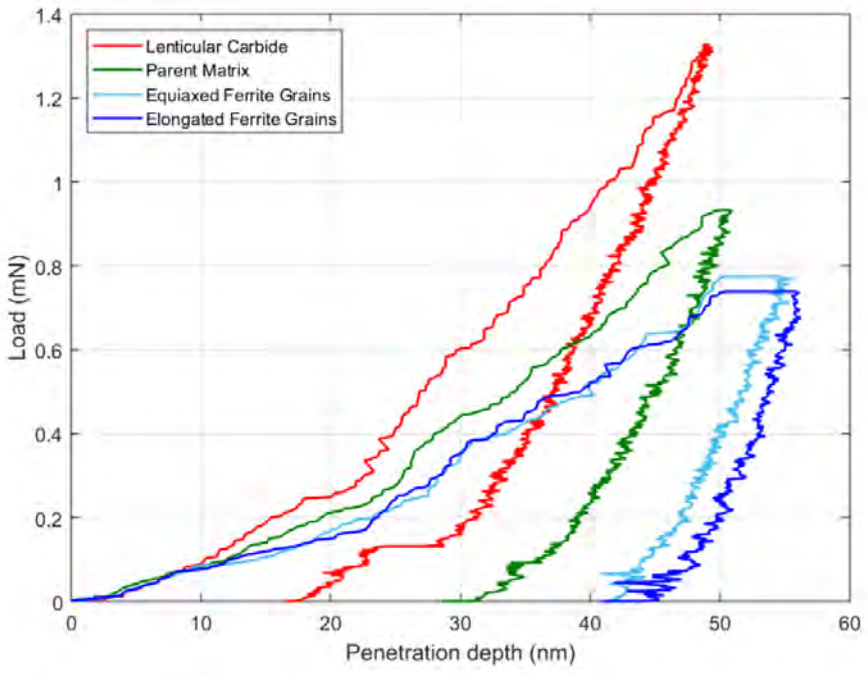

Figure 10.6: Load-displacement graphs from nanoindentation tests for lenticular carbides, parent matrix, equiaxed ferrite grains and elongated ferrite grains in WEB. Locations of each indent is from regions A-D respectively in Figure 10.5.

Appendix E

The calculated interplanar spacing (d) shown in Table 10.2 is calculated from the measured radius of the diffraction rings (r) in the areas highlighted in Figure 7.28 using Equation 10.31. These values are then compared to the theoretical d spacings of ferrite and cementite structures calculated later.

$$d = \frac{1}{2r} \tag{10.31}$$

Table 10.2: Detected interplanar d spacings measured in Area A-D.

Measured Interplanar d spacing (Å)			
Area A	**Area B**	**Area C**	**Area D**
2.02	2.32	2.03	2.01
1.49	2.11	1.44	1.47
1.19	2.02	1.17	1.17
1.02	1.87	1.02	1.02
0.92	1.60	0.92	0.91
0.78	1.43	0.84	0.83
	1.19	0.78	0.77
	1.01		
	0.91		
	0.83		
	0.77		

Theoretical d spacing of Ferrite (BCC):

Theoretical d spacing of ferrite shown in Table 10.3 is calculated based on Equation 10.32 using the lattice parameter a shown below [124] and the miller indices (hkl):

Lattice Parameter	Value (Å)
a	2.867

$$\frac{1}{d^2} = \frac{1}{a^2}(h^2 + l^2 + k^2) \tag{10.32}$$

Table 10.3: Interplanar d spacings calculated for BCC ferrite.

(hkl)	**Theoretical Interplanar d spacing (Å)**
110	2.03
002	1.43
121	1.17
022	1.01
031	0.91
222	0.83
123	0.77

Theoretical d spacing of Cementite (Orthorhombic):

Theoretical d spacing of cementite (Table 10.4) is calculated based on Equation 10.33 using the lattice parameters a, b and c (values shown below) and the miller indices (hkl) [203]:

Lattice Parameter	Value (Å)
a	4.5165
b	5.0837
c	6.7475

$$\frac{1}{d^2} = \frac{h^2}{a^2} + \frac{l^2}{b^2} + \frac{k^2}{c^2} \tag{10.33}$$

Table 10.4: Interplanar d spacings calculated for orthorhombic cementie.

(hkl)	**Theoretical Interplanar d spacing (Å)**
112	2.39
021	2.38
200	2.26
120	2.22
121	2.10
210	2.06
022	2.03
103	2.01
211	1.97
113	1.87
122	1.85
312	1.33
313	1.21
233	1.16
433	0.87
336	0.80
345	0.79
163	0.78

Appendix F

Journal Papers:

- M. El Laithy, L.Wang, Ling, T.J. Harvey, A.Schwedt, B.Vierneusel, J.Mayer, 'White Etching Bands Formation Mechanisms due to Rolling Contact Fatigue'. Acta Materialia (2021) – Under Review
- M.El Laithy, L.Wang, T.J. Harvey, B.Vierneusel, "Semi-empirical model for predicting LAB and HAB formation in Bearing Steel". International Journal of Fatigue, p. 106230, 2021
- M.El Laithy, L.Wang, T.J. Harvey, B.Vierneusel, "Re-investigation of dark etching regions and white etching bands in SAE 52100 bearing steel due to rolling contact fatigue". International Journal of Fatigue, p. 105591, 2020
- M.El Laithy, L.Wang, T.J. Harvey, B.Vierneusel, M.Correns and T.Blass, "Further understanding of rolling contact fatigue in rolling element bearings - a review" Tribology International, p. 105849, 2019

Conference Proceedings:

- "Rolling Contact Fatigue Induced Transformations of Dark Etching Region and White Etching Bands in Bearing Steels"
  M. El Laithy, L.Wang, T.Harvey, A. Schwedt, B.Vierneusel, J. Mayer
  7th World Tribology Congress, 10-15 July 2022, Lyon, France. Contribution: Accepted for Oral Presentation
- "Formation Mechanisms of Dark Etching Region in Bearing Steels due to Rolling Contact Fatigue"

  M. El Laithy, L.Wang, T.Harvey, A. Schwedt, B.Vierneusel, J. Mayer 76th STLE Annual Meeting and Exhibition, Orlando, Florida, USA
  Contribution: Accepted for Oral Presentation
- "Mechanistic Study of white etching bands formation in bearing steel due to RCF"
  M. El Laithy, L.Wang, T.Harvey, A. Schwedt, B.Vierneusel, J. Mayer
  75th STLE Annual Meeting and Exhibition Virtual Event, 17-20 May 2021
  Contribution: Virtual Presentation
- "Investigation of Formation Mechanism of White Etching Bands in SAE 52100 steel bearings"
  M. El Laithy, L.Wang, T.Harvey, B.Vierneusel
  2020 STLE Tribology Frontiers Virtual Conference, 8-11 November 2020
  Contribution: Virtual Presentation
- "Re-investigation of DER and WEBs in bearing steel due to Rolling Contact Fatigue"
  M. El Laithy, L.Wang, T.Harvey, B.Vierneusel
  28th Mission of Tribology, Institute of Mechanical Engineerins (IMechE), London, UK, 11 December 2019
  Contribution: Oral Presentation
- "Investigation of Subsurface Microstructural Alterations in Steel Bearings Due to Rolling Contact Fatigue"
  M. El Laithy, L.Wang, T.Harvey, B.Vierneusel
  46th Leeds-Lyon Symposium on Tribology, Lyon, France, 2-4 September 2019
  Contribution: Oral Presentation
- "The Evolution of Dark Etching Regions and White Etching Bands in Bearing Steels due to Rolling Contact Fatigue"
  M. El Laithy, L.Wang, T.Harvey, B.Vierneusel, M.Correns, T.Blass
  74th STLE Annual Meeting and Exhibition, Nashville, Tennessee, USA 19-23 May 2019
  Contribution: Oral Presentation and Poster
- "Investigation of Dark Etching Regions and White Etching Bands in Bearing Steel due to Rolling Contact Fatigue"
  M. El Laithy, L.Wang, T.Harvey, B.Vierneusel
  The Institute of Engineering and Technology: New Challenges in Tribology, IET Birmingham: Austin Court, 27-28 March 2019
  Contribution: Poster

- "The Evolution of Subsurface Microstructural Alterations in Steel Bearings during Rolling Contact Fatigue"
  M. El Laithy, L.Wang, T.Harvey, B.Vierneusel, M.Correns, T.Blass
  PGR Engineering Faculty Conference, Southampton, UK, 15 January 2019
  Contribution: Oral Presentation

Grants and Awards:

- Recipient of STLE Best Young Presenter Award 2021 at 75th STLE Annual Meeting and Exhibition Conference.
- Royce Student Equipment Access Scheme grant of £5,000 for APT analysis at Oxford University 2020
- Recipient of the 28th Mission of Tribology Prize 2019 awarded by IMechE for best presentation.
- Awarded 'Peter Jost Travel Fund' 2019 for attending STLE conference in May 2019 for £1,500.
- Awarded 2nd Place in student poster competition at The Institute of Engineering and Technology (IET): New Challenges in Tribology conference 2019.